Activity and degradation mechanisms of anodic electrocatalysts for the direct borohydride fuel cell

Clémence Lafforgue

Communauté
UNIVERSITÉ Grenoble Alpes

THÈSE

Pour obtenir le grade de

DOCTEUR DE LA COMMUNAUTE UNIVERSITE GRENOBLE ALPES

Spécialité : **Matériaux, Mécanique, Génie civil, Electrochimie**

Arrêté ministériel : 25 mai 2016

Présentée par

Clémence LAFFORGUE

Thèse dirigée par **Marian CHATENET, Professeur, Grenoble-INP**

préparée au sein du **Laboratoire d'Electrochimie et de Physicochimie des Matériaux et des Interfaces (LEPMI)**

dans l'École Doctorale **Ingénierie – Matériaux, Mécanique, Energétique, Environnement, Procédés, Production (I-MEP^2)**

Activité et mécanismes de dégradation d'électrocatalyseurs anodiques pour la pile directe à borohydrures

Activity and degradation mechanisms of anodic electrocatalysts for the direct borohydride fuel cell

Thèse soutenue publiquement le **28 octobre 2019** devant le jury composé de :

Mme Elena SAVINOVA
Professeur, Université de Strasbourg (Présidente du jury)
M. Christophe COUTANCEAU
Professeur, Université de Poitiers (Rapporteur)
M. Carlos PONCE de LEON
Maître de conférence, Université de Southampton (Rapporteur)
M. Fabien VOLPI
Maître de conférences, Grenoble-INP (Examinateur)
Mme Karen SWIDER-LYONS
Section head – Alternative Energy section, U.S. Naval Research Laboratory (Invitée)
M. Marian CHATENET
Professeur, Grenoble-INP (Directeur de thèse)

Remerciements

Il me tient à cœur de remercier toutes les personnes qui m'ont permis de réaliser ce travail de thèse, et qui ont contribué, chacune à sa manière, à ce que cette expérience soit très enrichissante et pleine de bons souvenirs ☺

Tout d'abord, je souhaite adresser un grand merci à Marian : merci de m'avoir accordé ta confiance pour mener à bien ce projet de thèse, et pour m'avoir accompagné tout au long de ce parcours semé de diverses difficultés. Merci d'avoir toujours su dégager rapidement des créneaux pour moi dans ton emploi du temps de ministre, pour répondre à mes questions, apaiser mes doutes (si nombreux !), et partager tes connaissances. Je te suis également reconnaissante pour m'avoir permis de participer à des conférences internationales, qui m'ont permis de prendre plus confiance en moi. Je suis fière du chemin parcouru, et heureuse d'avoir fait équipe avec toi pendant ces trois années !

Je remercie également Frédéric et Laetitia, pour m'avoir épaulé sur toute la partie « durabilité ». Fred, un grand merci pour ton investissement et la motivation dont tu as fait preuve avec les mesures infrarouge (qui nous ont donné bien du mal !), mais aussi pour ta rigueur scientifique ; Laetitia, merci beaucoup pour ton aide en microscopie, et pour ta positivité inaltérable. Un grand merci aussi pour votre implication dans la rédaction de l'article, votre aide m'a toujours été précieuse.

Je voudrais remercier les autres membres de l'équipe avec lesquels j'ai moins interagi sur le plan scientifique, mais dont la présence au laboratoire a été agréable, et pour leur bienveillance à mon égard notamment lors de la rédaction. Je remercie également Jean-Claude, pour ton énergie et ta bonne humeur !

Je souhaite vivement remercier l'ensemble des membres du jury, M. Christophe Coutanceau, M. Carlos Ponce de Leon, Mme Elena Savinova et M. Fabien Volpi, pour avoir accepté d'évaluer ce travail de thèse, et pour l'avoir fait de manière pertinente, constructive et bienveillante.

J'aimerai continuer ces remerciements en adressant un chaleureux merci à Thierry Encinas et Vincent Martin pour leur soutien technique avec les mesures DRX et XPS.

A toute l'équipe administrative du LEPMI, Claire, Claire, Yasmine et Corine, un grand merci pour avoir géré mes déplacements, pour avoir rattrapé mes bêtises administratives, pour votre

soutien lors de l'organisation de divers événements du laboratoire, et enfin, pour avoir si gentiment pensé à moi lorsque quelques babas au rhum abandonnés trainaient dans le frigo !

Let's flight over the Atlantic to land at Washington: a warm thank you to the NRL team, more specifically Karen, Marielle, Rob and Yannick, for our fruitful discussions during the project, and for your welcome in your lab during a few days.

Passons maintenant à toutes les personnes qui ont partagé mon quotidien au sein du laboratoire, mais aussi en dehors, que ce soit pour des virées au bar, des escape game, des via ferrata, ou des soirée jeux : ces trois années auraient été bien différentes sans vous ! Je voudrais commencer par mes compagnons de thèse, Marion et Fabien. Pour votre motivation et votre acharnement qui m'ont souvent inspiré, pour votre soutien dans les moments difficiles, pour toutes nos longues discussions, pour votre compagnie lors des conférences, pour votre bienveillance à mon égard, et pour les encouragements lors de la rédaction : merci ! J'ai évidemment une pensée pour Mathieu : tu n'as partagé qu'une seule année à nos côtés, mais je pense que mon quota de fous rires n'aura jamais été si élevé en ta compagnie ! A tous ceux qui m'ont accueilli quand je suis arrivée au LEPMI : Fanny, Gwenn, Anicet, Matthieu, Céline, Raph, Tristan, Charles, Alice, Juan, François, Rémi et Vincent, merci d'avoir partagé vos connaissances en tout genre et de m'avoir initié aux pratiques de l'électrochimie, et pour avoir facilité mon insertion dans l'équipe. Ma Fanny, ma copine, il ne nous aura pas fallu longtemps pour découvrir que le courant passe si bien entre nous ; merci pour ton amitié, ta générosité, et pour ce don que tu as de prendre les choses toujours du bon côté ! Comment ne pas faire également une mention spéciale à Tristan ?! Parce que nos caractères n'ont pas toujours été compatibles et qu'ils ont été source de tensions (bonne ambiance dans le bureau garantie !), mais parce que mine de rien, on a grandi, l'un et l'autre, grâce à ces quelques conflits, qui nous font sourire aujourd'hui ☺.

Merci à tous ceux qui sont arrivés en cours de route : Guillaume (mon compagnon de la BOR, merci pour ton soutien scientifique avec ces *** de boro, et pour m'avoir supporté (moi et mon rire discret…) pendant 3 ans dans le bureau !), Marine (pour m'avoir aidé à « limer » mes mails un tant soit peu **AGRESSIFS** ;), pour ton écoute attentive, tes conseils et ton accompagnement si précieux pendant la rédaction), Jérôme (pour m'avoir subtilement forcé à manger des Haribo !!!), Vivien (mon compagnon écolo, merci pour toutes nos discussions sur la construction d'un avenir plus durable), Killian (parce que les Bretons sont partout et qu'ils savent nous le rappeler), Maha (parce que j'adore ta force de caractère), Eris (tu es un cavalier de danse juste parfait !), Kavita (merci pour ta douceur, ta simplicité, et ta bonne humeur), Sofyane (merci pour

ta gentillesse et ton écoute attentive), Marie (pour ta crème de marron juste incroyablement délicieuse !), Delphine (merci pour ton sourire et la bonne énergie que tu dégages) et Estelle (enfin une personne avec qui écouter du Magic System et du Enrique Iglesias !!). A vous tous, un grand merci du fond du cœur ♥

En dehors du laboratoire, j'adresse un grand merci à la fine équipe des « poivrots du dimanche », pour m'avoir permis de décompresser autour d'une bonne bière, ou lors de nos randonnées à travers les massifs alpins. Un grand merci aussi à Milène, qui, malgré la distance, sait toujours me redonner le sourire et la motivation ! A ma famille, Papa, Maman, Violaine, Aurore et Manette, pour qui la science (tout du moins l'électrochimie) reste souvent un mystère : merci pour votre soutien, votre écoute, vos encouragements et votre amour. Pour finir, merci à Thibaud, pour tout l'amour que tu me portes, pour ta patience et pour ton soutien sans faille à chacune des petites ou grandes épreuves de ma vie.

Table of content

List of symbols and abbreviations **10**

General introduction **12**

CHAPTER I ENERGETIC CONTEXT AND DBFC TECHNOLOGY **15**

I.1 Global warming: the need for an energetic transition **17**

I.1.1 Humankind, energy and environmental consequences 17

I.1.2 Fuel cells overview and applications 19

I.1.3 Hydrogen, a very popular energetic vector 21

I.2 The direct borohydride fuel cell **22**

I.2.1 Operating principle, interest and technological issues 22

I.2.2 Production of sodium borohydride 26

I.2.3 Recent advances and remaining challenges 28

I.3 Stability issues and degradation mechanisms in alkaline fuel cells **39**

I.3.1 Anodic electrocatalysts do age upon DBFC operation 39

I.3.2 PEMFC electrocatalysts degradation mechanism 42

I.3.3 First steps towards the fate of electrocatalyst degradation in alkaline media 44

I.4 Conclusions and PhD outline **49**

CHAPTER II PALLADIUM-BASED ELECTROCATALYSTS FOR THE BOR **51**

II.1 Motivations of the study **53**

II.1.1 BOR on Pd/C electrocatalysts 53

II.1.2 BOR on Pd/C-CeO_2 electrocatalyst 54

II.2 Experimental details **56**

II.2.1 Electrocatalysts 56

II.2.2 Morphological characterizations 56

II.2.3 Electrochemical measurements 56

II.3 Analysis of the electrocatalysts morphology **59**

II.3.1 TEM micrographs 59
II.3.2 XRD diffraction patterns 61

II.4 Electrochemical surface area measurements 63
II.4.1 Existing and possible methods for Pd surfaces 63
II.4.2 Comparison of $ECSA_{PdO}$ and $ECSA_{CO}$ 68

II.5 Study of the BOR activity on the Pd-based electrocatalysts 70
II.5.1 Electrochemical behavior 70
II.5.2 Activity markers 79
II.5.3 Influence of the $NaBH_4$ concentration 85
II.5.4 Influence of the temperature 88
II.5.5 Influence of the catalytic layer thickness 91

II.6 Conclusions 95

CHAPTER III IMPACT OF THE CATALYTIC LAYER DESIGN ON THE BOR ACTIVITY 97

III.1 Motivations of the study 99

III.2 Experimental details 100
III.2.1 RDE configuration 100
III.2.2 Fuel cell configuration 102

III.3 Analysis of the electrocatalysts morphology 108

III.4 Impact of the catalytic layer on the BOR activity 110
III.4.1 RDE configuration measurements 110
III.4.2 H_2O_2-DBFC configuration measurements 115

III.5 Conclusions 127

CHAPTER IV DEGRADATION OF CARBON-SUPPORTED PGM ELECTROCATALYSTS IN ALKALINE MEDIA 129

IV.1 Motivations of the study 131

IV.1 Experimental details 133
IV.1.1 Electrocatalysts 133

IV.1.2 Physical and chemical characterizations 133
IV.1.3 Electrochemical measurements 134

IV.2 Preliminary study 139
IV.2.1 Influence of the potential range 139
IV.2.2 Influence of the alkali-metal cation of the electrolyte 143
IV.2.3 Exploratory measurements using *in situ* FTIR spectroscopy 145

IV.3 Insights into the degradation mechanism 147
IV.3.1 *In situ* FTIR spectroscopy on Pt/C 147
IV.3.2 Does the degradation of Pt/C come from a Pt-assisted local corrosion? 152
IV.3.3 CO_{ads}-electrooxidation on polycrystalline Pt 155

IV.4 Towards a generalization of the degradation mechanism 156

IV.5 Conclusions 163

General conclusion and outlook 165

Annex 173

References 185

List of symbols and abbreviations

Symbols

$\overline{d_n}$	Mean particle size (nm)
$\overline{d_s}$	Surface averaged particle size (nm)
E	Potential (V)
$E°_{M+/M}$	Standard equilibrium potential of the M^+/M redox couple (V)
H_{UPD}	Hydrogen under potential deposition
I	Current (A)
j	Current density (A cm^{-2})
PdO	Palladium oxides
Q_{PdO}	Coulometry charge during PdO reduction (C)
Q_{CO}	Coulometry charge during CO oxidation (C)
T	Temperature (°C)
v	Potential scan rate (V s^{-1})
μ_{CO}	First moment of the potential weight of the CO_{ads}-stripping (V)
ω	Rotation rate (rpm)
Hz	Hertz

Abbreviations

AEM	Anion-Exchange Membrane
AFC	Alkaline Fuel Cell
AST	Accelerated Stress Test
CEM	Cation-Exchange Membrane
CL	Catalytic Layer
CNT	Carbon NanoTube
CV	Cyclic Voltammetry (technique) or Cyclic Voltammogram (plot)
DEMS	Differential Electrochemical Mass Spectroscopy
DMFC	Direct Methanol Fuel Cell
ECSA	ElectroChemical Surface Area
FC	Fuel Cell
FTIR	Fourier-Transform Infrared

GC	Glassy Carbon
HER	Hydrogen Evolution Reaction
HOR	Hydrogen Oxidation Reaction
HSAC	High Surface Area Carbon
IL-TEM	Identical-Location Transmission Electron Microscopy
MA	Mass Activity
NHE	Normal Hydrogen Electrode
NP	NanoParticle
OCP	Open Circuit Potential
OCV	Open Circuit Voltage
ORR	Oxygen Reduction Reaction
PEM	Proton Exchange Membrane
PEMFC	Proton Exchange Membrane Fuel Cell
PFSA	PerFluoroSulfonic Acid
PGM	Platinum Group Metal
PSD	Particle Size Distribution
RDE	Rotating Disk Electrode
RHE	Reversible Hydrogen Electrode
Rpm	Revolution Per Minute
RRDE	Rotating Ring Disk Electrode
SA	Specific Activity
STEM	Scanning Transmission Electron Microscopy
TEM	Transmission Electron Microscopy
UPD	Under Potential Deposition
X-EDS	X-ray Energy Dispersive Spectroscopy
XPS	X-ray Photoelectron Spectroscopy
XRD	X-Ray Diffraction

General introduction

At a time where the energetic transition is at the core of political discussions, the development of new systems of energy production is more than ever essential. Indeed, this would enable to decrease the greenhouse gases emissions linked to fossil fuel combustion and to limit global warming and the subsequent climatic crisis. To that goal, the main strategy currently considered by the scientific community is to use renewable energies (via wind turbines and solar panels), and to store the generated electricity in, for example, batteries. Such storage is to mitigate the intermittent characteristic of renewable energies; however, batteries are limited by their intrinsic low specific energy. So, power-to-hydrogen via water electrolyzers, and then on-demand consumption of hydrogen in fuel cells could be an alternative. The most developed fuel cell to date is the proton-exchange membrane fuel cell (PEMFC). The widespread commercialization of such system for mobile devices is mostly hindered by hydrogen transport and storage issues. In parallel to hydrogen, other fuels were studied, such as sodium borohydride, which can feed the so-called direct borohydride fuel cell (DBFC). Being stored and transported in its liquid or solid form, this fuel enables to avoid the issues linked to hydrogen gas storage and transportation; but above all, sodium borohydride offers to the DBFC very interesting thermodynamic and energetic properties: high theoretical cell voltage, high theoretical specific energy and high number of mole of electrons (8) exchanged per mole of fuel. To date, the main impediment to the DBFC development is the complexity of the anodic reaction, the borohydride oxidation reaction (BOR). This reaction is misunderstood and poorly-efficient on most electrocatalysts (most of them are in the form of metal nanoparticles supported on carbon black) in DBFC operating conditions (*i.e.* high concentration and high temperature), due to side reactions, such as the borohydride hydrolysis and the hydrogen evolution reaction (at low potential), both leading to the production and eventually escape of hydrogen.

In addition, recent studies reported the aggressiveness of the alkaline medium on the durability of conventional carbon-supported electrocatalysts, revealing a large loss of the active catalytic surface, mainly due to the detachment of nanoparticles from the carbon support. However, fundamental insights on the origin of this particles detachment are still unclear.

Therefore, this PhD work was motivated by several questions:

- How do high fuel concentration and high temperature impact the BOR on carbon-supported Pd-based electrocatalysts?

- How the design of electrode architecture can impact the BOR efficiency and boost the subsequent DBFC performances?
- What is the origin of the particles detachment that occurs during a mild accelerated stress test on carbon-supported Pt electrocatalysts in liquid alkaline media?

To find answer to those questions, this PhD project was carried out in close collaboration with the group of Dr. Karen Swider-Lyons, from the U.S. Naval Research Laboratory (Washington DC, USA), who have good skills and knowledge in membrane-electrode assemblies, porous electrode, and the characterization of fuel cells, while LEPMI team and especially Pr. Marian Chatenet, has studied the kinetics and mechanism of the BOR extensively, for over a decade. Therefore, this project was a good opportunity to combine NRL and LEPMI expertise to explore the complex BOR.

The results obtained are presented in this manuscript, which is composed of four chapters:

- **Chapter I** presents the energetic context and a DBFC overview. Specifically, the operating principle of the DBFC and technological issues are given, as well as the production routes of sodium borohydride, the recent advances and remaining challenges regarding the anodic and cathodic electrocatalysts and the membrane in such systems; in addition, stability issues and degradation mechanisms in alkaline fuel cell are also presented;
- **Chapter II** deals with a thorough characterization of several carbon-supported Pd-based electrocatalysts for the BOR in DBFC operation conditions; the influence of several parameters on the BOR kinetics are surveyed, such as the Pd sites density, the presence of ceria and the catalytic layer thickness; in addition, BOR activity markers are proposed;
- **Chapter III** focuses on the study of the impact of five design of anodic catalytic layers on the BOR efficiency, based on carbon–supported Pt and Pd electrocatalysts, first using a fundamental approach and then using a unit DBFC;
- Finally, **chapter IV** deals with the investigation of the origin of the particles detachment occurring during the degradation of carbon-supported PGM electrocatalysts, using mostly *in situ* Fourier transform infrared spectroscopy and identical-location transmission electron microscopy.

Chapter I

Energetic context and DBFC technology

I.1 Global warming: the need for an energetic transition

I.1.1 Humankind, energy and environmental consequences

Like any living beings on Earth, humans cannot live without energy. Since the dawn of times, humans need energy mainly for eating, heating and traveling, and the evolution of human societies is very closely linked to the discovery of the different sources of energy. If the first humans could only rely on their own muscles' strength, they later learned to use other primary sources of energy such as wind, water, sun, wood, coal, oil, gas, elements from earth's crust and nuclear energy. Since then, energy needs have continued to increase in order to meet the needs and desires of a growing and increasingly demanding world population in terms of living comfort: the world population was estimated at 7.55 billion on July 1st 2017, compared to about 300 million a thousand years ago [1]. As a result, the Earth's resources have been exploited without limits.

In 2015, the estimation of the world Total Final Consumption (TFC, corresponding to the total energy consumed by end users) was 9 384 million tons of oil equivalent (Mtoe, 1 toe = 10^7 kcal) and 41% was provided by oil: this is twice as the world TFC estimated in 1973 [2]. Obviously, this (excessive) consumption of resources and energy has harmful consequences for human beings and the environment: global warming (due to greenhouse gases emissions, and especially carbon dioxide and methane), atmospheric pollution, resources depletion and nuclear waste accumulation are the main consequences of energy-consuming societies. According to **Figure I.1,** it is interesting to note that the quantity of CO_2 present in the atmosphere has increased significantly (by 40%) from the end of the 18th century, the date corresponding to the beginning of the industrial revolution, illustrating the high impact of human activities onto climate change. As an example, it was estimated that human activities caused approximately 1°C of global warming above pre-industrial level, and global warming is likely to reach 1.5°C between 2030 and 2052 if it continues to increase at the current rate, as shown in **Figure I.2**. Such a temperature increase could have dramatic consequences, like a rise in water level, climate refugee's migration movements, and massive ecosystem and wildlife extinction.

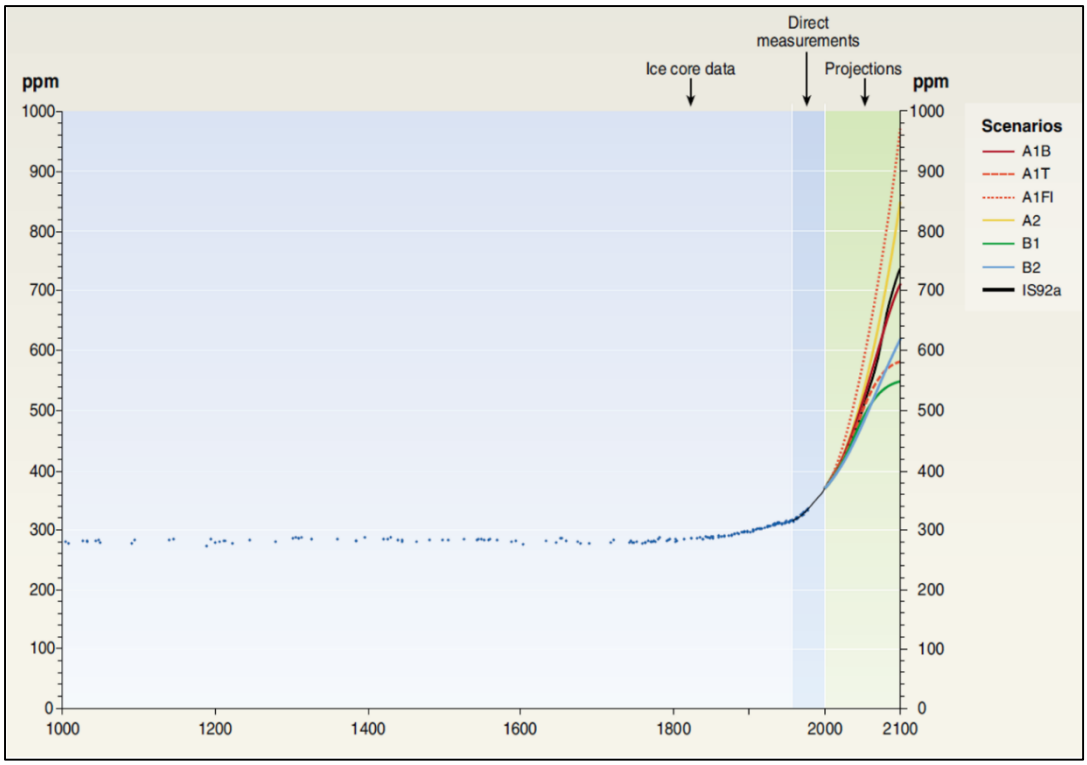

Figure I.1. Atmospheric CO_2 concentration (in ppm) from year 1000 to year 2000 from ice core data [3,4] and from direct atmospheric measurements over the past few decades. Projections of CO_2 concentrations for the period 2000 to 2100 are based on the six illustrative scenarios. From Ref.[5].

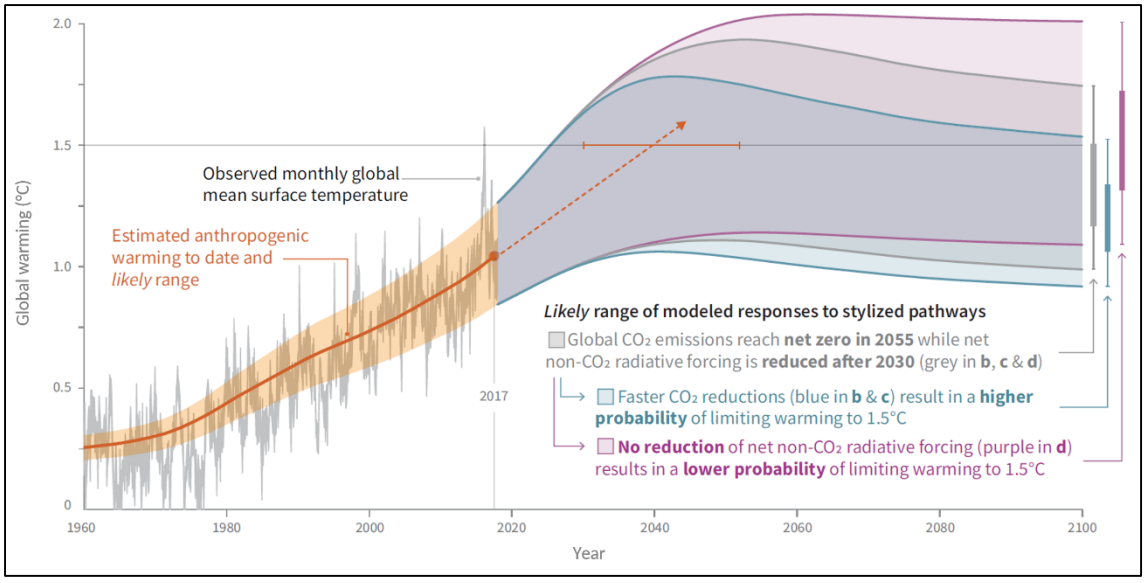

Figure I.2. Observed global temperature change and modeled responses to stylized anthropogenic emission and forcing pathways. From Ref.[6].

Since 1972, in response to this worrying situation, international policy makers have decided to meet and work together (in particular during Earth Summit and Conference of Parties) in order to urge a sustainable development, based on annual reports written by international expert groups (Intergovernmental Panel on Climate Change (IPCC)) who assess the scientific, technical and socio-economic information, in a neutral and objective manner, in relation to climate change. In that framework, over the past 50 years, scientists have been encouraged to develop new technologies for energy production, storage and conversion that generate a minimum of CO_2 emissions. Consequently, according to a recent report of the International Renewable Energy Agency (IRENA) entitled *Global energy transformation: A roadmap to 2050*, renewable energies (solar panels, wind turbines, hydroelectric power plant, geothermal power and biomass) enabled to supply the world electric energy needs by 25% in 2018 [7]. However, these types of energy production are highly dependent on meteorological conditions and need to be coupled with storage systems.

In the particular case of electronic applications (digital devices or electrical vehicles), the most developed and used generators are batteries, and especially the lithium-ion technology. However, these systems are limited by their intrinsically low specific energy (below 200 Wh kg^{-1}). On the contrary, fuel cells (FC) can be designed to optimize both their power (which scales to the electrode area) and energy (which scales to the size of the fuel tank). In that context, the development of fuel cells is a promising solution to address, in part, one of the most important challenges of the 21st century.

I.1.2 Fuel cells overview and applications

The principle of a FC, that convert a chemical energy into an electrical energy and heat, was first discovered by the Swiss scientist Christian F. Schönbein in 1839 [8] and then demonstrated at lab scale in 1842 with the collaboration of Sir William R. Grove [9] (they detected voltage between two Pt foils in presence of hydrogen and oxygen in acidified water), before the first "industrial" prototype of a FC was demonstrated in the 1950s by Francis T. Bacon [10]. To date, a wide range of fuel cells have been demonstrated (and for some of them developed), that are commonly organized into six families. Although each technology has its own characteristics, the overall operating principle and the macroscopic design remain similar.

To generate electricity, a fuel (liquid or gas) is oxidized at the anode and an oxidant is reduced at the cathode. These two electrochemical reactions proceed on both sides of an ion-conducting but electron-insulating separator. The six families of FC are listed hereafter: the Proton Exchange Membrane Fuel Cell (PEMFC), the Direct Methanol Fuel Cell (DMFC; this system is often put forth

as a model direct fuel cell, other such systems operating with similar principles having been conceptualized and tested later – these will not be further described in this manuscript), the Phosphoric Acid Fuel Cell (PAFC), the Solid-Oxide Fuel Cell (SOFC), the Molten Carbonate Fuel Cell (MCFC) and the Alkaline Fuel Cell (AFC). Their overall specific features are summed up in **Table I.1** [11,12], even if it is worth mentioning that the real systems can differ from the general characteristics presented below.

Table I.1 Specific features of the different types of fuel cells.

Type of FC	Fuel	Separator	Oxidant	Typical operating temperature (°C)	Targeted applications
PEMFC	H_2	proton-conductor polymer	O_2	80-100	vehicles, small stationary
DMFC	CH_3OH	proton-conductor polymer	O_2	60-90	portable
PAFC	H_2	H_3PO_4	O_2	160-220	stationary
SOFC	H_2	solid ceramic	O_2	700-1000	stationary
MCFC	H_2	molten carbonate salt	O_2	620-660	stationary
AFC	H_2	alkaline solution	O_2	60-90	undersea vehicles, spacecraft

Currently, even if most FC are still under development, these systems are considered either for small power portable devices (*i.e.* < 1 kW, like cell phones, laptops), transport (several kW to several 100 kW, for bikes, scooters, handling vehicles, cars, buses and trains) or stationary applications (from kW to MW range, for electricity production for industrial and domestic buildings, emergency electricity supply or electricity supply for isolated sites).

I.1.3 Hydrogen, a very popular energetic vector

Owing to its numerous advantages, hydrogen is an excellent candidate to be a promising energetic vector, and this is why most of the FC technologies operate with this fuel [13]. Hydrogen is indeed non-toxic, its energy density is very high (33 kWh kg^{-1}, this is 3 times more than liquid hydrocarbon [14]) and its combustion generates only water. However, the use of hydrogen faces three main issues: its production, storage and transport.

H_2 production. Today, 96% of hydrogen production comes from hydrocarbon steam reforming and coal gasification, generating a lot of CO_2 emissions [15]. In addition, because electrode materials are sensitive to pollution (especially CO), the H_2 used in FC must be very pure, which requires additional purification steps in the overall H_2 production process. H_2 could also be produced by cleaner processes, like water electrolysis. However, as of today, only 4% of H_2 production comes from water electrolysis; whereas this process enables to lower CO_2 emissions associated to H_2 production, its development is not fast due to its high costs compared to fossil fuel reforming [16].

H_2 storage. Hydrogen storage has been the subject of numerous studies that have led to three main technologies: pressurized H_2, liquefied H_2 or storage in solid material [13]. Due to a very low density (0.089 kg m^{-3}) and boiling point (-252°C), high pressures are needed to achieve high storage capacities and extensive cooling is required to liquefy H_2. The storage in solid material, through adsorption in metallic materials such as metal hydrides [17], Mg-based alloys [18], carbon-based materials [19], or chemical hydrides [20] have also been considered, but hydrogen diffusion within these materials can lead to local pressure increase, cause cracks and weaken the materials' lattice.

H_2 transport. The development of a distribution network is essential to consider the deployment of these technologies, because the current hydrogen distribution network is very limited. Hydrogen can be transported in its liquid or gaseous form by trucks or pipelines, depending on the distance to be covered and the H_2 volume to be transported. It is usually delivered to the consumption point (*e.g.* a factory) or dispensed in refilling stations. In the case of hydrogen station for vehicles, as an example, 82 hydrogen stations were referenced in 2015 in Europe [21], and their number increases fast. Besides, the region Auvergne-Rhône-Alpes could become the first region of hydrogen in France and in Europe, through the "Zero Emission Valley" project, which aim at deploying 1000 hydrogen vehicles, 20 hydrogen stations and 15 electrolyzers [22].

Last but not least, hydrogen is highly flammable and explosive in presence of > 4% air, and H_2 leakage is a serious problem that needs to be considered for the widespread commercialization of FC, which leads to a complex certification and construction for hydrogen devices.

All the difficulties listed above regarding the use of hydrogen led the scientific community to consider other types of fuels. This new approach is the oxidation of a liquid fuel; historically, the fuel of choice was methanol in so-called direct methanol fuel cells. Then, other types of carbon-fuels (such as ethanol, propan-1-ol, ethylene glycol, formic acid) have been suggested and demonstrated, firstly for acidic and then for alkaline systems. The common features of such direct fuel cells are their (i) low performances owing to the very complex fuel oxidation reaction at stake and (ii) related high catalyst consumption (to try to enhance the kinetics), the catalyst often being based on platinum. These strategies have therefore very little chances to become industrially successful (one would want high performances and low catalyst consumption). Other fuels are however compatible with direct fuel cells: sodium borohydride, ammonia borane and hydrazine borane are examples of fuels that can be valorized in alkaline fuel cells [23]. This PhD work focuses on the direct borohydride fuel cell (DBFC).

I.2 The direct borohydride fuel cell

I.2.1 Operating principle, interest and technological issues

In a DBFC, the electricity is generated via the electrooxidation of sodium borohydride ($NaBH_4$, in alkaline media) at the anode, a reaction which is ideally direct and releases 8 electrons (borohydride oxidation reaction, BOR, **Equation I.1**), and the electroreduction of oxygen (oxygen reduction reaction, ORR, **Equation I.2**) at the cathode side (in alkaline media). Hydrogen peroxide (H_2O_2) can also be used as the oxidant (hydrogen peroxide reduction reaction, HPRR, **Equation I.3**) to obtain a full liquid FC; in that case, the HPRR usually proceeds in acidic media.

BOR:

$$BH_4^- + 8\,OH^- \rightarrow BO_2^- + 6\,H_2O + 8\,e^- \qquad \textbf{Equation I.1}$$

(E^0 = -1.24 V *vs.* SHE, pH = 14)

ORR:

$$O_2 + 2\,H_2O + 4\,e^- \rightarrow 4\,OH^- \qquad \textbf{Equation I.2}$$

(E^0 = 0.40 V *vs.* SHE, pH = 14)

HPRR: $$H_2O_2 + 2\,H^+ + 2\,e^- \rightarrow 2\,H_2O$$ **Equation I.3**

(E^0 = 1.763 V *vs*. SHE, pH = 0)

At high pH, the standard potentials of the BOR and ORR are -1.24 V *vs*. the standard hydrogen electrode (SHE) and 0.4 V *vs*. SHE respectively, leading to a theoretical DBFC voltage of 1.64 V and the overall DBFC reaction given in **Equation I.4.** When hydrogen peroxide is used, the theoretical cell voltage is 3.01 V and the overall reaction is given in **Equation I.5**. However, the latter value will be necessarily lowered by the junction voltage (830 mV) between the anodic and cathodic compartments [24]. In both cases, a DBFC produces water and metaborate anion (BO_2^-).

Nota bene: in the whole manuscript, DBFC using O_2 or H_2O_2 as oxidant will be called O_2-DBFC and H_2O_2-DBFC respectively.

Overall O_2-DBFC reaction: $$BH_4^- + 2\,O_2 \rightarrow BO_2^- + 2\,H_2O$$ **Equation I.4**

(U_{cell} = 1.64 V)

Overall H_2O_2-DBFC reaction: $$BH_4^- + 4\,H_2O_2 \rightarrow BO_2^- + 6\,H_2O$$ **Equation I.5**

(U_{cell} = 3.01 V)

The BOR must proceed in alkaline media due to the rapid hydrolysis of BH_4^- in acidic media; this reaction may also be catalyzed by the electrode material, and can be partial (**Equation I.6.A**) or total (**Equation I.6.A.B**) [25,26]. The required alkaline nature of borohydride anolytes makes of the DBFC a subclass of AFC. Since the hydrolysis of BH_4^- generates highly pure H_2, the scientific community has also considered the use of $NaBH_4$ as storage material for H_2 generation [27] to be later used, for instance, in a PEMFC (this system is then called indirect borohydride fuel cell).

Hydrolysis of BH_4^-: $$BH_4^- + H_2O \rightarrow BH_3OH^- + H_2$$ **Equation I.6.A**

$$BH_3OH^- + H_2O \rightarrow BO_2^- + 3\,H_2$$ **Equation I.6.B**

Like for most fuel cells, the core of the elementary cell of a DBFC is composed of five components, usually assembled in multiple layers, as illustrated in **Figure I.3**:

- two catalytic layers (CLs), which are the sites of the electrochemical reactions that proceed at appropriate electrocatalyst surface; several types of materials have been studied as electrocatalysts (mainly noble and non-noble metal nanoparticles (NPs) supported on high surface area carbon (HSAC)) and this will be developed in section **I.2.3.2**;
- a polymer membrane as separator of the anodic and cathodic parts; both anionic and cationic membrane have been considered for DBFC (this will also be developed in section **I.2.3.5**);
- two diffusion layers (DLs), which enable fuel and oxidant supply in the cell, products evacuation as well as electrons transport.

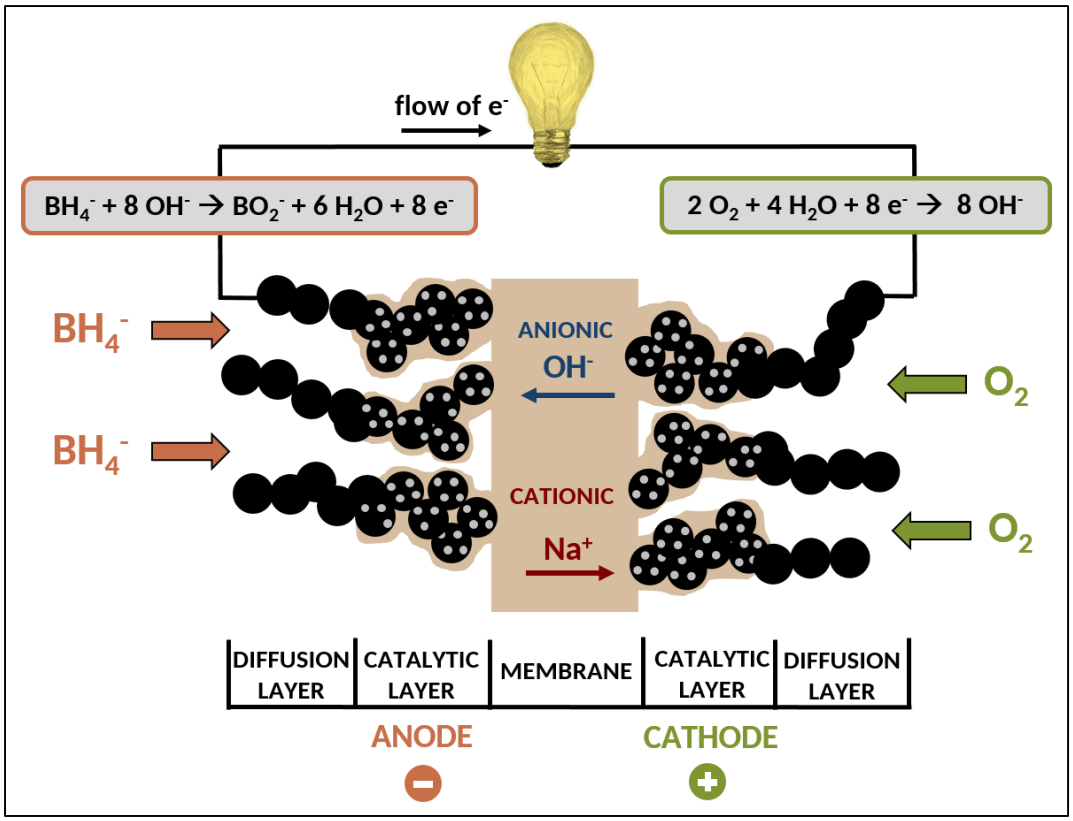

Figure I.3. Simplified architecture of the elementary cell of a DBFC.

The comparison of energetic and thermodynamic features of the DBFC in contrast with the PEMFC and DMFC highlights the interest for DBFC (see **Table I.2**): the high number of electrons released during the BOR (8, compared to 2 and 6 for PEMFC and DMFC respectively) leads to a

theoretical specific energy 50% higher than for a DMFC, although it remains under the specific energy of a PEMFC. However, the theoretical cell voltage of a DBFC (1.64 V) is higher than for a PEMFC and DMFC (1.23 V and 1.21 V respectively).

Table I.2. Energetic and thermodynamic features of the DBFC in comparison to PEMFC and DMFC.

Fuel cell	Number of mole of electrons exchanged per mole of fuel	Theoretical specific energy (kWh kg^{-1})	Theoretical cell voltage (V)
PEMFC	2	32	1.23
DMFC	6	6	1.21
DBFC	8	9	1.64

Today, despite the inherent assets of DBFC, their commercialization faces two main impediments: (i) the high cost of sodium borohydride (this will be further developed in the next section) and (ii) the gaseous hydrogen evolution via the hydrolysis (**Equation I.6**) that can occur via the chemical decomposition of sodium borohydride in the electrolyte (called the homogeneous hydrolysis) or the reaction of sodium borohydride on appropriate catalyst surface (called the heterogeneous hydrolysis). The hydrolysis reaction leads to a loss of fuel efficiency if the hydrogen released is not valorized afterwards, and to safety issues. In addition, the evolution of gaseous hydrogen in the anodic compartment can block the channel flow field and thus decrease the specific surface area of the electrocatalyst [28–30]. Two main parameters influence the rate of the homogeneous hydrolysis: the pH and the temperature. Acidic media and high temperature favor a high hydrolysis rate [25,26] as illustrated by the following empirical relation (**Equation I.7)** established by Mochalov in 1965 [31] for 7 < pH < 10 and 15 < *T* < 35°C, and more recently studied by other groups [32], where $t_{1/2}$ is the half-life of BH_4^- in minutes.

$$\log\left(\mathrm{t}_{\frac{1}{2}}\right) = \mathrm{pH} - 0.034 * T - 1.92 \qquad \textbf{Equation I.7}$$

As a consequence, in a DBFC, the BOR must proceed in alkaline environment. However, high pH may not be sufficient to completely prevent hydrolysis, as heterogeneous hydrolysis can proceed at non-negligible rate on the electrode materials, this reaction also being emphasized at lower pH and high temperature.

I.2.2 Production of sodium borohydride

In its natural state, the elementary form of boron does not exist, it is generally combined with oxygen to form borates. The main components of boron resources are oxygenated, carbonated or hydrogenated. For the DBFC application, it is the hydrogenated form of boron, sodium borohydride, which is of interest: it contains a high amount of hydrogen: 10.6 wt.%, and is a strong reducing agent. Its physicochemical properties make of $NaBH_4$ a widely-used chemical for industrial applications, as reducer and hydrogenating agent for organic and pharmaceutical compounds synthesis, wastewater treatment and as a bleaching agent in the paper industry [33]. The industrial production of $NaBH_4$ is carried out by two main processes: the Brown-Schlesinger process [34] and the Bayer process [35,36].

- **The Brown-Schlesinger process**

In the Brown-Schlesinger process, sodium hydride (NaH) reacts with trimethylborate ($B(OCH_3)_3$) in an inert mineral oil at 250–270°C to produce sodium borohydride and sodium methoxide ($NaOCH_3$) as in **Equation I.8**.

$$4\,\mathrm{NaH} + \mathrm{B(OCH_3)_3} \rightarrow \mathrm{NaBH_4} + 3\,\mathrm{NaOCH_3} \qquad \textbf{Equation I.8}$$

A concentrated alkaline solution is obtained that can be used in its liquid form or $NaBH_4$ can be extracted with an amine and crystallized to obtain a pure solid. However, when taking into account the production of raw materials, the overall $NaBH_4$ production proceeds in seven steps as presented in **Figure I.4**. This process is energetically inefficient due to sodium metal manufacturing: indeed, it is estimated that 50% of the electrical energy input is lost as heat [37]. Thus, although sodium metal can be recycled, the production of $NaBH_4$ via the Brown-Schlesinger process is expensive.

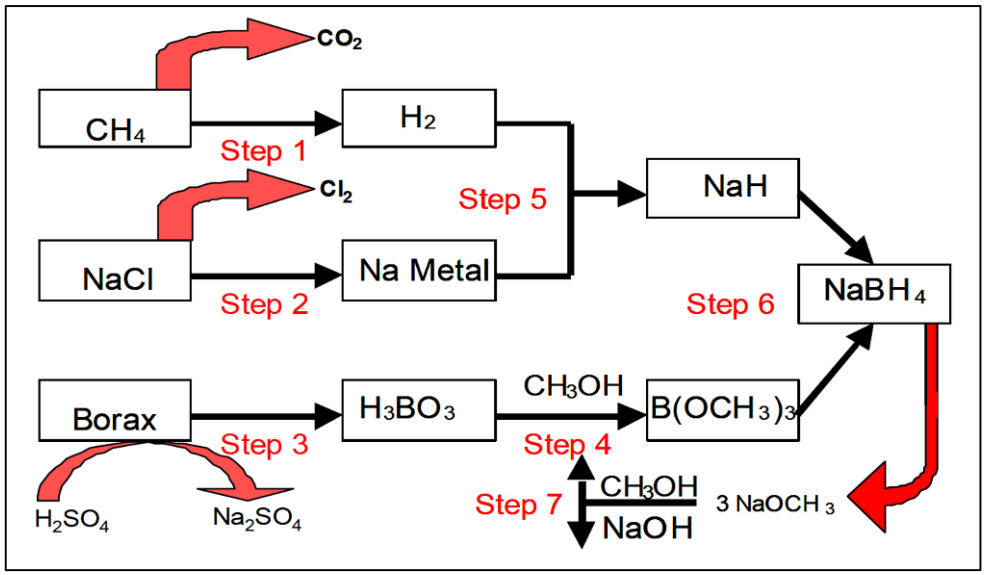

Figure I.4. Schematic diagram of the overall Brown-Schlesinger process for $NaBH_4$ synthesis. Step 1: Steam reforming of methane to produce hydrogen. Step 2: Electrolysis of sodium chloride to produce sodium metal. Step 3: Refining of borax to produce boric acid. Step 4: Conversion of boric acid to trimethylborate with methanol. Step 5: Reaction of sodium metal and hydrogen to produce sodium hydride. Step 6: Combination of sodium hydride and trimethylborate to produce sodium borohydride. Step 7: Recycling of sodium methoxide by-product to methanol. From Ref.[37].

- **The Bayer process**

The Bayer process is a one-pot synthesis at high temperature (400-500°C) combining borax ($Na_2B_4O_7$), metallic sodium, hydrogen, and silica (SiO_2) that produces sodium borohydride and sodium metasilicate (Na_2SiO_3) as shown in **Equation I.9**.

$$Na_2B_4O_7 + 16\,Na + 8\,H_2 + 7\,SiO_2 \rightarrow 4\,NaBH_4 + 7\,Na_2SiO_3 \qquad \textbf{Equation I.9}$$

Although the one-pot reaction is an interesting production route, the Bayer process operates in a batch mode, while a continuous mode would be more efficient; it also presents non-negligible risks of explosion and still uses sodium metal.

Finally, scientists have also investigated the production of sodium borohydride from sodium metaborate ($NaBO_2$) via electrosynthesis, which would be an efficient route for the sustainable development of DBFC (indeed, $NaBO_2$ is the combustion product of $NaBH_4$). Several patents between 1958 and 1990 indicated the possibility to convert $NaBO_2$ into $NaBH_4$ with a large yield (up to 80%). However, these results were found to be false due to an inappropriate method for

measuring $NaBH_4$ [38]. The chemical reduction of $NaBO_2$ has also been studied using reducing agent such as Mg_2Si alloy, MgH_2, methane or coke [39,40]. None of these reactions are thermodynamically favorable and their processes are then not sustainable at an industrial scale. As a result, the different ways of production of sodium borohydride still need improvements to reach high yields, fast reaction rate, while being cheap and sustainable.

I.2.3 Recent advances and remaining challenges

The use of $NaBH_4$ as a fuel was first demonstrated by Indig and Snyder in 1962 [41]. Nearly four decades later, in 1999, Amendola *et al*. characterized a single DBFC. The cell was made of dispersed 97% Au/3% Pt particles on a high surface area carbon silk cloth anode and an air-breathing cathode, separated by an anionic polymer membrane: Amendola's DBFC exhibited a maximum power density of 60 mW cm^{-2} at 70°C [42]. Since then, many studies have been published about DBFC (although only a few groups are really active on this field), and most of them deal with electrocatalysts for the BOR and membranes for the separation of the anode/cathode compartments [43]. To date, to the author's knowledge, the highest power density obtained with a O_2-DBFC was 810 mW cm^{-2} at 70°C: this result was achieved using Pd/C deposited on Ni foam with chitosan chemical hydrogel binder as anode electrocatalyst and a Pt/C cathode electrocatalyst separated by an ionically cross-linked chitosan hydrogel membrane [44]. The highest power density obtained with a H_2O_2-DBFC was 630 mW cm^{-2} at 70°C using Pd/C deposited on Ni foam with Nafion® binder as anode electrocatalyst and Pt/C cathode electrocatalyst separated by a pH-gradient-enabled microscale bipolar interface [45]. A quick review of knowledge and research advances about BOR and DBFC components is proposed hereafter.

I.2.3.1 BOR mechanism

One of the major challenges of DBFC studies has been to understand the BOR mechanism. This reaction is indeed very complex and highly depends on multiple parameters, including the catalyst nature and structure, the electrode architecture, the temperature, the fuel concentration and pH, that can lead to numerous intermediate species. In addition, non-faradaic reactions can occur and compete with the BOR. Despite the fundamental difficulties, understanding the BOR mechanism is critical, as it will enable to select efficient electrocatalysts and to design appropriate electrode architectures in order to develop high-performance DBFC systems. To shed light on this complex mechanism, numerous research groups investigated the intermediate species that are produced during the BOR, using electrochemical techniques such

as Rotating Disk Electrode (RDE) or Rotating Ring-Disk Electrode (RRDE), possibly coupled with physicochemical characterizations like Fourier Transform Infrared Spectroscopy (FTIR) and Differential Electrochemical Mass Spectrometry (DEMS) [46–53]. Combining their results with these previous studies, Olu *et al*. proposed in 2015 a BOR mechanism occurring on Pt for low $NaBH_4$ concentration (10 mM) at *T* = 25°C [54] and more recently, in 2018, they extended the study to Au and higher $NaBH_4$ concentrations (50 and 500 mM) at *T* = 25°C [55]; the BOR mechanism drawn in **Figure I.5** summarizes their findings.

On Pt surfaces, the BOR mechanism can proceed through two distinct pathways: (i) the fully-dissociative adsorption of BH_4^- into BH_{ads} (**Equation I.10**, s corresponds to a catalytic site) and (ii) the partially-dissociative adsorption of BH_4^- into $BH_{3,\ ads}$ (**Equation I.11)**. Depending on the number of available Pt sites, the potential region (basically *E* < 0.6 V *vs*. the reversible hydrogen electrode (RHE) or *E* > 0.6 V *vs*. RHE) and the $NaBH_4$ concentration (low or high), one route will be favored over the other.

$$BH_4^- + 4\,s \rightarrow BH_{ads} + 3\,H_{ads} + e^- \qquad \textbf{Equation I.10}$$

$$BH_4^- + OH^- + s \rightarrow BH_{3,ads} + H_2O + 2\,e^- \qquad \textbf{Equation I.11}$$

For low $NaBH_4$ concentrations (5, 10 mM) and low potentials (*E* < 0.6 V *vs*. RHE), the fully-dissociative adsorption occurs and this reaction requires many free Pt sites (4 free Pt sites per BH_4^- adsorption). Then, the BH_{ads} produced can react slowly with OH^- in a Eley-Rideal-type mechanism and the BOH_{ads} produced could react afterwards with OH^- in a similar mechanism to produce the final product BO_2^-. However, BH_{ads} species are stable on Pt sites and tend to block the surface. The BOR process can nevertheless continue at higher potentials, thanks to OH^- adsorption: OH_{ads} can indeed react with BH_{ads} in a Langmuir-Hinshelwood-type mechanism. However, OH^- adsorption can also be detrimental to the BOR process since it consumes surface Pt sites and therefore partially contributes to Pt surface poisoning and deactivation. Concomitantly, at high potentials, the partially-dissociative adsorption, which is less demanding in free Pt site than the fully-dissociative one, can proceed and leads to the production of $BH_{3,\ ads}$, that can then react according to four different pathways: $BH_{3,\ ads}$ can (i) desorb as BH_3OH^-, (ii) dissociate to form BH_{ads} + 2 H_{ads} if enough Pt sites are available, (iii) react with OH^- to form BH_{ads} or (iv) dehydrogenate into BH_{ads} + H_2. In addition to BOR intermediate species, the two main pathways discussed above produce H_{ads} or gaseous H_2. Both can be electrooxidized at low potentials on Pt, but not at high potential on Pt surface covered by Pt oxides, being admitted that Pt oxides are not active for hydrogen oxidation reaction (HOR) [56,57].

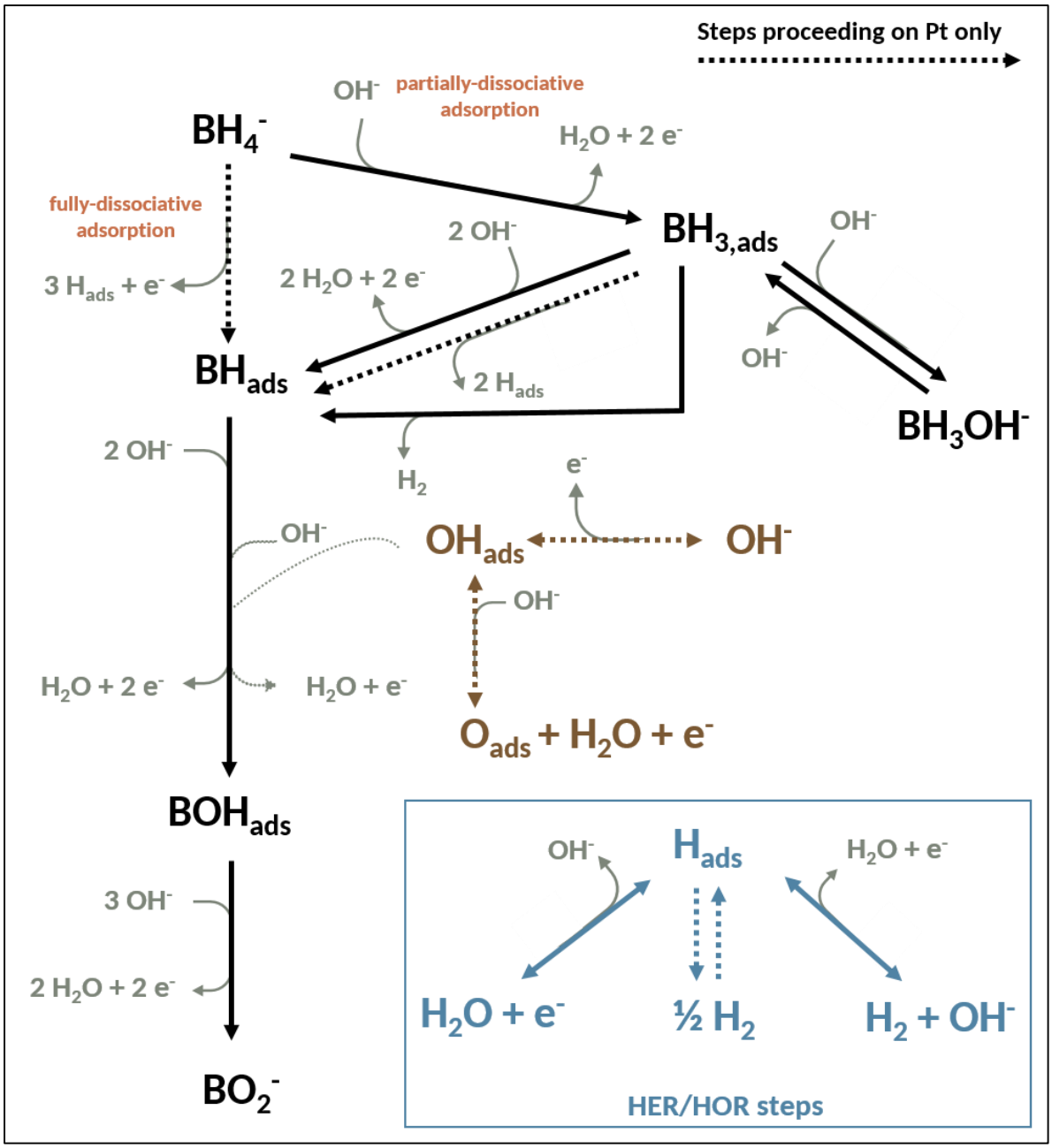

Figure I.5. Tentative BOR mechanism for Pt and Au surfaces. Adapted from Ref. [55].

For high $NaBH_4$ concentrations (50 – 500 mM), the Pt surface poisoning by BH_{ads} is faster, and the partially-dissociative adsorption becomes favorable even at low potential values. $BH_{3,ads}$ are produced and can then self-dehydrogenate to form BH_{ads} and H_2 (this reaction is the least site consuming), H_2 being lost, and thus reducing the faradaic efficiency.

In any case, at potentials lower than the hydrogen reversible potential, Pt electrodes promote the hydrogen evolution reaction (HER, electroreduction of water), leading to very large reduction currents and H_2 generation; as a result, any BOR activity of Pt below 0 V *vs.* RHE will be overwhelmed by intense HER currents, and the BOR on Pt cannot efficiently proceed unless the electrode operates above 0 V *vs.* RHE. As a result, the theoretical promises of **Equation I.1** (in terms of reaction potential) are beyond reach with a platinum electrode.

On Au surface, whatever the $NaBH_4$ concentration, the BOR only proceeds through the partial-dissociation adsorption of BH_4^- into $BH_{3,\,ads}$, that self-dehydrogenate and lead to H_2 generation, H_2 being lost because the HER and HOR kinetics are slow on Au electrodes.

These in-depth studies enable to conclude that Au alone is not an efficient catalyst for the BOR, whereas Pt-based anodes can be tailored by adjusting the number of Pt sites to the $NaBH_4$ concentration in order to maximize the BOR faradaic current and minimize H_2 generation. However, according to this mechanism, Pt electrodes will only lead to quantitative oxidation current above the hydrogen reversible potential (Pt valorizes hydrogen species originating from BH_4^- and is very efficient for hydrogen evolution from water reduction), and can therefore not be considered as an ideal BOR electrocatalyst. To date, the BOR mechanism has been deeply studied on these two metals but remains poorly understood for most electrocatalysts and in relevant conditions to DBFC operation.

I.2.3.2 Anodic electrocatalysts

In the light of the DBFC features and BOR mechanism discussed earlier, the ideal BOR electrocatalyst must meet the following requirements: promoting fast BOR kinetics and high faradaic efficiency at low potential, minimizing H_2 escape, being able to oxidize H_2, being inactive towards heterogeneous hydrolysis of BH_4^- and electroreduction of water into H_2, being stable and cheap. No electrocatalyst fulfilling at least high faradaic efficiency and low onset potential has been isolated so far. Particularly, no catalyst leading to an 8-electron BOR at potential close to the thermodynamic potential has been found. The different types of materials that have been studied to constitute the DBFC anode can be classified into four categories: monometallic catalysts, binary alloys and composite catalysts and hydrogen storage alloys.

Note that, unfortunately, the comparison of DBFC performances (especially in terms of power density and current density) between different labs is a tricky task, owing to the fact that the characterization methods used to evaluate the suitability of a given electrocatalyst have not been standardized, as it is the case for PEMFC (at least for accelerated stress test (AST) protocols)

[58,59]. To overcome this issue, Olu *et al*. suggested (quite recently in their DBFC review) common experimental methods and activity benchmarks [60], but the paper is too recent to have solved the issues of standardization of BOR/DBFC measurements. Despite this lack of homogeneity between the different studies, RDE measurements have enabled to highlight some properties for several electrocatalysts, in terms of onset potential of the reaction, faradaic efficiency, activity towards the BH_4^- heterogeneous hydrolysis, HER/HOR and surface passivation or poisoning.

- **Monometallic electrocatalysts**

Among noble and non-noble metals, Au [46,61–68], Pt [46,54,65,66,68–78], Pd [67,68,70,76,79–87], Ag [66,68,88–91] and Ni [63,76,82,92] have particularly received attention.

Pt has been identified as the most active towards the BOR, both as bulk electrodes [46,70,71,74,93,94] and carbon-supported NPs [75,76,94]. Of course, as noted above, Pt is very active towards the HER/HOR [95–98] and the heterogeneous hydrolysis of $NaBH_4$ [49,74,75]. Consequently, the HER prevails on BOR below E = 0 V *vs.* RHE and the HOR prevails on the BOR above E = 0 V *vs.* RHE, resulting in a BOR onset potential of *ca*. E = 0 V *vs*. RHE on Pt surfaces. The number of electrons exchanged during the BOR on Pt varies from 2 to 8 in the literature [73,76,99] and it was shown that the faradaic efficiency decreases with the $NaBH_4$ concentration [55,71,75,76].

Au has long been considered as an efficient electrocatalyst towards the BOR [61,100–102], owing to the fact that this metal does not promote as-severe BH_4^- heterogeneous hydrolysis than Pt [61,74]. However, this result was proved wrong [46,90,103,104]: Au yields 4.5 – 7.5 electron per BH_4^- species, since it generates hydrogen (both from heterogeneous hydrolysis and from $BH_{3,ads}$ dissociation, **Figure I.5**) which if cannot valorize, resulting in non-negligible H_2 escape. In addition, BOR currents are only generated at high potential (*ca*. E = 0.3 V *vs*. RHE) [105], making of Au an overall bad BOR electrocatalyst.

Pd exhibits good BOR activity but slightly smaller than for Pt [70] and good HER/HOR activities [106]. Its great interest relies on its low BOR onset potential (-0.2 V *vs*. RHE was measured in ref [67]); this effect is not fully-understood to date, but shows that the rate of HER can be significantly depreciated on Pd in presence of BH_4^-. Pd is also active towards the BH_4^- heterogeneous hydrolysis [67,68]. The number of electrons exchanged varies from 4 to 8 [67,107]. In addition, Oliveira *et al.* showed in successive papers [108,109] that the addition of a Pd monolayer on Pt (111) enhances its BOR activity. This improvement was attributed to a slower HER on Pd and a better ability to remove BH_{ads} species, due to the fact that Pd is more

oxophilic than Pt (this reasoning assuming that the BOR on Pd proceeds with a similar mechanism as on Pt, which still has to be verified).

Ag is reported to be inactive towards the BH_4^- heterogeneous hydrolysis [66,89] but leads to an incomplete BOR with a release of 2-6 electrons owing to the fact that Ag does not promote HOR, while still does not completely avoid H_2 generation [91]. It was shown that oxides formed upon Ag surface have catalytic effect on the oxidation of borohydride [88], but this proceeds at too-high potential to be relevant in a DBFC anode.

Finally, Ni has been found to be active for BOR but also for the BH_4^- heterogeneous hydrolysis thereby yielding 50-75% faradaic efficiency [76,92,110]. However, it seems that the formation of stable oxides on Ni surface along DBFC stability tests affects the overall DBFC performances [111] and especially their sustainability. As a result, whereas Ni electrodes can prove interesting for the BOR, tightly controlling their degree of surface oxidation is critical and very awkward in practice [112].

- **Binary alloys and composites**

The previous section illustrates that no monometallic electrocatalyst present all the required properties for an efficient BOR; so, many researchers tested binary alloys and composite electrocatalysts in order to take advantage of the interests of each component in the hope to boost the BOR activity/selectivity. More precisely, metal exhibiting good catalytic BOR activity have been combined with a metal being inactive towards the $NaBH_4$ heterogeneous hydrolysis. As an example, Atwan *et al*. studied Pt-Au alloy and Pd-Au alloy, that proved to enhance the BOR kinetics compared to Au-only catalyst (but not to Pt-only and Pd-only catalysts) [101]. In other studies [113,114], Pt has been alloyed with Ni and this catalyst led to good BOR performances, while reducing the rate of H_2 escape. Alloying Ag and Ni also showed to be an efficient combination leading to a 7-electron BOR [115]. However, none of these solutions have been completely satisfactory.

- **Hydrogen storage alloys**

Hydrogen storage alloys are metallic materials that have the ability to spontaneously react with hydrogen and store it as metal hydride; gaseous H_2 can be then re-generated via desorption. It was thus expected that these materials reduce H_2 evolution during DBFC operation. Two groups of hydrogen storage alloys have been considered: AB_2-type and AB_5-type alloys (A is a rare earth element or transition metal; B is a transition element or solid solutions based on magnesium, vanadium or palladium). Some authors reported the characterization of this type of materials as

anode electrocatalyst for DBFC [30,116–121]; however, most of the experiments were conducted only in fuel cell configuration (and not in RDE configuration) without comparison with a noble electrocatalyst. Thus, it is difficult to evaluate the properties and the possible interest of these materials for DBFC. However, their principle of operation (hydrogen evolution/insertion and hydrogen oxidation/deinsertion) leaves little hope of BOR current generation below the hydrogen potential.

I.2.3.3 Electrode composition and operating conditions

In addition to the chemical nature of the anodic electrocatalyst, the anode composition can influence the BOR mechanism and activity depending on numerous parameters, such as the nature of the binder and amount or the electrocatalyst support. As an example, Li *et al*. [110] reported that using Nafion® instead of PTFE as binder leads to better DBFC performances and Kim *et al*. [94] showed that an optimum of Nafion® content could be reached above which the DBFC performances started to decrease. In addition, Ponce-de-León *et al*. [122] investigated the use of three-dimensional electrodes such as reticulated vitreous carbon (RVC): they showed that the BOR kinetics is faster on low porosity grade supports. This suggests that the porous structure and texture of the electrode has a non-negligible influence on its apparent performances, as Olu *et al*. [70] and Freitas *et al*. [123] have put forth.

Moreover, the anolyte composition and flow rate also impact the DBFC performances. An increase in $NaBH_4$ concentration leads to larger power and current densities [124,125], by enhancing mass-transport; however it also increases the hydrolysis rate [64] as well the BH_4^- crossover [94]. Faster anolyte flow rates also improve the mass-transport, thereby leading to higher power density values [30,83,101,124–126]. Finally, larger temperatures promote high diffusion coefficients (hence mass-transport) of the reactants and membrane conductivity, which, along to the improved BOR/HOR kinetics, is beneficial to reach high performances [124,127,128]; on the other hand, increasing the temperature favors the BH_4^- hydrolysis and crossover, which is detrimental to the DBFC performances [70,125,129]. As a result, the optimization of the DBFC operation will be a matter of (numerous) compromises.

I.2.3.4 Cathodic electrocatalysts

As mentioned earlier, when O_2 is used as the oxidant of the DBFC, the ORR proceeds in the cathodic compartment. The ORR is a relatively complex and slow reaction, which has been deeply studied, owing to its large use in numerous technologies such as AFC, metal-air batteries or chlor-alkali process. In comparison with acidic media, alkaline environments lead to enhanced

ORR kinetics, due to the reduced adsorption energy of anions [130], which take part in the different possible ORR mechanisms (it is beyond the scope of this chapter to discuss those mechanisms) [131].

A wide range of ORR catalytic materials have been investigated for potential use in a BDFC cathode, including PGM (Pt-group metals), non-metal doped carbon, carbon–transition metal hybrids, and transition metal oxides, among others [132]. Pt-based electrocatalysts exhibit the highest ORR activity [132–134], but are also very sensitive to the fuel crossover; MnOx compounds have been proven more tolerant to the presence of fuel, but are still sensitive to the crossover [135]. In addition, several parameters such as oxygen partial pressure, relative humidity, and gas flow rate can be optimized to reach high ORR activity.

To sum up, the overall DBFC performances can be limited by the cathodic reaction and there is still work to be done to optimize parameters and to find sustainable cathodic catalytic materials. Because the potential crossover of $NaBH_4$ can be critical to the cathode operation, a wealth of work must be devoted to the membrane that separates the anode from the cathode.

I.2.3.5 Membrane

Membranes are polymer electrolytes that conduct anions (cations) as they contain positive (negative) charged groups bound covalently to a polymer backbone. The role of the membrane in a FC is to avoid reactants and products interaction and to electronically isolate the anodic and cathodic compartment, while allowing ionic conduction. Thus, the membrane must meet the following requirements: high conductivity, high ion exchange capacity (IEC, which is the number of functional groups (molar equivalents, eq.) per unit mass of polymer), high mechanical strength and high chemical resistance. The ideal membrane has all the properties listed above, while being cheap and eco-friendly produced. Of course, meeting all these requirements for a given material is not an easy task.

In the particular case of O_2-DBFC, in order to be able to reach high performances, the membrane must have the following properties:

- Prevent BH_4^- crossover from anodic compartment to cathodic compartment, to avoid fuel losses;
- Enable OH^- transport from cathodic compartment to anodic compartment, to prevent pH decreasing in the anodic side; indeed, OH^- are produced at the cathode and consumed at the anode;
- Prevent Na^+ transport from anodic compartment to cathodic compartment.

Ideally, an anion-exchange membrane (AEM) is more likely to fulfill the second and third point, but will most-probably not prevent BH_4^- crossover. A cation-exchange membrane (CEM) will have opposite properties. Both AEM and CEM have been considered for DBFC, each of them performing differently (**Table I.3**).

Table I.3. Advantages and drawbacks when using CEM and AEM in DBFC.

Membrane	Advantages	Drawbacks
CEM	Minimize BH_4^- crossover	pH decreasing in anodic compartment
	High cation conductivity (less for Na^+ than for H^+, though)	High Cost
	Commercial products available	Displaces NaOH from anode to cathode
	Large durability	
AEM	Enable OH^- transport from cathodic compartment to anodic compartment	BH_4^- crossover
	Prevent Na^+ transport from anodic compartment to cathodic compartment	No commercial products available
		Low durability

CEM offer the possibility to minimize BH_4^- crossover (but not totally avoiding it, as shown by Liu *et al.* [136]) but lead to OH^- exhaustion in the anodic compartment and thereby to more $NaBH_4$ hydrolysis. On the contrary, AEM enable the transport of OH^- from cathodic side to anodic side but cannot prevent BH_4^- crossover. Therefore, the use AEM appears to be more suitable for DBFC on the condition that only OH^- can cross the membrane (which is not granted), or if a BH_4^- tolerant cathode is used.

However, most DBFC characterizations were conducted using CEM [60], the most common choice being Nafion®, a perfluorosulfonic acid (PFSA) membrane manufactured by DuPont (made of poly(tetrafluoroethylene) backbone with perfluoroether pendant side chains terminated by sulfonic acid groups, see **Figure I.6**). This material presents the advantage of being commercially available and exhibits good cation conductivity (in the order of 100 mS cm^{-1}) and good mechanical and chemical stability, even in alkaline environment and in presence of strong reducer. On the contrary, very few studies report the use of AEM for DBFC characterizations [42,113,124,136–138] and most of them used the Morgane®-ADP membrane (from Solvay) which was (it is no longer commercialized) made of cross-linked fluorinated polymer backbone

with quaternary ammonium exchange groups. Most of AEM used in AFC have indeed low conductivity (below the required minimal value of 100 mS cm^{-1} to achieve high current densities), due to a low OH^- mobility which is 20.6 10^{-8} m^2 s^{-1} V^{-1} compared to 36.2 10^{-8} m^2 s^{-1} V^{-1} for H^+ [139], and poor mechanical stability [140]. The latter manifests by the chemical degradation of the anion-conducting polymer via an attack of the OH^- anions, leading to an increase in the cell resistance [139]. The scientific community still works to improve their properties, and the recent progresses enable to be optimistic about their optimization in a close future [140,141].

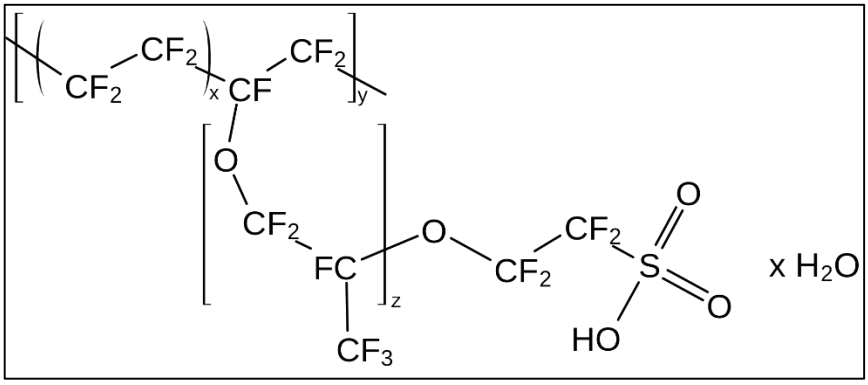

Figure I.6. PFSA membrane structure. For Nafion®: x = 6-10, y = z = 1.

The thickness of the membrane also influences DBFC performances: it was shown that thin membranes improve FC performances because of a lower Ohmic resistance [28,136,142–144]. As an example, Liu *et al.* [136] showed that the power density increases by 54% when the membrane thickness is divided by 4. This however means that the fuel inlet must be tightly controlled to prevent detrimental crossover.

In the particular case of H_2O_2-DBFC, finding an appropriate membrane has been challenging because of the disparate pH environment between the anodic compartment and the cathodic compartment. $NaBH_4$ is indeed stable at high pH while H_2O_2 is stable at low pH [145]. Bipolar membranes have been designed and developed to enable the optimization of the two half-cell reactions kinetics [146]. A bipolar membrane is composed of an AEM (in the anodic side) in direct contact with a CEM (in the cathodic side) and water is dissociated at the bipolar junction (see **Figure I.7**). The main drawback when using the bipolar membrane is the unavoidable high junction potential associated to water dissociation, which is 0.83 V [147].

Very recently, Wang *et al.* [45] reported the high interest of using a pH-gradient-enabled microscale bipolar interface (PMBI) for H_2O_2-DBFC in comparison with an all CEM or AEM configuration. They reported a power density of 300, 280 and 50 mW cm^{-2} and an open circuit

voltage (OCV) of 1.8, 1.7 and 1.3 V when using PMBI, AEM and CEM respectively. After DBFC parameters optimization (membrane thickness, cell active area, catalysts loading and fuel and oxidant flow rates), the PMBI-based H_2O_2-DBFC yielded an OCV of 1.95 V, a peak power density of 630 mW cm^{-2} at 1 V, and a peak current density of 330 mA cm^{-2} at 1.5 V.

To conclude, this study highlights the crucial importance of tailoring membrane that is one of the keys to boost DBFC performances.

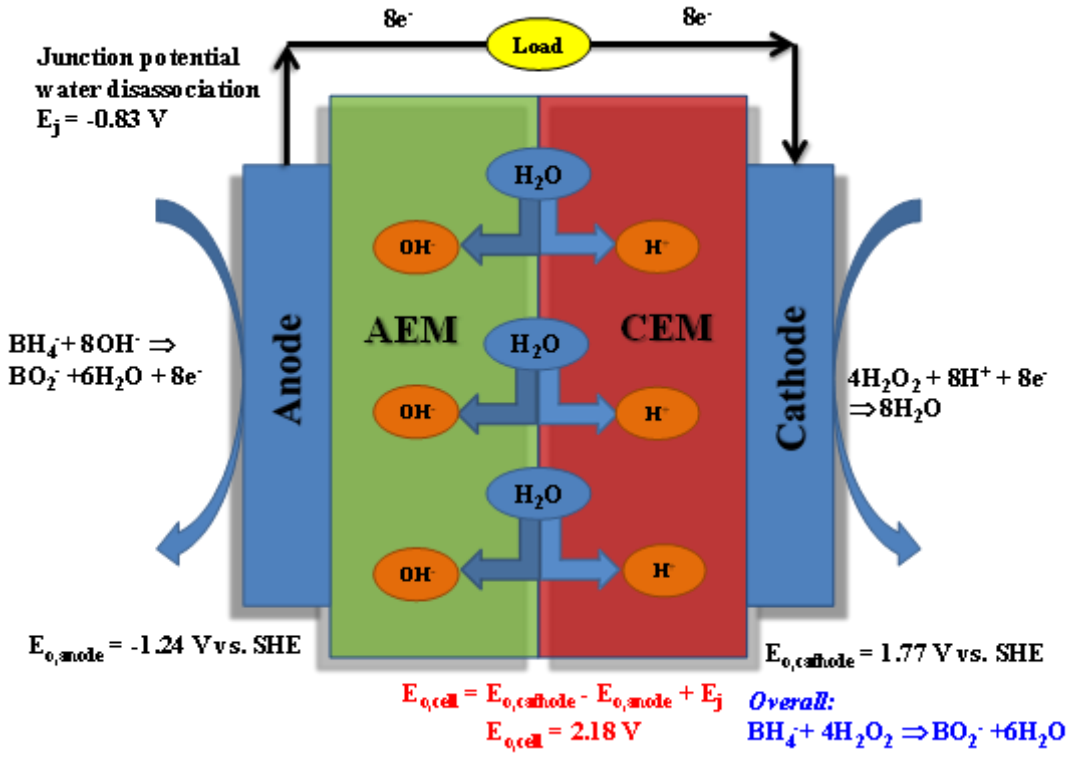

Figure I.7. H_2O_2-DBFC using a bipolar membrane. From Ref. [146].

In summary, the DBFC can be seen as a promising energy generator, owing to a high energy density and high theoretical voltage, while avoiding storage and transport issues (as it the case with the use of H_2). However, these promising features are contrasted by the very complex BOR. Although the BOR mechanism may have been established recently for Pt and Au electrocatalysts, this mechanism remains misunderstood on most catalysts and in DBFC operation conditions (*i.e.* high $NaBH_4$ concentration and high temperature). Among the materials studied for BOR, Pd showed interesting properties towards BOR. In addition to the chemical nature of the electrocatalyst, particular attention must be paid to the architecture of the electrode which can really boost the BOR kinetics and the overall DBFC performances. These aspects will be studied in this thesis.

I.3 Stability issues and degradation mechanisms in alkaline fuel cells

I.3.1 Anodic electrocatalysts do age upon DBFC operation

Among the advantages frequently cited for AFC and electrolyzers, the good stability of electrode materials is often mentioned. The common belief considers that AFC electrocatalysts are indeed stable in alkaline environment owing to the better thermodynamic stability of many metals and their oxides at high pH and high potential, based on their Pourbaix diagrams: an example of the Pourbaix diagram of platinum, palladium and nickel is given in **Figure I.8.A.B.C**. However, these diagrams also point out the formation of hydrated complexes (such as PtO_3^{2-}, PtO_4^{2-}, PdO_3^{2-}, PdO_4^{2-}) that could lead to dissolution. In the case of carbon, the Pourbaix diagram (**Figure I.8.D**) indicates no corrosion at high pH, thanks to the formation of solid carbonates that leads to the passivation of the carbon surface. However, the corrosion of carbon (acetylene black specifically) at high pH has been observed by Ross *et al*. in the 1980s [148–151] and the following observations were reported: (i) the dissolution of carbon into soluble carbonate ion (CO_3^{2-}) has been observed for E < 1.4 V *vs*. RHE and T < 50°C, (ii) the gasification (CO_2 formation) has been observed when E > 1.5 V *vs*. RHE and T > 60°C, (iii) the presence of Fe_2O_3, Cr_2O_3, NiO, Co_3O_4 and Ru on carbon catalyzed the carbon corrosion by a factor of 3 to 14 and (iv) graphitized carbon (structure with less edge atom) was proven to be more resistant to corrosion.

Surprisingly, the study of degradation mechanism of carbon-supported metal NPs electrocatalysts commonly used in AFCs had almost never been studied until 2015. In fact, in the case of DBFC, some studies reported long-term constant current operation [60] and the DBFC decline was mainly attributed to (i) the formation of solid compounds (carbonate and borate) [138,152] or (ii) the degradation of the membrane [153]. Few studies focused on the anode material stability, but Li *et al*. observed a faster anode degradation for high current density due to H_2 generation [153] and Cheng *et al*. observed the dissolution/detachment of Pd anode electrocatalyst upon DBFC operation [154]. In addition, Olu *et al*. [70] examined the evolution of two anodic materials morphology before and after fuel cell experiments: the TEM micrographs (see **Figure I.9**) revealed huge Pt/C and Pd/C deterioration with a lot of agglomeration and a pronounced decrease of the number of NPs (especially for Pt/C).

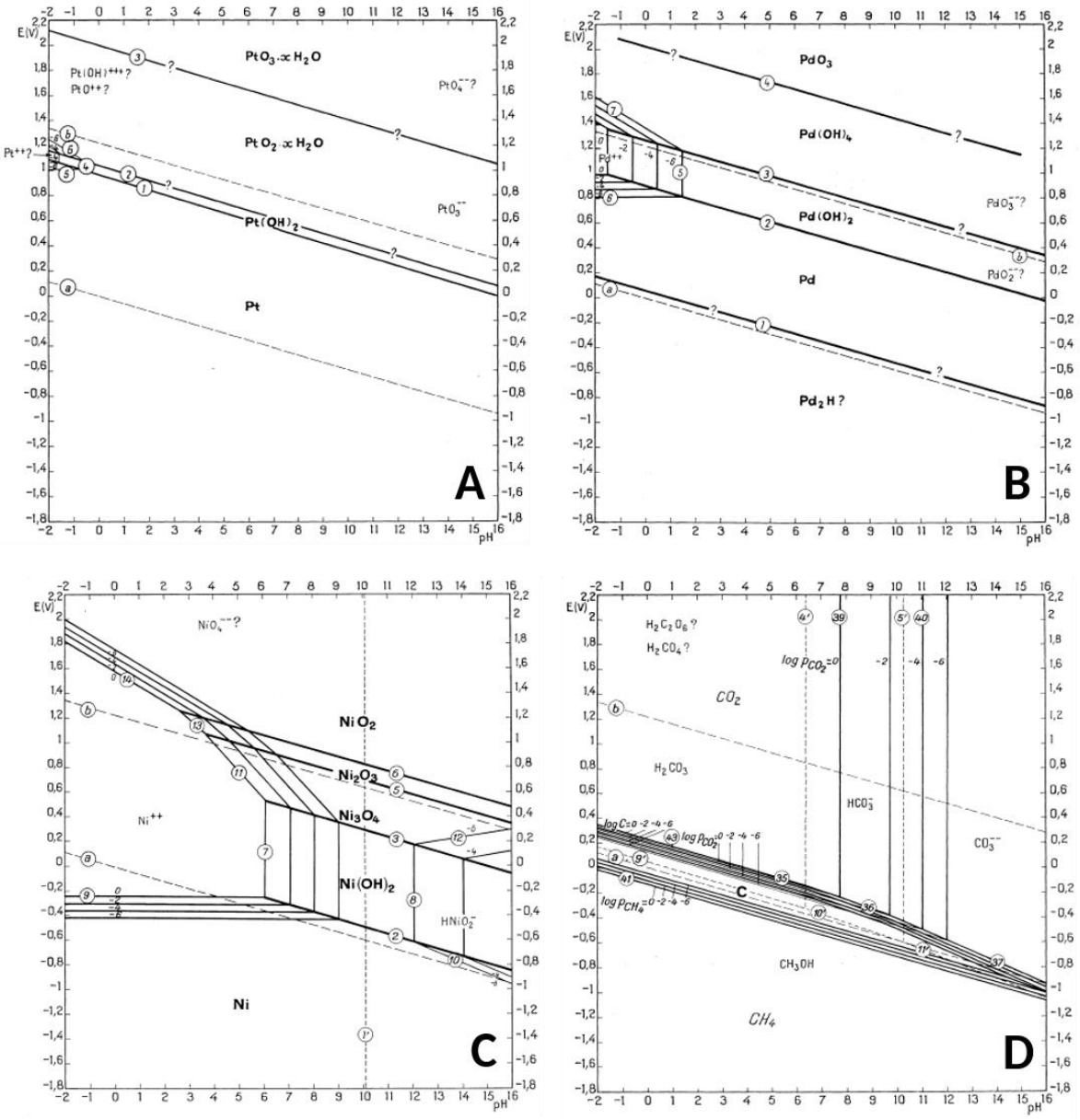

Figure I.8. Pourbaix diagram of (A) Platinum, (B) Palladium, (C) Nickel and (D) Carbon.

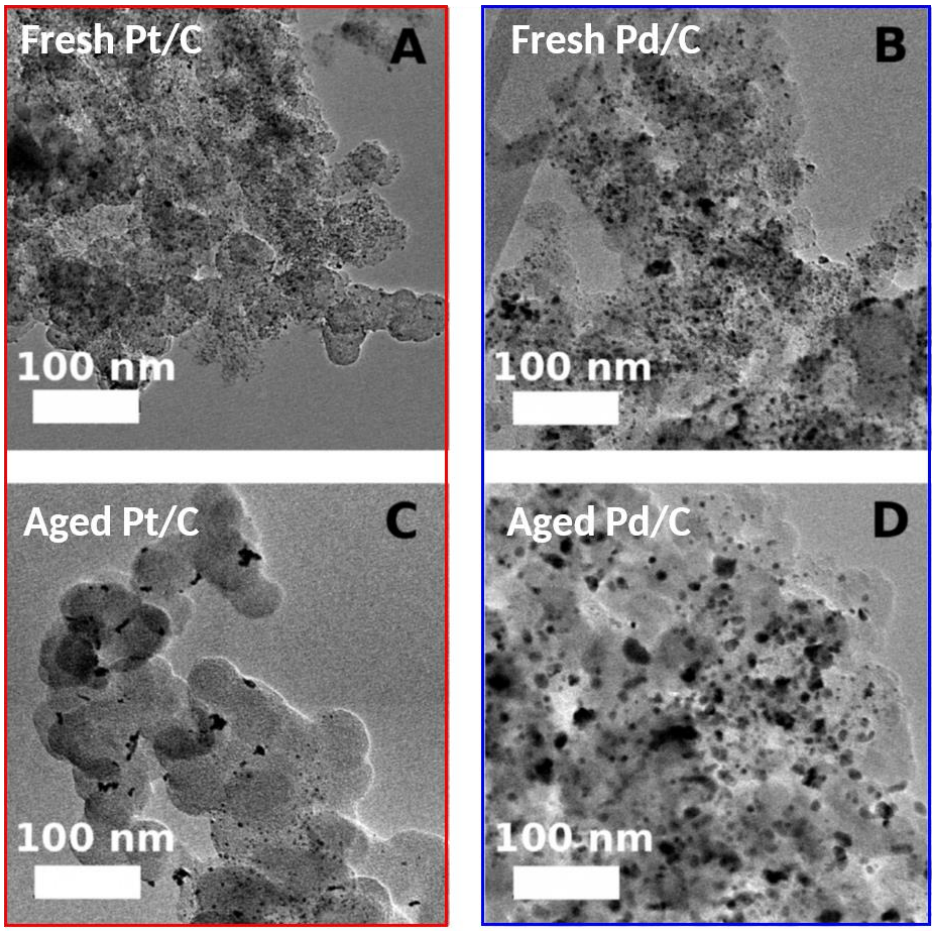

Figure I.9. TEM images of the anodic catalysts before the fuel cell characterizations: (A) Pt/C, (B) Pd/C and after the fuel cell characterizations: (C) Pt/C, (D) Pd/C. Adapted from Ref. [70].

As a consequence, just as the lack of knowledge about the BOR mechanism hinders the development of efficient anodic electrocatalysts, the lack of knowledge about degradation mechanisms impedes the selection of sustainable electrocatalysts; indeed, the durability criterion is just as important as the BOR efficiency criterion. The scientific community has understood this very well: the degradation mechanisms of carbon-supported Pt NPs electrocatalysts (the state-of-the-art electrocatalyst for ORR) used for PEMFCs are now well understood (details are given in the next section) and studies in that field are now focusing on the improvement of material stability.

I.3.2 PEMFC electrocatalysts degradation mechanism

In a PEMFC, the electrocatalysts represent one of the main sources of degradation due to the aggressive environment they have to operate in, especially in the cathode side (oxygen-saturated environment and high electrochemical potential). The Pt/C electrocatalyst degrades upon operation via two main processes [155]:

- The Pt NPs and Pt oxides can corrode (dissolved) through an electrochemical ($Pt \rightarrow Pt^{2+} + 2\,e^-$) or a chemical reaction ($PtO + 2\,H^+ \rightarrow Pt^{2+} + H_2O$) [156]. The dissolution process highly depends on the NPs size, the pH, the temperature, the gaseous atmosphere, the potential range and the potential sweep rate used in model or real PEMFC operating conditions [157–159]. This dissolution can be then followed by:
    - A re-deposition onto bigger NPs, according to 3D-Ostwald ripening (small NPs have the inherent tendency to dissolve at the expense of larger ones in order to reduce the high surface energy) [160,161];
    - The metal cations can also be transported into the membrane and be reduced by the H_2 coming from the anode via crossover [162,163].
- The carbon support can corrode:
    - In the case of a slight corrosion, oxygenated-containing groups form on the carbon surface (such as alcohol, quinone or carboxylic acid [164,165]) and lead to Pt NPs migration, that can further lead to Pt NPs agglomeration. If the cathode compartment is in a reducing environment due to H_2 crossover, the particles can also coalesce and form aggregates.
    - In the case of a strong carbon corrosion, CO_2 is evolved (**Equation I.12**, in priority from amorphous regions of carbon, but organized (graphitic) region are progressively amorphized via surface oxidation/surface groups formation and then converted into CO_2 also), thereby leading to the destruction of the carbon structure; Pt NPs can then detach and fall from the carbon support. Theses NPs are then lost and cannot catalyze the electrochemical reaction anymore because they are electronically disconnected. They can also re-deposit onto the membrane and contribute to its degradation.

In all cases, the degradation of the electrocatalyst leads to a decrease of the ElectroChemical Surface Area (ECSA, which the specific Pt surface used to catalyze the electrochemical reactions) and then a decrease of the overall FC performances.

To be more specific regarding carbon corrosion, the carbon oxidation corrosion (COR) is thermodynamically possible for E > 0.207 V *vs*. RHE but is kinetically limited for E < 0.9 V *vs*. RHE. The COR produces CO_2 (**Equation I.12**), to a lesser extent CO (**Equation I.13**) and also carbon surface oxides (CO_{surf}) [166,167].

$$C + 2\,H_2O \rightarrow CO_2 + 4\,H^+ + 4\,e^- \qquad \textbf{Equation I.12}$$

$E°$ = 0.207 *vs*. NHE

$$C + H_2O \rightarrow CO + 2\,H^+ + 2\,e^- \qquad \textbf{Equation I.13}$$

$E°$ = 0.518 V *vs*. NHE

In addition, it was shown, thanks to DEMS and FTIR, that the presence of Pt NPs catalyze the COR [166,168]: it is suggested that for 0.3 < E (V *vs*. RHE) < 0.6, carbon surface oxides form and the ones present at the vicinity of Pt NPs back-spillover from the carbon support onto the Pt NPs, where they are converted into CO_{ads} species (**Equation I.14**) and then oxidized at higher potential (*ca*. E = 0.8 V *vs*. RHE) into CO_2 (**Equation I.15**), the reaction being catalyzed by Pt at higher potential, *i.e*. when E > 0.6 V *vs*. RHE.

$$CO_{suf} + Pt \rightarrow Pt - CO_{ad} \qquad \textbf{Equation I.14}$$

$$Pt - CO_{ad} + H_2O \rightarrow CO_2 + 2\,H^+ + 2\,e^- \qquad \textbf{Equation I.15}$$

To mitigate the Pt NPs corrosion issue, alloying Pt with other metals and especially Co, demonstrated better stability than pure Pt NPs [169] and enabled reducing the cost of the electrocatalyst. However, the stability improvement was explained by the role of sacrificial anode of Co, that leads to Co dissolution, which pollutes the polymer electrolyte membrane afterwards, hindering O_2 and H^+ transport [170].

To alleviate the carbon corrosion issue, the scientific community has taken an interest in alternative supports and investigated two main strategies: (i) the replacement of the carbon support by corrosion-resistant materials and (ii) the modification of the carbon structure. In that spirit, boron-doped diamond, graphene, carbon nanotubes, carbon nanofibers, mesoporous carbon, titanium oxides, tungsten carbide, or tungsten oxide have been studied (among others) [171]. However, these alternative supports still suffer from expensive production costs, low

conductivity or low specific surface area and improvements are needed to obtain the ideal support.

In addition, several studies revealed that the COR was highly influenced by the carbon structure [172–175]: it was shown that graphitized carbons are more resistant to electrochemical corrosion than structurally-disordered carbon support (such as HSAC, which are generally used to support metal NPs owing to the very good dispersion of the NPs onto this support). However, these types of carbon supports have generally a low specific area and it is difficult to obtain a good dispersion of the NPs.

Finally, the COR kinetics and mechanisms are influenced by the structure of the carbon, the potential values and also the presence of metal NPs. All these studies and the technologies used to unveil the degradation mechanism of cathodic electrocatalyst in PEMFC enabled Zadick and coworkers to reveal in 2015 the first insights into the electrocatalyst degradation mechanism in AFC conditions.

I.3.3 First steps towards the fate of electrocatalyst degradation in alkaline media

I.3.3.1 The case of commercial carbon-supported platinum electrocatalyst

The lack of knowledge about electrocatalyst degradation in alkaline media incited Zadick and coworkers to investigate the stability of the most studied electrocatalysts in AFC, namely Pt/C and Pd/C (the case of Pd will be detailed in the next section) [140]. To that goal, they chose to subject the electrocatalyst to an AST consisting of 150 potential cycles between E = 0.1 and 1.23 V *vs*. RHE with a potential sweep rate v = 100 mV s^{-1}, at T = 25°C in 0.1 M NaOH electrolyte arguing that: (i) the low potential limit (0.1 V *vs*. RHE) was realistic for an anodic electrocatalyst but enable to prevent the HER (which would add another parameter), (ii) the high potential limit (1.23 V *vs*. RHE) was realistic for a cathodic electrocatalyst, (iii) this wide potential window is very often used in the literature to investigate numerous fuel electrooxidation and finally (iv) many electrocatalytic studies initiate with a "cleaning step" of the material in supporting electrolyte in such a potential window for several tens (if not hundreds) cycles. They also decided to subject these electrocatalysts to the same AST but in acidic media (0.1 M $HClO_4$ or H_2SO_4), for comparison. The degradation of each material was evaluated using the loss of the ECSA thanks to CO_{ads}-stripping measurements (conducted in acidic media before and after the AST) and the

evolution of the morphology of the material along the AST was monitored using Identical-Location Transmission Electron Microscopy (IL-TEM) (see **Figure I.10**).

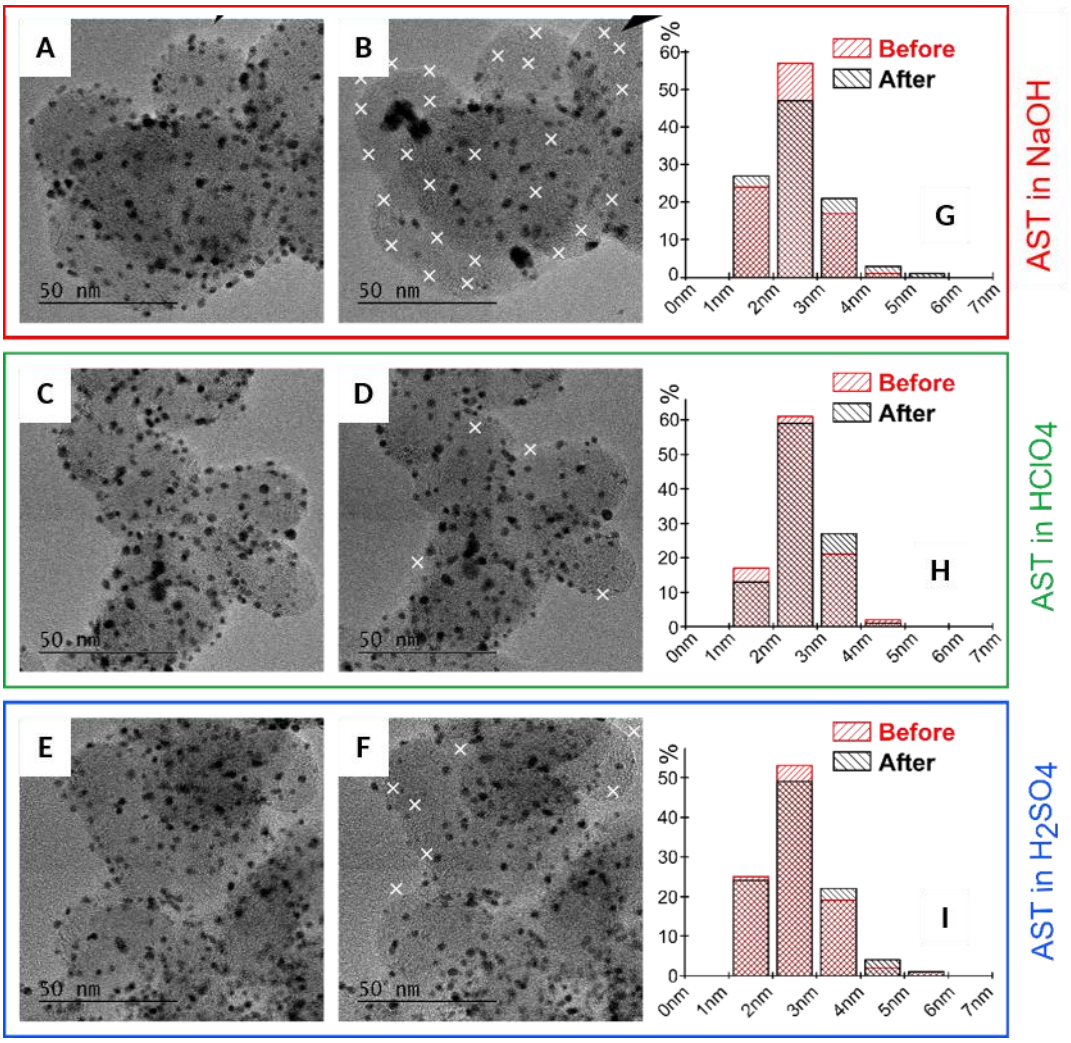

Figure I.10. IL-TEM micrographs pre- and post-AST at 25°C in NaOH (A, B), $HClO_4$ (C, D) and H_2SO_4 (E, F). The white crosses highlight the NPs loss (in a non-comprehensive manner). Corresponding particles size distribution histograms in NaOH (G) $HClO_4$ (H) and H_2SO_4 (I). Adapted from Ref. [176].

The Pt/C used was made of 2.5 nm-Pt NPs and the results revealed that 60% of the ECSA was lost after the AST conducted in alkaline media, which was three times more than the AST conducted in acidic media (almost no differences were observed between $HClO_4$ and H_2SO_4) [176]. The analysis of the IL-TEM micrographs recorded before and after the AST enabled to establish the particles size distribution (PSD) histograms (**Figure I.10**) and to provide insights into the degradation mechanism at stake: the authors concluded that the ECSA loss mostly resulted

from Pt NPs detachment from the carbon support. The analysis of the PSD indicated no extensive Pt dissolution; thus, a 3D Ostwald ripening mechanism was ruled out. However, it turns out that a severe carbon corrosion (investigated with Raman spectroscopy and XPS measurements) could not account for the NPs detachment. It was assumed that a modification of the anchoring site between the carbon support and the Pt NPs could explain such degradation.

I.3.3.2 The case of palladium-based electrocatalysts

A Pd/C electrocatalyst with a near-similar NPs size (4 nm) as the Pt/C was also subjected to an identical AST in both alkaline and acidic media [177]. The ECSA loss after 150 potential cycles in alkaline media turned out to be lower than for Pt/C: 35% ECSA loss was reported (so twice less than for Pt/C). On the contrary, the ECSA loss after a similar AST but conducted in acidic media lead to 65% ECSA loss: as expected, according to the literature, Pt/C is much more stable in acidic media than Pd/C, but the opposite seems verified in alkaline media. The Pd/C electrocatalyst was also subjected to a longer AST: the ECSA loss after 1000 potential cycles was 62%, so Pd cannot be considered stable in alkaline environments. The IL-TEM micrographs recorded before and after the 1000-cycle-long AST indicated similar morphology evolution than for Pt/C. Thus, the authors concluded that most of the damages caused by the repeated potential cycling consist of massive detachment of particles, probably because their anchoring sites/groups to the carbon substrate are irreversibly destroyed.

- **Influence of the Pd NPs size**

The influence of the Pd NPs size was also investigated using a Pd/C electrocatalyst with bigger NPs (11 nm) [177]. The results indicated 18% of ECSA loss (compared to 35% for the smaller NPs-electrocatalyst). However, it is worth noting that the CO_{ads}-stripping measurements contributed to the ECSA loss of up to 30% in the case of the small-NPs-Pd/C and 10% for the big-NPs-Pd/C. Finally, the NPs size did not significantly influence the extent of degradation.

- **Influence of the presence of a reducer**

The influence of the presence of a strong reducer was investigated using gaseous H_2 and hydrazine borane (HB) to mimic the environment of a liquid AFC anode [177]. The results revealed similar ECSA loss for the big-NPs-Pd/C in both cases but a slight increase of the ECSA loss was reported (up to 5 points) for the small-NPs-Pd/C, indicating the existence of a slight particle size effect on the durability of Pd NPs in reducing alkaline environment.

- **Influence of the carbon support morphology**

Kabir *et al*. [178] compared the degradation of Pd NPs supported on two different carbon supports: a partly amorphous commercial carbon (Vulcan XC-72) and a graphitized carbon (graphene nanosheets). Using the same AST protocol described above (with 150 and then 1000 cycles), the authors reported a similar ECSA loss but different morphology evolution: the Pd/Vulcan XC-72 degraded via major NPs detachment with minor agglomeration whereas the Pd/graphene degraded through a high rate of dissolution/redeposition of isolated NPs and coalescence of agglomerates on the graphene support. Again, in both cases, Raman spectroscopy measurements indicated no extensive carbon corrosion. Finally, using a more graphitized carbon support does not mitigate the degradation of the Pd/C electrocatalyst (when it is the case for PEMFC cathodic electrocatalyst degradation as mentioned earlier).

- **Influence of the Pd morphology**

The influence of the Pd morphology was studied using unsupported cubic Pd NPs [179]. The AST protocol was not composed of 150 successive CV but instead consecutive chronoamperometry (CA) and CV was used. IL-TEM micrographs (see **Figure I.11**) indicated that the AST leads to a modification of the morphology from a cubic NPs to coalesced and near-spherical NPs indicating a dissolution/redeposition process, at least at the local scale (from neighboring NPs).

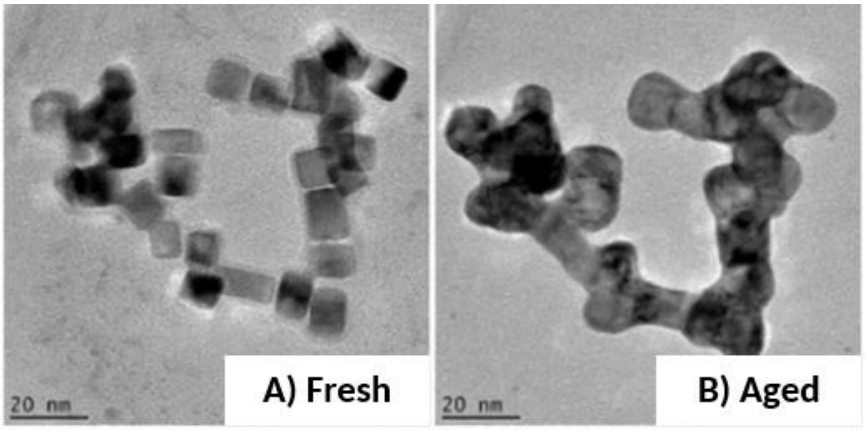

Figure I.11. IL-TEM micrographs of unsupported cubic Pd NPs obtained pre (A) and post (B) 150 CV cycles between E = 0.1 and 0.9 V *vs*. RHE at T = 25°C in Ar-purged 0.1 M NaOH. From Ref. [179].

I.3.3.3 The case of carbon-supported nickel-based electrocatalysts

Zadick *et al*. also investigated the case of three carbon-supported non-(entirely-)noble electrocatalysts: Ni_3M/C (M = Ag, Pd, or Co) [180]. The same AST (than for Pt/C studies) was applied and the IL-TEM micrographs revealed that the Ni_3Ag/C was the most degraded; the Ag-rich large NPs being the most affected by the electrochemical treatment; the Ni_3Pd/C sample was undergoing some loss of NPs, but the extent of this loss is well below that witnessed in similar conditions for pure Pd/C; finally, Ni_3Co/C material exhibited the best stability, the IL-TEM micrographs showing no evident morphology changes.

I.3.3.4 Can the degradation be mitigated?

In the light of these experiments, the destruction of the anchoring point seemed to account for the degradation of the carbon-supported Pt and Pd electrocatalyst. Thus, Miller *et al*. [181] tested the stability of an advanced electrocatalyst consisting of Pd NPs deposited onto a CeO_2/C support, the Pd NPs being preferentially deposited on the CeO_2 regions, thus creating a "buffer" layer between the carbon and the Pd NPs. After a 1000-cycle-long AST, the IL-TEM showed no major NPs detachment but instead the initially small and agglomerated NPs became larger and round-shape; this suggests that a dissolution/redeposition process was likely at stake. As a result, it is possible that the degradation of carbon-supported Pd NPs electrocatalyst could be mitigated if the metal NPs are not in direct contact with the carbon substrate.

In summary, Zadick and coworkers initiated the investigations about the degradation of carbon-supported and unsupported metal NPs electrocatalysts in alkaline media. They showed that the alkaline environment is very aggressive towards Pt and Pd electrocatalysts and leads to dramatic deterioration of this materials after a mild AST protocol, via a major NPs detachment. Consequently, the degradation of these electrocatalysts cannot be ignored anymore and should be taken into account, not only for long-term operation but also for kinetic studies. While no pronounced dissolution of Pt NPs nor extensive carbon corrosion could account for the NPs detachment, the destruction of the anchoring point between the NPs and the carbon substrate seems to rationalize such degradation. Especially for the case of Pd, a slight effect of the NPs size and morphology was reported as well as the carbon-support morphology onto the degradation mechanism. Finally, carbon-supported Ni-based electrocatalysts showed promising durability performances, since no morphology changes were noticed after a 1000-cycles-long AST.

I.4 Conclusions and PhD outline

At a time when the development of decarbonized energy generators is urgent, fuel cells present interesting properties and offer a serious alternative to conventional energy generators based on fossil fuel combustion. The PEMFC is currently the most mature technology but its commercialization is hampered by technological issues linked to hydrogen storage and transport.

In that context, alternative liquid fuels have been considered, and among them, the use of sodium borohydride as the fuel of the direct borohydride fuel cell shows promising theoretical performances in terms of energy density and cell voltage. However, in a DBFC, the electricity is generated via the electrooxidation of borohydride, a very complex reaction which is misunderstood on most electrocatalysts and in DBFC operation conditions. In addition to good BOR catalytic activity, the ideal electrocatalyst must be stable in operation. In that field, studies were very scarce until 2015, when the first insights into the fate of carbon-supported Pt and Pd electrocatalysts in alkaline media were revealed. It was shown that the alkaline environment was very aggressive and lead to significant particles detachment from the carbon support owing to the destruction of the anchoring point between the particles and the carbon substrate.

In that frame, this PhD was motivated by the necessary further understanding of the BOR on carbon-supported palladium-based electrocatalysts in relevant conditions to DBFC operation (*i.e.* high fuel concentration and high temperature) in addition to the impact of the electrode design on the BOR activity. Finally, this work also aimed to provide insights into the origin of the particles detachment occurring during carbon-supported Pt electrocatalyst degradation. Therefore, this thesis is articulated around three studies reported in **CHAPTER II**, **CHAPTER III** and **CHAPTER IV** respectively:

- **CHAPTER II** deals with a characterization of several Pd-based electrocatalysts for the BOR in DBFC operating conditions; the influence of several parameters on the BOR kinetics are surveyed;
- **CHAPTER III** focuses on the study of the impact of five design of anodic catalytic layers on the BOR efficiency, first using a fundamental approach and then using a unit cell of DBFC;
- Finally, **CHAPTER IV** deals with the investigation of the origin of the particles detachment occurring during the degradation of carbon-supported PGM electrocatalysts, using mostly *in situ* Fourier transform infrared spectroscopy.

Chapter II

Pd-based electrocatalysts for the BOR

II.1 Motivations of the study

II.1.1 BOR on Pd/C electrocatalysts

As discussed in the previous chapter, according to the literature, Pd-based electrocatalysts showed interesting properties and promising catalytic activity towards the BOR. However, both the BOR kinetics and mechanism are still poorly studied/documented and understood on palladium, and most of BOR investigations on carbon-supported Pd-only electrocatalysts are conducted for low $NaBH_4$ concentration (between 5 and 30 mM) and low temperature (20-30°C), *i.e.* in conditions that may not be relevant for the DBFC application.

Simoes *et al*. [67] studied the BOR on carbon-supported Pd nanoparticles (NPs) (Pd/Vulcan XC72) and reported an open circuit potential (OCP) of -0.2 V *vs*. RHE. They concluded that the BOR mechanism follows different pathways according to the electrode potential: (i) for low potentials, -0.2 < *E* < 0.1 V *vs*. RHE, partial heterogeneous hydrolysis proceeds and leads to the production of gaseous hydrogen (H_2) and BH_3OH^- (**Equation II.1**) which is electrooxidized afterwards according to **Equation II.2**; at higher potentials (*E* > 0.4 V *vs*. RHE), the direct BH_4^- electrooxidation occurs through a 6-electron reaction. In the intermediate potential range (0.1 < *E* < 0.4 V *vs*. RHE), the H_2 oxidation and the direct BH_4^- oxidation reactions proceed in parallel.

$$BH_4^- + H_2O \rightarrow BH_3OH^- + H_2 \qquad \textbf{Equation II.1}$$

$$BH_3OH^- + 3\,OH^- \rightarrow BO_2^- + 2\,H_2O + 3\,e^- \qquad \textbf{Equation II.2}$$

Grimmer *et al*. [107] also studied a Pd/Vulcan XC72 electrocatalyst and identified two potential domains: (i) a 4-electron oxidation pathway at low potentials (*E* < 0.4 V *vs*. RHE), and an 8-electron oxidation pathway at higher potentials (0.8 V *vs*. RHE). Using nuclear magnetic resonance (NMR) spectroscopy, they showed that a non-identified intermediate specie (but likely BH_2OH) poisons the Pd surfaces at low potential and is later oxidized at high potential.

Yang *et al*. [81] studied electrocatalysts made of Pd NPs supported on three different carbon substrates to evaluate the influence of the carbon support on the Pd nanoparticles distribution and BOR activity: an activated carbon (AC), a conventional carbon black (Vulcan XC72) and multiwalled carbon nanotubes (MWCNTs). The Pd NPs supported on MWCNTs exhibited better BOR activity than the two others electrocatalysts, due to smaller Pd NPs and a better dispersion on the carbon substrate (owing to a supposed larger specific surface area of the CNTs, which

apparently had not been measured). In addition, they showed that a high ratio $[OH^-]/[BH_4^-]$ reduced the H_2 escape for the Pd/AC catalyst, but this ratio had less impact on the H_2 escape for the two others materials. In the same line, Martins *et al*. [182] came to similar conclusions as Yang *et al*. [81] studying Pd NPs deposited on two different biobased carbon supports in comparison with Vulcan XC72: the former exhibited better BOR kinetics and activity due to high specific surface area of the carbon supports (*ca*. 6-fold higher than for Vulcan XC72), even though the relationship between the BOR activity and the surface area of the carbon was not precisely detailed.

As interesting as they are, these studies remain scarce and fall short to provide a complete understanding of the BOR on Pd electrodes, in particular in experimental conditions relevant to DBFC application. Thus, one of the objectives of this PhD work was to study the BOR on carbon-supported Pd electrocatalysts in conditions closer to the real DBFC system. To that goal, Pd/C electrocatalysts were synthetized and provided by our project partners from the Naval Research Laboratory; they were characterized for several $NaBH_4$ concentrations (5, 50 and 500 mM) and at higher temperature (T = 60°C), these conditions being close to the optimal ones for the DBFC performances [70].

II.1.2 BOR on Pd/C-CeO_2 electrocatalyst

In addition to the characterization of these Pd/C electrocatalysts, we had the opportunity to work with the group of Pr. Dario Dekel from Technion (Israel) and the group of Dr. Hamish A. Miller from CNR-ICCOM (Italy), who synthetized advanced electrocatalysts made of Pd NPs supported on a mixed support composed of Vulcan XC72 carbon black and cerium oxide (CeO_2). Ceria is a metallic oxide which adopts a fluorite (CaF_2)-type structure: Ce^{4+} cations form a cubic face-centered host network and O^{2-} anions occupy all tetrahedral sites. Ceria has received a lot of attention for its use in many heterogeneous catalytic reactions owing to its facile ability to switch between Ce^{4+} (CeO_2) and Ce^{3+} (Ce_2O_3) oxidation states, thereby enabling to store and release oxygen atoms [183]. Thus, such electrocatalysts were originally designed to enhance the hydrogen oxidation reaction (HOR) kinetics in alkaline media and proved to have indeed 5-fold higher activity in comparison to Pd/C towards the HOR [181,184]. The origin of such improvement lies in CeO_2 ability to provide OH_{ads} at low potentials to Pd-H_{ads}, thereby accelerating the HOR kinetics in base. For the same reason, the addition of ceria on carbon-supported Pt-based electrocatalysts also proved to be efficient to enhance methanol [185,186] and ethanol [186–189] electrooxidation activity.

The conventional route to prepare metal-oxide/catalyst composites consists in nanodispersing the catalytic metal on the metal oxide substrate; the latter can participate to the catalytic process in a so-called bifunctional mechanism (a good example is the enhanced CO-tolerance of Pt/WO_3 nanoparticles [190]). When indeed the metal oxide provides its own function, an inverse configuration is also possible, in which the metal oxide is deposited onto the (carbon-supported or not) catalytic nanoparticles (**Figure II.1**) [191], this configuration possibly giving superior performances than the conventional one or being more prone to provide understanding in fundamental studies [191,192]. For these two reasons, the group of Hamish A. Miller synthetized and provided us an electrocatalyst made by a first deposition of Pd NPs onto carbon support followed by deposition of CeO_2 onto the Pd/C. The abbreviation used for this electrocatalyst will be Pd/C-CeO_2.

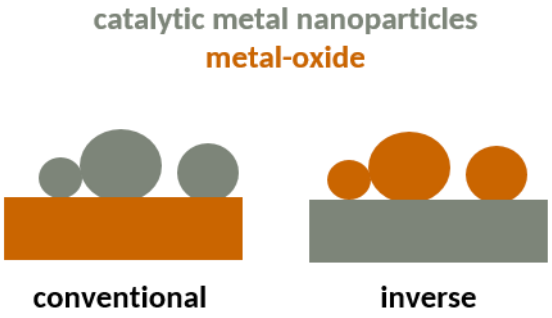

Figure II.1. Simple representation of the two main configurations of metal-oxide / catalytic nanoparticles composites used for catalytic reactions.

One initial postulate of the present study was that the addition of ceria on the Pd/C electrocatalyst could be interesting for the BOR as well, because CeO_2 ability to easily provide OH_{ads} at lower potential than Pd could assist the BH_4^- electrooxidation mechanism, at least if it proceeds for Pd as for Pt (see **Figure I.5** [54]).

Because working directly in a real DBFC system adds a lot of components (and their corresponding parameters) such as the membrane, the cathode, the electrode substrate or the fuel flow rate, parameters that can be strongly correlated and lead to a tricky understanding of the individual behavior of each component and of the overall system [60], it was decided to study the BOR in a more fundamental (and controlled manner). All the data presented in this chapter originate from 3-electrode cell measurements, using a rotating disk electrode (RDE) configuration, in order to isolate the anodic material and to reduce the number of parameters which can affect the BOR activity.

II.2 Experimental details

II.2.1 Electrocatalysts

The four carbon-supported Pd electrocatalysts (Pd/C) studied in this work were synthetized by Robert W. Atkinson III from the Naval Research Laboratory (Washington DC, USA) using a vapor deposition protocol described in **Annex 1.A**. The electrocatalysts are all supported on Vulcan XC72 carbon black and are referred to as 22, 33, 44 or 53 wt.% Pd/C depending on the metal weight fraction (wt.%). The Pd-based electrocatalyst supported on Vulcan XC72 carbon black and modified by ceria (CeO_2) deposition was synthetized by the group of Hamish A. Miller from the CNR-ICCOM (Florence, Italy), using a protocol also described in **Annex 1.B**. The Pd weight fraction is 20%, the ratio C/CeO_2 is 1/1 and the electrocatalyst will be identified as Pd/C-CeO_2 in this manuscript. A commercial Pt/C purchased from E-TEK was used as received without additional treatment for comparison purposes. Its carbon support is Vulcan XC72 and the metal weight fraction is 40%.

II.2.2 Morphological characterizations

The morphology of the electrocatalysts was analyzed by transmission electron microscopy (TEM) and/or scanning transmission electron microscopy (STEM) associated with X-ray energy dispersive spectrometry (X-EDS) elemental maps: **Annex 2.A** provides experimental details for these measurements. In addition, X-ray diffraction (XRD) patterns were obtained and **Annex 2.B** gives details of the measurements.

II.2.3 Electrochemical measurements

II.2.3.1 Material

The glassware and plastic accessories used for the experiments were soaked in Caro's acid (1-1 vol.% H_2O_2 (30 wt.%)-H_2SO_4 (> 95 wt.%)) overnight to eliminate organic and metallic pollution and thoroughly rinsed with ultrapure water (18.2 MΩ cm, < 3 ppb total organic carbon, Millipore Elix + Gradient, Millipore) prior to use. The electrochemical measurements were recorded thanks to a BioLogic® potentiostat (VMP3).

- **"Alkaline cell" for BOR activity measurements**

The electrochemical measurements for BOR activity were conducted in a four-electrode electrochemical cell with a poly chloro trifluoro ethylene (PCTFE) base in order to avoid glass contact with concentrated alkaline solution. The cell was composed of the following electrodes:

- The reference electrode was a mercury-mercury oxide (Hg/HgO) electrode filled with 1 M NaOH and connected to the cell via a Lugin capillary filled with 1 M NaOH to avoid any pollution by BH_4^- ions. The reference electrode was regularly checked with a reversible hydrogen electrode (RHE) and its potential was 0.925 V *vs.* RHE. However, all the potentials mentioned in this work are given relative to the RHE;
- The counter electrode was a glassy-carbon plate connected to the potentiostat with a gold wire;
- An additional electrode (the "fourth electrode"), made of a gold wire, was connected to the reference electrode via a capacitor bridge in order to avoid electrical noise [193];
- The working electrode was a rotating disk electrode (RDE) made of a glassy-carbon disk (0.196 cm^2, Sigradur®) on which a small volume of an electrocatalyst suspension was deposited. The drop was then dried with a heat gun to ensure the evaporation of the solvent while the electrode was rotated, as recommended by Garsany *et al.* [194] in order to obtain homogeneous catalytic layer. The electrocatalysts suspensions were prepared by mixing the electrocatalyst powder of choice with ultrapure water, 5 wt.% Nafion® solution (Sigma Aldrich) and isopropyl alcohol (IPA) in quantities given in **Table II.1** and then sonicated during 20 minutes. It is worth mentioning that it was decided to work with a constant catalytic layer thickness (so a constant amount of carbon), while the metal loading on the electrode varied according to the metal weight fraction of the electrocatalyst; this methodology enables to study the influence of the Pd sites density on the BOR kinetics.

Fresh electrolyte solutions (5, 50 or 500 mM $NaBH_4$ in 1 M NaOH) were prepared daily using $NaBH_4$ powder (> 98%, Merck) and NaOH-H_2O crystals (Suprapur®, Merck) dissolved in ultrapure water. All the experiments were performed in deaerated electrolytes by bubbling argon in the solutions (Ar, > 99.999%, Messer). The cell was immersed in a thermostatic bath (Julabo) to heat the electrolyte at T = 60°C.

- **"Acidic cell" for CO_{ads}-stripping measurements**

CO_{ads}-stripping measurements were also performed in acidic electrolyte to assess the electrochemical surface area (ECSA) of the various electrocatalysts. Fresh electrolyte solution (0.1 M H_2SO_4) was prepared using H_2SO_4 (Suprapur®, Merck) and ultrapure water. The four-electrode cell used for the CO_{ads}-stripping measurements was composed of the following electrodes: (i) the reference electrode was a freshly-prepared RHE and used during maximum 2 hours; (ii) the counter electrode was a platinum mesh; (iii) the fourth-electrode was a platinum wire and (iv) the working electrode was similar to the one used for the BOR measurements.

Table II.1. Composition of the electrocatalyst suspensions and metal loadings used on the RDE.

Electrocatalyst	Mass of electrocatalyst (mg)	H_2O (µL)	5 wt.% Nafion solution (µL)	IPA (µL)	Volume of ink deposited on the RDE (µL)	Metal loading on RDE (μg_{metal} cm_{geom}^{-2})
22 wt.% Pd/C	10	3900	53.5	1650	10	20
33 wt.% Pd/C	10	3225	46	1250	10	37.2
44 wt.% Pd/C	10	3200	38.4	1100	10	52
53 wt.% Pd/C	10	2600	32.2	1000	10	74.4
20 wt.% Pd/C-CeO_2	10	2180	27.4	864	10	33.2
40 wt.% Pt/C	10	3240	41.2	1330	10	44.2

II.2.3.2 Methods

Linear scan cyclic voltammetry (hereafter simply denoted as cyclic voltammetry, CV) was used to get insights into the surface properties and reactivity of the different electrocatalysts. A CV consists in scanning the working electrode potential in a triangular profile between a low and high value for a fixed scan rate, while measuring the current resulting from the electrochemical processes. The following procedures were used:

- **BOR activity measurements**

a) Ar-bubbling in the supporting electrolyte (1 M NaOH) during 15 minutes to remove all the oxygen dissolved in the solution;
b) 3 CV recorded in the potential range from *E* = 0.1 to 1.5 V *vs*. RHE at a potential sweep rate v = 100 mV s^{-1} and an electrode rotation rate ω = 400 revolution per minutes (rpm) in 1 M NaOH;
c) 3 identical CV as in step b) but for v = 20 mV s^{-1};
d) Addition of $NaBH_4$ in the supporting electrolyte;
e) Ar-bubbling during 15 minutes;
f) 1 CV recorded from low potential value (which is adapted depending on the $NaBH_4$ concentration and the electrocatalyst) to *E* = 1.5 V *vs*. RHE at v = 20 mV s^{-1}, this CV being repeated for different rotation rates of the RDE in the following order: 400, 900, 1600, 2500, 0 and 400 rpm. The first BOR CV at 400 rpm was repeated twice and only the second cycle is kept.

- **CO_{ads}-stripping measurements**

a) Ar-bubbling in the supporting electrolyte (0.1 M H_2SO_4) during 15 minutes to remove all the oxygen dissolved in the solution;
b) 15 CV recorded from *E* = 0.1 to 1.33 V *vs*. RHE at v = 50 mV s^{-1};
c) CO bubbling during 6 minutes followed by a purge of the solution with Ar bubbling during 39 min, while the electrode potential was maintained at *E* = 0.15 V *vs*. RHE;
d) 3 CV recorded from *E* = 0.1 to 1.33 V *vs*. RHE at v = 20 mV s^{-1}.

For both measurements, the Ohmic drop was corrected in dynamic mode at 85% for all the CVs. Three different tests were carried out for each electrocatalyst for reproducibility assessment and the error bars were calculated using the standard deviation.

II.3 Analysis of the electrocatalysts morphology

II.3.1 TEM micrographs

TEM micrographs of the Pd/C electrocatalysts are displayed in **Figure II.2**. The images reveal that the 22 and 33 wt.% Pd/C are mainly composed of a bimodal population of isolated particles (3-5 nm for the small ones, *ca*. 10 nm for the large ones) and rather small extent of agglomerates. The 44 wt.% sample is more heterogeneous, with regions where the Pd NPs are rather small and isolated, and others where large agglomerates are encountered. The 53 wt.%

electrocatalyst is made of small particles (2-4 nm; larger isolated nanoparticles are also encountered, but in a lesser extent than in the other cases) and a lot of agglomerates.

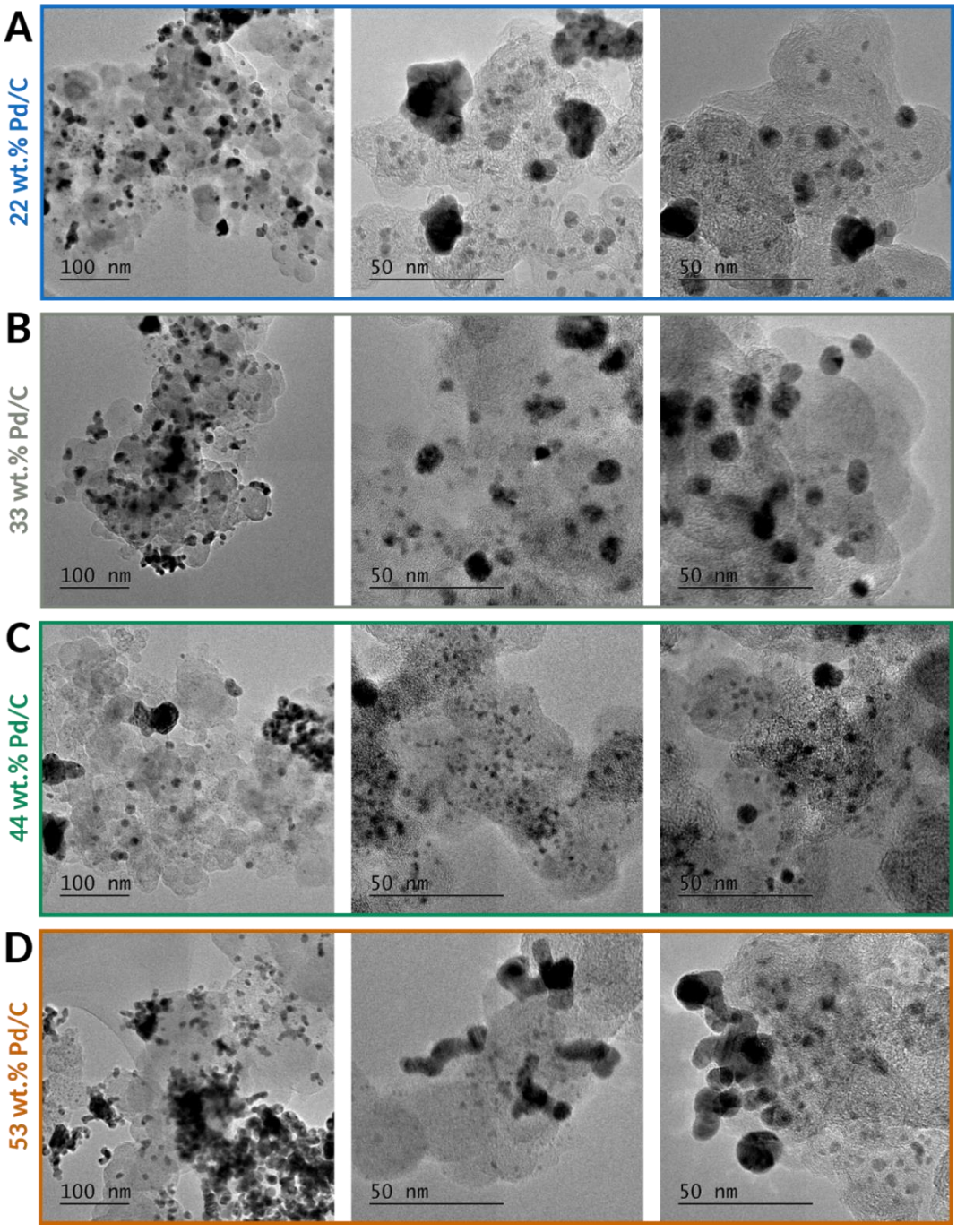

Figure II.2. TEM micrographs obtained on the four Pd/C electrocatalysts: (A) 22 wt.% Pd/C, (B) 33 wt.% Pd/C, (C) 44 wt.% Pd/C and (D) 53 wt.% Pd/C.

The TEM micrographs of the Pd/C-CeO_2 are shown in **Figure II.3.A.** The poor contrast between the Pd NPs and the cerium oxide prevents an easy analysis of the size and dispersion of the Pd NPs, as well as of the distribution of CeO_2. However, the few isolated particles that could be analyzed were rather small (*ca*. 2 nm). The morphology of this electrocatalyst was further analyzed using STEM coupled with X-EDS elemental maps. As an example, a representative image is displayed in **Figure II.3.B.C**. These techniques enabled to reveal that the Pd NPs (highlighted in green) are poorly dispersed on the carbon support (highlighted in blue) and the CeO_2 (highlighted in red) is globally well dispersed with some aggregates at the edge of the carbon grains. Overall, this means that nearly all the Pd NPs are in contact with some CeO_2.

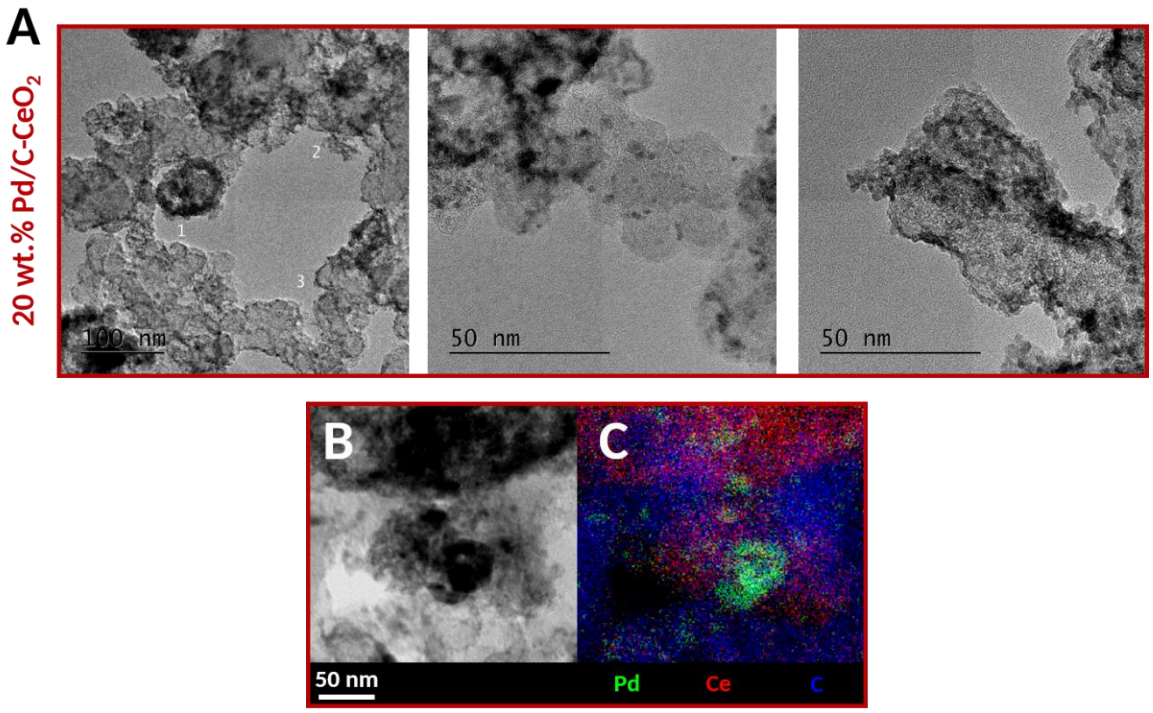

Figure II.3. (A) TEM micrographs, (B) STEM micrograph and (C) corresponding X-EDS elemental map of the 20 wt.% Pd/C-CeO_2 electrocatalyst.

II.3.2 XRD diffraction patterns

The XRD diffraction patterns of the Pd-based electrocatalysts are displayed in **Figure II.4**. They reveal that for the Pd/C electrocatalysts, all the peaks are indexed by the face-centered cubic structure of Pd. In the case of Pd/C-CeO_2, all the peaks are indexed by the face-centered cubic structure of Pd or the cubic structure of CeO_2. In addition, no shift of the main peak located at $2\theta \approx 40$ ° is noticeable, indicating that Pd and Ce do not form an alloy: the Pd/C-CeO_2 material is

a composite composed of Pd/C NPs surrounded by CeO_2 crystallites. The crystallites sizes were calculated using the Scherrer's equation:

Scherrer's equation: $$d = \frac{k\,\lambda}{\sqrt{H^2 - s^2}\cos\theta}$$ **Equation II.3**

with d the crystallite size, k the shape factor (1), λ the X-ray wavelength, H the integral width of the peak, s the contribution of peak enlargement due to defects in instrumental optics and θ the incident angle.

The crystallites sizes were calculated from the (111), (220) and (311) peaks for the Pd/C electrocatalysts and from the (111) and (311) peaks of palladium for the Pd/C-CeO_2; indeed, the (220) peak of Pd interferes with the (400) peak of CeO_2. The calculations from the different peaks lead to similar results, revealing that the crystallites did not experience preferential growth in any direction. The crystallites size are summed up in **Table II.2** and the error bars come from the measurements from the different peaks.

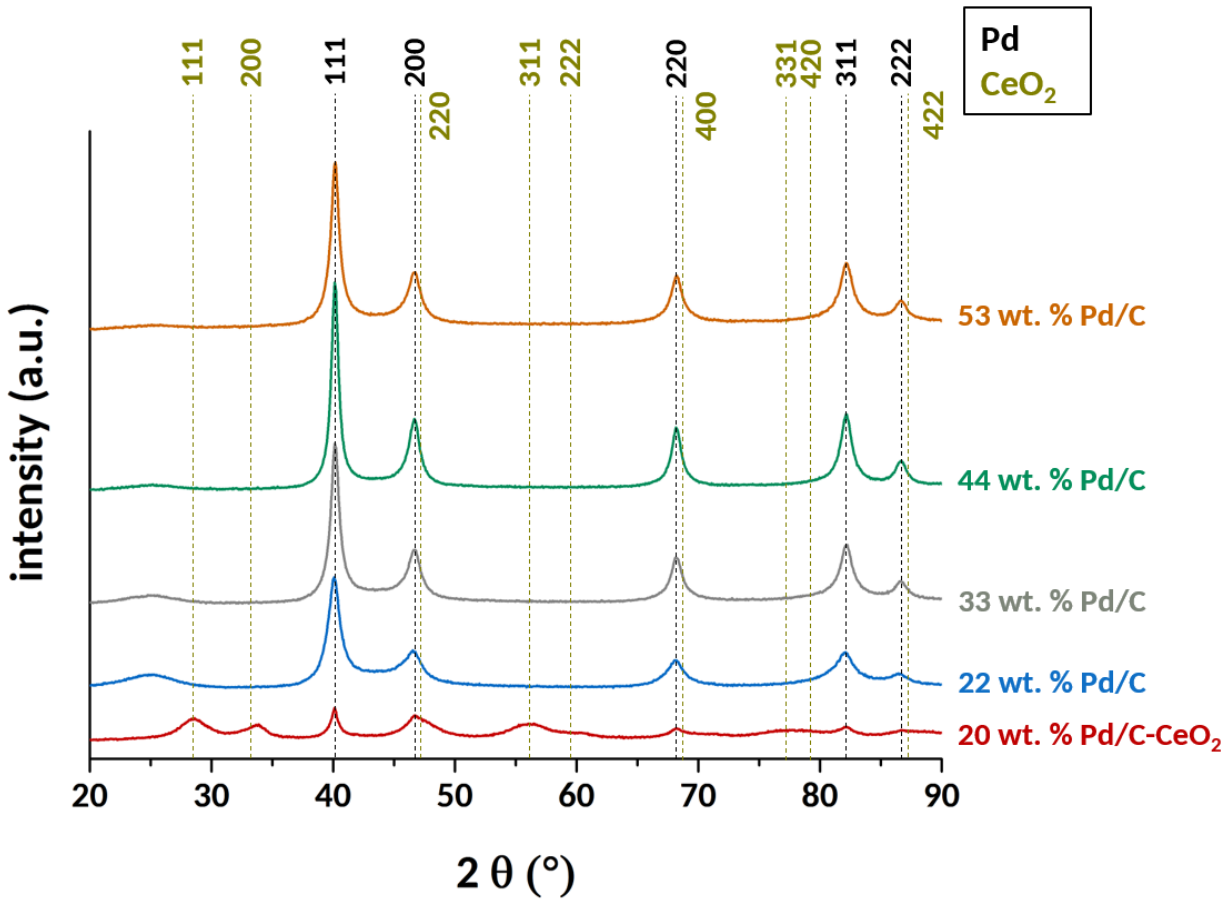

Figure II.4. XRD diffraction patterns of the Pd-based electrocatalysts studied in this work.

Table II.2. Crystallites size calculated from XRD patterns for the Pd-based electrocatalysts using the Scherrer's equation.

Electrocatalyst	Crystallite size (nm)
22 wt.% Pd/C	4.8 ± 0.5
33 wt.% Pd/C	6.3 ± 0.4
44 wt.% Pd/C	7.5 ± 1.1
53 wt.% Pd/C	6.0 ± 0.6
20 wt.% Pd/C-CeO_2	4.6 ± 0.7

II.4 Electrochemical surface area measurements

The determination of the electrochemical surface area (ECSA) of an electrocatalyst, which is the real active surface area available to catalyze electrochemical reactions, is crucial in order to provide a meaningful comparison of the activity for a given reaction for different materials [195]. Several methods (three based on electrochemistry and one based on microscopy) can be applied to estimate the ECSA. However, it is worth noting that all of them rely on a number of assumptions that can compromise their precision. This is especially the case regarding the electrochemical methods with palladium surfaces. The different methods are presented and discussed hereafter.

II.4.1 Existing and possible methods for Pd surfaces

II.4.1.1 Coulometry of H_{UPD} or PdO reduction

A typical CV obtained on a Pd/C electrocatalyst in supporting alkaline electrolyte, for 0.1 < *E* < 1.5 V *vs*. RHE, is shown in **Figure II.5**. During the potential scan, several species can adsorb on and desorb from the Pd surface.

At low potentials, for 0.1 < *E* < 0.4 V *vs*. RHE, the electrochemical adsorption of hydrogen occurs [196,197]: this phenomenon is called the "hydrogen under-potential deposition" (H_{UPD}), because it takes place above the thermodynamic reversible potential of hydrogen evolution reaction (HER). Assuming that a monolayer of adsorbed hydrogen covers all metallic NPs, the ECSA can be calculated using the coulometry of the H_{UPD} (corrected from the double-layer capacitive current), knowing the charge density associated with the adsorption of one monolayer of H_{UPD}.

However, in addition to H_{UPD}, Pd surfaces have the ability to absorb hydrogen into the Pd lattice from adsorbed hydrogen, to form Pd hydrides [198,199]. It was reported that this process occurs concurrently (in similar potential domains) to the under-potential deposition of hydrogen and HER for bulk polycrystalline Pd electrodes [200]; however suitable electrochemical conditions can enable to separate the specific features of H_{UPD}, H absorption and HER for nano-architectured Pd electrodes [201]. Nevertheless, in most cases, it is complicated to differentiate the corresponding charge density values between the adsorption and absorption processes, and the H_{UPD} method is almost never used to quantify the ECSA of Pd surfaces.

At higher potentials, from *E* = 0.6 - 0.7 V *vs*. RHE, oxygenated species can adsorb on Pd to form Pd oxides (PdO, PdOH; hereafter, Pd oxides will be abbreviated as the generic notation PdO) [202]. On the cathodic sweep, the peak located around 0.7 V *vs*. RHE in the present experimental conditions (see **Figure II.5**) corresponds to the reduction of PdO. In their review, Grden *et al*. [202] indicate that the charge associated to the reduction of the first monolayer of PdO formed on the metal surface is 424 µC cm_{Pd}^{-2}, this value being based on the work of Rand and Woods [203]. Other studies report values that vary from 405 to 424 µC cm_{Pd}^{-2} [67,107,204–209]. Thus, in a similar manner to H_{UPD}, the coulometry of the reduction of one monolayer of PdO (Q_{PdO}, µC, corrected from the double-layer capacitive current) can be used to calculate the ECSA (cm^2) using **Equation II.4.** However, the high potential value of the CV must be chosen correctly in order to form one full PdO monolayer (no less, no more) [210], the potential sweep rate having less impact [210,211]. Grden *et al*. [202] indicate that the potential limit of the formation of the first monolayer of PdO is in the potential range 1.45 - 1.5 V *vs*. RHE. In addition, the formation and desorption of the PdO depends on the particles size of the electrocatalyst: several authors [204–206,212] have reported that the peak corresponding to PdO reduction shifts to more negative potentials with decreasing particle size of Pd, indicating that the adsorption of oxygen-containing species is stronger on small particles; this phenomenon is also observed for Pt/C catalysts [213]: smaller NPs are more oxophillic (less noble) than larger ones. It is not reported whether the presence of metal oxide (*e.g*. CeO_2) affects or not the peak potential of PdO reduction, but this is likely.

$$\mathrm{ECSA_{PdO}} = \frac{Q_{\mathrm{PdO}}}{424} \qquad \textbf{Equation II.4}$$

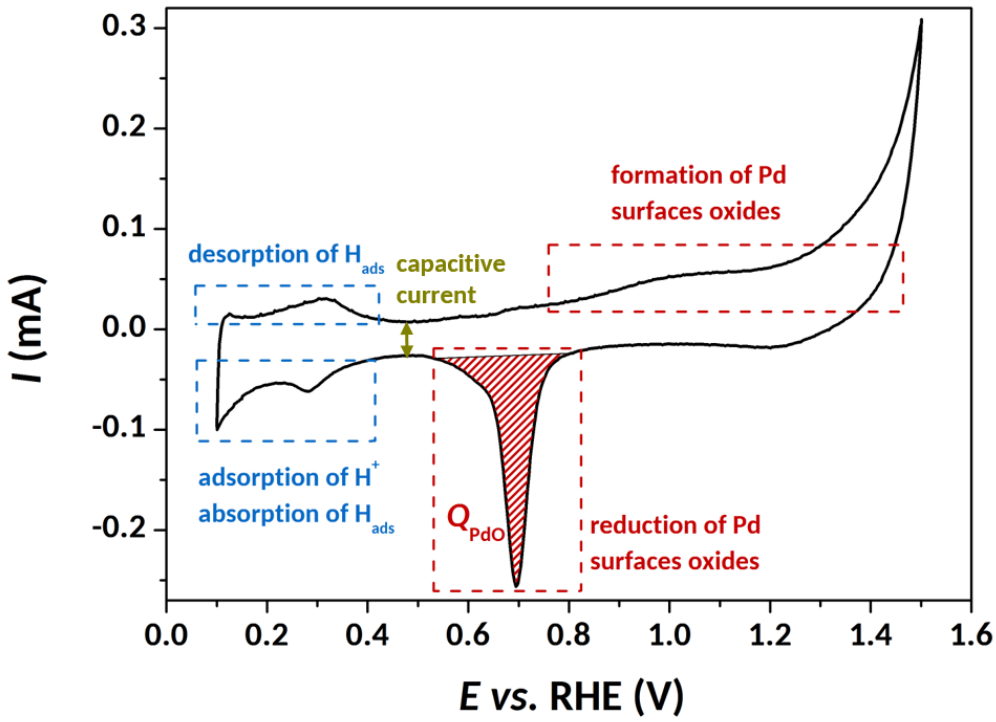

Figure II.5. Cyclic voltammogram obtained for a Pd/C electrocatalyst in 1 M NaOH. Conditions: Ar-saturated electrolyte, v = 20 mV s^{-1}, *T* = 25°C.

II.4.1.2 Coulometry of CO_{ads}-stripping

The CO_{ads}-stripping coulometry is a widely-used method to calculate the ECSA of Pt-based surfaces [214]. This method, generally used in acidic electrolyte, consists in: (i) the adsorption of CO on a Pt surface at low potential (typically 0.1 V *vs.* RHE), (ii) the removal of the remaining CO in the electrolyte and (iii) the stripping of CO_{ads} from the Pt surface by increasing the electrode potential using three successive CV. A typical CO_{ads}-stripping voltammogram obtained on a Pt/C electrocatalyst in acidic media is presented in **Figure II.6**: the green-stripped area corresponds to the total charge necessary to electrooxidize one monolayer of CO_{ads} (Q_{CO}, µC), the third CV cycle being used as baseline to integrate the peak. CO molecules can adsorb in a linear, bridged or threefold mode on 1, 2 or 3 atoms of Pt respectively, but the linear mode is predominant for Pt surfaces. Thus, the ECSA (cm^2) can be calculated using **Equation II.5**, assuming that all particles are covered by a monolayer of CO_{ads} molecules in a linear mode and that the charge density associated with the adsorption of one monolayer of CO_{ads} is 420 µC cm_{Pt}^{-2}.

$$\mathrm{ECSA_{CO}} = \frac{Q_{\mathrm{CO}}}{420} \qquad \textbf{Equation II.5}$$

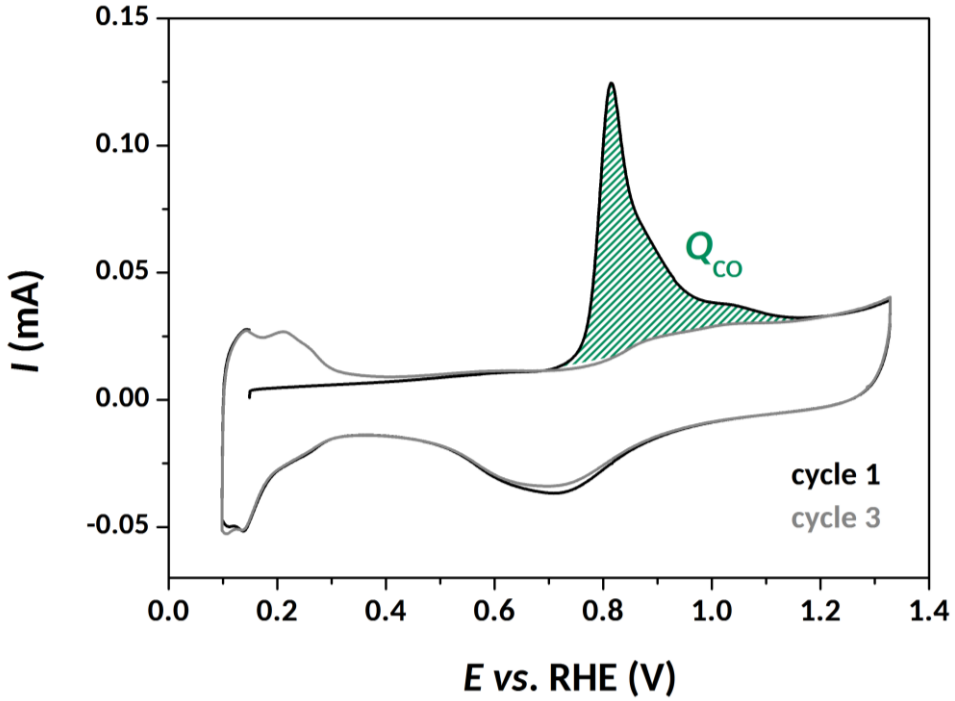

Figure II.6. CO_{ads}-stripping CV obtained on a Pt/C catalyst in 0.1 M H_2SO_4, v = 20 mV s^{-1}, *T* = 25°C.

For Pd surfaces, it was reported that CO adsorption occurs in both linear and bridged configurations [215,216], the bridged configuration being sometimes announced as the main mode [217]. In addition, some researchers perform CO-adsorption at a potential between 0.3 and 0.4 V *vs*. RHE in order to avoid any interference from hydrogen absorption [212,218,219]. This precaution does however not seem necessary, since CO-adsorption blocks the hydrogen adsorption and absorption processes [215,218,220]; it can even be considered detrimental, owing to the fact that CO adsorption might not be quantitative above 0.3 V *vs*. RHE. The charge density associated with the adsorption of one monolayer of CO_{ads} is similar for Pt and Pd surfaces (420 µC cm_{Pd}^{-2}) [207,212,221,222]. A typical CO_{ads}-stripping on Pd/C is shown in **Figure II.7**. To the author's knowledge, no study has reported the agreement between the CO_{ads}-stripping method with other electrochemical method to estimate the ECSA of carbon-supported Pd electrocatalysts, so far.

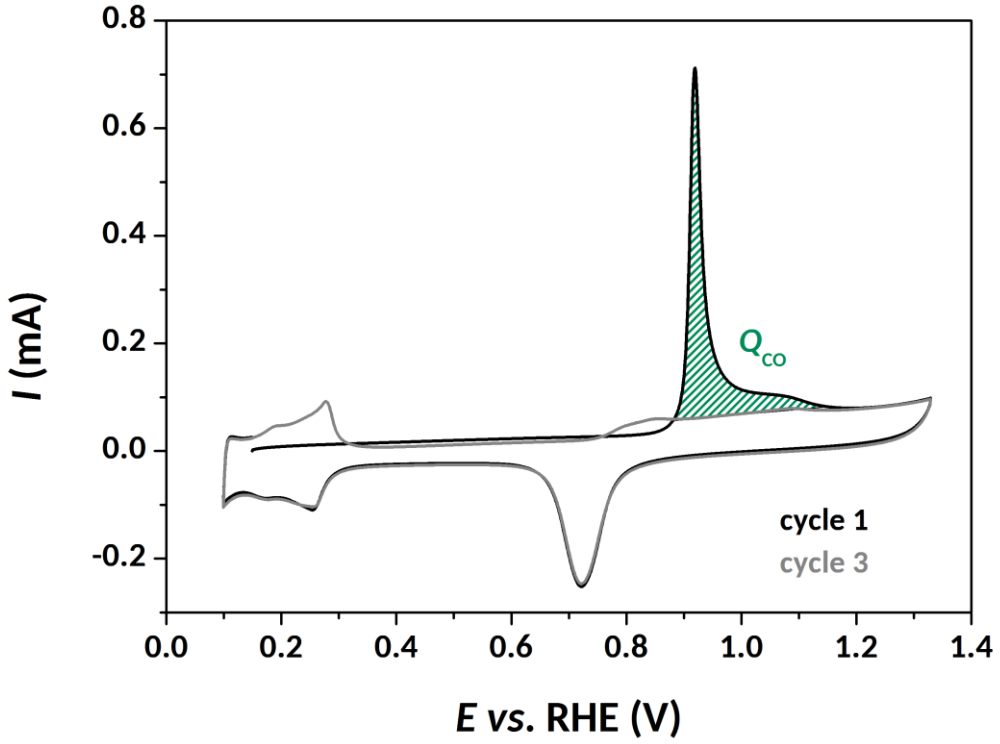

Figure II.7. CO_{ads}-stripping CV obtained on a Pd/C electrocatalyst in 0.1 M H_2SO_4, v = 20 mV s^{-1}, *T* = 25°C.

II.4.1.3 TEM micrographs

TEM micrographs enable to build the particle size distribution (PSD) of an electrocatalyst based on the analysis of a statistically-relevant number of NPs, provided their shapes and sizes are not too heterogeneous. Classically, counting at least 200 NPs (isolated and round shape) is sufficient. From the PSD, the number-averaged diameter ($\overline{d_n}$, nm) and the surface-averaged diameter ($\overline{d_s}$, nm) are determined according to **Equation II.6** and **Equation II.7** respectively, where n_i stands for the number of particles having the diameter d_i and N is the total number of the counted particles.

$$\overline{d_n} = \frac{\sum_{i=1}^{N} n_i \, d_i}{n_i} \qquad \textbf{Equation II.6}$$

$$\overline{d_s} = \frac{\sum_{i=1}^{N} n_i \, d_i^3}{n_i d_i^2} \qquad \textbf{Equation II.7}$$

The value $\overline{d_n}$ is the average mathematical diameter of the particles, whereas $\overline{d_s}$ is the diameter related to the average surface area of the particles; the latter enables to calculate the specific surface area (S_{TEM}, $m^2\ g^{-1}$) of the electrocatalyst according to **Equation II.8** with ρ the density of

the metal (11.99 g cm^{-3} for Pd). From this value, the ECSA (cm^2) can be calculated and compared with the values obtained from the electrochemical methods described above using **Equation II.*9*** with L_{metal} (μg_{metal} cm_{geom}^{-2}) the metal loading on the electrode and S_{geom} (cm^2) the geometrical surface area of the electrode.

$$S_{\mathrm{TEM}} = \frac{6000}{\rho \times \overline{d_s}} \qquad \textbf{Equation II.8}$$

$$\mathrm{ECSA}_{\mathrm{TEM}} = \frac{S_{\mathrm{TEM}} \times L_{\mathrm{metal}} \times S_{\mathrm{geom}}}{100} \qquad \textbf{Equation II.9}$$

This microscopy-based method matches well with electrochemical method in the condition that the NPs are well dispersed on the support and poorly agglomerated, as it is the case in the study of Durst *et al.* [221] who found a very good agreement between $ECSA_{TEM}$ and $ECSA_{CO}$ for Pd/C electrocatalysts. However, Mittermeier *et al.* [212] indicated that $ECSA_{TEM}$ was 25-30% lower in comparison to $ECSA_{CO}$ when the electrocatalysts were made of small NPS (*ca.* 3 nm); on the contrary, for electrocatalysts made of bigger NPs (*ca.* 7 nm), $ECSA_{TEM}$ was 6-fold higher than $ECSA_{CO}$.

II.4.2 Comparison of $ECSA_{PdO}$ and $ECSA_{CO}$

In the light of the earlier discussion, the comparison of ECSA determination methods seemed essential for the Pd/C and Pd/C-CeO_2 electrocatalysts. Thus, the methods based on the coulometry of PdO reduction and the coulometry of CO_{ads}-stripping were used and compared to calculate the ECSA of two Pd/C electrocatalysts among the five studied in this work, namely the 22 wt.% Pd/C and the 53 wt.% Pd/C, and the results are shown in **Figure II.8**. For the method based on the coulometry of PdO reduction, the high value of the vertex potential of the CV was 1.5 V *vs*. RHE and the ECSA was calculated using **Equation II.4**; for the method based on the coulometry of CO_{ads}-stripping, the CO was adsorbed at 0.15 V *vs*. RHE and the ECSA was calculated using **Equation II.5**.

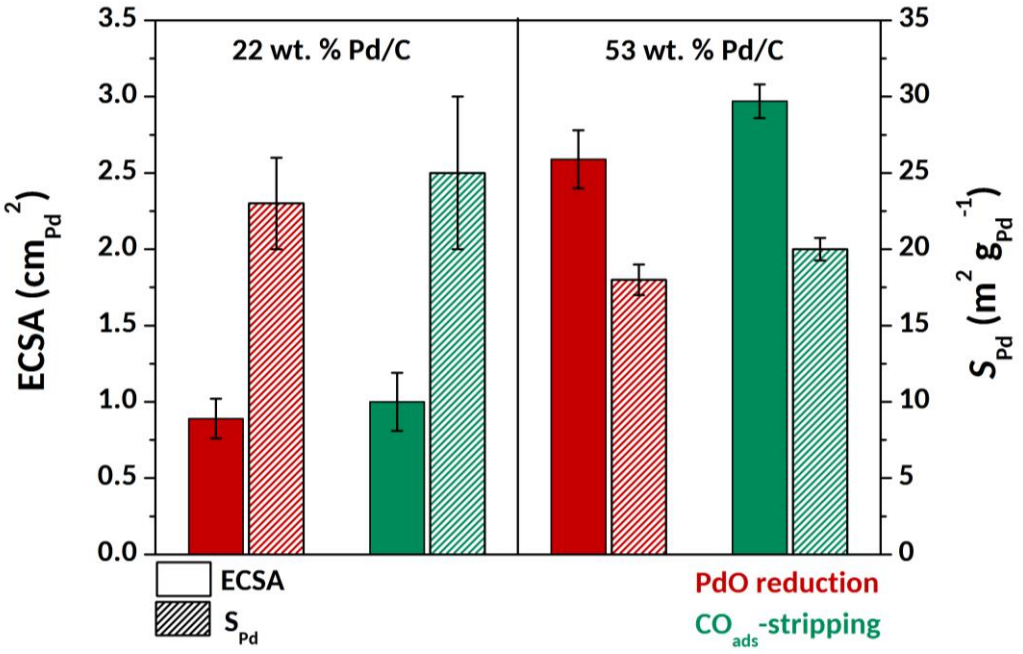

Figure II.8. Electrochemical surface area (ECSA) and specific surface area (S_{Pd}) of two Pd-based electrocatalysts studied in this work estimated using the coulometry of the reduction of PdO in alkaline media (1 M NaOH) or the coulometry of the CO_{ads}-stripping in acidic media (0.1 M H_2SO_4) at T = 25°C.

One can note that the two methods are in reasonable agreement for the two materials. In both cases, $ECSA_{CO}$ is higher than $ECSA_{PdO}$ (by 12% for 22 wt.% Pd/C and 14% for 53 wt.% Pd/C). In addition, the error bars, calculated using the standard deviation, are close for both methods: 14 and 7% (for 22 wt.% Pd/C and 53 wt.% Pd/C respectively) when using the PdO reduction coulometry; 19 and 3% (for 22 wt.% Pd/C and 53 wt.% Pd/C respectively) when using the coulometry of CO_{ads}-stripping. These results indicate that both methods seem suitable for an accurate estimation of the ECSA of the Pd/C electrocatalysts studied in this work.

For comparison purposes, the ECSA was also calculated using the microscopic-based method. However, the low definition of the particles and the presence of many agglomerates did not enable to count enough isolated particles to establish a sufficiently-representative statistic (only 133 particles were counted for 22 wt.% Pd/C and 52 for 53 wt.% Pd/C). The $ECSA_{TEM}$ is 146 m^2 g_{Pd}^{-1} for 22 wt.% Pd/C and 188 m^2 g_{Pd}^{-1} for 53 wt.% Pd/C which is 6 to 10-fold higher than $ECSA_{PdO}$: these values are obviously overestimated and absolutely not accurate, and demonstrate that the small, isolated and round-shaped NPs of Pd are not-at-all representative of the Pd/C samples (which was obvious on the TEM micrographs of **Figure II.2**). The use of this method seems to be reserved for electrocatalysts with very well dispersed and rather small particles (3-4 nm), *i.e.* not for the present electrocatalysts.

Finally, the method using the coulometry of PdO reduction was used to calculate the ECSA and the specific surface area of all the Pd-based electrocatalysts and the results are summed up in **Table II.3**: they indicate that all the electrocatalysts display similar specific surface area, from 18 to 25 $m^2\ g_{Pd}^{-1}$. Note that for the Pd/C-CeO_2 electrocatalyst, the calculation of ECSA was double-checked with CO_{ads}-stripping, because we did not know how the presence of CeO_2 could disrupt the measurement. Both methods lead to relatively similar results: 18 $m^2\ g_{Pd}^{-1}$ for the former and 22 $m^2\ g_{Pd}^{-1}$ for the latter. In the case of the commercial Pt/C studied for comparison purposes, only the method using CO_{ads}-stripping was used.

Table II.3. Specific surface area of the catalysts studied in this work calculated using the coulometry of PdO reduction for Pd-based electrocatalysts and CO_{ads}-stripping for Pt/C.

Electrocatalyst	S ($m^2\ g_{metal}^{-1}$)
22 wt.% Pd/C	23 ± 3
33 wt.% Pd/C	18 ± 2
44 wt.% Pd/C	25 ± 2
53 wt.% Pd/C	18 ± 1
20 wt.% Pd/C-CeO_2	18 ± 5
40 wt.% Pt/C	55 ± 4

II.5 Study of the BOR activity on the Pd-based electrocatalysts

II.5.1 Electrochemical behavior

II.5.1.1 Surface characterization in supporting electrolyte

Before measuring the BOR activity, the catalytic surfaces of each electrocatalyst was firstly characterized in the supporting electrolyte (1 M NaOH). The corresponding CVs are displayed in **Figure II.9**. The current densities are relative to the ECSA of each electrocatalyst.

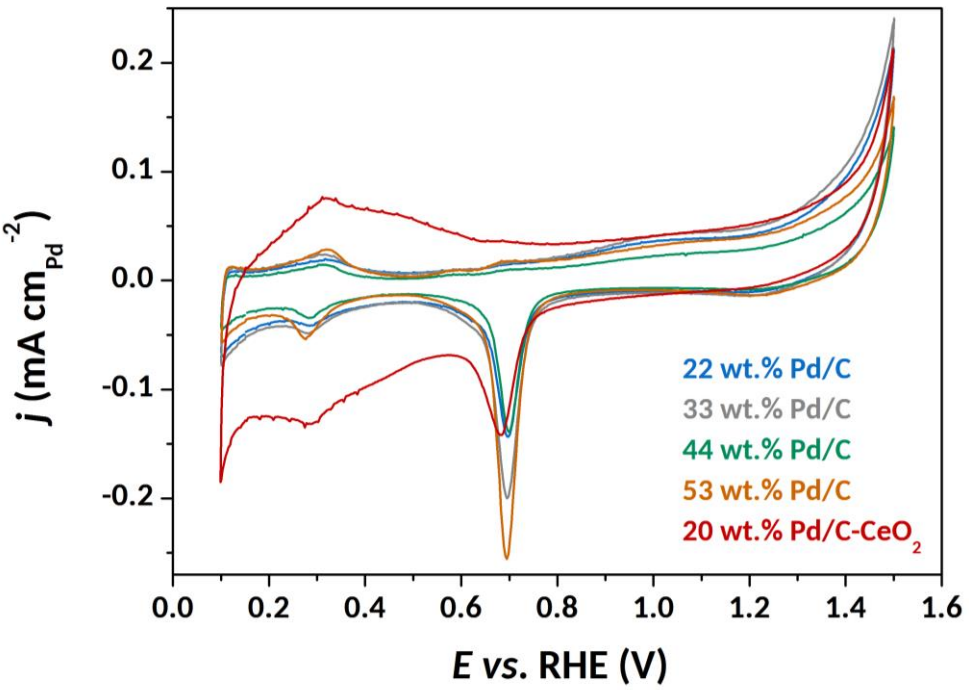

Figure II.9. CV obtained on the Pd-based electrocatalysts studied in this work in supporting electrolyte. Conditions: Ar-saturated 1 M NaOH, *T* = 60°C, v = 20 mV s^{-1}, ω = 400 rpm.

In the potential range 0.1 < *E* < 0.4 V *vs*. RHE, one can observe the peaks related to hydrogen adsorption on the backward scan (potential sweep towards negative values) and hydrogen desorption on the forward scan (potential sweep towards positive values) located at 0.28 and 0.32 V *vs*. RHE, respectively. The presence of CeO_2 does not affect the position of those peaks, but the current densities obtained with the Pd/C-CeO_2 electrocatalyst are higher than those obtained for the Pd/C electrocatalysts, as already observed by Miller *et al*. [184] and Bambagioni *et al*. [223]. This current increase could be due to dual hydrogen adsorption on Pd NPs and on CeO_2. Indeed, according to the work of Bernal *et al*. [224], hydrogen can adsorb on ceria surface via an exclusive surface process, but cannot lead to the formation of ceria bronzes, which are non-stoichiometric compounds (H_xCeO_2), as proposed earlier in the literature [225]. This situation differs, as an example, to that of Pt NPs supported on tungsten oxide (the presence of Pt catalyzes the formation of hydrogen tungsten bronzes (H_yWO_x) [226,227]).

At higher potentials, one can observe the features related to the formation (above *E* = 0.7 V *vs*. RHE on the forward scan) and the reduction (below *E* = 0.8 V *vs*. RHE on the backward scan) of Pd oxides. The position of the current peak associated to the reduction of PdO is rather similar for the four Pd/C electrocatalysts (around 0.7 V *vs*. RHE), but the very small shift of this peak could enable to rank the Pd/C electrocatalysts in the order from smaller to bigger NPs as 53 < 33 < 22 < 44 wt.% Pd/C (this dependence of PdO reduction peak on the

average Pd NP size was discussed in section **II.4.1.1**). However, this trend is not in agreement with the TEM and XRD observations. Being admitted that (i) the Pd NPs are obviously composed of bimodal population and non-negligibly agglomerated in these samples, and (ii) the differences of PdO reduction peak are very subtle, we think wise not to discuss any further these values at that stage. For the Pd/C-CeO_2 catalyst, this peak is located at 0.68 V *vs*. RHE. This shift towards negative potential can indicate that: (i) Pd NPs are smaller than the Pd NPs present in the Pd/C electrocatalysts, which is in agreement with the TEM micrographs observations (see section **II.3.1** and **Figure II.2**) and/or (ii) that the formation of Pd oxides is less reversible due to a slower oxide formation/reduction in presence of ceria. This observation can be linked to previous works: in the case of Pt NPs supported on titanium or tungsten oxide (TiOx, WOx) [228,229], a decrease of the signal linked to the formation and reduction of Pt oxides as well as a shift of the peak of the PtO reduction towards negative potentials were observed; Hayden *et al*. associated these phenomena to slower kinetics of the formation of oxides/hydroxides on the Pt NPs deposited on such supports [230]. However, in our case, the current densities linked to the formation of Pd oxides on the Pd/C-CeO_2 electrocatalyst are rather similar to the current densities obtained on the Pd/C electrocatalysts. Thus, the presence of small Pd NPs seems to be responsible for the shift of the PdO reduction peak towards negative potentials.

II.5.1.2 BOR evaluation

The kinetics and the activity of each electrocatalyst towards the BOR was investigated for three $NaBH_4$ concentrations at high temperature (T = 60°C). A CV obtained on each material for an electrode rotation rate of 1600 rpm is displayed in **Figure II.10.A.B.C** for 5, 50 and 500 mM $NaBH_4$ (in 1 M NaOH) respectively. As specified in the experimental section, the catalytic layer thickness (*i.e*. the amount of carbon deposited on the electrode) is kept identical for all the electrocatalysts (this thickness having a strong influence on the results obtained, as demonstrated for Pt/C-based electrodes [123]). Thus, an electrocatalyst with high metal weight fraction automatically leads to a high metal loading on the electrode. The current densities presented in **Figure II.10** were obtained by dividing the current by the corresponding ECSA (cm^2) of each electrocatalyst. CVs were also plotted by dividing the current by the electrode's geometric area (only for 5 and 50 mM $NaBH_4$): these CVs are presented in **Figure A.4** in **Annex 4**. To analyze the mass-transport limitations, CVs obtained on one of the Pd/C electrocatalyst (the 22 wt.% Pd/C) for four electrode rotation rates and the three $NaBH_4$ concentrations are displayed in **Figure II.11** (the trend observed is similar for all the electrocatalysts). In addition, the recent publication of Braesch *et al*. [105], who investigated the BOR for the same $NaBH_4$

concentrations but on bulk polycrystalline Pd electrode for T = 20°C, will be a very good basis to compare and discuss the results presented below. More precisely, these authors used RDE to characterize the BH_4^- electrooxidation and differential electrochemical mass spectroscopy (DEMS) to study H_2 generation and escape in order to get insights into the BOR mechanism on Pd surfaces.

- **BOR analysis for 5 mM $NaBH_4$**

For the lowest $NaBH_4$ concentration, the onset potential (E_{onset}), defined for j = 0 A, is in the potential range from -90 to -155 mV *vs*. RHE for the Pd-based electrocatalysts and is -25 mV *vs*. RHE for the Pt/C electrocatalyst. This potential corresponds to the start of the BOR and will be further discussed in the next section. In addition, two main humps are noticeable on the CVs obtained on the four Pd/C electrocatalysts: the first one is located in the potential range from 0.1 to 0.4 V *vs*. RHE; the second one is located in the potential range from 0.5 to 0.8 V *vs*. RHE. In both cases, the potential of the hump is shifted positive in the order 53 < 44 < 33 < 22 wt.% Pd/C. It is interesting to compare this observation with the work of Olu *et al*. [69], who studied the BOR on well-defined Pt NPs supported on smooth glassy carbon, for 1 mM $NaBH_4$ and T = 20°C. They observed faster kinetics and larger faradaic efficiency for larger particles diameter (4 *vs*. 2 nm) and shorter inter-particle distance (7 *vs*. 11 nm), indicating a clear influence of the electrocatalyst morphology on the BOR activity, as it is the case for many other electrochemical reactions [159,213,230–232]. In our case, the TEM micrographs (**Figure II.3**) revealed that the Pd/C electrocatalysts are composed of poorly defined NPs, with a mix of small, big, and agglomerated NPs. Thus, it seems that a high metal weight fraction, and consequently, a high Pd sites density (to some extent, because higher metal weight fraction also leads to more agglomerates), could account for the apparent better BOR kinetics on the Pd/C electrocatalysts with high metal weight fraction. Above 0.8 V *vs*. RHE, the current density starts to decrease rapidly (on the 22 and 33 wt.% Pd/C) or slowly (on the 44 and 53 wt.% Pd/C) owing to the formation of Pd surface oxides that lead to the passivation of the electrode. In addition, the current density recorded in the potential range from E = 0.4 to 0.8 V *vs*. RHE for ω = 1600 rpm are twice higher than those recorded at ω = 400 rpm (see **Figure II.11**), indicating that the kinetics is controlled by the BH_4^- diffusion/convection in this potential range. These observations are in line with the study of Braesch *et al*. [105]: for 5 mM $NaBH_4$, the authors identified a first hump located at E = 0.3 V *vs*. RHE and a sharp peak located at E = 0.8 V *vs*. RHE followed by a slow passivation of the electrode by Pd oxides.

Interestingly, the CV obtained on the Pd/C-CeO_2 electrocatalyst is slightly different from the Pd/C electrocatalysts. The two humps mentioned above are not noticeable, but instead, the current increases continuously from E = 0 to 0.8 V *vs*. RHE and remains rather constant above 0.8 V *vs*. RHE instead of dropping. The presence of ceria seems to have antagonistic influences; on the one hand it prevents the complete deactivation of the electrode (at high potential values, a positive effect in theory, but practically not interesting because it occurs at too high potential to be relevant for a DBFC anode), but on the other hand seems to delay the BOR towards larger potential values (a negative effect). The presence of ceria may affects the oxidation state of the Pd NPs, as already put forth by Miller *et al*. [184], who reported that Pd NPs in Pd/C-CeO_2 electrocatalyst were mostly oxidized, while Pd NPs were mostly in their metallic state in a Pd/C electrocatalyst. Thus, the formation of Pd oxides at high potential may process differently for the Pd/C-CeO_2 electrocatalyst than for Pd/C, thereby explaining the incomplete deactivation of the electrode. Another reason could be that the formation and disinsertion of Pd hydrides (PdH) could be blocked or limited by the presence of ceria. Indeed, Braesch *et al*. [105] reported that PdH formation should be taken into account in the BOR mechanism on Pd surfaces. The authors suggested that at low potential, the full dissociation of BH_4^- into BH_{ads} + H_{ads} is followed by the absorption of H_{ads} into the Pd lattice. However, the disinsertion of hydrogen can only proceeds at relatively high potential in presence of $NaBH_4$ (*ca*. 0.8 V *vs*. RHE) since other intermediates species of the BOR may adsorb on the Pd surface and block the disinsertion of PdH.

For comparison purposes, since Pt/C can be considered as a reference electrocatalyst for the BOR [60], the CV obtained on this material is also displayed in **Figure II.10**. The BOR kinetics on Pt/C is significantly faster than for the Pd-based electrocatalysts in the potential range from 0 to 0.1 V *vs*. RHE, because Pt/C is an efficient electrocatalyst for the HOR. However, from E = 0.1 V *vs*. RHE, the current density increases less rapidly and it remains constant from E = 0.2 to 0.6 V *vs*. RHE, owing to the poisoning of Pt sites by BH_{ads}, according to the BOR mechanism described in the previous chapter.

For such $NaBH_4$ concentration, thanks to DEMS measurements, Braesch *et al*. [105] identified that gaseous hydrogen was generated in the potential range from E ≈ 0 to 0.3 V *vs*. RHE, but H_2 was electrooxidized only from E = 0.3 to 0.8 V *vs*. RHE. However, when the potential exceeded 0.8 V *vs*. RHE, H_2 was not electrooxidized anymore, since Pd oxides prevent the electrooxidation of BH_4^- and H_2 species. In our case, it is likely that more H_2 escapes from the electrode, because the BOR is studied at higher temperature (60°C), favoring the heterogeneous hydrolysis of BH_4^-.

- **BOR analysis for 50 mM $NaBH_4$**

For higher $NaBH_4$ concentration, the onset potential is negatively-shifted, in the potential range from -140 to -200 mV *vs*. RHE for the Pd-based electrocatalysts; it is -50 mV *vs*. RHE for Pt/C. The CVs shape obtained on the different electrocatalysts are rather similar to the ones obtained for 5 mM $NaBH_4$. However, one can notice that the CVs are shifted towards positive potentials, indicating more severe limitation from the charge transfer kinetics (there are more BH_4^- species to be electrooxidized); the mass-transport limitation is generally similarly-observed between 5 and 50 mM $NaBH_4$, although of course with *ca*. 10-fold larger limiting currents at 50 *vs*. 5 mM $NaBH_4$ (see **Figure II.11**). The two humps identified earlier on the Pd/C electrocatalysts are now located in the potential range from 0.4 to 0.6 V *vs*. RHE (instead of 0.1 to 0.4 V *vs*. RHE) and from 0.9 to 1 V *vs*. RHE (instead of 0.5 to 0.8 V *vs*. RHE); this is also in line with the results obtained by Braesch *et al*. [105], who identified those humps at E = 0.5 and 1 V *vs*. RHE, respectively. Above E = 1 V *vs*. RHE, the current densities decrease rapidly. The Pd sites density seems to affect the BOR kinetics in a similar manner than for 5 mM $NaBH_4$.

The modifications of the CVs observed for the Pd/C electrocatalysts are also observed for the Pd/C-CeO_2 electrocatalyst: the general shape is rather unchanged compared to 5 mM $NaBH_4$, but the charge-transfer kinetics is more limiting and the current density plateau starts later, for $E \approx 1$ V *vs*. RHE (instead of 0.8 V *vs*. RHE).

In the case of Pt/C, the same modifications are noticed: the BOR kinetics slows down and the electrode surface starts to be poisoned from E = 0.3 V *vs*. RHE (instead of 0.2 V *vs*. RHE).

DEMS measurements performed by Braesch *et al*. with 50 mM $NaBH_4$ [105] revealed that the faradaic current and the equivalent H_2 escape current were 10-fold higher in comparison to 5 mM $NaBH_4$, suggesting that the two currents were linked to the same process. However, the evolution of the faradaic current was slightly different from the CVs obtained on bulk polycrystalline Pd, electrode since the electrode used for DEMS measurements had a porous structure (sputtering deposition from massive Pd); anyways, the results indicated that H_2 escapes from E = 0 to 0.9 V *vs*. RHE and not above E = 0.9 V *vs*. RHE, where it is either not generated or quantitatively oxidized.

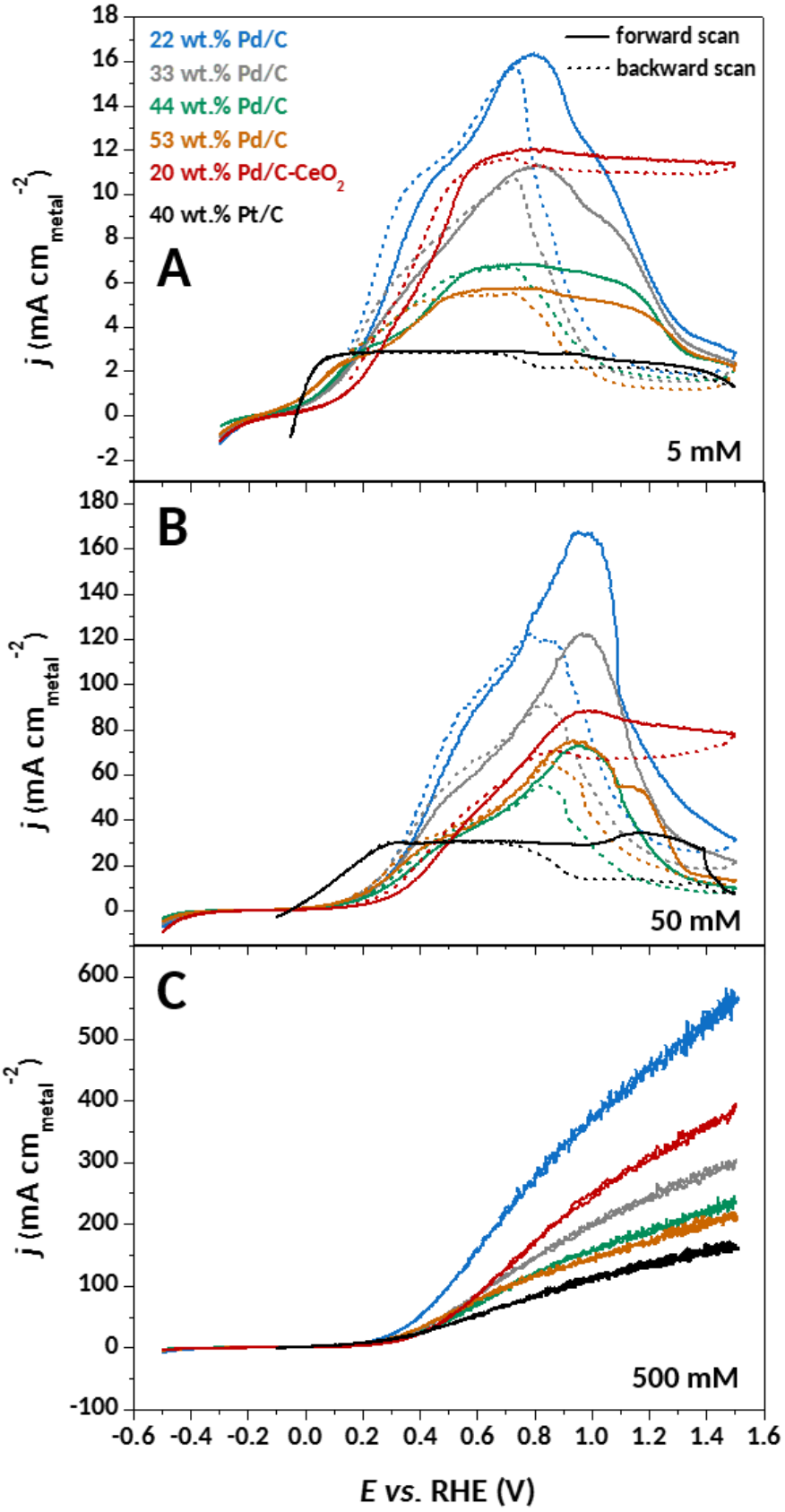

Figure II.10. BOR voltammograms obtained on the electrocatalysts studied in this work for (A) 5 mM $NaBH_4$, (B) 50 mM $NaBH_4$ and (C) 500 mM $NaBH_4$ in 1 M NaOH.
Other conditions: Ar-saturated electrolytes, T = 60°C, v = 20 mV s^{-1}, ω = 1600 rpm.

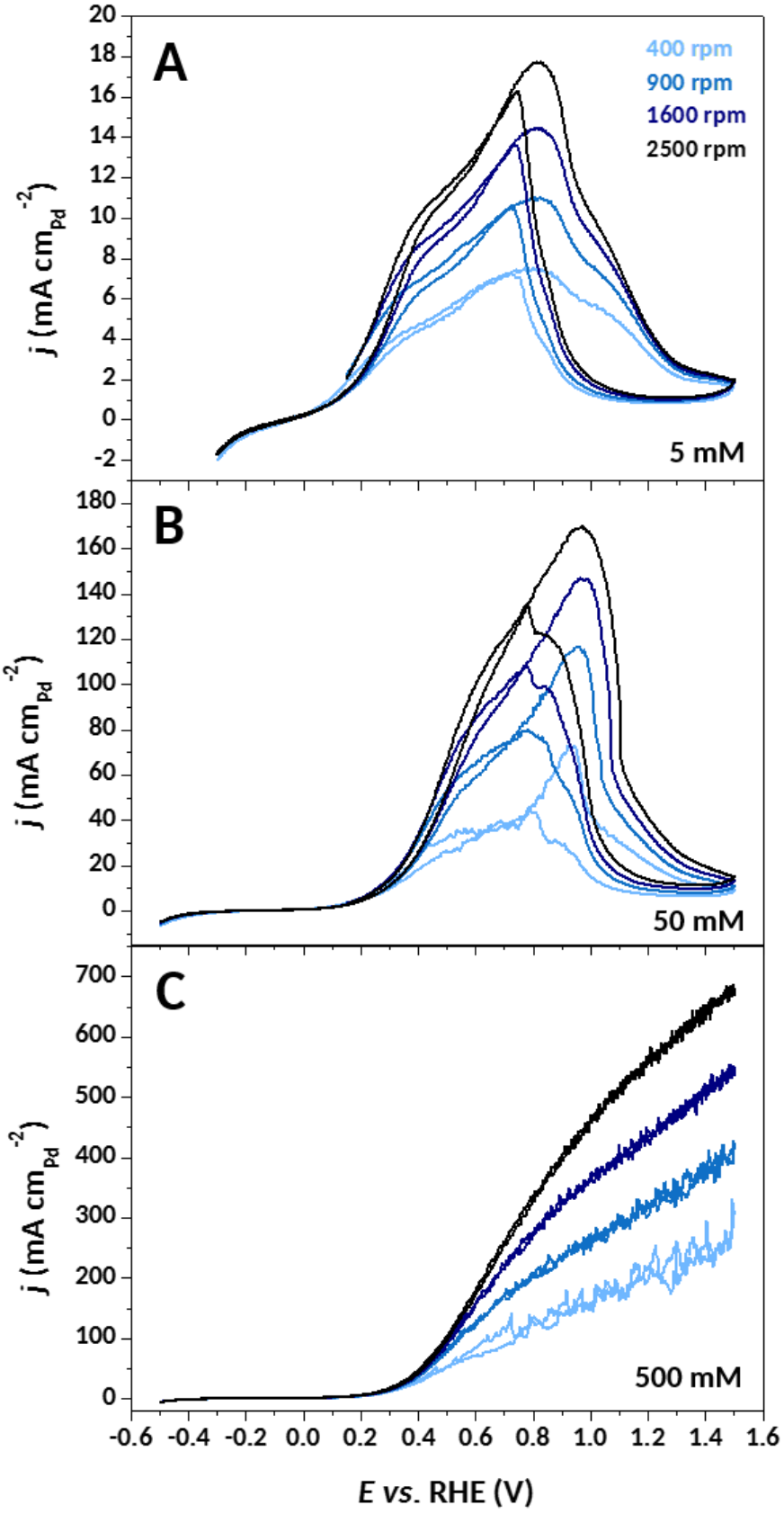

Figure II.11. BOR voltammograms obtained on the 22 wt.% Pd/C electrocatalyst for different electrode rotation rates and for (A) 5 mM $NaBH_4$, (B) 50 mM $NaBH_4$ and (C) 500 mM $NaBH_4$ in 1 M NaOH. Other conditions: Ar-saturated electrolytes, T = 60°C, v = 20 mV s^{-1}.

- **BOR analysis for 500 mM $NaBH_4$**

For the highest $NaBH_4$ concentration, the onset potential further shifts negative, in the potential range from -170 to -230 mV *vs.* RHE for the Pd-based electrocatalysts and to -70 mV *vs*. RHE for Pt/C. The CVs shape are very different from the lower $NaBH_4$ concentrations but remain identical for all the electrocatalysts: the current density increases continuously and significantly from E = 0.35 V *vs*. RHE and the electrochemical signals are very noisy. In addition, all the CVs are shifted towards positive potentials in comparison to 5 and 50 mM $NaBH_4$: it is clear that the charge transfer kinetic is limiting for the BOR in that case. Besides, it is not clear how the BOR is influenced by the quantity of electrocatalyst. Indeed, for the Pd/C electrocatalysts, the BOR kinetics is better in the following order: 22 > 53 > 33 > 44 wt.% Pd/C. The comparison of the CVs obtained on Pd-based electrocatalysts and on the Pt/C electrocatalyst points out the better BOR kinetic on Pd surfaces for high $NaBH_4$ concentration.

For such concentration, DEMS measurements [105] showed that H_2 escaped from the electrode but was not electrooxidized on the whole potential range (from E = -0.2 to 1.5 V *vs*. RHE).

In the light of these observations, it seems that for high $NaBH_4$ concentration, the HOR prevails on the BOR because the heterogeneous hydrolysis is enhanced. The high amount of H_2 bubbles is most certainly at the origin of the very noisy electrochemical signal: the bubbles form at the electrode surface thereby modifying the amount of Pd sites available for the BOR. Increasing the electrode rotation rate from 400 to 2500 rpm (see **Figure II.11**) enables to decrease the noise of the signal, likely owing to the better evacuation of the H_2 bubbles from the electrode surface. In addition, the very slow BOR apparent kinetics observed for this concentration might be ascribed to non-negligible poisoning of the Pd surfaces in these conditions. However, it is also likely that the BOR kinetics might have been limited by the low concentration and diffusion of OH^-, since the $[OH^-]/[BH_4^-]$ ratio is only two in the present conditions. Indeed, Yang *et al*. [233] investigated the BOR on Au/C and Ag/C electrocatalysts for various $[OH^-]/[BH_4^-]$ ratio, and their results revealed that when this ratio is below five, H_2 escapes from the electrode, the faradaic efficiency decreases and the BOR kinetics is slow.

To sum up, the comparison of the CVs obtained on all the electrocatalysts for the three $NaBH_4$ concentrations enabled to highlight several observations:

- Increasing the $NaBH_4$ concentration up to 50 and 500 mM leads to higher surface poisoning and points towards limiting charge transfer kinetics, which is not desirable to reach high BOR activity; however, the current densities obtained at 50 mM are 10-fold higher in comparison to 5 mM, showing that for these concentrations, the BOR is mass-transport limited (at sufficient high potential);
- For the highest $NaBH_4$ concentration, the low OH^- concentration used here might account for the very slow BOR kinetics;
- A high amount of Pd (so a high Pd sites density) enables to enhance the BOR kinetics when the $NaBH_4$ concentration is 5 and 50 mM, but the influence of the Pd sites density does not show particular trend for 500 mM $NaBH_4$;
- Contrary to our expectations, the presence of ceria does not seem to help the BOR processes and the BOR current densities are even lower on the Pd/C-CeO_2 electrocatalyst than on the Pd/C for 5 and 50 mM $NaBH_4$;
- At low potential values and low $NaBH_4$ concentrations (5 and 50 mM), the Pd-based electrocatalysts exhibit slower BOR kinetics than Pt/C, in agreement with the literature [70]; however, for the highest $NaBH_4$ concentration, the BOR kinetics is faster on Pd-based electrocatalysts in comparison to Pt/C.

In addition to the CVs shape analysis, one of the main goals in electrocatalysis is to evaluate and compare the catalytic activity obtained on various electrode material. The specific approach used for the case of the BOR needs to be further discussed, which will be attempted hereafter.

II.5.2 Activity markers

The previous CVs of BOR activity on the Pd-based electrocatalysts have been analyzed in a very basic manner: the BOR activity was only evaluated based on the value of the onset potential and the limiting currents, a simplistic strategy which is often (and most widely) adopted in the literature [46,66,67,70,123,234]. This makes the analysis of the BOR kinetics vague and poorly quantitative; the attempts of Santos *et al*. to analyze the BOR kinetics based on non-stationary voltamperometry (see *e.g*. [235,236]) are interesting, but cannot be considered reliable for such a reaction, owing to its inherent complexity and to the possibility of surface hindering/poisoning by H_2 bubbles and adsorbed boron “poisons”. In order to go beyond these limitations, activity

markers shall be defined, as it is for example the case of the mass and specific activities that are measured/calculated for the oxygen reduction reaction in proton exchange membrane fuel cell electrocatalysis [213].

There are many possible such markers which could be defined; the onset potential and the current densities (extracted from the CV on the forward scan) obtained at low potentials, more precisely at *E* = 0 and 0.2 V *vs*. RHE, are relevant activity markers since the BOR can, in theory, proceed at low potential. We decided also to consider the current density at *E* = 0.5 V *vs*. RHE, because this potential corresponds to the value of the anode potential when the maximum power density is reached in a real DBFC [70]. However, to measure the catalytic activity of a given reaction, one needs to access the kinetic current only, since the total faradaic current ($j_{tot,F}$) is function of the kinetic current (j_K); j_k depends on the electrode potential, and the current limited by the diffusion/convection (j_{lim}), which does not depend on the electrode potential, but rather on the electrode rotation rate, as illustrated by the Koutecky-Levich equation (**Equation II.10**) [237]. This expression can be modified when the reaction proceeds in a thick film of catalyst [238], but in the present case, the Pd/C loadings where kept sufficiently small to avoid mass-transport limitation in the thin-film.

Koutecky-Levich equation:

$$\frac{1}{j_{\mathrm{tot,F}}} = \frac{1}{j_{\mathrm{K}}} + \frac{1}{j_{\mathrm{lim}}} \qquad \textbf{Equation II.10}$$

To estimate the limiting current, the use of the rotating disk electrode enables to set a forced convection regime and to obtain a stationary diffusion regime. Under the influence of the centrifugal force, an electrolyte flow perpendicular to the electrode plane is formed and is then evacuated from the center to the edge of the electrode. Solving the hydrodynamic equations enables to access the current limited by the diffusion/convection process. Thus, one can use the Levich equation to calculated the expected value of the limiting current density (j_{lim}, **Equation II**.11), with n the number of electrons involved in the reaction, F the Faraday's constant (A mol^{-1}), D the diffusion coefficient of the reactant (cm^2 s^{-1}), ν the cinematic viscosity of the electrolyte (cm^2 s^{-1}), c_0 the reactant concentration (mol cm^{-3}) and ω the electrode rotation rate (rad s^{-1}).

Levich equation:

$$j_{\mathrm{lim}} = 0.62\, n\, F\, D^{\frac{2}{3}}\, \nu^{\frac{-1}{6}}\, c_0\, \omega^{\frac{1}{2}} \qquad \textbf{Equation II.11}$$

$\frac{1}{j_K}$ can be determined using the limit value of $\frac{1}{j_{tot,F}}$ when ω tends towards infinite [237]. In practice, several voltammograms are recorded for various electrode rotation rate; then, the graph $1/j_{tot,F}$ (for a given potential) is plotted versus $1/\omega^{1/2}$. The value j_K can be obtained with the zero-abscissa point.

However, the kinetic current can also be determined, in a more direct way, using the Koutecky-Levich equation written as:

$$j_K = \frac{j_{lim} \times j_{tot,F}}{j_{lim} - j_{tot,F}} \qquad \textbf{Equation II.12}$$

with j_{lim} the current limited by the diffusion/convection for a potential situated a few tens of millivolts above the equilibrium potential on the CVs.

In addition, the Tafel relation can also be used (once the total faradaic current is corrected from the mass-transport) to access the exchange current density j_0 and the Tafel slope that gives insights into the charge transfer kinetic process:

Tafel equation: $$\log\left(\frac{j_k}{j_0}\right) = \frac{\alpha F}{RT} \times \eta \qquad \textbf{Equation II.13}$$

with α the transfer coefficient, R the universal gas constant, T the temperature, and η the overpotential.

This methodology is very classical in electrocatalysis. However, in the case of the BOR, the determination of the kinetic currents is not straightforward, and potentially not relevant, for several reasons:

1) The electrocatalyst surface is subject to poisoning by BOR intermediates, thereby leading to unknown extent of available active sites in operation;
2) The evolution of gaseous hydrogen generates bubbles, which can partially block a part of the electrocatalyst ECSA, thereby impacting (decreasing) the kinetic current and creating a noisy electrochemical signal; this is especially the case for high $NaBH_4$ concentrations (> 100 mM);
3) The BOR mechanism is not well known, so the limiting current that should be reached is not known (the number of electrons exchanged depends on the electrode potential and BOR completion);
4) The BOR completion may depend on the residence time of the reactants, intermediates and products, so it is very important to fix the active layer thickness (hence the operating

conditions of the present study) and to have a rather small thickness to avoid side reactions and gradients of concentration for the active species in the active layer;

5) The definition of the electrocatalyst surface highly depends on the "history" of the electrode (owing to poisoning and bubbles, but also to the possible accumulation of boron oxide products, not speaking from durability issues on the long-term, which will be addressed in the next chapters of the present thesis).

In addition, all of the process mentioned above highly depend on the nature and structure of the electrocatalyst. One understands that the use of the conventional methods to calculate the kinetic current, which are efficient in the case of the oxygen reduction reaction for example, is very tricky and leads to uncertain values in the case of the BOR. Moreover, the concentration of $NaBH_4$ used in this work (5, 50 and 500 mM) are high, and the diffusion coefficients of BH_4^- in the conditions of the study (high temperature) are, based on the work of Chatenet *et al*. [90], around 3.7 10^{-5} cm^2 s^{-1} which is, for comparison, twice higher than the diffusion coefficient of dissolved oxygen. Then, we postulate that the mass-transport should not be very limiting in the conditions of the study and this is why we chose to neglect any mass-transport correction.

However, we decided to test our hypothesis and to plot the BOR CVs corrected from the mass-transport using **Equation II.12** for 5 and 50 mM $NaBH_4$ concentrations only (at 500 mM, we consider that the mass-transport is not limiting since the BOR CVs are almost overlapping for all the electrode rotation rates at low potential values). We chose to take as j_{lim} value the current value of the peak located at E = 0.8 and 1 V *vs*. RHE on the forward scan for 5 and 50 mM $NaBH_4$ concentrations respectively. For comparison purposes, the (potential) theoretical value of j_{lim} was also calculated using **Equation II.11** with n = 8 electrons, D = 3.71 10^{-5} and 3.63 10^{-5} cm^2 s^{-1} for 5 and 50 mM $NaBH_4$ respectively, ν = 9 10^{-3} and 8.4 10^{-3} cm^2 s^{-1} for 5 and 50 mM $NaBH_4$ respectively, and ω = 1600 rpm; the values of D and ν come from the study of Chatenet *et al*. [90] for experimental conditions that most closely correspond to those of this work. **Table II.4** gathers the j_{lim} values obtained for all the electrocatalysts.

Table II.4. Comparison of the j_{lim} values obtained from the Levich equation or directly extracted from BOR CVs.

Electrocatalyst	5 mM $NaBH_4$		50 mM $NaBH_4$	
	$j_{L,\ theoretical}$ (mA cm_{geom}^{-2})	$j_{L,measured}$ (mA cm_{geom}^{-2})	$j_{L,\ theoretical}$ (mA cm_{geom}^{-2})	$j_{L,measured}$ (mA cm_{geom}^{-2})
22 wt.% Pd/C	76	72 ± 3	753	709 ± 42
33 wt.% Pd/C		68 ± 9		733 ± 59
44 wt.% Pd/C		74 ± 6		832 ± 5
53 wt.% Pd/C		76 ± 1		917 ± 62
20 wt.% Pd/C-CeO_2		68 ± 3		495 ± 7
40 wt.% Pt/C		71 ± 1		723 ± 21

One can notice that for 5 mM $NaBH_4$, the j_{lim} values are rather consistent with the theoretical value for nearly all electrocatalysts (22, 44 and 53 wt.% Pd/C and Pt/C), indicating that 8 electrons are reached for E = 0.8 V *vs*. RHE and that the hypotheses for the calculation are verified. For the other two electrocatalysts (33 wt.% Pd/C and Pd/C-CeO_2), the measured j_{lim} value is slightly lower than the theoretical value, indicating that *ca*. 7 electrons are exchanged in the process.

For 50 mM $NaBH_4$, the j_{lim} values are rather in agreement with the theoretical value only for the 22 and 33 wt.% Pd/C and the Pt/C electrocatalysts. For the others electrocatalysts, the j_{lim} value is either higher than the theoretical value, indicating that an additional reaction contributes to the total faradaic current, or lower than the theoretical value, indicating that the 8 electrons are not reached. However, the theoretical value of the limiting current must be compared with caution with the measured values, since our conditions slightly differ from the conditions used by Chatenet *et al*. [90] to measure the values of D and ν (T = 40°C *vs*. 60°C, [$NaBH_4$] = 1 and 10 mM *vs*. 5 and 50 mM).

Figure II.12 shows the BOR CVs obtained on the 22 wt.% Pd/C electrocatalyst corrected from the mass-transport in the potential range from E = -0.3 (or -0.5) to 0.5 V *vs*. RHE for 5 mM (**Figure II.12.A**) and 50 mM (**Figure II.12.B**) $NaBH_4$. The comparison of the current densities obtained at E =0, 0.2 and 0.5 V *vs*. RHE with and without mass-transport correction reveals that the mass-transport correction is: (i) not necessary at E = 0 V *vs*. RHE, both for 5 and 50 mM $NaBH_4$, (ii) rather unnecessary and not necessary at E = 0.2 V *vs*. RHE for 5 and 50 mM $NaBH_4$ respectively, (iii) necessary at E = 0.5 V *vs*. RHE both for 5 and 50 mM $NaBH_4$. Consequently, it is

decided that the total faradaic current will not be corrected from the mass-transport for the current densities obtained at *E* = 0 and 0.2 V *vs*. RHE. For *E* = 0.5 V *vs*. RHE, **Figure II.12** highlights that the mass-transport correction should be taken into account. However, we considered that it was irrelevant to correct the total faradaic current from a "limiting" (rather a peak) current, the origin of which is uncertain. Thus, we preferred to deliberately not apply any correction of the mass-transport; we are nevertheless conscious that the "catalytic activity" determined as such will be underestimated for *E* = 0.5 V *vs*. RHE. However, as the extent of underestimation will be near-similar for all the electrocatalysts tested, the methodology shall enable easy comparison between the tested materials.

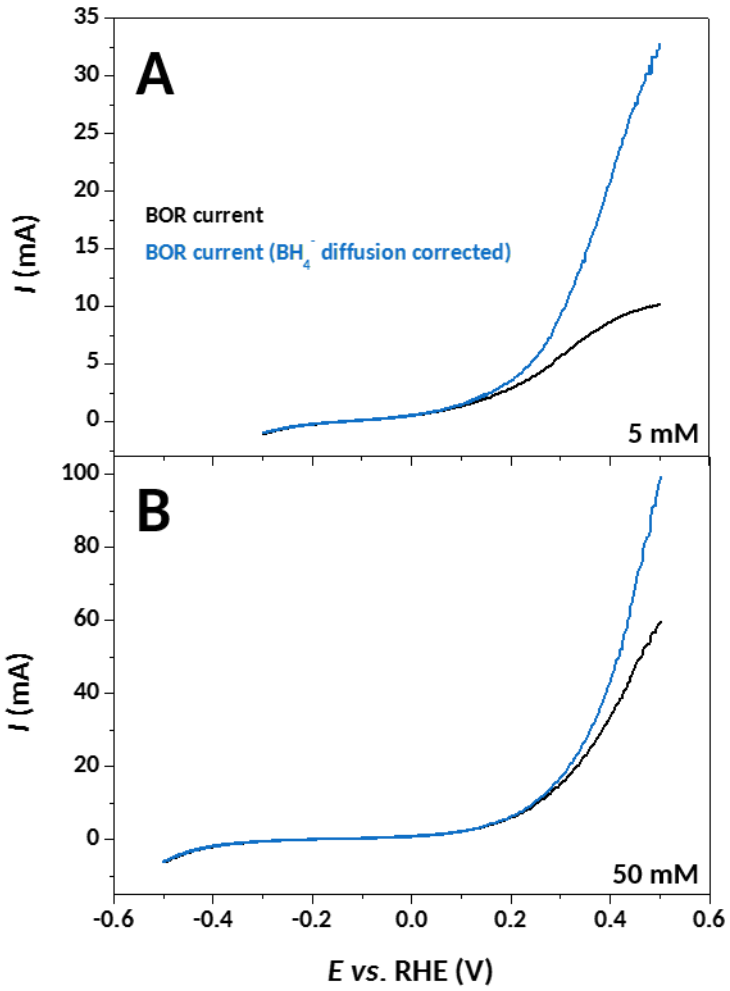

Figure II.12. Illustration of the mass-transport correction on BOR CV obtained on the 22 wt.% Pd/C electrocatalyst for (A) 5 mM $NaBH_4$ and (B) 50 mM $NaBH_4$ in 1 M NaOH. Other conditions: Ar-saturated electrolytes, *T* = 60°C, v = 20 mV s^{-1}, ω = 1600 rpm.

II.5.3 Influence of the $NaBH_4$ concentration

Figure II.13 shows the onset potentials (E_{onset}) obtained on all the electrocatalysts and for the three $NaBH_4$ concentrations. The onset potential can be influenced not only by the nature of the electrocatalyst, but also its structure. Indeed, this potential is a mixed potential, that originates from the conjunction of several competing reactions, such as the HER/HOR, the heterogeneous hydrolysis of BH_4^- and/or the electrooxidation BH_4^- or of the BOR intermediate species. Thus, depending on whether bubbles are forming or whether there are more or less adsorbed species, the morphology of the electrocatalyst will most certainly have an influence on the value of the onset potential.

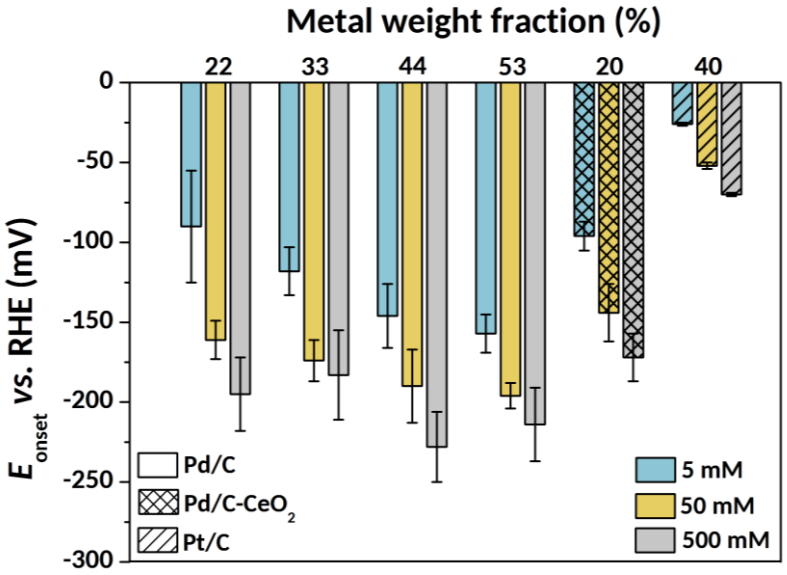

Figure II.13. Influence of the $NaBH_4$ concentration (5, 50 or 500 mM in 1 M NaOH) on the onset potential (E_{onset}) obtained on each electrocatalyst studied in this work at T = 60°C.

Figure II.13 highlights that the onset potential systematically decreases when the $NaBH_4$ concentration increases (a positive effect). In addition, the larger the amount of Pd, the greater the potential shift towards negative values, for 5 and 50 mM $NaBH_4$; the lowest onset potential (-230 mV *vs*. RHE) is reached on the 44 wt.% Pd/C for 500 mM $NaBH_4$. When ceria is present, the onset potential is similar to the 22 wt.% Pd/C electrocatalyst for 5 mM $NaBH_4$, but it is slightly more positive than the ones obtained on the 22 wt.% Pd/C for 50 and 500 mM $NaBH_4$ (by 15 mV and 25 mV, respectively), maybe because ceria covers, in part, the Pd NPs (or possibly because it directly reacts with / is reduced by $NaBH_4$). With no surprise, the onset potential obtained on the Pt/C electrocatalyst is well above the onset potentials obtained on the Pd-based

electrocatalysts, illustrating the incapability of Pt to efficiently electrooxidize $NaBH_4$ at low potential.

Figure II.14 gives the specific activity (SA, mA cm_{metal}^{-2}) and the mass activity (MA, mA μg_{metal}^{-1}) for the three electrode potentials (0, 0.2 and 0.5 V vs. RHE) and the three $NaBH_4$ concentrations. For the lowest potentials (E = 0 and 0.2 *vs*. RHE), the SA and MA increases when the $NaBH_4$ concentration increases from 5 to 50 mM, for all the electrocatalysts. On the contrary, it decreases from 50 to 500 mM $NaBH_4$ (reaching the SA and MA obtained at 5 mM) for all the electrocatalysts except for the 22 wt.% Pd/C. As seen on the BOR CVs, this evolution between 50 and 500 mM illustrates that the charge transfer kinetics becomes very limiting for the high $NaBH_4$ concentration, likely owing to the poisoning of the electrode surface by strong adsorbates species (in other words, the electrocatalyst fails to electrooxidize quantitatively the abundant BH_4^- species in these conditions). The results also highlight that the amount of Pd poorly influences the values of SA and MA; however, one can note that the highest SA and MA are obtained on the 53 wt.% Pd/C for 5 and 50 mM $NaBH_4$ (for E = 0 V *vs*. RHE), and the highest SA and MA are also obtained on the 53 wt.% Pd/C for 50 and 500 mM $NaBH_4$ (for E = 0.2 V *vs*. RHE), but only by a small extent in comparison to the other Pd-based electrocatalysts. In addition, the SA and MA obtained on Pt/C are well higher (≈ 4-fold higher) than those obtained on the Pd-based electrocatalysts for 50 mM $NaBH_4$. This must be associated to the exceptional HOR activity of Pt and illustrates that this latter material oxidizes more H_2 originating from the HER or the catalytic decomposition (or heterogeneous hydrolysis) of BH_4^- (in an indirect oxidation reaction) than directly the BH_4^- species, in line with the values of onset potential of Pt/C, which where all close to 0 V *vs*. RHE.

For the highest electrode potential (E = 0.5 V *vs*. RHE), the SA and MA increase when the $NaBH_4$ concentration increases, except for Pt/C. Interestingly, the highest SA and MA are obtained on the 22 wt.% Pd/C. This result seems to indicate that a lower Pd sites density is beneficial for the BOR mechanism for a high $NaBH_4$ concentration, but this surprising statement must not be considered as granted.

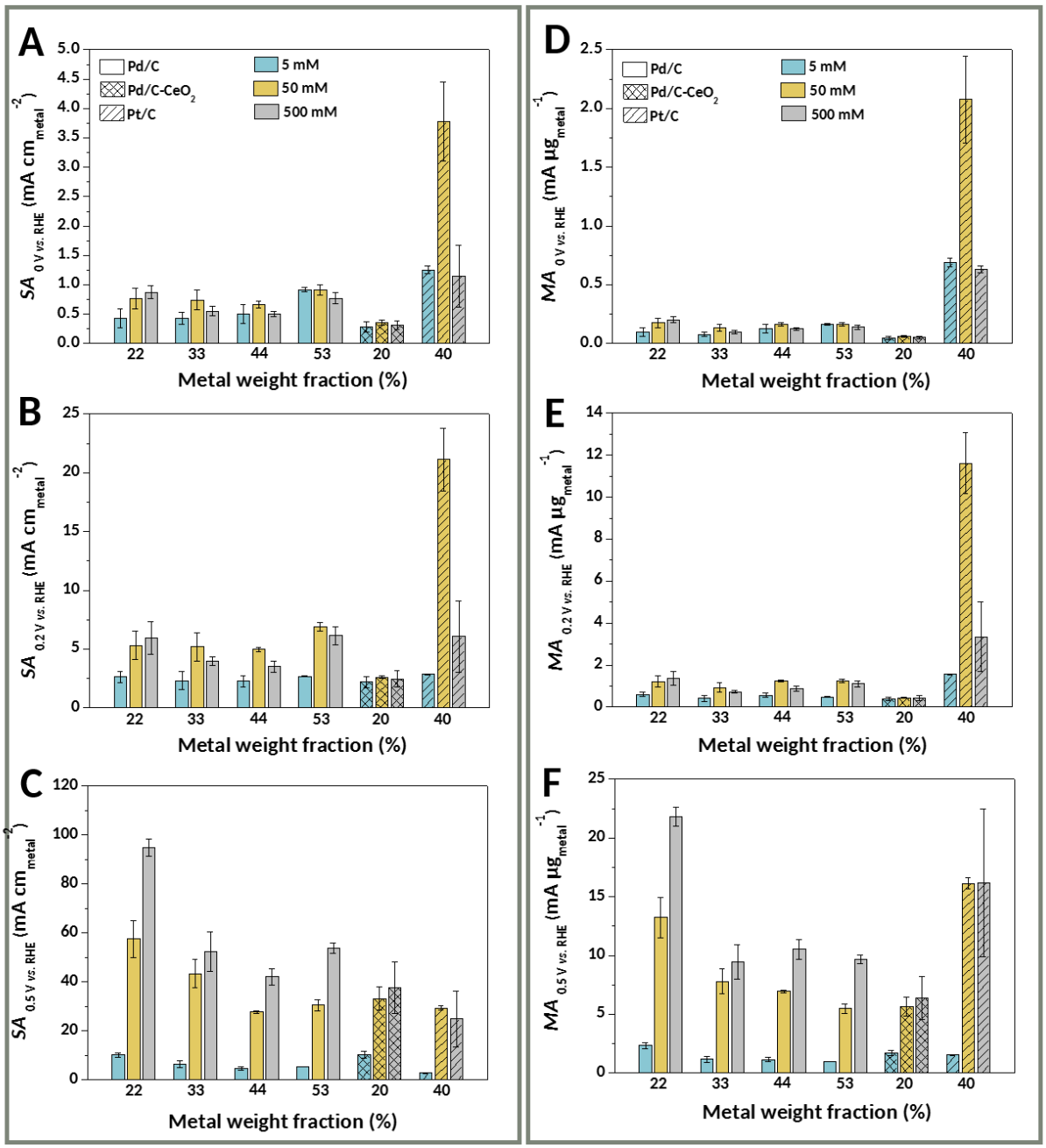

Figure II.14. Influence of the $NaBH_4$ concentration (5, 50 and 500 mM in 1 M NaOH) on the (A, B, C) specific activity (SA) and (D, E, F) mass activity (MA) obtained on the electrocatalysts studied in this work at (A, D) *E* = 0 V *vs*. RHE, (B, E) *E* = 0.2 V *vs*. RHE, and (C, F) *E* = 0.5 V *vs*. RHE and at *T* = 60°C.

To summarize, in conditions that approach the ones used in real DBFC systems (50 and 500 mM $NaBH_4$), the 22 and 53 wt.% Pd/C electrocatalysts exhibit the best SA and MA at low potentials (0 and 0.2 V *vs*. RHE), and the 22 wt.% Pd/C exhibits the best activities at high potential (0.5 V *vs*. RHE). The reasons that could explain such results are not clear since the morphology of these electrocatalysts are different: the 22 wt.% Pd/C is made of small and big NPs with a small extent of agglomeration, while the 53 wt.% Pd/C electrocatalyst is made of small NPs and a lot of agglomerates. Pt/C leads to the fastest reaction at low electrode potentials (0 and 0.2 V *vs*. RHE), its activity being optimal for 50 mM $NaBH_4$. At the highest potential (0.5 V *vs*. RHE) and 500 mM $NaBH_4$, it is tied or even outperformed by 22 wt.% Pd/C, likely owing to more severe poisoning issues at Pt than at Pd in these conditions.

II.5.4 Influence of the temperature

The influence of the temperature on the BOR activity was also studied for two Pd-based electrocatalysts, the 22 and 53 wt.% Pd/C. Three temperatures were tested: T = 20, 40 and 60°C, and **Figure II.15** shows the influence of the temperature on the onset potential. For the two electrocatalysts and the three $NaBH_4$ concentrations, the onset potential shifts negative when the temperature increases, which is positive in terms of reaction kinetics. However, one can notice that this negative shift is rather small, around 10 mV from 20 to 40°C and from 40 to 60°C.

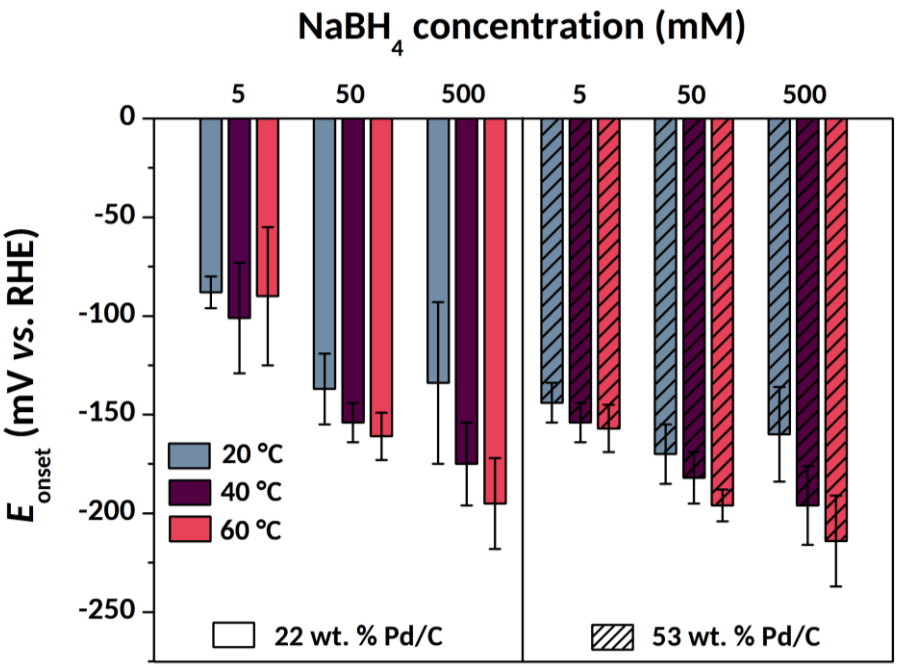

Figure II.15. Influence of the temperature (T = 20, 40, or 60°C) on the onset potential (E_{onset}) obtained on the 22 and 53 wt.% Pd/C electrocatalysts for 5, 50 and 500 mM $NaBH_4$ in 1 M NaOH.

In a similar manner, **Figure II.16** highlights that the SA and the MA increase with the temperature for the two electrocatalysts and the three $NaBH_4$ concentrations at each electrode potential (0, 0.2 and 0.5 V *vs*. RHE): the activity is around 3-fold higher from 20 to 40°C and around 2-fold higher from 40 to 60°C owing to combined and antagonistic effects; on the positive side, higher temperatures lead to faster mass-transport and charge-transfer, while on the negative side it increases the hydrogen evolution (the electrochemical signals on the BOR CVs are more noisy at 60°C than for 20°C, see **Figure A.5** in **Annex 4**). Thus, it seems that working at T = 60°C leads to a beneficial compromise to boost the BOR activity in the $NaBH_4$ concentration range from 5 to 500 mM, and this matches the results in unit DBFC of Olu *et al.* [70].

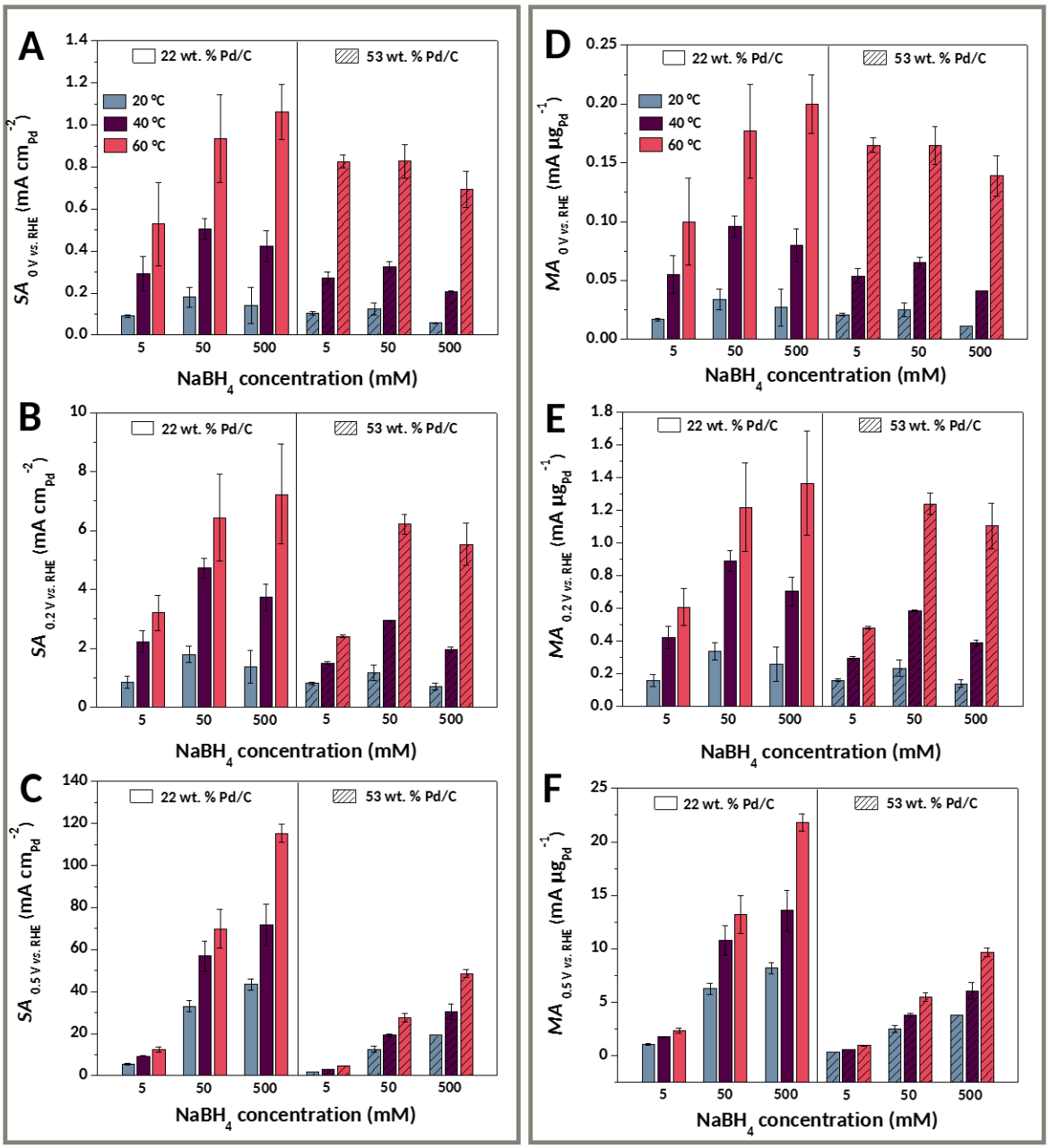

Figure II.16. Influence of the temperature on the (A, B, C) specific activity (SA) and (D, E, F) mass activity (MA) evaluated for the 22 and 53 wt.% Pd/C electrocatalysts at (A, D) *E* = 0 V *vs*. RHE, (B, E) *E* = 0.2 V *vs*. RHE, and (C, F) *E* = 0.5 V *vs*. RHE for 5, 50 and 500 mM $NaBH_4$ concentrations.

II.5.5 Influence of the catalytic layer thickness

Another parameter that can also strongly influence the faradaic efficiency of the BOR is the structure of the electrode, more precisely the geometry of the electrode and the thickness of the catalytic layer. These two parameters directly affect the mass-transport of the reactant and intermediate species within the electrode and the management of gaseous hydrogen. In that frame, several authors [28,70,122,126,239,240] reported that open-structure electrodes enable to enhance the BOR faradaic efficiency (in DBFC configuration), by increasing the residence time of the reactants and intermediate species and enabling faster hydrogen gas bubbles release. Such open-structure electrode were obtained, for instance, when coating the anodic catalytic layer on a carbon cloth instead of the membrane [70], when using aerogel or macroporous carbon supports [239], when using Ni foam instead of carbon cloth [240], or when using three-dimensional carbon support such as reticulated vitreous carbon [122]. In a more fundamental study, Freitas *et al*. [123] highlighted the impact of the catalytic layer thickness on the reaction onset and BOR faradaic efficiency in RDE configuration for Pt/C electrocatalysts. Their results revealed that thick active layer (3 µm) yields larger limiting current than thin layer (0.38 µm) and a slight shift of the onset potential towards negative values. They attributed the apparent better BOR faradaic efficiency for thick active layer to a higher residence time of the reactant and intermediate species, thereby enabling the completion of their electrooxidation.

The effect of the catalytic layer thickness towards the BOR onset potential and faradaic efficiency should vary between Pt/C and Pd/C electrocatalysts. Indeed, as Pt essentially decomposes BH_4^- into H_2 and valorizes H_2, the catalytic layer thickness will mostly influence the apparent BOR faradaic efficiency, while the onset potential shall remain nearly identical. On the contrary, because Pd is capable to valorize BH_4^- and/or its reaction intermediates in a more direct manner (in addition to its HOR activity), it may be expected that the mass-transport will affect both the onset potential and the BOR activity with that material.

It is worth mentioning that an in-depth study of the influence of the catalytic layer thickness was not the initial goal of the present work. However, data enabling to conduct a preliminary study of this effect were acquired, because BOR CVs were initially performed with a constant amount of Pd on the RDE; operating in this manner leads to different electrode thicknesses. Three different catalytic layer thickness with identical amount of Pd could be obtained using Pd/C electrocatalysts with three different metal weight fractions (22, 33 and 44 wt.% Pd/C). The thickness of the electrodes were evaluated considering the density of the dry material

(0.264 g cm^{-3} for Vulcan XC72, 11.9 g cm^{-3} for Pd and 0.2 g cm^{-3} for Nafion) [241] and were estimated to be 2.8, 1.6 and 1 µm, for 22, 33 and 44 wt.% Pd/C electrocatalysts respectively.

Figure II.17 exhibits the values of the onset potentials obtained depending on the catalytic layer thickness. The results reveal that the trend is not very clear, owing to a huge uncertainty of the results obtained on the 1-µm electrode thickness, especially for 50 and 500 mM $NaBH_4$. However, it seems that the results are not in agreement with the study of Freitas *et al*. [123] (but again, these were obtained for Pt/C electrodes): the onset potential shift to more negative values, for the three $NaBH_4$ concentrations, when the electrode thickness decreases. As an example, for 5 mM $NaBH_4$, the onset potential is -90, -105 and -146 mV *vs*. RHE for 2.8, 1.6 and 1-µm catalytic layer thickness respectively. The slight influence of the catalytic layer thickness measured here points towards a negative influence of thick catalytic layers for Pd/C electrodes. One could postulate (but again the trend is slim) that in larger catalytic layers, BH_4^- species and their primary product of heterogeneous hydrolysis (BH_3OH^-) can be too-efficiently decomposed into the final products of heterogeneous hydrolysis (H_2 and BO_2^-), thereby driving the electrode operation from "direct BOR" to "indirect HOR" (the latter being only efficient at potentials close to 0 V *vs*. RHE. However, there could also be other explanations to this trend: the lower onset potential is obtained on the 1-µm electrode, *i.e*. with the 44 wt.% Pd/C electrocatalyst. According to the results presented above (see **Figure II.13**), the onset potential obtained on this electrocatalyst was also lower than the onset potential obtained on the 22 and 33 wt.% Pd/C electrocatalysts, which corresponds to the present 2.8 and 1.6-µm electrode respectively. Thus, it cannot be excluded that the observed trend may also be strongly influenced by the morphology of the Pd NPs (size and extent of agglomeration). So to conclude better about a possible influence of the active layer thickness with Pd/C electrodes, it would be desirable to make the study with more model Pd/C electrocatalysts, for which the materials texture does not evolve with the wt.% Pd. Also, and finally, it must be stated that the potential effect of the catalytic layer thickness shall depend on the ratio between the amount of catalytic sites in the catalytic layer and the borohydride concentration; in other words, the "optimal" thickness of catalytic layer shall depend on the $NaBH_4$ concentration at stake but also the nature/structure of the electrocatalyst used. This has also been put forth by Olu *et al*. [55], who showed (for a smooth Pt surface), that the optimal onset potential and "kinetic current" was obtained with *ca*. 0.1 M $NaBH_4$ (see Figure 5 in [55]); it is believed that the "optimum" would depend on the Pt roughness of the electrode, hence on the catalytic layer thickness, and similarly for Pd/C (or any other catalyst) active layer.

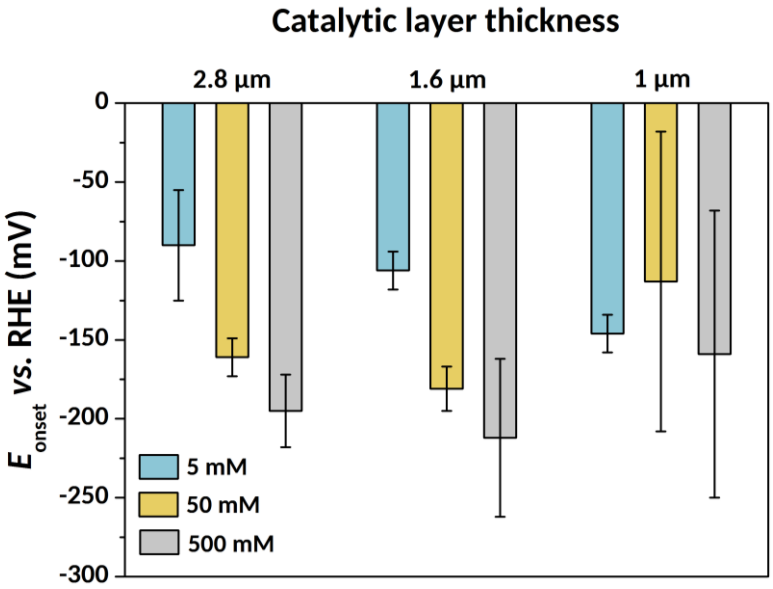

Figure II.17. Influence of the catalytic layer thickness on the onset potential (E_{onset}) obtained on the 22 and 53 wt.% Pd/C electrocatalysts for 5, 50 and 500 mM $NaBH_4$ in 1 M NaOH.

The SA and MA are reported in **Figure II.18**. The trend is still not very clear, since the results obtained on the 1-µm electrode are uncertain, especially for 50 mM $NaBH_4$. However, when E = 0 V *vs*. RHE, 2-fold higher activities are obtained for the thickest electrode for 5 mM $NaBH_4$. One can notice that the activities obtained on the 1.6-µm electrode are slightly lower than the ones obtained on the 1 µm electrode. As mentioned above, this can be explained by the differences of the Pd NPs morphology between the 33 and 44 wt.% Pd/C. For the highest $NaBH_4$ concentrations (50 and 500 mM), 6-fold higher activities are obtained when the thickness of the electrode increases from 1 to 2.8 µm, showing a positive effect of thicker active layers.

The influence of the electrode thickness is more evident for the highest $NaBH_4$ concentration and high potential values. Indeed, when E = 0.2 and 0.5 V *vs*. RHE, which corresponds to potentials values where mass-transport starts to be limiting, thicker electrodes clearly help to enhance the BOR efficiency: 4-fold higher activities are obtained when the thickness of the electrode increases from 1 to 2.8 µm for 500 mM $NaBH_4$.

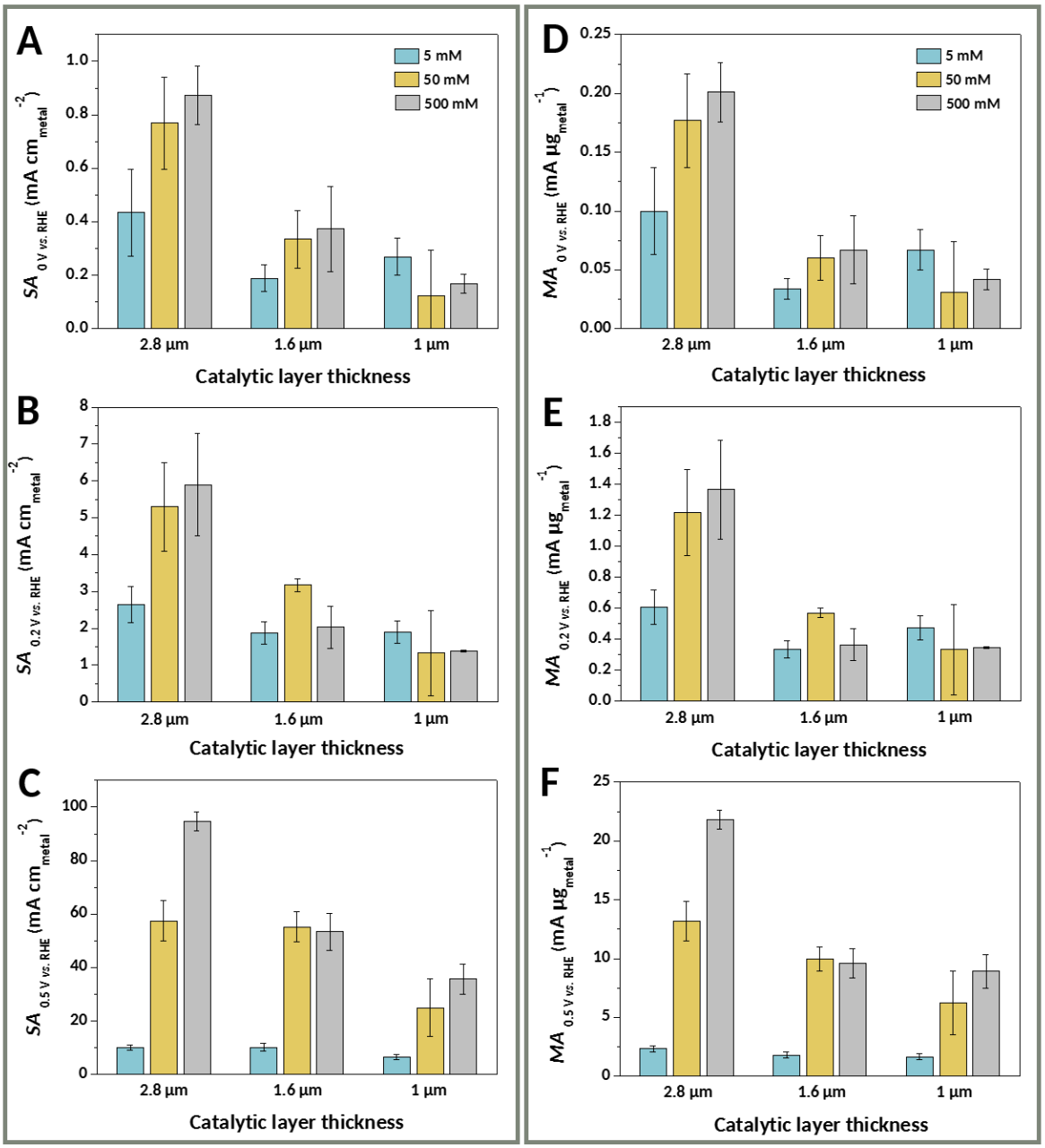

Figure II.18. Influence of the catalytic layer thickness on the (A, B, C) specific activity (SA) and (D, E, F) mass activity (MA) evaluated at (A, D) *E* = 0 V *vs*. RHE, (B, E) *E* = 0.2 V *vs*. RHE, and (C, F) *E* = 0.5 V *vs*. RHE for 5, 50 and 500 mM $NaBH_4$ concentrations.

Globally, these preliminary results are in agreement with the observations of Freitas *et al.* [123]: thick electrodes enable to enhance the residence time of electroactive species within the electrode and lead to higher BOR activities, especially for high $NaBH_4$ concentrations. In that regard, it seems that the activity markers isolated in this thesis are representative of the complexity of the BOR. On the one hand, the onset potential is more negative when the electrode is less active towards the catalytic decomposition of $NaBH_4$: lower thickness of active layer and lower loading of Pd would lead to lower onset potential values. However, when the electrode is polarized to trigger the BOR, thin active layers or poorly-loaded electrodes do not enable to quantitatively electrooxidize BH_4^- and valorize the reactive BOR intermediates. This explains why the SA and MA values (measured at 0, 0.2 and 0.5 V *vs.* RHE) are also very useful markers of the BOR activity.

II.6 Conclusions

In this chapter, the BOR was studied on various Pd-based electrocatalysts, and the influence of several parameters on the BOR kinetics, such as the morphology of the Pd NPs, the Pd sites density, the presence of ceria, the $NaBH_4$ concentration and the temperature were investigated. In addition, activity markers have been proposed to evaluate the BOR activity.

In conditions which are close to the ones used in real DBFC configuration (50 and 500 mM $NaBH_4$ and T = 60°C), the charge transfer kinetics is clearly limiting, but the low ratio $[OH^-]/[BH_4^-]$ might account for the slow BOR kinetics measured here. Moreover, the influence of the Pd sites density does not show particular trend for 500 mM $NaBH_4$.

In addition, the presence of ceria in the Pd/C-CeO_2 electrocatalyst, which was suspected to boost the BOR kinetics by supplying the Pd surfaces with OH_{ads}, did not confirm its promises: Pd/C-CeO_2 revealed to be less active than the Pd/C electrocatalysts. However, the poor Pd NPs dispersion on the Pd/C-CeO_2 electrocatalyst could account for the poor BOR activities monitored, and prior concluding that Pd/C-CeO_2 is not a good BOR material, one should test better-defined Pd/C-CeO_2 materials, which was not possible in the time frame allotted to this PhD.

Finally, preliminary results on the influence of the catalytic layer thickness were obtained. They indicate that thick electrodes enable to enhance the residence time of BH_4^- and of the reactive BOR intermediates within the electrode and lead to higher apparent BOR activities, especially for high $NaBH_4$ concentrations. In a more general approach, the influence of the catalytic layer

design seems to impact the BOR faradaic efficiency: this will be more thoroughly investigated in the next chapter.

Chapter III

Impact of the catalytic layer design on the BOR

III.1 Motivations of the study

If the BOR can, theoretically, release 8 electrons per BH_4^- anion, no single electrocatalyst yielding 100% faradaic efficiency at low potential (close to the thermodynamic potential) has been isolated so far. Thus, as mentioned in **CHAPTER I**, one of the strategies used to enhance the BOR apparent efficiency has been to work with composite materials, combining (mixing or alloying) two electrocatalysts/metals with complementary properties in a single electrode. Another issue, revealed in part by Stroman and Jackson [242] who studied the relationship between cell design and DBFC performances with a 2-D steady state finite volume model, is that the current density is maximum at the fuel inlet and then decreases rapidly along the flow channel, leading to low fuel utilization due to compact BH_4^- and BO_2^- concentration boundary layers near the anode. A similar phenomenon also occurs in PEMFC, where large variation of the local current density was observed along the channel due to locally-reduced concentration of the reactant gases; to mitigate this issue, Zhang *et al*. [243] reported the use of a graded catalyst loading configuration along the gas channel.

In that context, it was believed that combining the two solutions, *i.e*. the use of mixed electrocatalysts within an appropriate electrode structure, could enable to reach high BOR faradaic efficiency and to boost DBFC performances. Thus, in this study, we probed whether there is any merit to create a graded anode electrocatalyst structure instead of homogeneous single electrocatalyst electrode using carbon-supported Pt and Pd electrocatalysts (Pt/C and Pd/C) to optimize the BOR efficiency. Pt/C and Pd/C electrocatalysts were chosen for the following reasons: (i) Pt is one of the most studied electrocatalyst for the BOR and the one for which the BOR mechanism is well-documented and understood (see part **I.2.3**), thereby facilitating the study of a new electrode design on the BOR efficiency; (ii) Pd is a promising electrocatalyst for the BOR, and was at the core of the study of **CHAPTER II**; (iii) Pt/C and Pd/C present similar and complementary properties: although the BOR kinetics is faster on Pt than Pd, both metals can electrooxidize hydrogen (Pt being the most active) [95], and Pd can trigger the BOR at a lower potential than Pt [70]. In addition, Oliveira *et al*. showed in successive papers [108,109] that the addition of a Pd monolayer on Pt (111) enhances the apparent BOR activity of the resulting surface. This improvement was attributed to a slower HER on Pd and a better ability to remove BH_{ads} species due to the fact that Pd is more oxophilic than Pt (this reasoning was based on the assumption that the BOR on Pd proceeds with a similar mechanism as on Pt, which is now believed to be wrong, according to the results presented in **CHAPTER II** and the recent study conducted by Braesch *et al*. [105]).

The impact of the anodic catalytic layer (CL) design on the BOR was investigated both in RDE and in fuel cell configuration (precisely a H_2O_2-DBFC configuration), thanks to the collaboration with the U.S. Naval Research Laboratory; the former experiments were performed by the LEPMI team, and the latter by the U.S. Naval Research Laboratory team (especially Marielle Hjelm, who made all the FC experiments presented in this chapter). The experiments were conducted for two $NaBH_4$ concentrations (10 and 100 mM) at low temperature (*ca.* 25°C). It is worth mentioning that no comparison with literature data could be done: indeed, to the best of the author's knowledge, no study dealing with the impact of alloying or mixing Pt/C and Pd/C electrocatalysts on the BOR activity has been carried out, neither in RDE nor in DBFC configuration.

The results presented in this chapter were published in the following paper:

R. M. E. Hjelm, C. Lafforgue, R. W. Atkinson III, Y. Garsany, R. O. Stroman, M. Chatenet, K. Swider-Lyons, Impact of the anode catalyst layer design on the performance of H_2O_2-direct borohydride fuel cell, J. Electrochem. Soc. 166 (2019) F1-F11.

Contribution: C.L. performed the RDE experiments, analyzed the data, discussed the results, wrote the part about the RDE experiments in the manuscript and approved the final version of the manuscript.

III.2 Experimental details

III.2.1 RDE configuration

III.2.1.1 Electrocatalysts

The carbon-supported Pd electrocatalyst (Pd/C) used in this work for RDE measurements was synthetized by Robert W. Atkinson III from the Naval Research Laboratory (Washington DC, USA) using a vapor deposition protocol described in **Annex 1.A**. The electrocatalyst is supported on Vulcan XC72 carbon black, the metal weight fraction (wt.%) is 22, and the ECSA is 23 $m^2\ g_{Pd}^{-1}$ (calculated using **Equation II.4**). It is the same as the one used in **CHAPTER II**. The carbon-supported Pt electrocatalyst (Pt/C) was purchased from Tanaka Kikinzoku (TKK) and used as received without additional treatment. Its carbon support is also Vulcan XC72 carbon black, the metal weight fraction is 20%, and the ECSA is 78 $m^2\ g_{Pt}^{-1}$ (calculated via CO_{ads}-stripping).

III.2.1.2 Electrochemical measurements

The electrochemical measurements were conducted using the same electrochemical cell described in the previous chapter (see part **II.2.3.1**). The working electrodes were prepared using suspensions made of electrocatalyst, ultrapure water, 5 wt.% Nafion® solution and isopropyl alcohol (IPA) in quantities given in **Table III.1**. After 20 min of sonication, the single Pd/C and Pt/C electrodes and the mixed electrode were prepared by depositing, respectively, 20 µL of ink#1, ink#2 and ink#3 on a 5 mm-diameter glassy-carbon disk that was rotated throughout film drying. The graded Pt/C|Pd/C and Pd/C|Pt/C electrodes were prepared by first depositing 10 µL of ink#1 (respectively ink#2) and then rotating it until dry. Subsequently, a second film was formed by deposition of 10 µL of ink#2 (respectively ink#1) and then dried under rotation. It gives a graded porous RDE, in which the Pt/C layer is at the outer surface, *i.e.* in direct contact with the electrolyte (respectively, in which the Pd/C layer is at the outer surface, *i.e.* in direct contact with the electrolyte). The five RDE configurations are illustrated in **Figure III.1**.

Table III.1. Composition of the electrocatalyst suspensions and metal loadings used on the RDE.

Ink	20 wt.% Pt/C amount (mg)	22 wt.% Pd/C amount (mg)	H_2O (µL)	5 wt.% Nafion® solution (µL)	IPA (µL)	Metal loading on RDE (μg_{metal} cm_{geom}^{-2})
Ink #1	0	10	8000	53.5	3150	20
Ink #2	10	0	7130	55	3000	20
Ink #3	5	5	7130	55	3000	20

The electrochemical measurements were performed using the same protocols as those described in the previous chapter (see part **II.2.3.2**). The electrolyte was 10 mM $NaBH_4$ + 1 M NaOH and the measurements were performed at T = 25°C. Three different tests were carried out for each electrode configuration for reproducibility assessment and the error bars were calculated using the standard deviation.

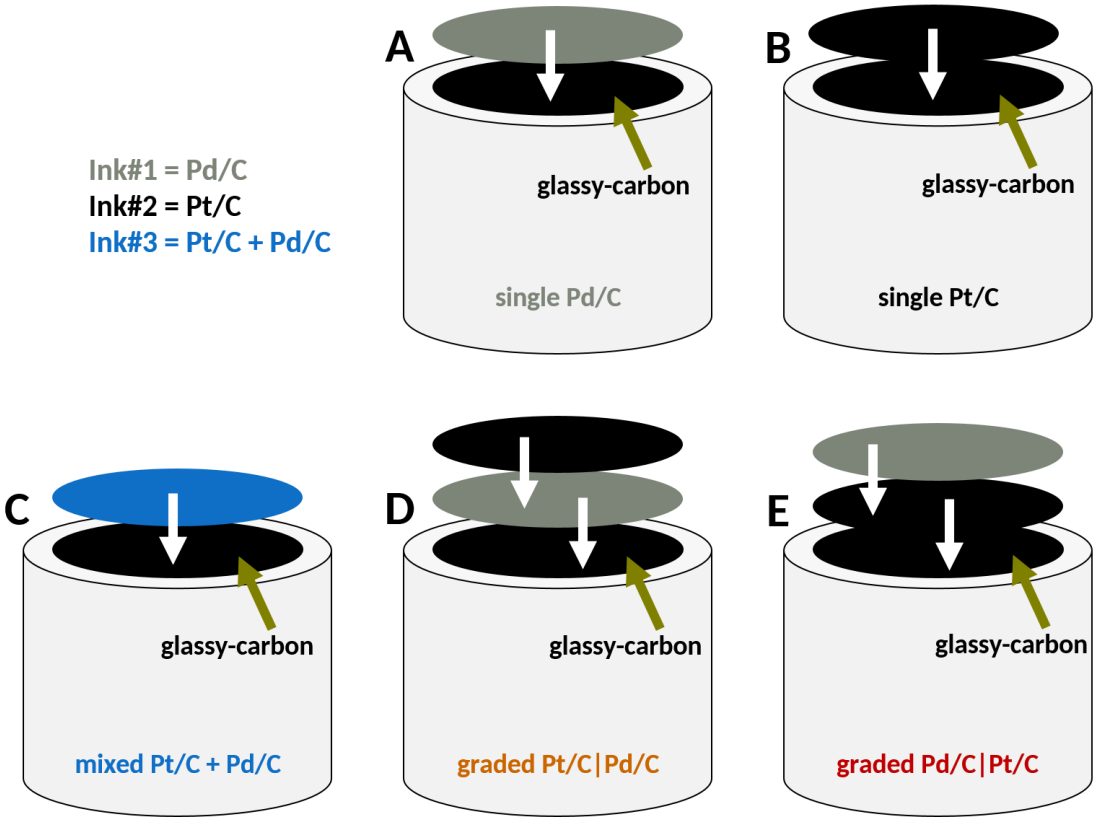

Figure III.1. Illustration of the five rotating disk electrode configurations; (A) single Pd/C, (B) single Pt/C, (C) mixed Pt/C + Pd/C, (D) graded Pt/C|Pd/C, (E) graded Pd/C|Pt/C.

III.2.2 Fuel cell configuration

III.2.2.1 Electrocatalysts

The carbon-supported Pd electrocatalyst (Pd/C) used in this work for fuel cell measurements was synthetized by Robert W. Atkinson III from the Naval Research Laboratory (Washington DC, USA) using a vapor deposition protocol described in **Annex 1.A**. The electrocatalyst is supported on Vulcan XC72 carbon black, the metal weight fraction is 53% and the ECSA is 64 $m^2\ g_{Pd}^{-1}$ (calculated via CO_{ads}-stripping). It is not the same as the one used in the previous chapter, the difference being the temperature of the final heat treatment, that led to higher ECSA electrocatalyst. The carbon-supported Pt electrocatalyst (Pt/C) was purchased from Ion Power (IP) and used as received without additional treatment. The metal weight fraction is 50% and the ECSA is 72 $m^2\ g_{Pt}^{-1}$ (calculated via CO_{ads}-stripping).

III.2.2.2 Cell design and global set up

An exploded 3D-view of the design of the fuel cell used in this study is shown in **Figure III.2** and the global set up is shown in **Figure III.3**. The anodic and cathodic compartments are separated by a Nafion® 117 membrane (183 µm-thick) and two PTFE gaskets (200 µm-thick) cut in the center to create a 2.45 cm^2-flow channel. The catalytic layers are deposited onto impervious bipolar graphite plates (BGP, Fuel Cell Store) with gold plated brass current collector plates at each end. The flow inlet and outlet are at the ends of each catalytic layers. The fuel and oxidant are stored in reservoirs and bring to the cell in a single-pass mode with parallel flow using two peristaltic pumps (NE-9000, Chemyx.com).

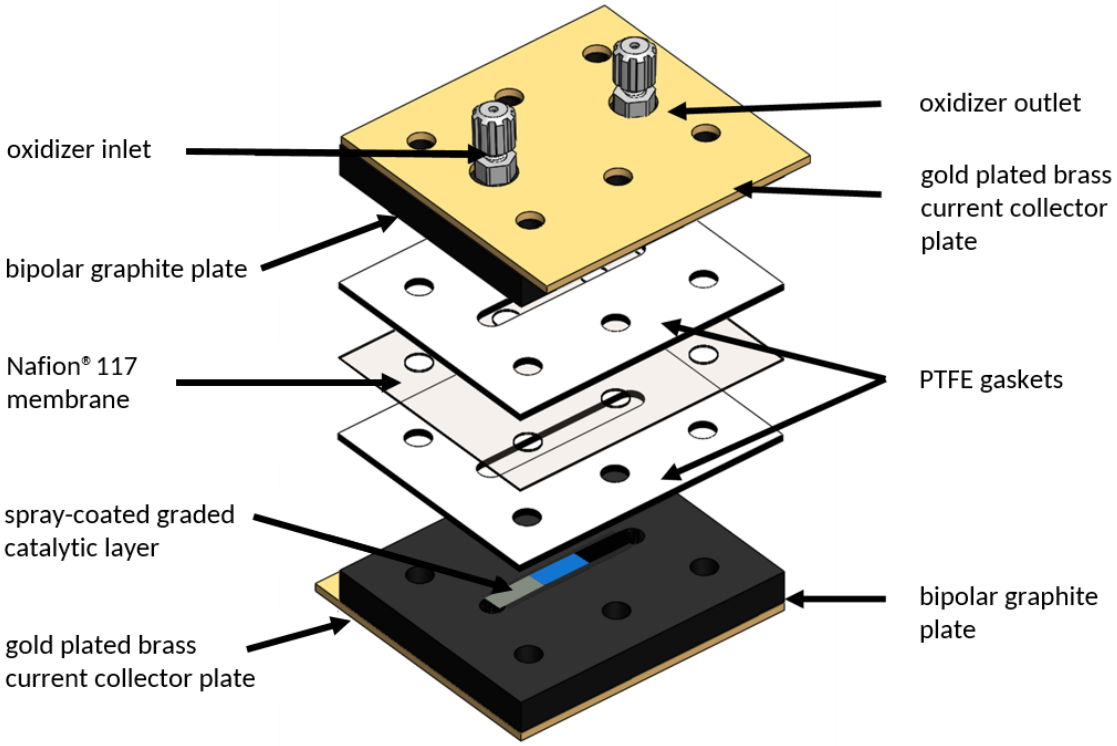

Figure III.2. Exploded 3D-view of the design of the H_2O_2-DBFC cell used in this study showing a graded anode catalytic layer with Pd/C (gray), 1:1 wt.% Pt/C + Pd/C (blue), and Pt/C (black). Fuel inlet and outlet are hidden at bottom.

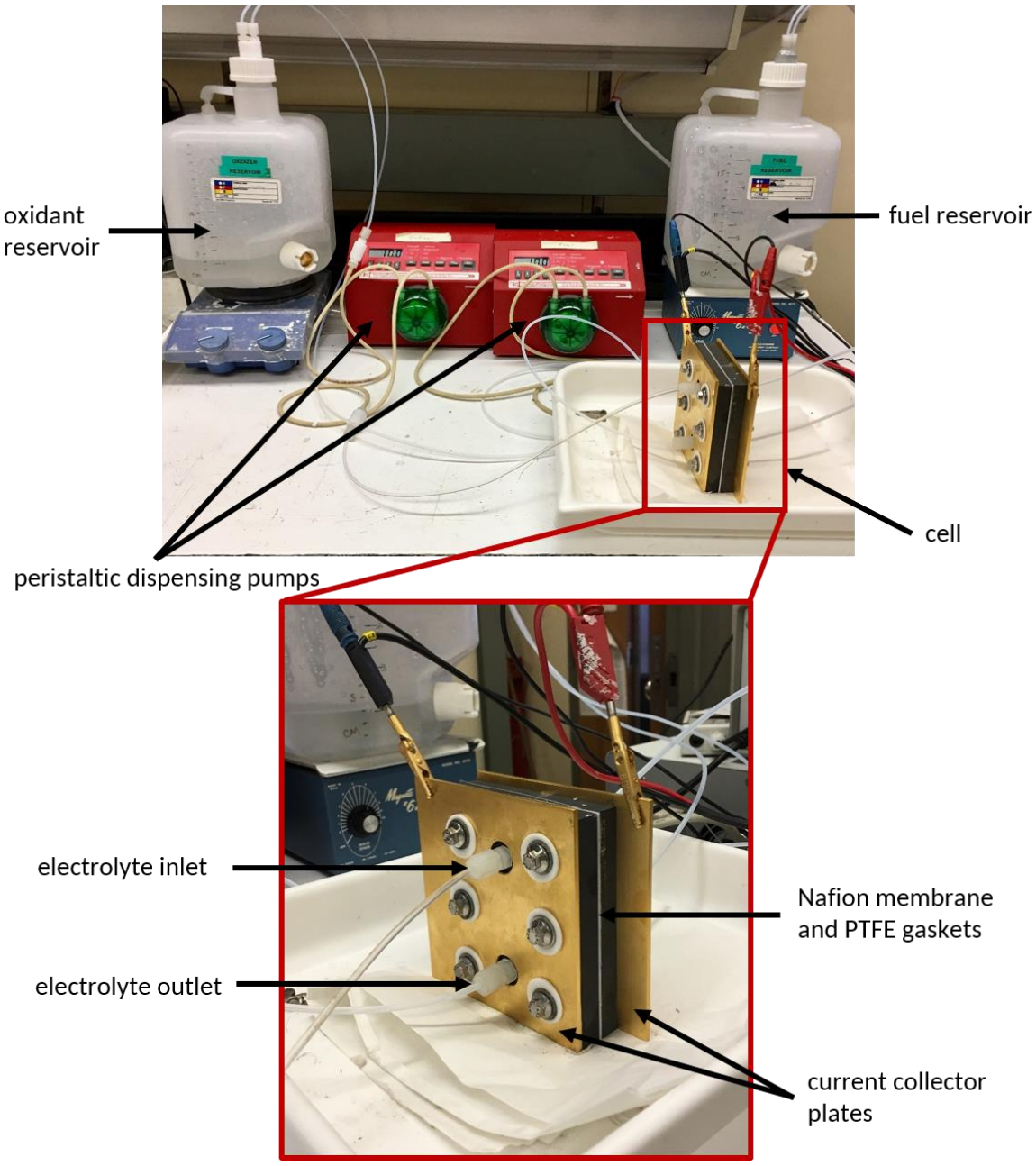

Figure III.3. Picture of the global set up of the H_2O_2-DBFC used for the experiments.

III.2.2.3 Electrodes preparation and composition

The anode and cathode were prepared using an ultrasonic spray-coating method. To that goal, electrocatalysts suspensions (inks) were prepared by mixing the electrocatalyst powder with ultrapure water, 6 wt.% Aquivion® 830 EW ionomer (D83-06A, Sigma Aldrich) and isopropyl alcohol (IPA). The mass ratio of the ionomer binder to carbon was adjusted to 0.95 (*i.e.* 32 wt.% ionomer in the dry CL) for all the electrodes. For some experiments, a 1:1 wt.% mixture of Pt/C and Pd/C was combined using the same weight for each electrocatalyst and the same ionomer

binder to carbon ratio as for the homogenous inks. The freshly-prepared inks were then mixed with a high shear mixer during 5 h.

Then, the inks were ultrasonically spray-coated onto the BGPs via a layer-by-layer method described in **Annex 3** using an automated ultrasonic spray apparatus. The catalyst area for each electrode was a 0.965 cm x 5.08 cm rectangle (active area: 4.9 cm^2), spanning from inlet to outlet. For the anodes, Pt/C and Pd/C were sprayed as individual electrodes, in 1:1 wt.% mixtures (Pt/C + Pd/C), or as gradients. For single and mixed CLs, inks were deposited uniformly along the entirety of the flow field area. For anodes with graded CLs, masks were used to spray 1/3 of the area at a time with no overlap of catalyst such that Pt/C and Pd/C were deposited at each end of the flow field with a Pt/C + Pd/C mixture at the center, as illustrated in **Figure III.4**, in order to create a gradual transition from Pt/C to Pd/C or Pd/C to Pt/C in the graded design. Each sprayed electrode was allowed to dry overnight before testing to ensure complete evaporation of the solvent.

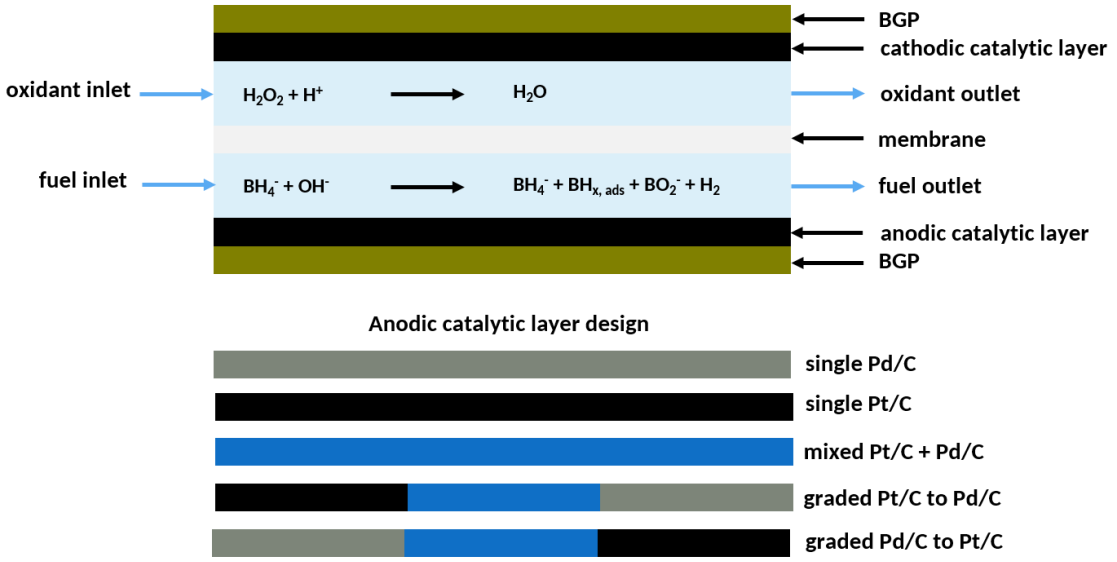

Figure III.4. Illustration of the five anodic catalytic layer design used in the H_2O_2-DBFC.

The CLs were similarly deposited as dummy electrodes onto Kapton® foil and weighed five times after overnight drying. The average of the resulting weights was used to calculate the approximate metal loading of the single and mixture electrodes. The total loadings for Pt/C, Pd/C, and mixed samples were 0.31 ± 0.02 mg cm^{-2}, 0.30 ± 0.01 mg cm^{-2}, and 0.30 ± 0.02 mg cm^{-2}, respectively. **Table III.2** recaps the different H_2O_2-DBFC configurations studied in this work.

Table III.2. Composition of the catalytic layer designs and metal loadings of the electrodes studied in this work.

Catalytic layer design	Anode electrocatalyst	Cathode electrocatalyst
	Metal loading (mg_{metal} cm_{geom}^{-2})	**Metal loading (mg_{metal} cm_{geom}^{-2})**
Pd/C	53 wt.% Pd/C 0.31 ± 0.02	50 wt.% Pt/C 0.30 ± 0.01
Pt/C	50 wt.% Pt/C 0.30 ± 0.01	50 wt.% Pt/C 0.30 ± 0.01
Mixed Pt/C + Pd/C	50 wt.% Pt/C + 53 wt.% Pd/C 0.31 ± 0.02	50 wt.% Pt/C 0.30 ± 0.01
Graded Pt/C|Pd/C	50 wt.% Pt/C 50 wt.% Pt/C + 53 wt.% Pd/C 53 wt.% Pd/C x	50 wt.% Pt/C 0.30 ± 0.01
Graded Pd/C|Pt/C	53 wt.% PdC 50 wt.% Pt/C + 53 wt.% Pd/C 50 wt.% Pt/C x	50 wt.% Pt/C 0.30 ± 0.01

III.2.2.4 Electrochemical measurements

The H_2O_2-DBFC performances measurements were conducted for two combinations of electrolytes:

1) 10 mM $NaBH_4$ in 1 M NaOH at the anode and 40 mM H_2O_2 in 1 M H_2SO_4 at the cathode;
2) 100 mM $NaBH_4$ in 1 M NaOH at the anode and 400 mM H_2O_2 in 1 M H_2SO_4 at the cathode.

The solutions were prepared using H_2SO_4 (98%, Fisher Scientific) and H_2O_2 (30%, Fisher Scientific), or NaOH pellets (Fisher Scientific) and $NaBH_4$ granules (98%, Alfa Aesar). A flow rate of 10 mL min^{-1} was maintained at both the cathode and anode with parallel flows, thanks to the

two peristaltic pumps. The Nafion® membrane was prepared for Na^+ ion transfer by first cleaning in a boiling solution of 1 wt.% H_2O_2 for one hour, followed by boiling in 0.1 M NaOH for one hour. Then, the membrane was stored in 1% NaOH solution until use. All cells were operated at room temperature. **Table III.3** recaps the experimental parameters used in the study.

Table III.3. Summary of the experimental parameters used in this study; *S* is the geometric surface area of the flow field.

Anolyte composition **Flow rate** **(mL min^{-1})**	**Separator**	**Catholyte composition** **Flow rate** **(mL min^{-1})**	***S*** **(cm²)**	***T*** **(°C)**
10 mM $NaBH_4$ + 1 M NaOH 10	N117	40 mM H_2O_2 + 1 M H_2SO_4 10	2.45	ambient (≈ 25)
100 mM $NaBH_4$ + 1 M NaOH 10	N117	400 mM H_2O_2 + 1 M H_2SO_4 10	2.45	ambient (≈ 25)

The electrochemical measurements were recorded using an Autolab potentiostat/galvanostat coupled with an Autolab Eco Chemie 10 A current booster and NOVA 2.1 software. The different protocols used to characterize the FC performances are detailed hereafter.

- **Polarization curves measurements**

The open circuit voltage (OCV) of each cell was measured for 5 min prior a multiple-step chronoamperometry (CA) was run. Cell voltages (U_{cell}, V) were held for 150 seconds starting at OCV and measured every 100 mV *vs*. OCV until 1.4 V polarization. The current measured at each cell voltage was recorded every second and the last 20 points were averaged. Three different tests were carried out for each anode design for reproducibility assessment.

- **H_2 escape measurements**

The volume of escaped gaseous H_2 was measured concurrently with the CA measurements, using an inverted graduated cylinder connected to the flow channel outlet at the anode. The measured volumes were divided by the time of each CA measurement to give the rate of H_2 escape (µL s^{-1}).

III.3 Analysis of the electrocatalysts morphology

TEM micrographs of the electrocatalysts used to create the different CL layers studied in this work are displayed in **Figure III.5**. As a reminder, the 22 wt.% Pd/C is mainly composed of a bimodal population of isolated particles (3-5 nm for the small ones, *ca*. 10 nm for the large ones) and rather small extent of agglomerates. Then, the micrographs reveal that the 53 wt.% Pd/C is composed of two families of rather homogeneous particles (*ca*. 2-3 nm for the small ones and 10 nm for the large ones), but with larger extent of (larger) agglomerates (essentially of the larger NPs); the commercial Pt/C catalysts are made of well dispersed small NPs (2 - 2.5 nm). The catalysts corresponding to **Figure III.5.A.B** and **Figure III.5.C.D** were used for the RDE and DBFC measurements respectively.

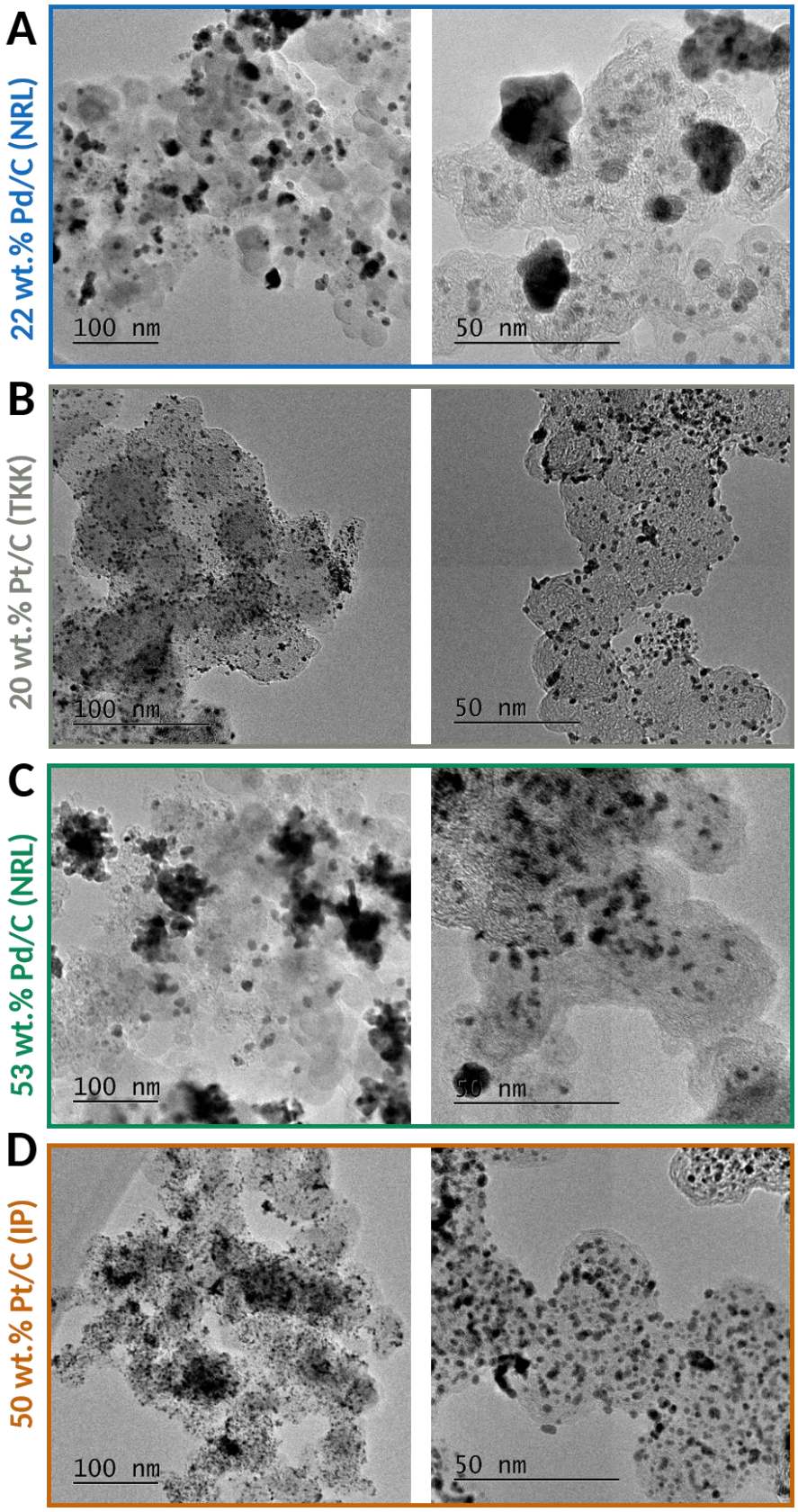

Figure III.5. TEM micrographs obtained on the different electrocatalysts used in this study to create the different catalytic layer design: (A) 22 wt.% Pd/C (NRL), (B) 20 wt.% Pt/C (TKK), (C) 53 wt.% Pd/C (NRL) and (D) 50 wt.% Pt/C (IP).

III.4 Impact of the catalytic layer on the BOR activity

III.4.1 RDE configuration measurements

The BOR activity obtained on each electrode structure in RDE configuration was investigated for 10 mM $NaBH_4$ in 1 M NaOH at T = 25°C. A typical CV of each electrode configuration for an electrode rotation rate ω = 1600 rpm is displayed in **Figure III.6**. The current densities presented in the CVs were obtained by dividing the current either by the corresponding ECSA (cm^2) of each electrocatalyst (see **Figure III.6.A**; in the case of the mixed and graded electrodes, the ECSA used to calculate the current densities is the average between the Pt/C ECSA and Pd/C ECSA) or by the electrode's geometric area (**Figure III.6.B**).

One can notice that the overall CVs shape obtained with the mixed (Pt/C + Pd/C) electrode and the graded (Pt/C|Pd/C or Pd/C|Pt/C) electrodes remains unchanged in comparison to the single Pt/C electrode. In addition, the onset potential values (here, simply the open-circuit potential, OCP, which is a mixed potential resulting from the competition between the HER/HOR and the BOR) reached on all the Pt-containing electrodes are around -45 mV *vs*. RHE whereas the onset potential reached on the single Pd/C electrode is -115 mV *vs*. RHE (the onset potential values are gathered in **Figure III.7**). These results suggest that the mixed and graded electrode configurations may lead to a similar apparent BOR mechanism than the single Pt/C electrode, and that, consequently, the behavior of Pt/C dominates in these conditions. Indeed, as a reminder, for Pt-based electrocatalysts, the HER prevails on the BOR below E = 0 V *vs*. RHE; above this potential, the HOR prevails on the BOR [55]. This is because Pt tends to decompose BH_4^- into $BH_{x,\,ads}$ + H_{ads} (H_{ads} likely combining into H_2 below the hydrogen potential and being electrooxidized above this potential) and because Pt is highly active for the HER/HOR. As a result, the onset potential is dominated by the HER/HOR on Pt and is not majorly affected by the addition of Pd in the mixed and graded electrodes.

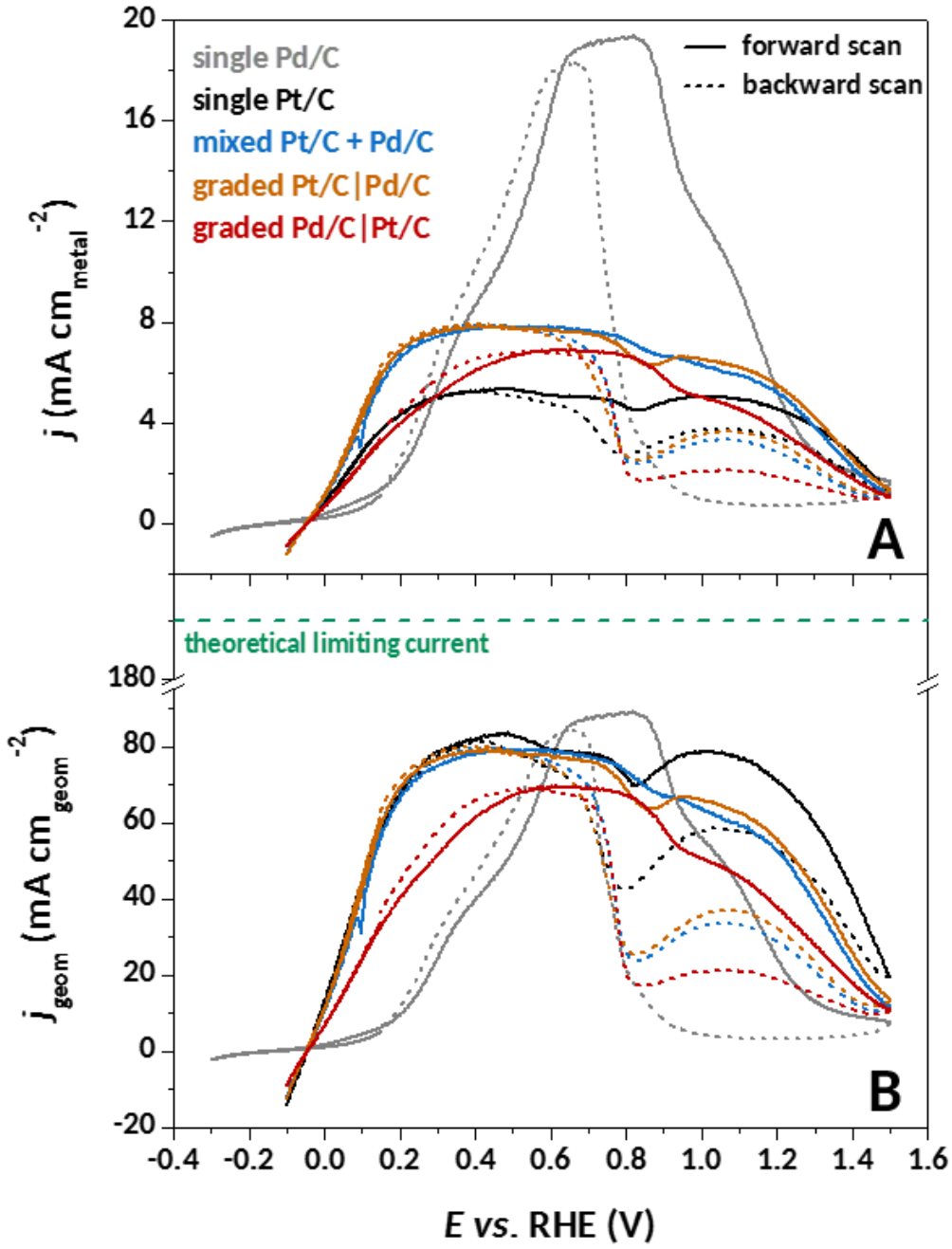

Figure III.6. BOR voltammograms obtained on the catalytic layers studied in this word in 10 mM $NaBH_4$ + 1 M NaOH; (A) the current densities are relative to the electrochemical surface area of each electrocatalysts, (B) the current densities are relative to the electrode's geometric area. Other conditions: Ar-saturated electrolyte, T = 25°C, v = 20 mV s^{-1}, ω = 1600 rpm.

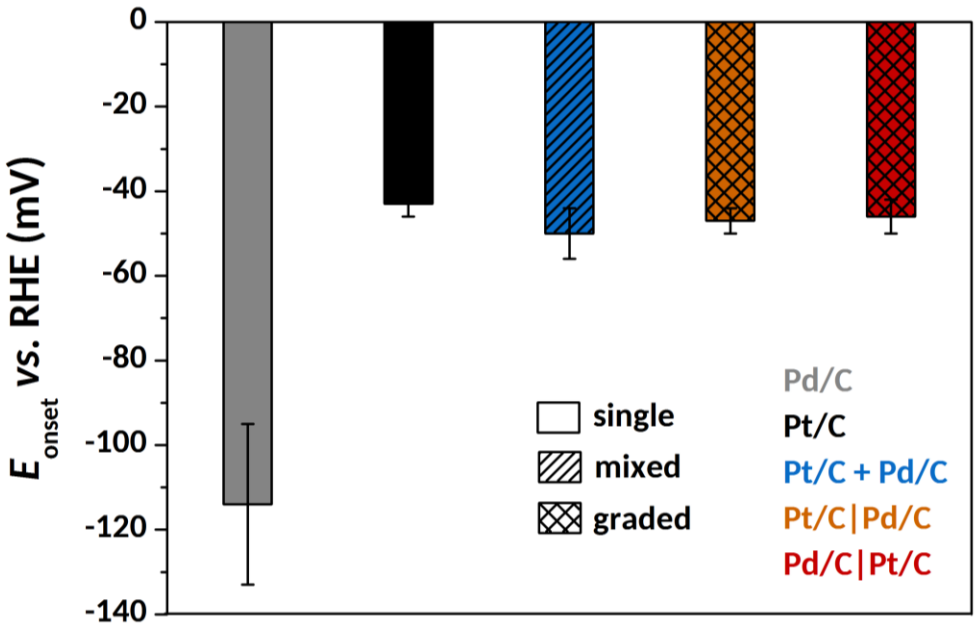

Figure III.7. Onset potential (E_{onset}) obtained on the catalytic layers studied in this word in 10 mM $NaBH_4$ + 1 M NaOH at T = 25°C.

When looking closely at the five CVs in **Figure III.6.A**, especially in the potential range from E = 0 to 0.3 V *vs*. RHE, it is interesting to observe that the BOR kinetics is similar for the single Pt/C electrode and the graded Pd/C|Pt/C electrode, but the BOR kinetics is faster on the mixed electrode and the graded Pt/C|Pd/C electrodes. These results indicate that, for the graded electrodes, the position of the electrocatalyst influences the resulting BOR kinetics. Because Pt/C is essentially active for the HOR, the Pd/C|Pt/C graded electrode (that has the Pd/C layer in direct contact with the electrolyte), yields lower apparent BOR kinetics, owing to (i) the smaller kinetics of BOR (and of HOR) at Pd/C than at Pt/C and (ii) the fact that most H_2 produced at the electrode surface does not "see" Pt/C, and can be evacuated (because of the revolution rate of the RDE) prior reaching any Pt/C site, that are all located in the inner layer of the graded thin-film (*i.e.* not in direct contact with the electrolyte).

In addition, the theoretical limiting current that should be obtained in the conditions of the study was calculated using the Levich equation (**Equation II.11**), with $n = 8$, $D = 3.01 \times 10^{-5}$ cm^2 s^{-1}, v = 0.0114 cm^2 s^{-1} and ω = 167.55 rad s^{-1}. The values of D and v come from the study of Chatenet *et al*. [90] for experimental conditions that most closely correspond to those of this work. The theoretical limiting value was calculated to be 185 mA cm$_{geom}^{-2}$ and is highlighted in **Figure III.6.B** by the dashed green line. As mentioned in the previous chapter, one can see that no clear limiting current densities appear on the BOR voltammograms (**Figure III.6.B**) obtained with each electrode configuration; thus, the theoretical limiting current density is compared to the

maximum current density obtained (around *E* = 0.8 V *vs*. RHE) with each electrode configuration which is 90, 83, 80, 80 and 70 mA cm_{geom}^{-2} for the single Pd/C, single Pt/C, mixed, graded Pt/C|Pd/C and graded Pd/C|Pt/C electrodes, respectively. These values are well below the theoretical limiting current density value calculated above, indicating that the 8 electrons are not reached. This means that the BOR is limited by the amount of catalytic sites (and cannot be complete), hence that the ratio [catalytic sites]/[BH_4^-] is too low.

The BOR activity was further analyzed by extracting the specific activities (SA) and mass activities (MA) obtained at *E* = 0, 0.2 and 0.5 V *vs*. RHE from the CVs; the results are displayed in **Figure III.8**. At low potentials (*E* = 0 and 0.2 V *vs*. RHE), even if the BOR starts sooner on the single Pd/C electrode than the Pt-containing electrodes, the SA obtained with the single Pd/C electrode are significantly lower (4 to 6-fold lower at *E* = 0 V *vs*. RHE and 2 to 3-fold lower at *E* = 0.2 V *vs*. RHE) than the SA obtained with the Pt-containing electrodes, likely owing to the faster HOR kinetics on Pt. This result shows, again, that fast valorization of H_2 is key in obtaining large currents at low BOR potentials, at least on Pt and Pd electrodes. However, at higher potential, when *E* = 0.5 V *vs*. RHE, the SA obtained with the single Pd/C electrode is *ca*. 2-fold higher than the other electrodes, because at this potential, Pt sites are poisoned by BH_{ads} (and possibly $BH_{3,ads}$ species) [55] and Pt can therefore not completely electrooxidize the hydrogen species (and $BH_{x,ads}$ moieties) produced during the BOR. The disparities of the mass activities in comparison to the specific activity can essentially be rationalized by the high ECSA of the Pt/C electrocatalyst (78 $m^2\ g_{Pt}^{-1}$) and the low ECSA of the Pd/C electrocatalyst (23 $m^2\ g_{Pd}^{-1}$).

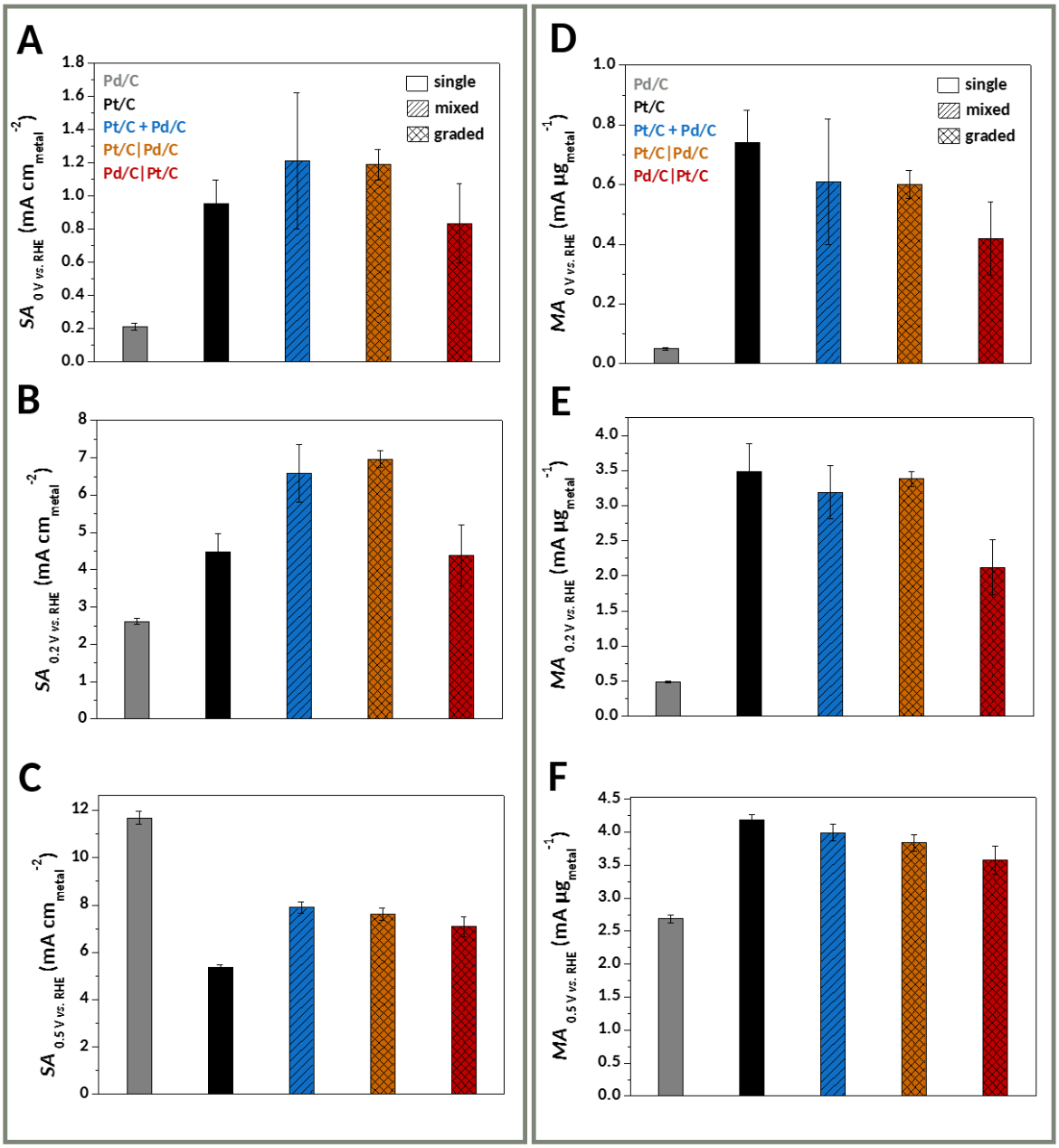

Figure III.8. (A, B, C) Specific activities (SA) and (D, E, F) mass activities (MA) obtained on the catalytic layers studied in this work for (A, D) E = 0 V *vs.* RHE, (B, E) E = 0.2 V *vs.* RHE, (C, F) E = 0.5 V *vs.* RHE in 10 mM $NaBH_4$ + 1 M NaOH. Other conditions: Ar-saturated electrolyte, T = 25°C, ω = 1600 rpm.

For the graded electrodes, when Pt/C is layered on top of the Pd/C, the SA obtained at E = 0 V *vs.* RHE increases by *ca.* 30% in comparison to the inverse configuration, illustrating, as discussed above, that the position of the electrocatalyst influences the BOR activity. This confirms that fast HOR (on Pt) is key in obtaining good apparent kinetics of the BH_4^- oxidation (at least, as long Pt sites are not poisoned by too large BH_4^- concentration – and this is the case

at 10 mM $NaBH_4$). In addition, one can notice that the SA and MA obtained on the mixed electrode are not an average of the SA and MA obtained on the single Pt/C and the single Pd/C electrodes, indicating a good synergy between the two materials when they are in close contact. This statement can be extended to the overall RDE results: mixed or graded electrode structures (in general) enable to improve the BOR activity (in terms of low-potential kinetics) due to the synergy between the two materials in these configurations. The impact of mixing and grading the electrocatalysts in the anodes of H_2O_2-DBFCs was further elucidated in fuel cell configuration.

III.4.2 H_2O_2-DBFC configuration measurements

III.4.2.1 Polarization curves and power curves

The H_2O_2-DBFC performances obtained with the different anodic catalytic layer configurations were investigated for low (10 mM $NaBH_4$ + 1 M NaOH and 40 mM H_2O_2 + 1 M H_2SO_4) and high (100 mM $NaBH_4$ + 1 M NaOH and 400 mM H_2O_2 + 1 M H_2SO_4) electrolyte concentrations at room temperature. The corresponding polarization curves and power curves are displayed in **Figure III.9** (the curves displayed are an average between the three experiments). The geometric current densities (j_{geom}) were obtained by dividing the current by the geometric active area of the flow field (2.45 cm^2). It is in principle assumed that the H_2O_2-DBFCs performances are not cathode-limited and that the electrochemical response is mainly due to the anode. However, because the polarization and power curves correspond to the performances of the complete H_2O_2-DBFC, they may include some losses from the reduction of H_2O_2 at the cathode, especially at low cell voltage, and also Ohmic losses (essentially originating from poor Na^+ migration in the Nafion 117 membrane).

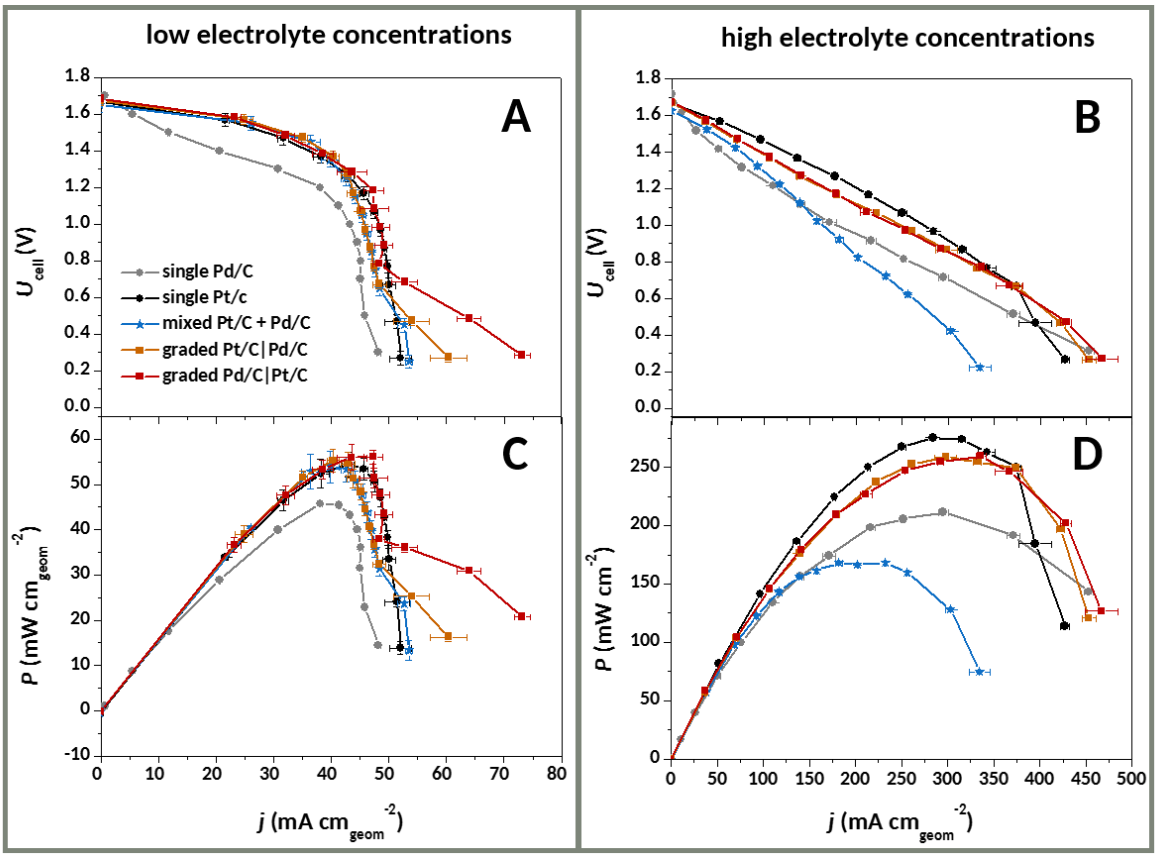

Figure III.9. H_2O_2-DBFC performances obtained on the different anodic catalytic layer configurations studied in this work; (A, B) polarization curves and (C, D) power curves obtained for (A, C) 10 mM $NaBH_4$ + 1 M NaOH and 40 mM H_2O_2 + 1 M H_2SO_4 and (B, D) 100 mM $NaBH_4$ + 1 M NaOH and 400 mM H_2O_2 + 1 M H_2SO_4 at room temperature.

- **H_2O_2-DBFC performances analysis for 10 mM $NaBH_4$**

For low fuel concentration (**Figure III.9.A.C**), it is interesting to notice that the trend observed from the FC results is similar to the trend observed in RDE configuration: the H_2O_2-DBFCs made with the mixed and graded anodes exhibit similar polarization curves than the single Pt/C anode, specifically for high cell voltages (U_{cell} > 1.3 V). This observation nicely confirms that the BOR mechanism is dominated by Pt in these conditions (low $NaBH_4$ concentration, low temperature, and low anodic potential) and that the BOR is not affected by the addition of Pd in the mixed and graded configurations. When U_{cell} decreases, H_2O_2-DBFCs with Pt-containing anodes show a slight variance in performance from each other but in general exhibit the same electrochemical behavior until U_{cell} ≈ 0.8 V. Below this cell voltage value, a distinct change in the polarization curves is observed for all fuel cells but it is more pronounced for the graded anodes. The H_2O_2 - DBFC with single Pd/C anode displays lower current densities and different polarization curve than the Pt-containing anodes, suggesting a different BOR mechanism (and slower overall

BOR kinetics). The OCV obtained (see **Table III.4**) with this anode is slightly higher (1.7 V) than the Pt-containing ones (*ca.* 1.67 V), which is in agreement with the observations in RDE configuration (the lowest onset potential was obtained with the single Pd/C electrode); a higher contrast could have been expected between the OCV reached with the single Pd/C anode and the Pt-containing anodes, though, since the onset potential was 70 mV lower on the single Pd/C electrode than the Pt-containing electrodes in RDE configuration, but RDE are not subjected by fuel (and oxidant) crossover, which presently affects DBFC performances.

When looking closely at the polarization curves, they seem to be composed of two distinct parts: the first one for U_{cell} > 0.8 V, and the other one for U_{cell} < 0.8 V, suggesting that two main electrochemical processes occur, as observed in RDE configuration (corresponding to low and high anodic potential domains). According to the results obtained in the previous chapter, it is likely that the first process corresponds to the overall BOR (with the succession of the electrooxidation of BOR intermediate species), and that at lower cell voltage, *i.e.* high anodic potential, the apparent curve rupture could correspond to the disinsertion of Pd hydrides, since this change is mostly observed for the Pd-containing anodes. The rupture of the curve observed for U_{cell} < 0.8 V could also be due to the cathode limitation.

The highest maximum power densities values (P_{max}, see **Table III.4**) are obtained with the Pt-containing anodes reaching *ca.* 55 mW cm^{-2}, while the lowest maximum power density is obtained on the single Pd/C anode (46 mW cm^{-2}); in all cases, the maximum power density is reached for U_{cell} ≈ 1 V. Besides, the maximum power densities are obtained when the current densities reach the "limiting current densities" observed in the range 0.8 < U_{cell} < 1.2 V.

According to these observations, this limiting current value obtained for each anode configuration was measured for U_{cell} = 1 V and compared to the theoretical maximum current that could be reached in the conditions of the study, according to the fuel concentration and flow rate. The latter was calculated using **Equation III.1**, assuming that each BH_4^- anion was completely electrooxidized via an 8-electron reaction without H_2 generation (and that the H_2O_2 cathode is not limiting).

$$I_{\max,\mathrm{theo}} = [\mathrm{BH}_4^-] \times \mathrm{VFR} \times F \times n_e \qquad \textbf{Equation III.1}$$

where $[BH_4^-]$ is the concentration of BH_4^- (mol cm^{-3}) feeding into the cell at the volumetric flow rate (VFR, cm^3 s^{-1}), F is the Faraday's constant (96 500 C mol^{-1}) and n_e is the theoretical (maximal) number of electrons released per BH_4^- species ($n_e = 8$).

Given a flow rate of 10 mL min^{-1} (0.167 cm^3 s^{-1}), the theoretical maximum current for 10 mM $NaBH_4$ is 1.29 A, corresponding to j_{geom} = 526 mA cm_{geom}^{-2}. The limiting current density values obtained at U_{cell} = 1 V are rather similar for the five anode configuration, between 43 and 48 mA cm_{geom}^{-2}, which is well below the expected theoretical value. Several reasons could account for the important difference observed between the theoretical value and the measured values of "limiting currents". Regarding the electrochemical process, the BOR kinetics might be very slow (especially on Pd sites), the catalytic surface might be poisoned by BOR intermediate species or blocked by H_2 bubbles; these two explanations would mean that the limiting current observed experimentally may not originate from a mass-transport limitation, but instead by a surface limitation (number of adsorbed intermediate species that can be formed/oxidized), as it was also observed for RDE thin-film (see section **III.4.1**); also, the BOR mechanism might not be an 8-electron process (this is very likely, especially on Pt electrodes, see the RDE results above presented in **Figure III.6.B**), and other reactions (such as HER, at low potential, and HOR, at higher potential) might occur in parallel to the main BOR process (but in a non-quantitative manner, resulting in H_2 losses – these will be asserted by H_2 escape measurements, see below). To be more specific regarding the last point, the present cell design may lead to imperfect electrooxidation of the H_2 produced via the hydrolysis of BH_4^-, because the membrane is not in close contact to the electrode: this configuration likely creates a fuel flow layer, thereby leading to more facile H_2 bubbles escape from the catalytic surface (in other words, should H_2 bubbles be formed, they are not forced to flow through the anode, hence a non-negligible H_2 escape, see below). Finally, cross-over of fuel and oxidant may be more pronounced in this configuration, again, because the reactants first "see" the membrane before being depleted in the anode and cathode.

From these observations, the percent fuel utilization (η) can also be calculated, simply by dividing the limiting current measured at U_{cell} = 1 V ($I_{max,1V}$) by the maximum theoretical current ($I_{max,\,theo}$):

$$\eta = \frac{I_{\mathrm{max,1V}}}{I_{\mathrm{max,theo}}} \times 100 \qquad \textbf{Equation III.2}$$

The value of the percent fuel utilization (see **Table III.4**) is 9% for almost all the anode configuration (it is 8% for the single Pd/C anode), which is well below the ideal 100%. The reasons mentioned above could account for this result, but the very low percent fuel utilization is most likely due to the fact that the fuel flow rate was not adapted to the current density in

these experiments. This is the strategy adopted in the case of PEMFC, where the hydrogen and oxygen stoichiometry values are adapted (via the gas flow rate) to the current density in order to optimize the FC efficiency [244,245]. In other words, the electrocatalysts were "saturated" with reactants in the present conditions, which, knowing the possible poisoning of the anode by $BH_{x,\,ads}$ species could be counter-productive. This strengthens the proposition that the "limiting currents" monitored experimentally could be due, at least to some extent, to adsorption-limitations at the anode, owing to a too small [catalytic sites]/[BH_4^-] ratio. Now, optimizing the cell efficiency (electrode thickness, membrane thickness, metal loading, electrode substrate, flow rate, etc.) would require non-negligible experimental effort, which was beyond the scope of the present study. In addition, enhancing the fuel utilization would mean using more catalyst at the anode, which we did not want to apply, to try to keep limiting anodes in the results.

Finally, for the graded anode configurations, the results highlight that (i) the nature of the electrocatalyst which is the closest to the fuel inlet does not influence the fuel cell performances (in terms of OCV, maximum power density and percent fuel utilization), and (ii) that the performances obtained with the mixed and graded anodes are not an average of the performances obtained on the single Pt/C and Pd/C anode; this result nicely confirms the existence of a positive synergy between the two materials.

Table III.4. OCV, power density, and percent fuel utilization values obtained from the H_2O_2-DBFCs with the different catalytic layer configurations for 10 and 100 mM $NaBH_4$ in 1 M NaOH.

CL configuration	OCV (V)		P_{max} (mW cm^{-2})		η (U_{cell} = 1 V) (%)	
	10 mM $NaBH_4$	100 mM $NaBH_4$	10 mM $NaBH_4$	100 mM $NaBH_4$	10 mM $NaBH_4$	100 mM $NaBH_4$
Single Pd/C	1.70 ± 0.01	1.72 ± 0.02	46 ± 3	210 ± 2	9	5
Single Pt/C	1.67 ± 0.03	1.67 ± 0.01	54 ± 2	275 ± 3	8	3
Mixed Pt/C + Pd/C	1.65 ± 0.03	1.63 ± 0.02	54 ± 3	168 ± 2	9	3
Graded Pt/C|Pd/C	1.67 ± 0.02	1.67 ± 0.01	55 ± 2	258 ± 2	9	5
Graded Pd/C|Pt/C	1.69 ± 0.01	1.67 ± 0.02	56 ± 1	260 ± 4	9	5

- **H_2O_2-DBFC performances analysis for 100 mM $NaBH_4$**

When the fuel concentration is increased to 100 mM, the trend of the polarization curves (see **Figure III.9.B.D**) is different from the one observed for low $NaBH_4$ concentration: the polarization curves obtained with the single Pt/C and the graded anodes are rather similar even if the single Pt/C anode slightly outperforms (in terms of current densities) the graded electrodes. The polarization curves obtained on the single Pd/C and the mixed anodes exhibit lower current densities. This possibly originates from an apparent different BOR mechanism, since the overall polarization curve shape differs from the ones obtained with single Pt/C anode and the graded anodes. In addition, the mixed anode outperforms the single Pd/C anode, but only when U_{cell} > 1.1 V. It is interesting to notice that the OCV values (see **Table III.4**) are overall identical to the ones obtained for low $NaBH_4$ concentration. Higher OCV values could have been expected, as it was observed in the previous chapter that the onset potential shifts towards negative values when the $NaBH_4$ concentration increases from 5 to 500 mM $NaBH_4$ for Pd-containing electrocatalysts. This indicates that parameters not accounted for in RDE may be at stake in DBFC configuration; a likely reason for the lower-than-expected OCV is the reactant cross-over through the Nafion membrane (both of H_2O_2 and of BH_4^-, this cross-over provoking mixed potentials at the two electrodes, because none of the electrocatalysts used are selective to their respective reactants).

In addition, the overall shapes of the polarization curves are different from the ones obtained for low electrolyte concentration: no clear limiting current densities are observed, but a change of electrochemical process seems to operate when U_{cell} = 0.5 – 0.6 V. The highest maximum power densities are obtained with the single Pt/C anode and the graded anodes: 275 and 260 mW cm^{-2} are measured, respectively. These performances are quite good given the rather low fuel concentration (100 mM $NaBH_4$ in 1 M NaOH), the moderate metal loading of the anodes (≈ 0.3 mg_{metal} cm_{geom}^{-2}) and the low temperature of operation (T ≈ 25°C) in comparison to the existing literature [45,87,121,246–257]. For all anode configurations, the maximum power density value is obtained in the cell voltage range 0.9 < U_{cell} < 1 V.

In a similar manner than what was done for low electrolyte concentration, the theoretical maximum current that could be reached in the conditions of the study was calculated using **Equation III.1:** it is 12.9 A, corresponding to j_{geom} ≈ 5300 mA cm_{geom}^{-2}. The current density values obtained for the five catalytic designs at U_{cell} = 1 V are between 160 and 275 mA cm_{geom}^{-2}, which is, again, well below the theoretical value. Even at lower cell voltage, the current density fails to exceed 500 mA cm_{geom}^{-2}. The reasons that could rationalize this result are identical to the ones

mentioned above (for the low $NaBH_4$ concentration); in addition, the low ratio [catalytic sites]/[BH_4^-] could also account for this result. In these conditions, the percent fuel utilization, calculated for U_{cell} = 1 V using **Equation III.2**, is 5% for the graded anodes and the single Pd/C anode, and it is 3% for the mixed anode and the single Pt/C anode, again highlighting the necessity to optimize the fuel flow rate to the current density values if one wants to target higher fuel/cell efficiency, and also to heighten the catalytic loading in the anode.

Finally, regarding the influence of mixing and grading the electrocatalysts within the anode, the results indicate that: (i) for the graded anodes, the nature of the electrocatalyst located at the fuel inlet does not affect the overall fuel cell performances for such high $NaBH_4$ concentration; and (ii) the performances obtained with the mixed and graded anodes are, still in these conditions, not an average of the performances obtained on the single Pt/C and Pd/C anodes. Of course, these conclusions are likely to depend on the chosen experimental parameters (*e.g.* cell temperature, ratio [catalytic sites]/[BH_4^-], etc.), and studying these effects should be the scope of forthcoming studies.

III.4.2.2 H_2 escape measurements

The H_2O_2-DBFCs performances were further analyzed with gaseous H_2 escape (HE) measurements. HE is defined as the difference between the generated hydrogen (via the chemical heterogeneous hydrolysis of BH_4^- and BOR intermediates or of the electrochemical reduction of water at low anode potential) and the consumed hydrogen (via its electrooxidation on the anodic electrocatalyst). As mentioned in **CHAPTER I**, hydrogen generation is one of the main impediment to the development of DBFC. Indeed, it can reduce the faradaic efficiency if the hydrogen generated within the anodic compartment is not electrooxidized in a quantitative manner, and the gas bubbles can also block the channel flow fields. Thus, HE measurements are essential to obtain more insights into the BOR mechanism and explain fuel cell performances. **Figure III.10** shows the rate of HE measured at each current density for each catalytic layer configuration for low (**Figure III.10.C**) and high (**Figure III.10.D**) electrolyte concentrations. For comparison purposes, the polarization curves are also displayed in **Figure III.10.A.B.**

- **HE analysis for 10 mM $NaBH_4$**

For low $NaBH_4$ concentration, all Pt-containing anodes exhibit similar HE trends, each starting with a relatively high HE value when U_{cell} = OCV (HE ≈ 8 µL s^{-1}). As U_{cell} decreases, the HE rapidly decreases, approaching 0 µL s^{-1} between 30 and 45 mA cm_{geom}^{-2} (corresponding to U_{cell} = 1.5 and 1.3 V respectively). The single Pd/C anode exhibits the lowest HE at the OCV, with only 1.8 µL s^{-1},

which is *ca*. 4-fold lower than the Pt-containing anodes. As U_{cell} decreases, the single Pd/C anode exhibits a gradual HE decrease, which ceases at the comparable current densities but lower U_{cell} than the Pt-containing anodes (*ca*. 1.2 V). For the single Pt/C and Pd/C anodes, the amount of HE increases again for high current densities values, after reaching zero. Overall, the results indicate that in these conditions, the number of active sites available for the different electrochemical processes, and the HOR specifically, enables to electrooxidize quite efficiently the H_2 produced by the hydrolysis/catalytic decomposition of BH_4^-, leading to minimal HE.

These trends are in overall agreement with recent differential electrochemical mass spectrometry (DEMS) measurements obtained for Pt [55] and Pd [105] electrodes for low $NaBH_4$ concentration (5 mM). Briefly, it was reported that for such $NaBH_4$ concentration, when the electrode potential is in the range $0 < E < 0.3$ V *vs*. RHE, the equivalent HER current starts from a high value and decreases on Pt electrodes (indicating that H_2 is electrooxidized in this potential range), while H_2 escapes from Pd electrodes; when $0.3 < E < 0.8$ V *vs*. RHE, no H_2 is detected on Pt electrodes and H_2 is electrooxidized on Pd electrodes; finally, when $E > 0.8$ V *vs*. RHE, H_2 escapes both for Pt and Pd electrodes, owing to the inactivity of Pt and Pd oxides towards the HOR, and the non-negligible H_2 production by BH_4^- decomposition in this potential region [54,105].

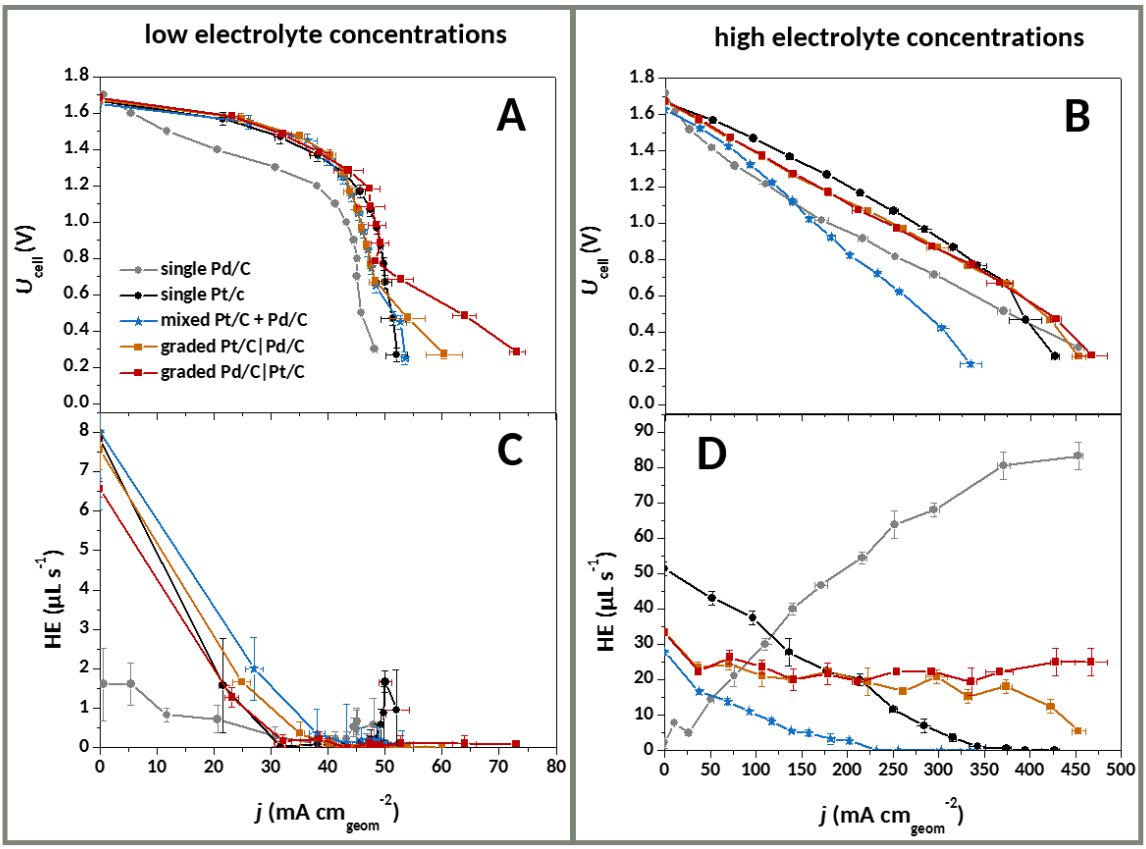

Figure III.10. H_2O_2-DBFC performances obtained on the different anodic catalytic layer configurations studied in this work; (A, B) polarization curves and (C, D) hydrogen escape (HE) obtained for (A, C) 10 mM $NaBH_4$ + 1 M NaOH and 40 mM H_2O_2 + 1 M H_2SO_4 and (B, D) 100 mM $NaBH_4$ + 1 M NaOH and 400 mM H_2O_2 + 1 M H_2SO_4 at room temperature.

- **HE analysis for 100 mM $NaBH_4$**

For high $NaBH_4$ concentration, the HE trends is more distinct between each anode configuration. The single Pt/C and the mixed anodes show a similar HE trend as with low $NaBH_4$ concentration, where HE decreases with increasing current densities. However, the decrease is more gradual and can be attributed to a lower [catalytic sites]/[BH_4^-] ratio. The mixed anode exhibits approximately half the HE of the single Pt/C anode at the OCV (28 µL s^{-1} for the mixed anode *vs.* 51 µL s^{-1} for the single Pt/C anode) and reaches zero HE at lower current densities than the single Pt/C anode (230 mA cm^{-2} for the mixed anode *vs.* 400 mA cm^{-2} for the single Pt/C anode). These results illustrate that the addition of Pd/C to Pt/C, as composite material, enables to reduce significantly the H_2 production and the subsequent H_2 escape (in comparison to Pt/C). Pt being more active than Pd to electrooxidize the produced H_2 [95], mixing electrocatalysts is beneficial; unfortunately, mixing Pt/C and Pd/C also non-negligibly alters the DBFC performances (see **Figure III.10.B**). The graded anodes display relatively constant HE for current densities between

50 and 300 mA cm^{-2} (*ca*. 20 µL s^{-1}). Above 300 mA cm^{-2}, the HE decreases at the graded Pt/C|Pd/C anode, while a small increase is observed with the graded Pd/C|Pt/C anode. The single Pd/C anode shows the opposite behavior from the other anodes and from low $NaBH_4$ concentration. The HE escape at the OCV is low (2 µL s^{-1}) and increases to *ca*. 80 µL s^{-1} when the current density exceeds 400 mA cm^{-2} (which corresponds to U_{cell} ≈ 0.4 V). This effect was also observed by Braesch *et al*. [105] and was rationalized by the inability of Pd to completely electrooxidize H_2 coupled to its larger $BH_{x,ads}$ poisoning at large borohydride concentration. From that prospect, addition of Pt/C in a Pd/C-based electrode is beneficial.

DEMS measurements performed on Pt [55] and Pd [105] electrodes in conditions close to the ones used in this study (50 mM $NaBH_4$ concentration) are also rather in line with the present HE measurements. The authors reported that for 0 < *E* < 0.9 – 1 V *vs*. RHE, H_2 was generated and electrooxidized on Pt electrodes but lost on Pd electrodes; when *E* > 0.9 – 1 V *vs*. RHE, H_2 was not detected on Pt electrodes and electrooxidized on Pd electrodes.

III.4.2.3 Discussion

In the light of all the different measurements performed, a further analysis and discussion of the results obtained is proposed hereafter.

- **10 mM $NaBH_4$**

When the fuel concentration is low, both RDE and FC measurements indicate that the overall apparent BOR mechanism is controlled by the Pt/C electrocatalyst for all the Pt/C-containing electrodes: similar voltammograms or polarization curves, as well as similar OCV, maximum power densities and HE feature are obtained. However, some differences can be noticed between the RDE measurements and the H_2O_2-DBFC measurements. In RDE configuration, the graded Pt/C|Pd/C electrode outperforms the graded Pd/C|Pt/C one, especially at low electrode potential (0 and 0.2 V *vs*. RHE, corresponding to approximate cell voltages of 1.65 and 1.45 V, respectively). On the contrary, in FC configuration, both graded anodes have similar performances at most cell voltages. These differences could most probably come from the different electrode architecture and cell design between the two configurations. In RDE configuration, the graded electrodes are composed of two electrocatalyst layers, graded one on top of the other, while in FC configuration, the electrodes are composed of three catalytic layers, graded along the flow field from fuel inlet to fuel outlet. Thus, in the former configuration, the "on top" electrocatalyst is closer to the convection boundary layer than the one which is close to the glassy-carbon support; alternatively, in the latter configuration, each

electrocatalyst/catalytic layer has similar boundary layer thickness, but may be exposed to different concentrations of ions in the fuel, depending on which type of catalyst is upstream. Also, each catalytic layer in the H_2O_2-DBFC is on one wall of a flow field, and fed with large excess of reactant, leading some reactants to flow through the cell without interacting with the electrocatalysts. Additionally, the RDE electrodes have more chance to be kinetically controlled (because the loading of the catalyst is smaller), whereas the H_2O_2-DBFCs are more likely mass-transport limited, at least at the lower concentrations and in the region close to the electrode, according to the cell design (see **Figure III.4**), even though we have noted above, that surface limitation (*e.g.* poisoning by stable adsorbates) could also be at stake. One can also not rule out that the cathode can be, to some extent, limiting the H_2O_2-DBFC performance.

Finally, for low fuel concentration, the RDE measurements indicate that mixing and grading electrocatalysts enable to enhance the BOR kinetics and activity in comparison to single Pt/C and single Pd/C electrode. In FC configuration, mixing and grading the electrocatalysts leads to better performances in comparison to single Pd/C anode, except for the HE, which is still lower with the single Pd/C anode.

- **100 mM $NaBH_4$**

When moving to higher fuel concentration, more variation in performances between each H_2O_2-DBFC with Pt-containing anodes is witnessed. Specifically, the changes in polarization curves shapes and the HE trends indicate that Pd/C plays a more substantial role in the H_2O_2-DBFCs performances, especially for the mixed anodes. To understand the role of Pd in the overall cell performances, several factors including the production and escape of gaseous H_2 need to be considered.

The results displayed in **Figure III.10.C.D** show minimal HE on the single Pd/C anode prior to current flow at both $NaBH_4$ concentrations and significant increases when current is flowing at high $NaBH_4$ concentration. It is assumed that at the OCV, little H_2 is produced via the hydrolysis of BH_4^- (and HER) at the Pd surface (**Equation III.3**); then, when a load is applied, more H_2 can be produced via the hydrolysis of BH_3OH^- (**Equation III.4**) and the partial dissociative adsorption of BH_4^- into BH_3-like intermediates could proceed (**Equation III.5**Erreur ! Source du renvoi introuvable.), followed by the dehydrogenation of $BH_{3,\,ads}$ into $BH_{ads} + H_2$ (**Equation III.6**).

$$BH_4^- + H_2O \rightarrow BH_3OH^- + H_2 \qquad \textbf{Equation III.3}$$

$$BH_3OH^- + H_2O \rightarrow BO_2^- + 3\,H_2 \qquad \textbf{Equation III.4}$$

$$BH_4^- + OH^- \rightarrow BH_{3,ads} + H_2O + 2\,e^- \quad \textbf{Equation III.5}$$

$$BH_{3,ads} \rightarrow BH_{ads} + H_2 \quad \textbf{Equation III.6}$$

The poisoning of Pd surface by the adsorbate BOR intermediate species and a slower HOR kinetics on Pd than Pt in alkaline media [95] could prevent the complete oxidation of H_2, leading to an increase in HE as the cell voltage decreases, in comparison to Pt-containing anodes. Thus, we can conclude that Pd/C is not an effective electrocatalyst for a full 8-electron BOR when used alone, in particular at high $NaBH_4$ concentration, in line with the previous study of Olu *et al.* [70].

A significant difference in HE is observed between H_2O_2-DBFCs with Pt-containing anodes in comparison to singe Pd/C anode. As discussed above, HE caused by hydrolysis of BH_4^- (and/or HER) at the OCV at the single Pd/C anode is minimal in comparison to single Pt/C anodes. Therefore, it can be concluded that most H_2 production and subsequent escape are the result of BH_4^- hydrolysis (and/or HER) at the Pt surface in the mixed and graded anodes at high cell voltage; as the cell voltage decreases, the source of HE might shift from H_2 production at Pt surface (mostly by HER) to H_2 production at Pd surface (mostly by BH_4^- decomposition). In addition, one can observe from **Figure III.10.D** that HE decreases on the graded Pt/C|Pd/C anode when the current density exceeds 350 mA cm_{geom}^{-2} (corresponding to *ca*. 0.7 V), which is not the case with the graded Pd/C|Pt/C anode. This result indicates that there is a benefit to put Pd/C at the fuel outlet since it is enable to electrooxidize gaseous H_2 at high potential (*i.e*. low cell voltage) in these conditions, while Pt/C cannot. It is also likely that Pt surface is more subject to (i) adverse oxides formation and (ii) severe poisoning at such concentration, in comparison to Pd, thereby leading to more HE when Pt/C is located at the fuel outlet.

The question remains why the H_2O_2-DBFC with the mixed anode perform so poorly in terms of current density and maximum power density in comparison to the other anodes, whereas the HE is significantly lower with this anode. The low current density in addition to the low HE may suggest more poisoning by adsorbate species both on Pt and Pd surface in this configuration, but the authors fall short to understand why.

Finally, for high fuel concentration, the main advantage of the graded and mixed anodes is to decrease the HE; but surprisingly, the single Pt/C anode still leads to the highest current density and maximum power density, demonstrating, again, that if Pt is winner in generating H_2, it is also the best material to valorize it fast.

III.5 Conclusions

In this chapter, the impact of five different catalytic layer design on the BOR kinetics and activity was studied in RDE configuration and in H_2O_2-DBFC configuration, for low (10 mM) and high (100 mM) fuel concentration, at room temperature. Specifically, Pt/C and Pd/C electrocatalysts were used as single (Pt/C or Pd/C), mixed (Pt/C + Pd/C) and graded (Pt/C to Pd/C or Pd/C to Pt/C) electrodes.

The results reveal that the main advantage of mixing and grading the electrocatalysts is the reduction of the rate of H_2 escape, especially at high $NaBH_4$ concentration and high cell voltage, in comparison to the use of a single Pt/C anode. This indicates that the presence of Pd/C in an in-plane-graded configuration with Pt/C and when mixed with Pt/C is beneficial to the overall performances of a H_2O_2-DBFC. Besides, the OCV and maximum power density values obtained with the graded anodes are rather similar to the ones obtained with the single Pt/C anode.

The modifications of the overall BOR mechanism occurring in each catalytic layer design are still unclear and would require a significant amount of work to be understood; however, some assumptions were suggested. Besides, these modifications may change when the cell temperature is increased and further research into the effects of temperature using graded anodes would be necessary to uncover the scientific truth.

Finally, the advantage of graded electrodes design highlighted in this study offers future prospects for the combination of other electrocatalysts, that could provide superior DBFC performances and warrant larger cell efficiency.

Now, if the research of the best anode for the DBFC, via the combination of electrocatalyst(s) in an appropriate electrode structure is often focused on the BOR activity and efficiency, the stability in operation of the latter is a major issue: the last part of this manuscript is dedicated to this issue and studies the degradation mechanism of carbon-supported electrocatalysts in liquid alkaline media.

Chapter IV

Degradation mechanism of carbon-supported PGM electrocatalysts in alkaline media

IV.1 Motivations of the study

The recent work of Zadick and coworkers [176] revealed that state-of-the-art carbon-supported platinum electrocatalysts suffer extensive degradation during an accelerated stress test (AST), which consists of 150 cyclic voltammetry (CV) in the potential range 0.1 < *E* < 1.23 V *vs.* RHE in 0.1 M NaOH at *T* = 25°C. The authors reported that the electrochemical surface area (ECSA) decreased by *ca.* 60% after the AST. Surprisingly, this intense degradation was neither connected to major dissolution of the nanoparticles (NPs), nor to corrosion of their carbon substrate (no features of such processes were monitored by Raman spectroscopy and X-Ray photoelectron spectroscopy). It was thus postulated that the degradation occurs mostly via the detachment of the Pt NPs, likely via the destruction of the anchoring point between the Pt NPs and the carbon support.

According to the work of Ross *et al.* [148–151], who revealed that carbonates (or even gaseous CO_2) could form during carbon black degradation in alkaline media, it was believed that the destruction of the anchoring point between the Pt NPs and the carbon substrate could result from the formation of solid carbonates at the vicinity of the Pt|C interface. Precisely, it was suspected that the Pt|C interface was gradually and irreversibly destroyed by local and very superficial carbon corrosion catalyzed by the metal NPs, resulting in local CO_2 formation, which transforms into solid carbonates (in alkaline environment) between the metal NPs and their support, thereby leading to the detachment of the Pt NPs. Such a process is simply depicted in **Figure IV.1**, where the different steps could be: (i) at low potential, oxygen-containing surface groups form on the carbon support, (ii) at higher potential, OH_{ads} spontaneously form on the Pt surface and react with the oxygen-containing surface group on the carbon support to form CO_2, (iii) CO_2 is converted into solid carbonates at the Pt|C interface. The process would be repeated along the 150 CVs leading to the accumulation and growth of solid carbonates at the interface between the Pt NPs and their carbon support, which would lead to their detachment. This mechanism was however not supported by experimental evidences, so several questions remained unanswered:

- Is the degradation mechanism linked to a CO-stripping-like process at the Pt NPs surface?
- Is the extent Pt NPs detachment reduced if the solid carbonates are more soluble?
- Can the carbonates be experimentally tracked?
- Is the degradation mechanism really a Pt-assisted local corrosion of the carbon?

- Is the degradation mechanism linked to the ability of the electrocatalyst to electrooxidize CO-containing species into CO_2?

To answer these questions and gain further insights into the degradation mechanism of Pt/C in alkaline media, several experiments were set up, including the modification of the benchmark AST protocol used by Zadick and coworkers: the influence of the nature of the alkaline electrolyte was notably studied. In addition, *in situ* Fourier transform infrared (FTIR) spectroscopy was used to track the carbonates species in the course of the aging of the electrocatalysts. Besides, in a tentative to extend this mechanism to other carbon-supported platinum group metal (PGM) electrocatalysts, the degradation of PtRu/C and Pd/C was also surveyed.

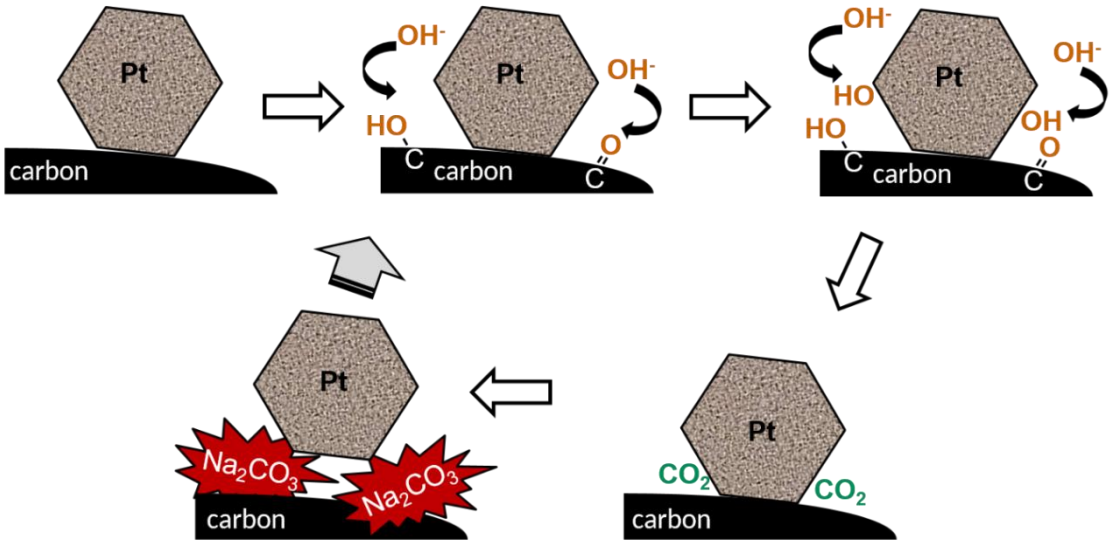

Figure IV.1. Illustration of the tentative degradation mechanism of Pt/C occurring during 150 CV in the potential range 0.1 < *E* < 1.23 V *vs.* RHE at v = 100 mV s^{-1} in 0.1 M NaOH, *T* = 25°C.

Most of the results presented in this chapter were published in the following papers:

C. Lafforgue, M. Chatenet, L. Dubau, D. Dekel, Accelerated stress test of Pt/C nanoparticles in an interface with an anion-exchange membrane – an identical-location transmission electron microscopy study, ACS Catal. 8 (2018) 1278-1286.

Contribution: C.L. performed the AST in liquid electrolyte, analyzed the data, discussed the results and approved the final version of the manuscript.

C. Lafforgue, A. Zadick, L. Dubau, F. Maillard, M. Chatenet, Selected review of the degradation of Pt and Pd-based carbon-supported electrocatalysts for alkaline fuel cells: towards mechanisms of degradation, Fuel Cells. 18 (2018) 229-238.

Contribution: C.L. performed the FTIR experiments and the AST conducted in several alkaline electrolytes, analyzed the data, discussed the results and approved the final version of the manuscript.

C. Lafforgue, F. Maillard, V. Martin, L. Dubau, M. Chatenet, Degradation of carbon-supported platinum-group-metal electrocatalysts in alkaline media studied by *in situ* Fourier transform infrared spectroscopy and identical-location transmission electron microscopy, ACS Catal. 9 (2019) 5613-5622.

Contribution: C.L. performed the electrochemical experiments, analyzed the data, discussed the results and wrote the first version of the manuscript.

IV.1 Experimental details

IV.1.1 Electrocatalysts

The carbon-supported electrocatalysts were purchased from E-TEK or Premetek and used as received. They are all supported on Vulcan XC72 carbon black and are referred to as 10, 40 or 80 wt.% Pt/C, 10 or 40 wt.% PtRu/C and 10 or 40 wt.% Pd/C depending on the metal weight percent.

IV.1.2 Physical and chemical characterizations

The electrocatalyst morphology of all these materials was analyzed by TEM and/or STEM associated with X-EDS elemental maps. **Annex 2.A** provides experimental details for these measurements.

XPS patterns were acquired to study the evolution of the oxygen content during the AST. They were analyzed by dividing the peak areas of the O1s and the C1s signal (without the contribution of Nafion®-related envelopes), after proper background subtraction by their respective atomic sensitivity factors:

$$\left(\frac{\mathrm{O1s}}{\mathrm{C1s}}\right) = \frac{\mathrm{I_{O1s}}}{0.63} \times \frac{0.205}{\mathrm{I_{C1s}}}$$

Annex 2.C provides experimental details for these measurements.

IV.1.3 Electrochemical measurements

All the electrochemical measurements were performed using a Bio-Logic® potentiostat. The glassware and plastic accessories used for the experiments were soaked in Caro's acid (1-1 vol.% H_2O_2 (30 wt.%)-H_2SO_4 (> 95 wt.%)) overnight to eliminate organic and metallic pollution and thoroughly rinsed and boiled with ultrapure water (18.2 MΩ cm, < 3 ppb total organic carbon, Millipore Elix + Gradient, Millipore) prior to use.

IV.1.3.1 Accelerated stress test (AST)

AST were performed in a four-electrode electrochemical cell: (i) the reference electrode was a freshly-prepared RHE used during maximum 2 hours; (ii) the counter electrode was a glassy-carbon plate, to avoid possible pollution of the working electrode from its dissolution [195]; (iii) the fourth-electrode was a gold wire and (iv) the working electrode was made of a 10 µL-deposition of electrocatalyst suspension on a 5 mm-glassy-carbon RDE, to yield a loading of 20 $\mu g_{metal}\ cm_{geom}^{-2}$. The electrocatalyst suspension contains 10 mg of electrocatalyst (10 wt.% Pt/C, 10 wt.% PtRu/C or 10 wt.% Pd/C), 1755 µL of ultrapure water, 61 µL of 5 wt.% Nafion® solution and 730 µL of isopropanol (IPA). This drop was then dried with a heat gun while the electrode was rotated. Fresh electrolyte solutions (0.1 M MOH, M = Li, Na, K, Cs) were prepared using LiOH (Aldrich), NaOH (Suprapur, Merck), KOH (Alfa Aesar), CsOH (Aldrich) and ultrapure water.

A second cell was required to perform characterization step and CO_{ads}-stripping measurements in acidic electrolyte before and after the AST conducted in alkaline electrolyte. The corresponding four-electrode electrochemical cell contained (i) a freshly-prepared RHE used during maximum 2 hours; (ii) a platinum mesh counter electrode; (iii) a platinum wire as the fourth-electrode and (iv) each of the working electrodes that were used for the AST.

The overall AST protocol used (the same used by Zadick *et al*. [176]) is detailed hereafter:

- The electrode is first introduced in the acidic cell (in Ar-saturated electrolyte) where it undergoes the following steps:
  a) 15 CV recorded in the potential range from *E* = 0.1 to 1.23 V *vs*. RHE at a potential sweep rate v = 50 mV s^{-1};
  b) CO-bubbling during 6 min followed by Ar-bubbling during 39 min while the electrode potential is maintained at *E* = 0.1 V *vs*. RHE;
  c) 3 CV in the potential range from *E* = 0.1 to 1.23 V *vs*. RHE at v = 20 mV s^{-1};

- The electrode is removed from the “acidic cell”, thoroughly rinsed with ultrapure water and introduced in the “alkaline cell” (in Ar-saturated electrolyte) where the AST is performed as follow:

  d) 150 CV recorded in the potential range from *E* = 0.1 to 1.23 V *vs*. RHE at v = 100 mV s^{-1};

- The electrode is removed from the “alkaline cell”, thoroughly rinsed with ultrapure water and put back in the “acidic cell” (in Ar-saturated electrolyte) where step a) to c) are performed again.

The CO_{ads}-stripping CV enabled to estimate the ECSA loss during the AST assuming that the charge density associated with the adsorption of one monolayer of CO_{ads} is 420 µC cm_{Pt}^{-2}. Zadick et *al*. verified that the characterization had very little impact for Pt/C electrocatalyst, but a little more for Pd/C electrocatalyst [176,177].

AST were also performed using a specific TEM grid as working electrode in order to study the evolution of the electrocatalyst morphology after the AST via the identical-location transmission electron microscopy (IL-TEM) technique. This technique was introduced by Mayrhofer *et al*. in 2008 [258]; it enables to observe the electrocatalysts on identical and well-identified zones before and after an electrochemical treatment. To that goal, a drop of an electrocatalyst suspension was deposited onto a gold TEM grid baring a Lacey-carbon membrane, which was used as the working electrode in dedicated experiments. In practice, the gold TEM grid was maintained between two carbon plates, themselves pressed together thanks to a crocodile clip, which serves as current collector. In this configuration, only step d) is performed, the grid being maintained in a hanging-meniscus configuration.

IV.1.3.2 *In situ* FTIR spectroscopy measurements

The *in situ* FTIR measurements were performed using a Bruker Vertex 70V spectrometer equipped with a liquid-N_2-cooled MCT (mercury-cadmium-telluride) detector. The spectra were collected in external reflection using *p*-polarized light, each single-beam spectrum being obtained by co-adding 256 (or 512) interferograms acquired at 4 cm^{-1} spectral resolution with an interferometer frequency of 40 kHz and then Fourier transformed. More details about this technique are given in **Annex 2.D**.

A picture of the global set up is displayed in **Figure IV.2.A**. A homemade three-electrode electrochemical cell (**Figure IV.2.B**) was used and a CaF_2 prism beveled at 60° constituted the bottom of the cell (**Figure IV.2.C**): (i) the reference electrode was a freshly-prepared RHE used

during maximum 2 hours; (ii) the counter electrode was a platinum mesh and (iii) the working electrode was made of 8 µL-deposition of electrocatalyst suspension on a 5-cm-gold electrode (**Figure IV.2.D**); the drop was then dried in an oven at T = 110°C. The same quantity of carbon was deposited on the gold electrode whatever the initial metal weight fraction, so as to compare thin-film electrodes of the same thickness. The electrocatalysts suspensions compositions are given in **Table IV.1**. The electrolyte (0.1 M NaOH) was prepared using NaOH-H_2O crystals (Suprapur, Merck) dissolved in ultrapure water.

Two AST electrochemical protocols coupled with *in situ* FTIR measurements were used:

- **Cycling-protocol**

a) Ar-bubbling during 15 min;
b) 5 CV were recorded in the potential range from E = 0.1 to 1.23 V *vs.* RHE at v = 50 mV s^{-1} in a hanging-meniscus configuration;
c) the working electrode was pressed against the CaF_2 prism (thin layer configuration), its potential being maintained at E = OCP. When an electrode position with an optimum reflectivity was obtained, 5 spectra were registered;
d) 150 CV were recorded in the potential range from E = 0.1 to 1.23 V *vs.* RHE at v = 20 mV s^{-1}; 256 interferograms were collected every *ca.* 1 min.

The data were plotted using relative reflectivity R/R_{OCV}, where R and R_{OCV} are the reflectivity obtained during the acquisition and at the OCV, respectively. With this methodology, positive-going bands correspond to species consumption and negative-going bands correspond to species production.

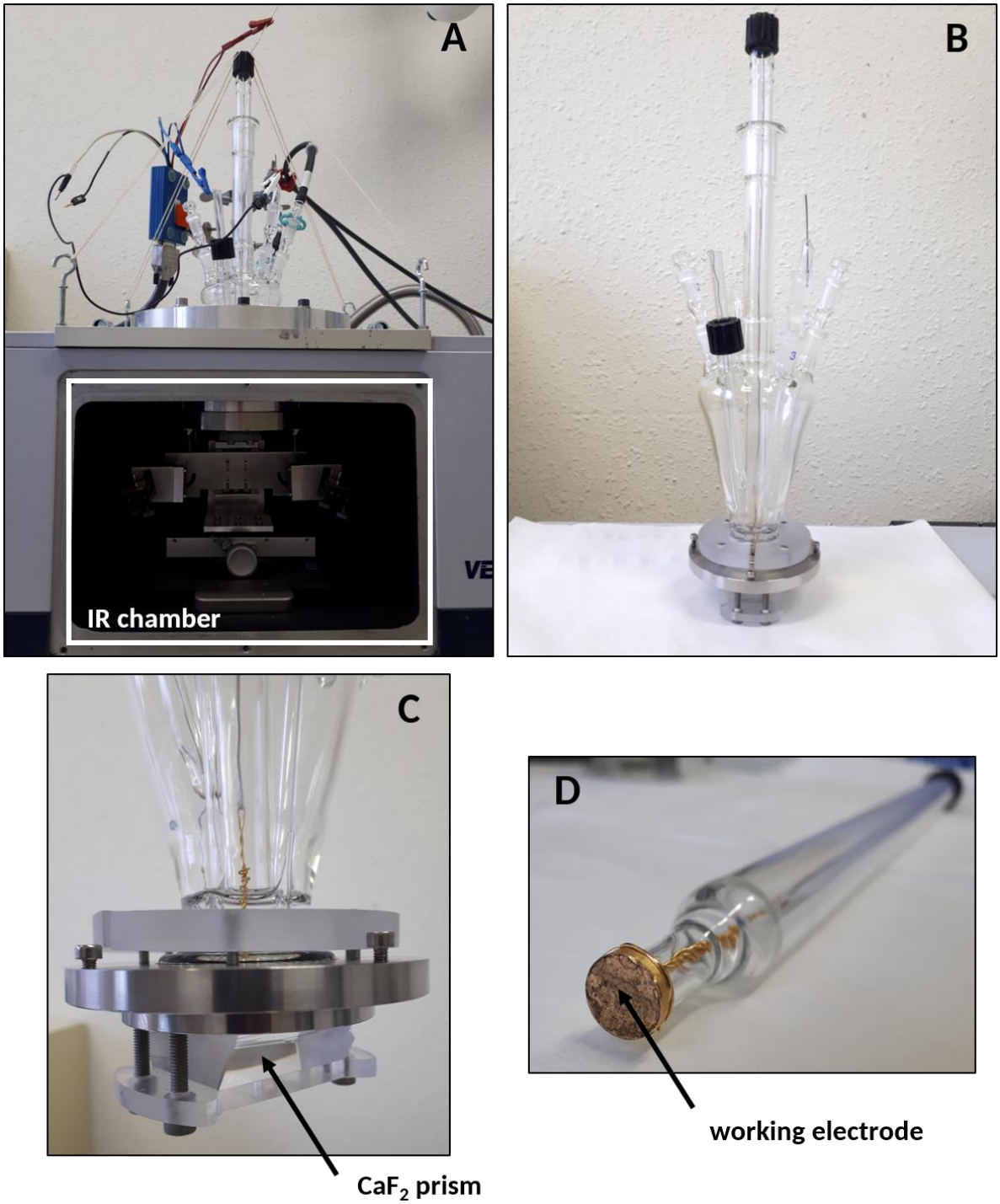

Figure IV.2. Pictures of the *in situ* FTIR measurements setup and materials: (A) electrochemical cell introduced in the spectrometer; (B) electrochemical cell; (C) CaF_2 prism pressed against the bottom of the cell, (D) working electrode.

Table IV.1. Composition of the electrocatalysts suspensions used for the FTIR measurements.

Electrocatalyst (commercial)	Electrocatalyst amount (mg)	H_2O (µL)	Nafion® 5 wt.% (µL)	IPA (µL)
10 wt.% Pt/C E-TEK	10	5770	18.3	2000
40 wt.% Pt/C E-TEK	10	3590	41.2	1600
80 wt.% Pt/C E-TEK	10	1405	1.37	330
40 wt.% PtRu/C E-TEK	10	3590	41.2	1600
40 wt.% Pd/C Premetek	10	3590	41.2	1600

- **Stepwise-protocol**

a) Ar-bubbling during 15 min;
b) 5 CV were recorded in the potential range from E = 0.1 to 1.23 V *vs.* RHE at v = 50 mV s^{-1} in a hanging-meniscus configuration;
c) the working electrode was pressed against the CaF_2 prism (thin layer configuration), its potential being maintained at E = 0.1 V *vs.* RHE. When an electrode position with an optimum reflectivity was obtained, 5 spectra were monitored;
d) a succession of 100 mV steps increased the working electrode potential up to E = 1.2 V *vs.* RHE, an intermediate step to the low (control) potential E = 0.1 V *vs.* RHE being applied between each potential step; 512 interferograms were collected at each step.

The data were plotted using relative reflectivity R_E/R_{ref}, where R_E and R_{ref} are the reflectivity obtained at the desired potential (E = 0.2, 0.3, …, 1.2 V *vs.* RHE) and the reference potential (mainly 0.1 V *vs.* RHE), respectively. With this methodology, positive-going bands correspond to species consumption and negative-going bands correspond to species production.

In situ FTIR CO_{ads}-stripping experiments were also performed. In that case, the working electrode was polycrystalline Pt. The electrolyte was purged with CO for 6 min, and then with Ar for 39 min. During this process, the working electrode was permanently pressed against the CaF_2 prism while keeping its potential at E = 0.1 V *vs.* RHE. Then, the same succession of potential steps as described above (stepwise protocol) was applied.

IV.2 Preliminary study

IV.2.1 Influence of the potential range

The influence of the potential range on the extent of degradation was firstly investigated in order to know if the degradation mechanism could be linked to a CO_{ads}-stripping-like process. To that goal, the main potential range (0.1 < *E* < 1.23 V *vs*. RHE) used in the "benchmark" AST protocol was divided into two ranges: a low-potential range (0.1 < *E* < 0.6 V *vs*. RHE) and a high-potential range (0.6 < *E* < 1.23 V *vs*. RHE). It is worth mentioning that the electrocatalyst used in the whole present study, *i.e.* a commercial 10 wt.% Pt/C from E-TEK, was different from the one used by Zadick *et al*. [176], who used a commercial 20 wt.% Pt/C electrocatalyst (from E-ETK). However, the morphology (particle size) of the two electrocatalysts was rather similar, and this study enabled to evaluate the impact of the platinum weight fraction on the Vulcan XC72 carbon at the exclusion of any major particle size effect.

The CO_{ads}-stripping obtained pre and post-AST in 0.1 M NaOH in the three different potential ranges ("full", "low" and "high") are displayed in **Figure IV.3**. As a reminder, the CO_{ads}-stripping CVs enable to give insights into the degradation mechanism, since this technique is highly sensitive to the electrocatalyst surface morphology (particle size, extent of agglomeration) [231,259]. As an example, the pre-peak located at *E* ≈ 0.7 V *vs*. RHE is due to agglomerated NPs [231].

When the AST is performed in the full-potential range, the results obtained are in line with the ones obtained by Zadick *et al*. with 20 wt.% Pt/C [176]: the extent of agglomeration is important (see the pre-peak located at *E* = 0.7 V *vs*. RHE on the red CV in **Figure IV.3**), and the ECSA decreases by 61% (Zadick *et al*. [176] reported *ca*. 57%). This demonstrates that the fate of Pt/C NPs is not linked to the initial metal weight fraction of the electrocatalyst. When the AST is performed in a reduced potential range, the ECSA decreases by 18% and 30%, for the low and high-potential range, respectively. In addition, one can notice that the extent of agglomeration is much less important in comparison to the case of the full potential range (see the pre-peak at *E* ≈ 0.7 V *vs*. RHE on the blue and green CV in comparison to the red one). Besides, according to the evolution of the shape of the main peak located at *ca*. 0.8 V *vs*. RHE, one can conclude that the AST performed in the low-potential range leads to the loss of the smaller NPs (highlighted by a decrease of the "peak trail" observed in the potential range from 0.85 to 1 V *vs*. RHE), while the AST conducted in the high-potential range leads to the loss of the "mean-size" NPs (*i.e*. the ones that constitute most of the initial population of NPs).

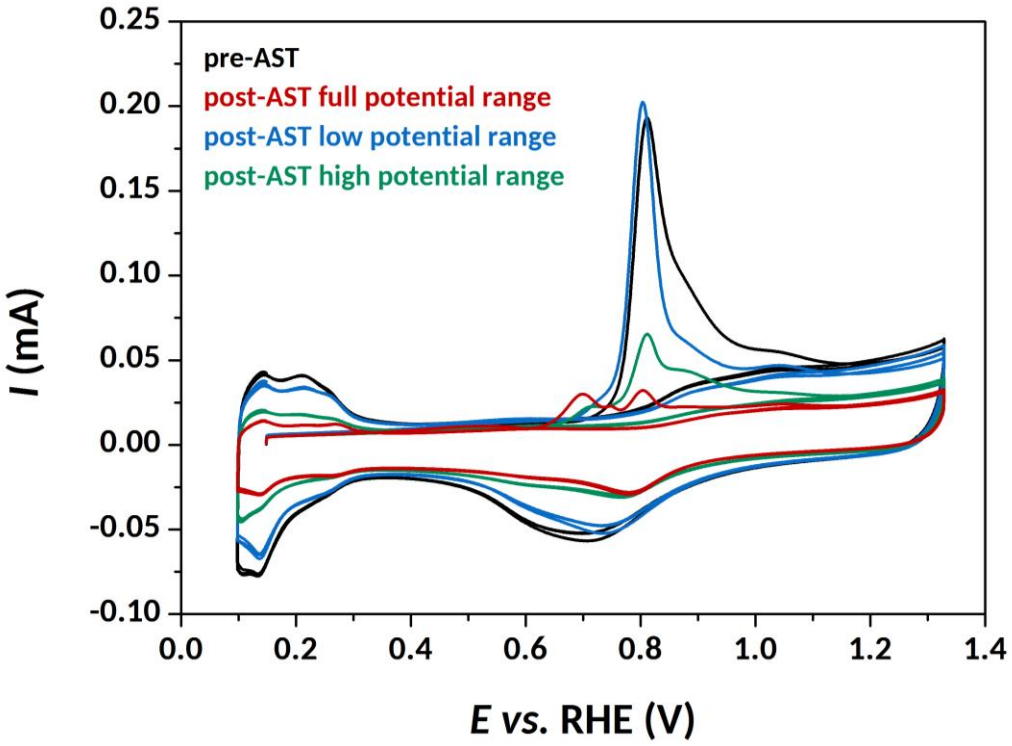

Figure IV.3. CO_{ads}-stripping voltammograms obtained on 10 wt.% Pt/C in 0.1 M H_2SO_4 at v = 20 mV s^{-1} pre and post-AST performed in several potential domains using the cycling-protocol at *T* = 25°C.

N.B.: for easier comparison purposes, the four CVs are plotted in the same figure; however, the CO_{ads}-stripping performed before each type of experiments can little differ from the one plotted in this figure (see **Figure A.6** *in* **Annex 4***); as a result, the loss of ECSA might seem incoherent with what it is visually observed in this figure.*

The evolution of the Pt/C morphology was further analyzed thanks to the IL-TEM micrographs obtained pre and post-AST in the three potential ranges (see **Figure IV.4**). As expected, the representative images obtained for the full-potential range-AST (**Figure IV.4.A.B**) reveal a similar trend as for the study of Zadick *et al*. [176]: the degradation occurs mostly by detachment of the Pt NPs from the carbon support (highlighted by the white crosses, used as non-comprehensive markers of the NP detachment). One could postulate that dissolution and/or redeposition are also possible in these conditions, but the evolution of the particle size distribution (PSD) after the AST (**Figure IV.4.C**) is not in agreement with such mechanism. Indeed, would the dissolution/redeposition mechanism prevail on the Pt NPs detachment, an increase in the Pt NPs size would be observed, which is not the case here.

When the AST is conducted in a reduced potential range, the corresponding representative IL-TEM micrographs of Pt/C pre and post-AST confirm the more moderate extent of degradation

in these conditions than in the full range. In the low-potential range, the degradation markers illustrate the main degradation mechanisms at stake during the potential cycling procedure: Ostwald ripening (dissolution/redeposition mechanism: small NPs have the inherent tendency to dissolve at the expense of larger ones into bigger NPs in order to reduce the high surface energy, confirming the loss of smaller NPs observed in the CO_{ads}-stripping in **Figure IV.3**) and detachment of Pt NPs from the carbon support do proceed (**Figure IV.4.D.E.F**), but in a much weaker manner than for the full-potential range. In the high-potential range, the loss of Pt NPs is nearly absent (**Figure IV.4.G.H**). The shape of some neighboring Pt NPs is nevertheless changing, but unlike for the case of the low-potential range, this is not following an agglomeration–coalescence mechanism (local Ostwald ripening). It rather consists of the separation of initially agglomerated Pt NPs (or the opposite), which signs the surface mobility of the Pt NPs on a carbon substrate which must be heavily functionalized (large presence of oxygen-containing surface group on carbon) in this high potential range.

These differences between the low and high-potential ranges of cycling can be understood in terms of difference of “oxidizing” conditions. In the low-potential range (where the Pt NPs are never completely oxidized), neighboring Pt NPs are more prone to coalescence, in a process that can be compared to that occurring in the gas phase under H_2: several studies [260–262] report the growth of Pt/C NPs in these conditions (recrystallization), together with a “reforming” of the carbon (formation of hydrocarbon species), which enables to explain why some NPs detach here. On the contrary, in the high-potential domain (where the Pt NPs are never completely reduced), recrystallization of Pt is not likely, but instead, Pt and Pt-oxides can assist carbon corrosion, in a process that resembles the thermal oxidation process of Pt/C in a neutral or oxidizing atmosphere [262]: in this scenario, Pt NPs would migrate at the functionalized carbon surface until they “self-stabilize” by forming agglomerate structures.

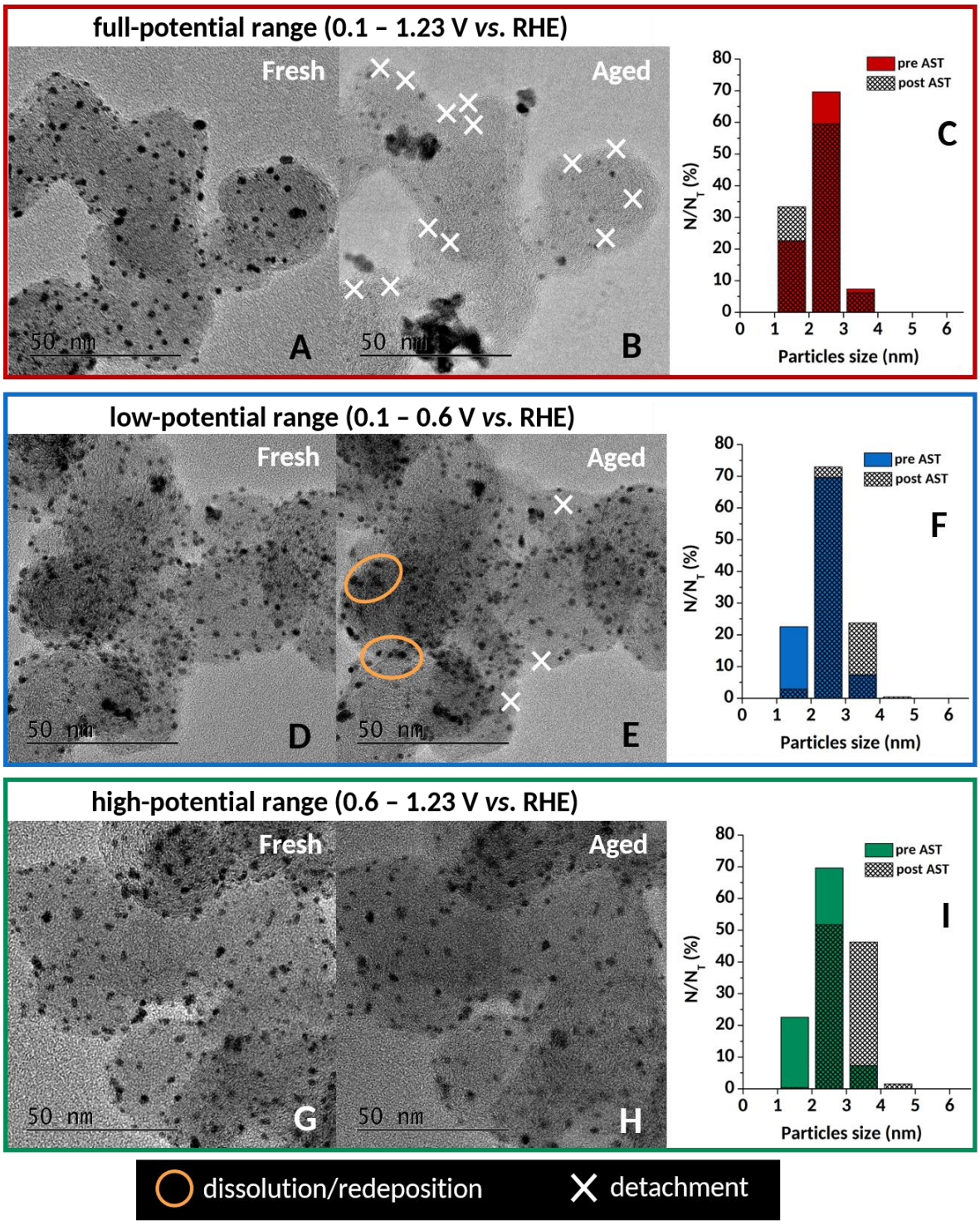

Figure IV.4. Representative IL-TEM micrographs (A, D, G) pre-AST and (B, E, H) post-AST on 10 wt.% Pt/C electrocatalyst in the full potential range (0.1 < *E* < 1.23 V *vs.* RHE, red), low potential range (0.1 < *E* < 0.6 V *vs.* RHE, blue) and high potential range (0.6 < *E* < 1.23 V *vs.* RHE, green) and (C, F, I) corresponding particle size distribution. The markers are not comprehensive but illustrate the main degradation mechanism at stake during the cycling procedure.

These results reveal that the positive and negative vertex potential values highly influence the extent of Pt/C degradation and the nature of the degradation mechanism. More precisely, they suggest that the detachment of the Pt NPs occurs mainly when the Pt NPs can assist the local corrosion of the carbon support, *i.e.* when oxygen-containing surface group of the carbon support form at low potential and can be electrooxidized at higher potential by the Pt NPs. To pursue the investigation, the influence of the alkali-metal cation of the electrolyte on the extent of degradation was investigated.

IV.2.2 Influence of the alkali-metal cation of the electrolyte

Because in the proposed scenario of loss of Pt NPs, the formation of solid carbonates is involved, it was decided to evaluate the influence of the alkali-cation of the electrolyte on the extent of degradation of the 10 wt.% Pt/C electrocatalyst; indeed, varying this cation enables to modulate the solubility (hence the stability or ease of formation) of solid carbonates. To that goal, the electrocatalyst was subjected to an AST using the cycling-protocol in the potential range $0.1 < E < 1.23$ V *vs.* RHE in several electrolytes: LiOH, NaOH, KOH and CsOH at 0.1 M. **Figure IV.5** shows the CO_{ads}-stripping CVs obtained pre and post-AST in the different electrolytes. The ECSA loss calculated for each AST and the values of the solubility of the metal carbonates are reported in **Table IV.2**.

The carbonates can be ranked from the least to the most soluble in the order: LiOH < NaOH < KOH < CsOH. One can notice that, as expected, the ECSA loss is larger when the carbonates are more stable (*i.e.* when the solubility is low). In addition, the CO_{ads}-stripping CVs (**Figure IV.5**) clearly indicate that the rate of agglomeration is larger when the solid carbonates are highly stable. Both results tend to suggest that the detachment (and agglomeration) of the Pt NPs is indeed due to the formation of solid carbonates at the vicinity of the interface between the Pt and the carbon support.

For information, the same AST was also performed at the interface with an anion-exchange membrane in a so-called dry cell (these experiments were conducted by Marian Chatenet) to test whether the absence of water, and consequently the absence of solid carbonates, do affect the degradation mechanism [263]. The results showed that because there is no excess of water to dissolve the Pt^{z+} species formed by corrosion of the Pt NPs, Ostwald ripening and local redeposition on existing NPs become more likely. The absence of free alkali metal cation avoids the precipitation of solid carbonates, and therefore, the detachment of the Pt NPs from their support is not favored. As a result, these observations reinforced our assumption of carbonates formation during the degradation of Pt/C in liquid alkaline media.

In order to track such carbonates species, FTIR spectroscopy appeared to be a tool of choice: this is studied in the next section.

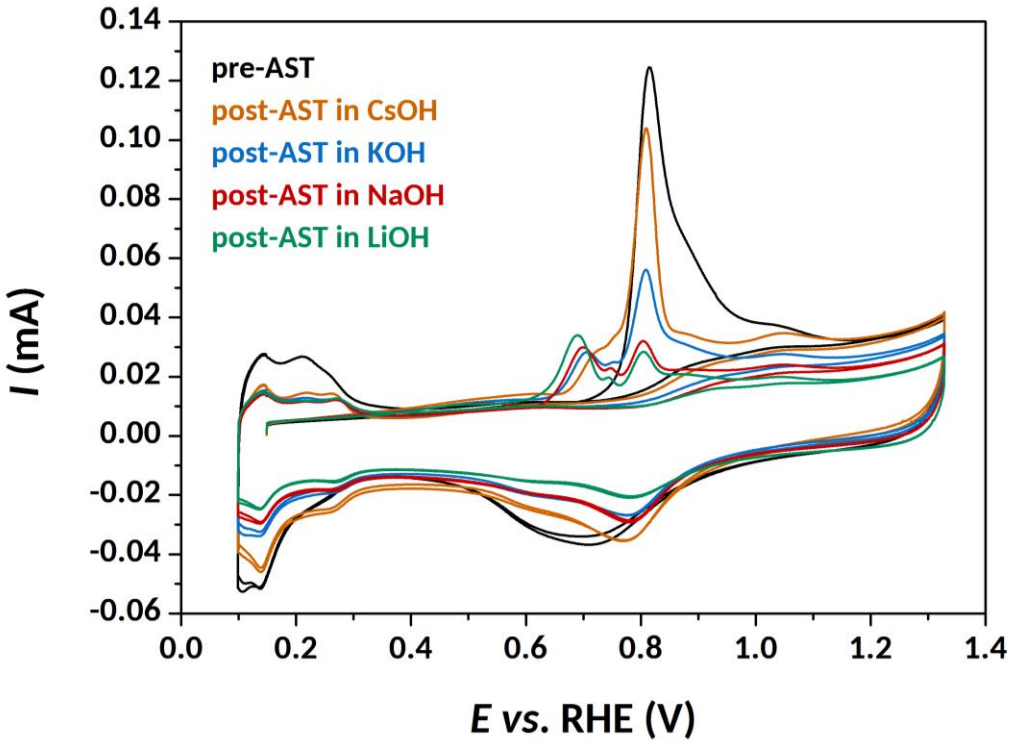

Figure IV.5. CO_{ads}-stripping voltammograms obtained on 10 wt.% Pt/C in 0.1 M H_2SO_4 at v = 20 mV s^{-1} pre and post-AST performed in 0.1 M MOH (M = Li, Na, K, Cs) using the cycling-protocol at *T* = 25°C.

Table IV.2. Metal carbonates solubility values and corresponding ECSA loss after 150 CV in 0.1 M MOH (M = Li, Na, K and Cs) in the potential range 0.1 < *E* < 1.23 V *vs.* RHE at v = 100 mV s^{-1} and *T* = 25°C.

Electrolyte	M_2CO_3 solubility in water @ 25°C		ECSA loss
	(g L^{-1})	(mol L^{-1})	(%)
LiOH	12.7 [264]– 12.9 [265]	≈ 0.53	67
NaOH	285 [265] – 294 [264]	≈ 7.2	60
KOH	1,123 [265]	≈ 20	52
CsOH	2,605 (20°C) [266]	≈ 17 (20°C)	37

IV.2.3 Exploratory measurements using *in situ* FTIR spectroscopy

In situ FTIR spectroscopy measurements were performed in order to detect the formation of carbonates species that are supposed to form during the AST. *In situ* FTIR measurements were first acquired using the cycling-protocol on the 10 wt.% Pt/C: **Figure IV.6** shows FTIR spectra obtained for several cycles of AST. Four negative-going bands, located at 1310, 1400, 1610, 1730 and 2070 cm^{-1}, are observed. In agreement with past studies [267–274], the bands located at 1400 and 1310 cm^{-1} were assigned to carbonate ions (CO_3^{2-}) and bicarbonate ions (HCO_3^-), respectively. The bands located at 1610 cm^{-1} and 1730 cm^{-1} were assigned to oxygen-containing surface groups on carbon, namely quinone or carboxylate and carbonyl/carboxylic acid group, respectively [167,274–279]. As the standard potential of carbon oxidation reaction in strong bases (pH = 14) is E^0 = 0.06 V *vs.* RHE according to the Pourbaix diagram [280], the production of CO, CO_2, surface oxides or organic-carbon products are expected in the potential range investigated in this study (0.1 < *E* < 1.23 V *vs.* RHE). These results strongly support our assumption that the degradation mechanism of Pt/C NPs involves the production of carbonate ions and oxygen-containing surface groups of the carbon support.

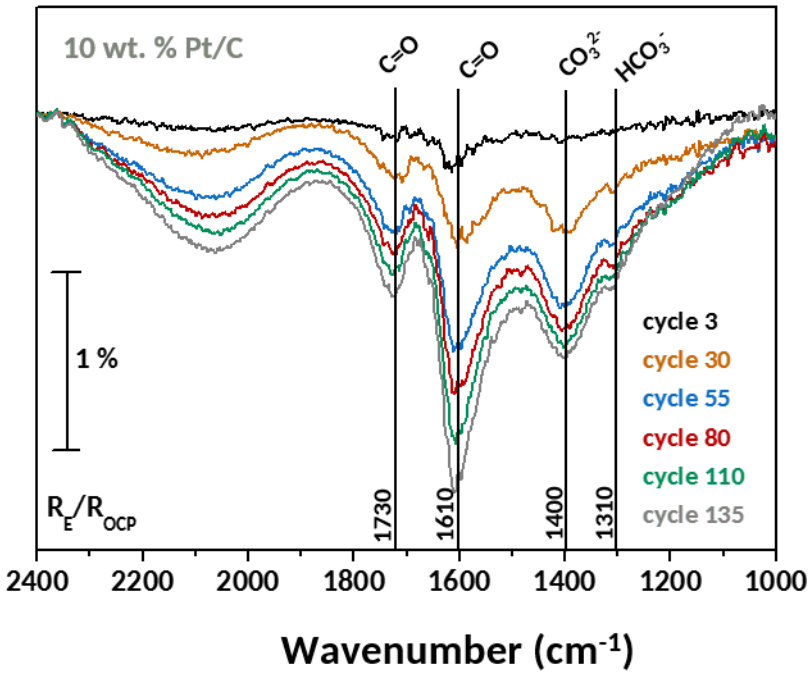

Figure IV.6. FTIR spectra obtained under cycling oxidation conditions from *E* = 0.1 to 1.23 V *vs.* RHE in 0.1 M NaOH on 10 wt.% Pt/C. The relative reflectivity is calculated using the spectra obtained at *E* = OCP as the reference reflectivity.

To confirm that the degradation of Pt/C electrocatalysts in alkaline media comes from a Pt-assisted local corrosion of the carbon support, similar FTIR experiments were performed on bare Vulcan XC72; the results are presented in **Figure IV.7**. Two negative-going bands are detected at 1590 and 1740 cm^{-1} and assigned to oxygen-containing surface groups of the carbon. However, no band relative to carbonate species was detected, putting into evidence that no or limited quantities of (bi)carbonates are produced in the absence of Pt: this result supports our hypothesis that (bi)carbonates are formed following the electrooxidation of CO-containing groups on Pt sites or on the carbon surface at the vicinity of the Pt sites (this will be further discussed later).

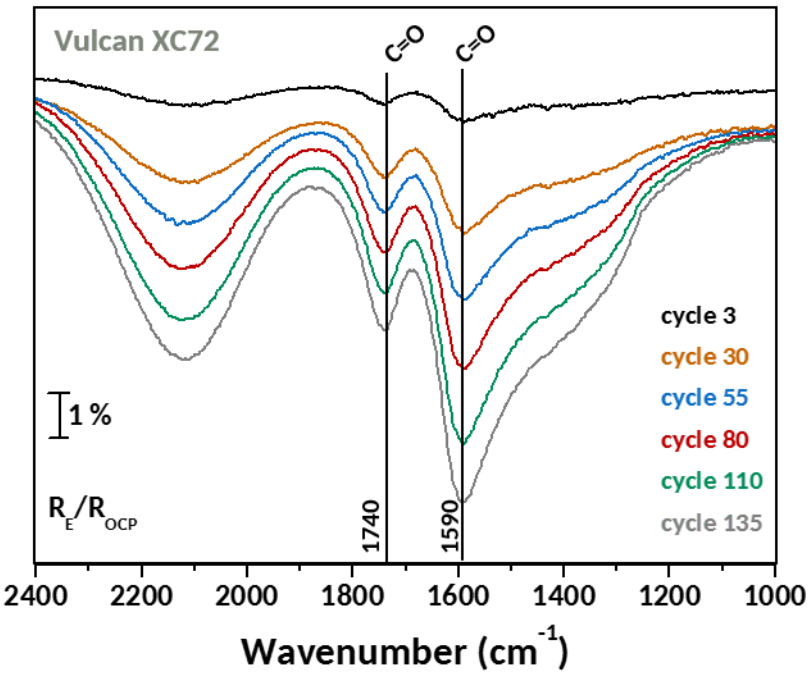

Figure IV.7. FTIR spectra obtained under cycling oxidation conditions from *E* = 0.1 to 1.23 V *vs.* RHE in 0.1 M NaOH on 10 wt.% Pt/C. The relative reflectivity is calculated using the spectra obtained at *E* = OCP as the reference reflectivity.

The different experiments performed as a "preliminary study" of the degradation mechanism highlight several phenomena. Firstly, the positive and negative vertex potential values of the AST yield different degradation processes and rates, suggesting that the degradation mechanism is a CO-stripping-like process. Secondly, the extent of degradation, when evaluated by the ECSA loss, is higher when the carbonates (which are supposed to form at the vicinity of the Pt|C interface) are poorly soluble. Thirdly, *in situ* FTIR spectroscopy measurements enable to detect the production of carbonates during the AST.

However, the cycling-protocol used for these FTIR measurements appeared to be ill-adapted to get clear fundamental insights into the degradation mechanism; it is in particular not adapted to detect at which potential the carbonates and the oxygen-containing surface groups form. Thus, complementary FTIR measurements were performed using a stepwise-protocol. In addition, both the influence of Pt weight fraction and the nature of the metal NPs (Pd and PtRu in addition to Pt) were investigated, in the hope to (i) assert the degradation mechanism of Pt/C in base, but also to (ii) possibly generalize this proposed mechanism to the most studied carbon-supported PGM electrocatalysts in alkaline fuel cells and water electrolyzers.

IV.3 Insights into the degradation mechanism

IV.3.1 *In situ* FTIR spectroscopy on Pt/C

The FTIR spectra obtained under stepwise oxidation conditions on 10, 40 and 80 wt.% Pt/C in 0.1 M NaOH are shown in **Figure IV.8**. Four negative-going bands, located at 1380, 1610, 1710 and 1960 cm^{-1}, and one positive-going band at 1670 cm^{-1}, are noticed on 10 wt.% Pt/C. Similarly, the FTIR spectra measured on the 40 and 80 wt.% Pt/C are composed of five negative-going bands at 1310, 1390, 1580, 1730-1760 and 2010 cm^{-1} and one positive-going band at 1670 cm^{-1}. The band wavenumbers observed in these FTIR spectra and their corresponding assignment are summed up in **Table IV.3**.

As mentioned in the previous section, the bands located at 1380-1390 cm^{-1} and 1310 cm^{-1} were assigned to carbonate ions (CO_3^{2-}) and bicarbonate ions (HCO_3^-), respectively. For all the electrocatalysts, the intensity of the carbonate features increased along with an increase of the electrode potential: this supports, again, our assumption that the degradation of Pt/C NPs involves the production of carbonate ions. The impact of the Pt weight fraction is also noticeable: the carbonate band (1380-1390 cm^{-1}) appears at E = 0.8 V *vs.* RHE for 10 wt.% Pt/C and at E = 0.5 V *vs.* RHE for 40 and 80 wt.% Pt/C. The area of this band was integrated at each electrode potential, as shown in **Figure IV.9.A**, and the results are displayed in **Figure IV.9.B**.They reveal that higher Pt ECSA enables formation of carbonate species at lower potential (therefore quantitatively more carbonate formation at a given potential).

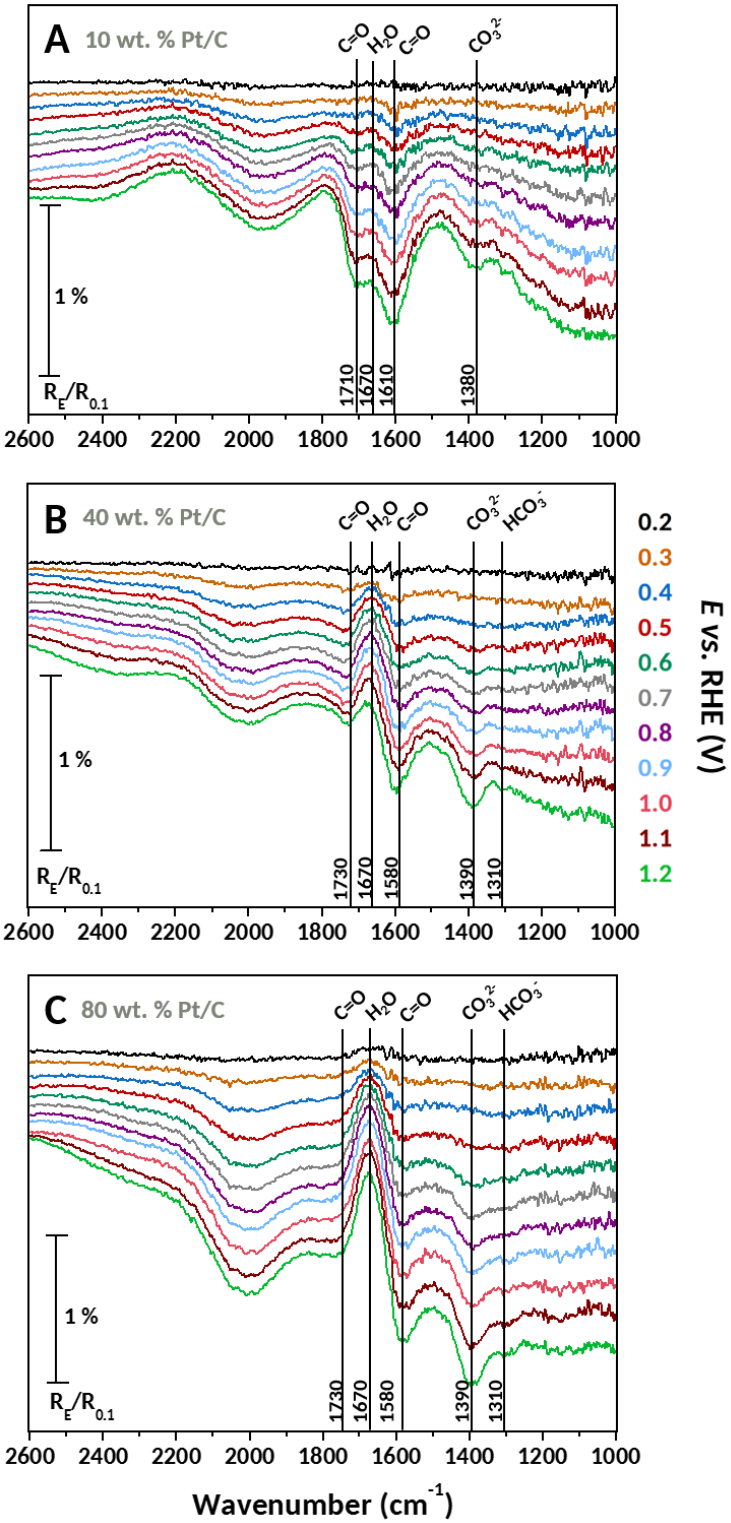

Figure IV.8. FTIR spectra obtained under stepwise oxidation conditions from *E* = 0.1 to 1.2 V *vs.* RHE in 0.1 M NaOH on (A) 10 wt.% Pt/C, (B) 40 wt.% Pt/C and (C) 80 wt.% Pt/C. The relative reflectivity is calculated using the spectra obtained at *E* = 0.1 V *vs.* RHE as the reference reflectivity.

Table IV.3. Band wavenumbers observed in FTIR spectra and their corresponding assignment.

Wavenumber (cm^{-1})	Bond	Mode	Assignment	Reference
1310	O=C-O	symmetric stretching	HCO_3^-	[267–270]
1380-1390	O=C-O	double degenerate stretching	CO_3^{2-}	[267–274]
1580 - 1610	C=O	stretching	quinone and/or carboxylate	[167,275–279]
1670	H-O-H	bending	H_2O	[274]
1710-1730-1760	C=O	stretching	carbonyl and carboxylic acid group	[167,274,276–279]
1960-2010			hydroxide/oxide adsorption on gold	

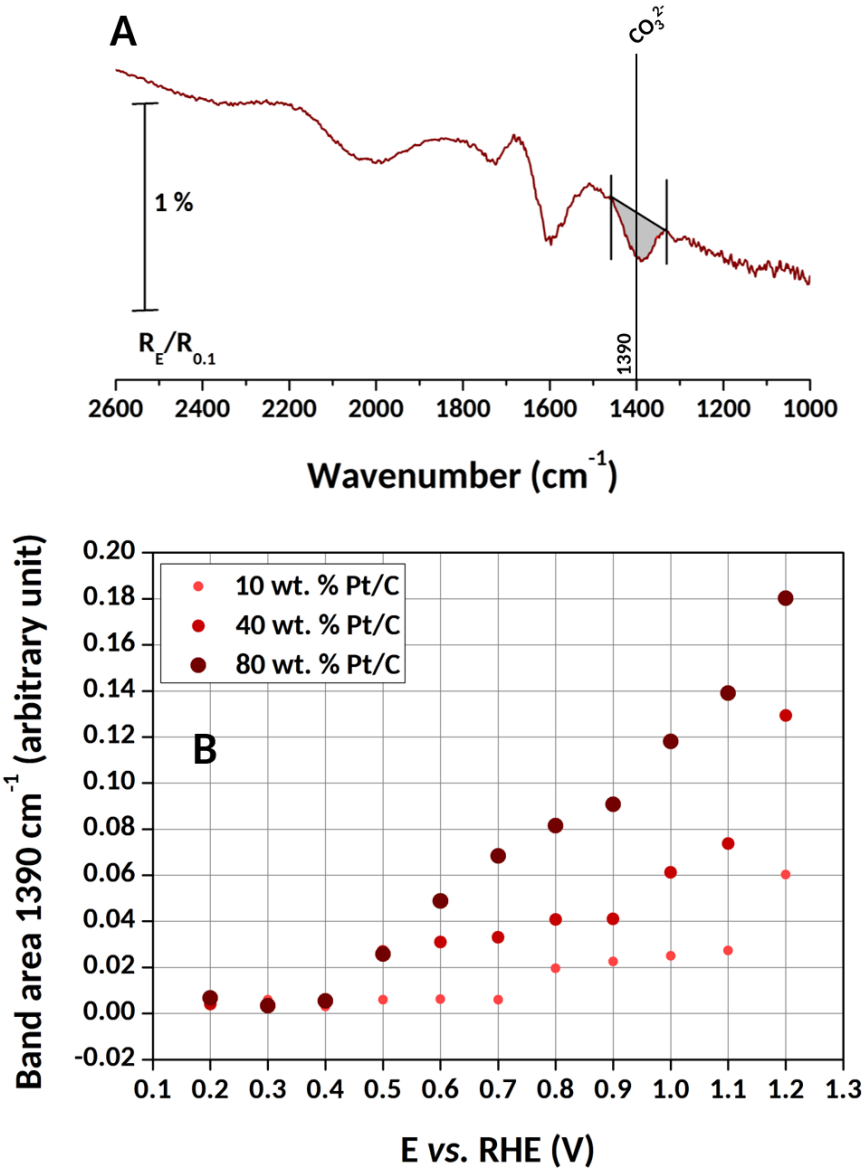

Figure IV.9. (A) Example of baseline integration; (B) Area developed by the 1390 cm^{-1} band at different electrode potential on 10, 40 and 80 wt.% Pt/C.

The bands located at 1580-1610 cm^{-1} and 1710-1730-1760 cm^{-1} were assigned to oxygen-containing surface groups on carbon, namely quinone or carboxylate and carbonyl/carboxylic acid group, respectively [167,274–279]. More practically, the band at 1710-1730-1760 cm^{-1} (carbonyl/carboxylic acid groups) appears at E = 0.5, 0.3 and 0.3 V *vs.* RHE for Pt/C 10, 40 and 80 wt.%, respectively, while the band at 1580-1610 cm^{-1} (quinone and/or carboxylate) appears at E = 0.3, 0.3 and 0.4 V *vs.* RHE for Pt/C 10, 40 and 80 wt.%, respectively. This means that, for all Pt/C electrocatalysts, oxygen-containing surface groups form on carbon at low potential ($0.2 < E < 0.6$ V *vs.* RHE, see **Equation IV.1**). Then, two *scenarios* can be considered:

- In *scenario 1*, the oxygen-containing surface groups that form on the carbon near the Pt NPs are oxidized at high potential (*E* > 0.6 V *vs*. RHE) by combination with Pt-OH_{ads} (**Equation IV.3** and **Equation IV.5**) to form CO_2, that converts into solid alkali-metal carbonates M_2CO_3 (M= Na in NaOH, K in KOH, etc.) (**Equation IV.6**);

- In *scenario* 2, these groups backspillover on the Pt NPs (when they are reduced, hence "available" to accommodate their adsorption) to create CO_{ads}-containing adsorbates (CO_{ads} and COH_{ads}, see **Equation IV.2**); when the potential exceeds 0.6 V *vs*. RHE, the CO_{ads}-containing adsorbates react with OH_{ads} species (formed by adsorption of OH^- ions on Pt, **Equation IV.3**) to form CO_2 (**Equation IV.4**), that converts into solid carbonates in alkali cations-containing bases (**Equation IV.6**).

These two *scenarios* are both equally likely in the author's opinion and both allow rationalizing the destruction of the anchoring site between the NP and the carbon support.

$$C_n - C + 2OH^- \rightarrow C_n - CO_{ads} + H_2O + 2e^- \quad \textbf{Equation IV.1}$$

$$Pt + C_n - CO_{ads} \rightarrow Pt - CO_{ads} + C_n \quad \textbf{Equation IV.2}$$

$$Pt + OH^- \rightarrow Pt - OH_{ads} + e^- \quad \textbf{Equation IV.3}$$

$$Pt - CO_{ads} + Pt - OH_{ads} + OH^- \rightarrow CO_2 + H_2O + 2\,Pt + e^- \quad \textbf{Equation IV.4}$$

$$C_n - CO_{ads} + Pt - OH_{ads} + OH^- \rightarrow CO_2 + H_2O + Pt + C_n + e^- \quad \textbf{Equation IV.5}$$

$$CO_2 + 2\,OH^- + 2\,M^+ \rightarrow M_2CO_3 \quad \textbf{Equation IV.6}$$

In the two suggested degradation mechanisms, water and carbonate species are supposed to be produced simultaneously. Thus, a negative-going band is expected for water bending at 1645 cm^{-1} [274]. This band is located at 1670 cm^{-1} in our study and points positive for the three electrocatalysts, which suggest consumption (or loss) of water. One possible explanation for the apparent contradiction (consumption/loss of water instead of production/accumulation of water) would imply a change of carbon surface properties from hydrophilic to hydrophobic. Indeed, it is well-known that oxygen-containing surface groups are present on the native carbon surface (**Equation IV.1**): the surface of the carbon support is thus necessarily hydrophilic in the fresh state. It is therefore expected that the consumption of these oxygenated functions (**Equation IV.2** and **Equation IV.5**) leads to a change in its wetting properties. Because the thin layer formed between the electrode surface and the prism has a fixed volume and is diffusionally-isolated, the repulsion of water from the carbon support (C_n) occurring upon

electrode potential increase would result in a positive-going water bending band at 1645 cm^{-1} in the FTIR spectra. The higher this intensity, the more hydrophobic the carbon surface, as a result of the more pronounced corrosion of the oxygen-containing surface groups into CO_2 and production of metal carbonates. The corrosion of oxygen-containing surface groups also takes place in acidic media, as described in ref. [281,282].

According to the proposed mechanisms, two other species should have been detected: CO_2 (in both scenarios) and CO (only in *scenario* 2). The main infrared spectroscopy features of these species are bands with strong intensities located at 2345 cm^{-1} and *ca*. 2045 cm^{-1} respectively [168,267,271,283], but none of them was detected in our study. This apparent discrepancy can be explained, though. Firstly, CO_2 is an intermediate species in the proposed corrosion mechanism, but this product should be rapidly converted to CO_3^{2-} in alkaline media. FTIR spectroscopy being a quasi-stationary measurement, the detection of transient species is very tricky and can explain the absence of CO_2 related bands in our experiments. Secondly, regarding the formation of CO in *scenario* 2, it is postulated that too little CO is produced (well below a complete monolayer on the Pt NPs), because CO-containing groups mostly originate from a limited reservoir (the Pt | C interface) and are oxidized at potential above 0.4 V *vs*. RHE (**Figure IV.8** and **Figure IV.9.B**). Hence in the conditions of our study, CO_{ads} species will hardly accumulate on the Pt surface, and in any case, the CO_{ads}-like coverage should be well below a monolayer (as it initially exists in CO_{ads}-stripping experiments).

Finally, according to FTIR measurements performed on polycrystalline gold (the electrode used for FTIR measurements) in the same conditions (see **Figure A.7** in **Annex 4**), the very broad negative-going band located around 2000 cm^{-1} on all the spectra might be assigned to a change of gold reflectivity during the experiment (*e.g*. because gold progressively gets covered by OH_{ads} and/or surface oxides [284]). This broad band is noticeable on all the spectra presented in this study and the assignment is identical for all of them.

IV.3.2 Does the degradation of Pt/C come from a Pt-assisted local corrosion?

To confirm that the degradation of Pt/C electrocatalysts in alkaline media comes from a Pt-assisted local corrosion of the carbon support, similar FTIR experiments were performed on bare Vulcan XC72, and the results are presented in **Figure IV.10**.

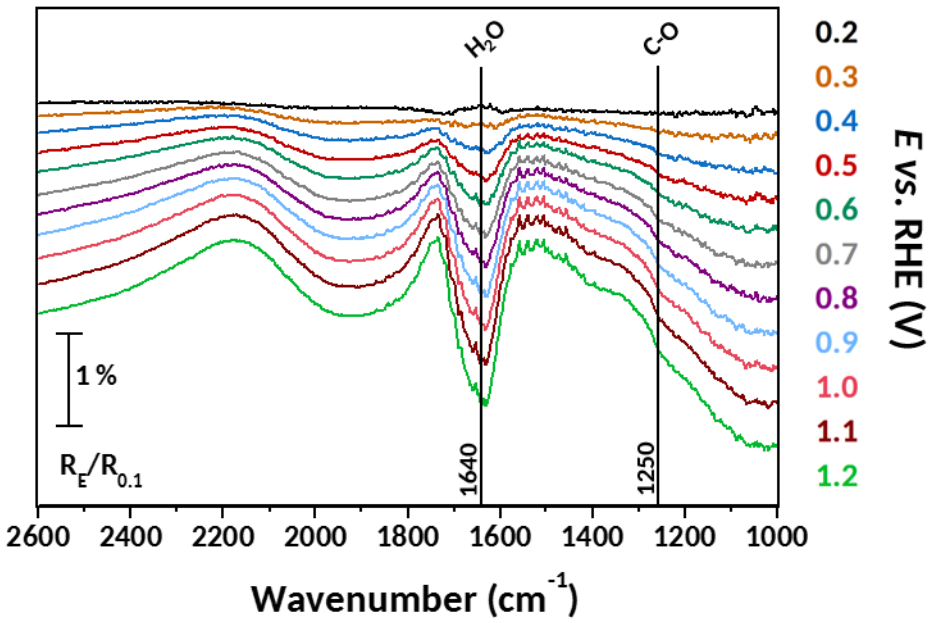

Figure IV.10. FTIR spectra obtained under stepwise oxidation conditions from *E* = 0.1 to 1.2 V *vs.* RHE in 0.1 M NaOH on Vulcan XC72. The relative reflectivity is calculated using the spectra obtained at *E* = 0.1 V *vs.* RHE as the reference reflectivity.

During the stepwise oxidation, a very weak shoulder located at 1250 cm^{-1} develops on the FTIR spectra, which is assigned to C-O stretching [167]; a broad negative-going band located at 1640 cm^{-1} was assigned to H-O-H bending, signing water production. However, no band relative to carbonate species was detected, in agreement with the results obtained using the cycling-protocol (see **Figure IV.7**). This confirms that no or limited quantities of (bi)carbonates are produced in the absence of Pt, and further supports our hypothesis that (bi)carbonates are formed following CO_2 production on Pt sites. Nevertheless, no band (other than the one located at 1250 cm^{-1}) related to oxygen-containing surface groups was detected in the absence of Pt NPs (even if a small shoulder can be identified around 1710 cm^{-1}), whereas they were observable on the spectra obtained using the cycling-protocol (**Figure IV.7**). It is possible that the bands linked to the oxygen-containing surface groups could be drowned in the broadband located at 1640 cm^{-1}, that may be dominated by the change of reflectivity of the Au substrate (see **Figure A.7**).

The evolution of the oxygen content during the AST was further investigated using XPS measurements performed pre and post 150 CV cycles for bare Vulcan XC72 and 40 wt.% Pt/C (**Figure IV.11**). The evolution of the oxygen content during AST was estimated using the O1s/C1s ratio (without the contribution of Nafion®-related envelopes and corrected from the atomic sensitivity factors). The O1s/C1s ratio increases from 0.10 to 0.18 upon the AST for Vulcan XC72,

but remains stable for 40 wt.% Pt/C (O1s/C1s = 0.19 and 0.18 pre and post AST, respectively). These results suggest that oxygen-containing surface groups do form and accumulate (their signature increases) on the carbon surface when Vulcan XC72 carbon is free of Pt NPs, whereas their proportion remains stable when Pt NPs are present, because the Pt NPs help to oxidize them into CO_2 and then carbonates upon their formation.

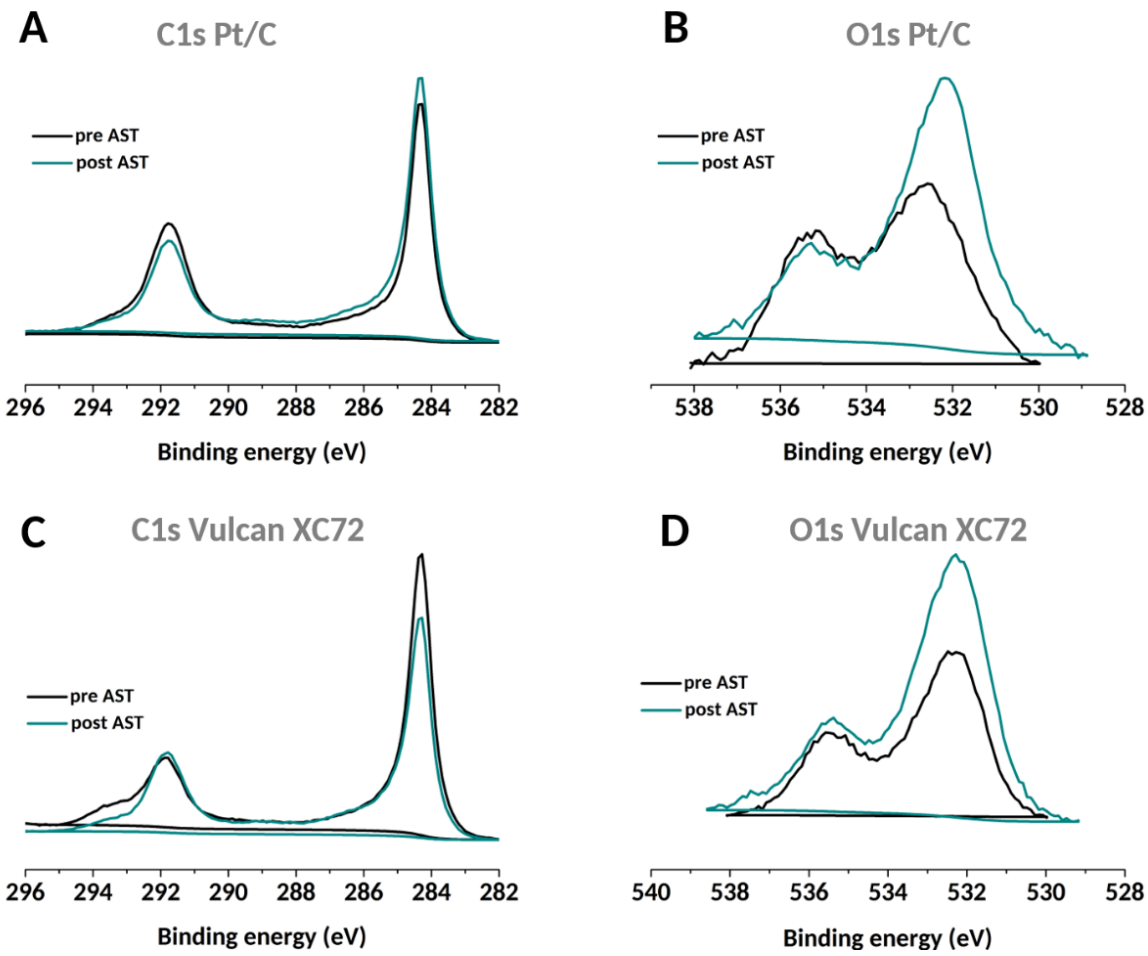

Figure IV.11. XPS spectra obtained on (A, B) 40 wt.% Pt/C and (C, D) Vulcan XC72 pre and post-AST: (A, C) C1s and (B, D) O1s.

Another possible mechanism when the carbon support is free of Pt NPs could eventually resemble to the one described by Yi and coworkers [285], who recently studied the electrochemical corrosion of glassy carbon (GC) in alkaline media. FTIR spectroscopy measurement on GC oxidized in alkaline media (U = 1.8 V *vs.* RHE during 24 hours in 0.1 M KOH) revealed no change compared to the pristine GC. Similarly, the Raman and XPS spectra and the cyclic voltammograms measured on the pristine and aged GC were nearly identical. To

rationalize their findings, the authors postulated that the oxidation of GC in alkaline media occurs via a reaction of OH° radicals (produced by discharge of OH^- ions) with alkyl side chains, leading to transient oxidation of the edges of carbon layers until they become hydrophilic and dissolve, thus exposing a "fresh" GC surface.

IV.3.3 CO_{ads}-electrooxidation on polycrystalline Pt

To support our hypotheses, the electrooxidation of a CO_{ads} monolayer in alkaline media was investigated on polycrystalline Pt. The results are displayed in **Figure IV.12**, and data are plotted using either the spectrum measured at *E* = 0.1 V *vs.* RHE (**Figure IV.12.A**) or that measured at *E* = 1.1 V *vs.* RHE (**Figure IV.12.B**) as a reference spectrum.

Figure IV.12.A shows two negative-going bands located at 1390 and 1630 cm^{-1}, corresponding to carbonates and water production, respectively. **Figure IV.12.B** shows that CO_{ads} consumption is concomitant with CO_3^{2-} production: the CO_{ads} feature, located at 2014 cm^{-1} for *E* = 0.1 V *vs.* RHE starts to disappear for 0.3 V *vs.* RHE and above, in parallel to the appearance of a positive band of water, sign of its generation in the process (as expected).

It is interesting to notice that carbonates are produced at lower potential on polycrystalline Pt relative to Pt/C electrocatalysts: the band at 1390 cm^{-1} is detected at *E* = 0.3 V *vs.* RHE on polycrystalline Pt, and at *E* = 0.8 or 0.5 V *vs.* RHE for Pt/C at low or high metal weight fraction, respectively. Moreover, the carbonates feature grows up to *E* = 0.5 V *vs.* RHE and starts to decrease above *E* = 0.6 V *vs.* RHE on polycrystalline Pt (likely because the CO source is limited), whereas the band keeps growing on the Pt/C electrocatalysts (likely because the CO source is huge). Since all conditions were kept identical, this result nicely confirms that an equilibrium between the rate of carbonate formation and dissolution takes place in the thin layer formed between the electrode surface and the CaF_2 prism. In the CO_{ads}-stripping experiment on polycrystalline Pt, the limited quantity of CO species facilitates the dissolution of carbonate species on the long term. In contrast, the corrosion of the carbon support promotes the renewal of a native carbon surface on Vulcan XC72, which is then oxidized into CO_2 and ultimately carbonate species. The process is operating until the Pt nanoparticle detaches from the support.

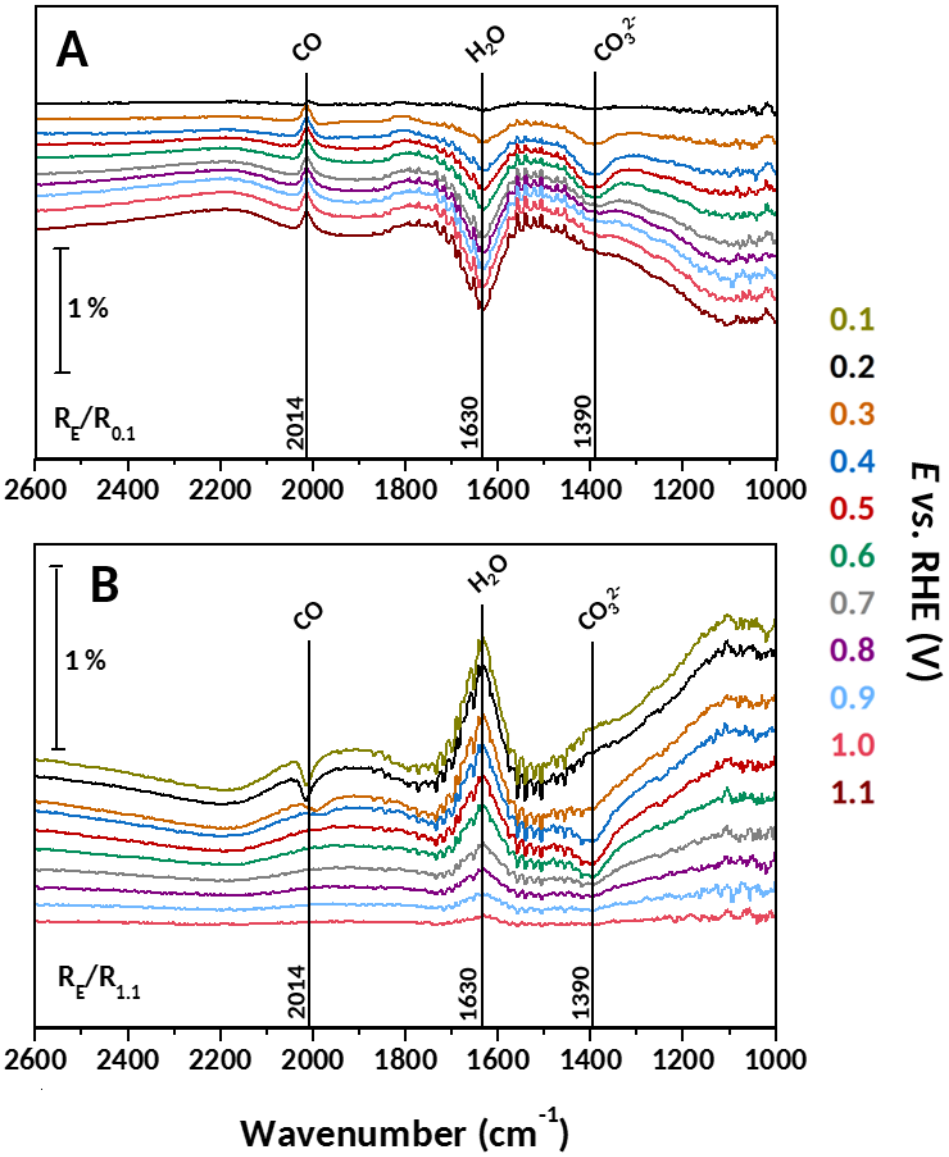

Figure IV.12. FTIR spectra obtained for CO_{ads} electrooxidation on polycrystalline Pt under stepwise oxidation conditions in 0.1 M NaOH. The electrode potential was stepped from *E* = 0.1 to 1.2 V *vs.* RHE; the relative reflectivity was calculated using the FTIR spectra obtained at (A) *E* = 0.1 V *vs.* RHE and (B) *E* = 1.1 V *vs.* RHE as the reference reflectivity.

IV.4 Towards a generalization of the degradation mechanism

To generalize our findings, FTIR spectra were recorded on 40 wt.% PtRu/C and 40 wt.% Pd/C in the same experimental conditions (**Figure IV.13**). The high metal weight fraction allowed to highlight whether these PGM catalyze the electrochemical corrosion of the carbon support. This is definitely the case for 40 wt.% PtRu/C. Indeed, four negative-going bands are observed on this catalyst (**Figure IV.13.A**), in particular the bands assigned to the presence of carbonate and

bicarbonate ions. Similarly, Pd NPs corrode the carbon support, although to a minor extent: the band assigned to carbonates is indeed noticeable (**Figure IV.13.B**), but its intensity is very weak. In addition, both FTIR spectra show the positive-going band assigned to water and located at 1670 cm^{-1}: the intensity of this band increases with the production of carbonates as observed previously with the three Pt/C electrocatalysts.

The results were quantitatively confirmed by subjecting the three different materials to an AST using the cycling-protocol. Meanwhile, IL-TEM images were recorded on the fresh and aged electrocatalysts in the exact same location (**Figure IV.14**). Note however that, to facilitate the visualization of the degradation and rebuild the particle size distributions, 10 wt.% catalysts were used. **Figure IV.14.B.C** reveals that the majority of the PtRu NPs are detached from the carbon support after the AST (highlighted with the white crosses – these do not pretend to be comprehensive) and that the remaining ones are agglomerated. More precisely, the extent of the NPs detachment reached 86%. Furthermore, a metal-containing deposit could be observed on the membrane of the TEM grid upon ageing (see **Figure IV.15** and **Figure IV.16**): X-EDS analyses revealed that this deposit is essentially composed of Ru. This finding is in line with the thermodynamic instability of Ru in alkaline environment [280] and illustrates the fact that Ru likely does not play any role in terms of carbon oxidation reaction catalysis (except in the initial cycles before its dissolution). The more robust catalyst was clearly Pd/C for which only 10% of the metal NPs were lost after the AST whereas 63% are lost in the case of Pt/C. The evolution of the particle size distribution is overall similar for the three electrocatalysts: the proportion of isolated larger NPs lowers, while the proportion of isolated smaller NPs increases, suggesting that small particles are more stable than the big ones in these conditions. In the case of PtRu/C, this result could also result from the preferential dissolution of Ru during the AST.

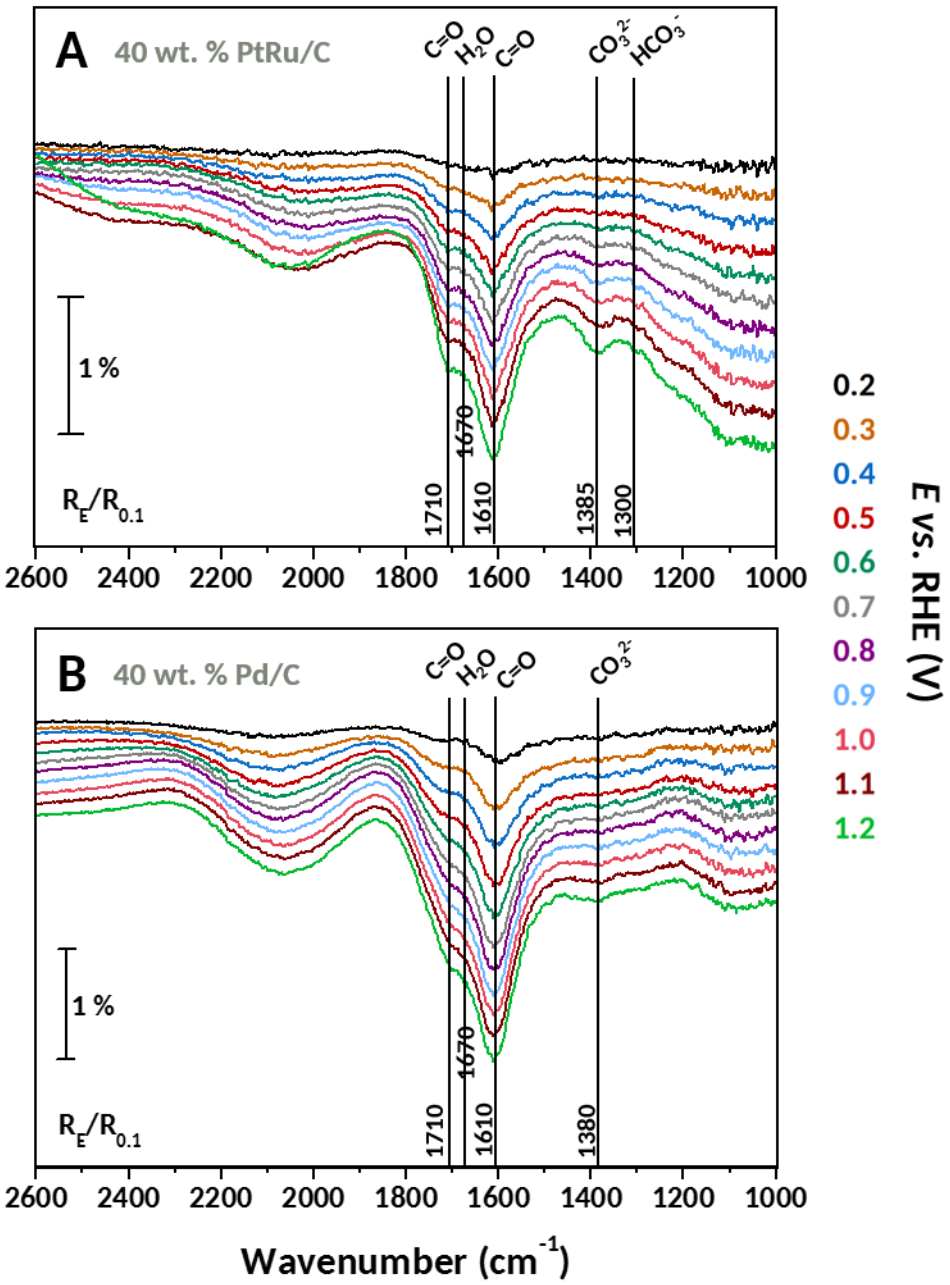

Figure IV.13. FTIR spectra obtained under stepwise oxidation conditions from *E* = 0.1 to 1.2 V *vs.* RHE in 0.1 M NaOH on (A) 40 wt.% PtRu/C and (B) 40 wt.% Pd/C. The relative reflectivity is calculated using the spectra obtained at *E* = 0.1 V *vs.* RHE as the reference reflectivity.

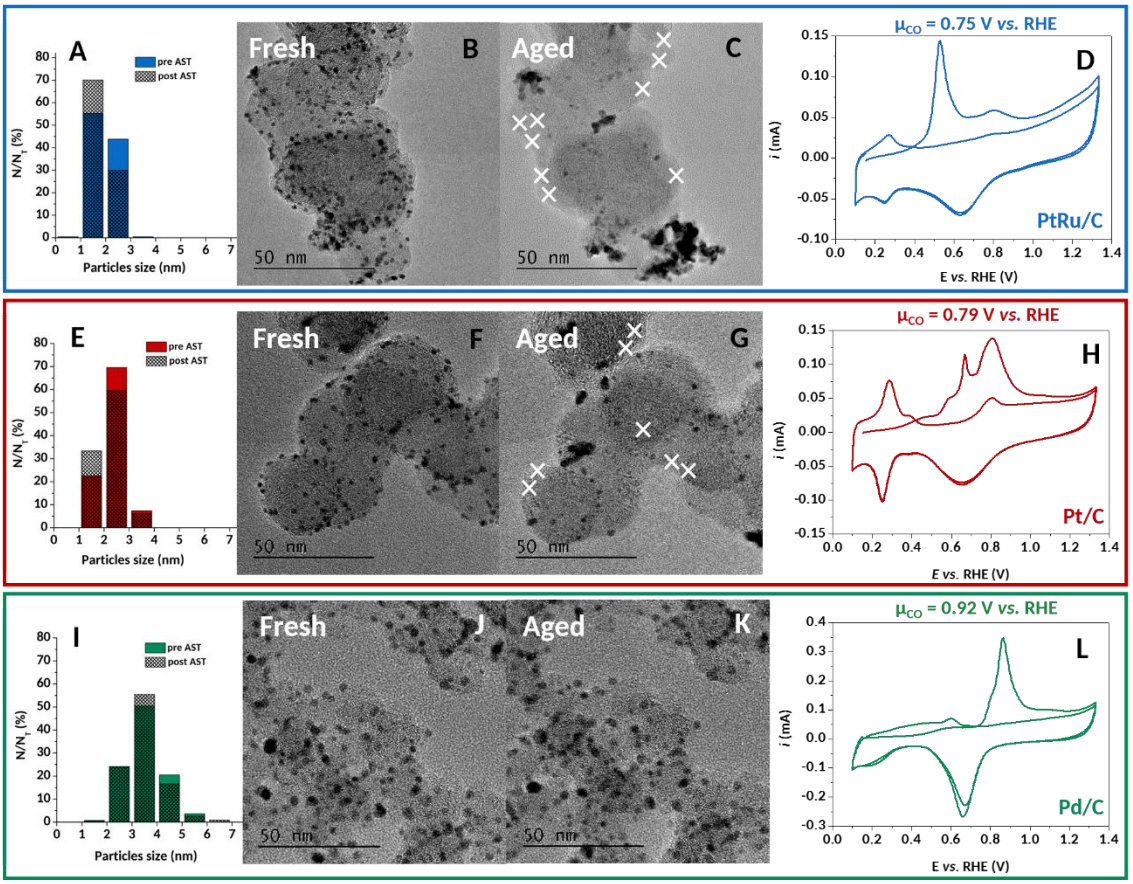

Figure IV.14. (A, E, I) Particle size distribution for 10 wt.% PtRu/C (blue), 10 wt.% Pt/C (red) and 10 wt.% Pd/C (green) electrocatalysts, N_T is the total number of counted particles (*ca.* 200). IL-TEM micrographs (B, F, J) pre-AST and (C, G, K) post-AST on 10 wt.% PtRu/C (blue), 10 wt.% Pt/C (red) and 10 wt.% Pd/C (green). (D, H, L) CO_{ads} stripping voltammograms obtained at v = 20 mV s^{-1} in 0.1 M NaOH on 10 wt.% PtRu/C (blue), 10 wt.% Pt/C (red) and 10 wt.% Pd/C (green).

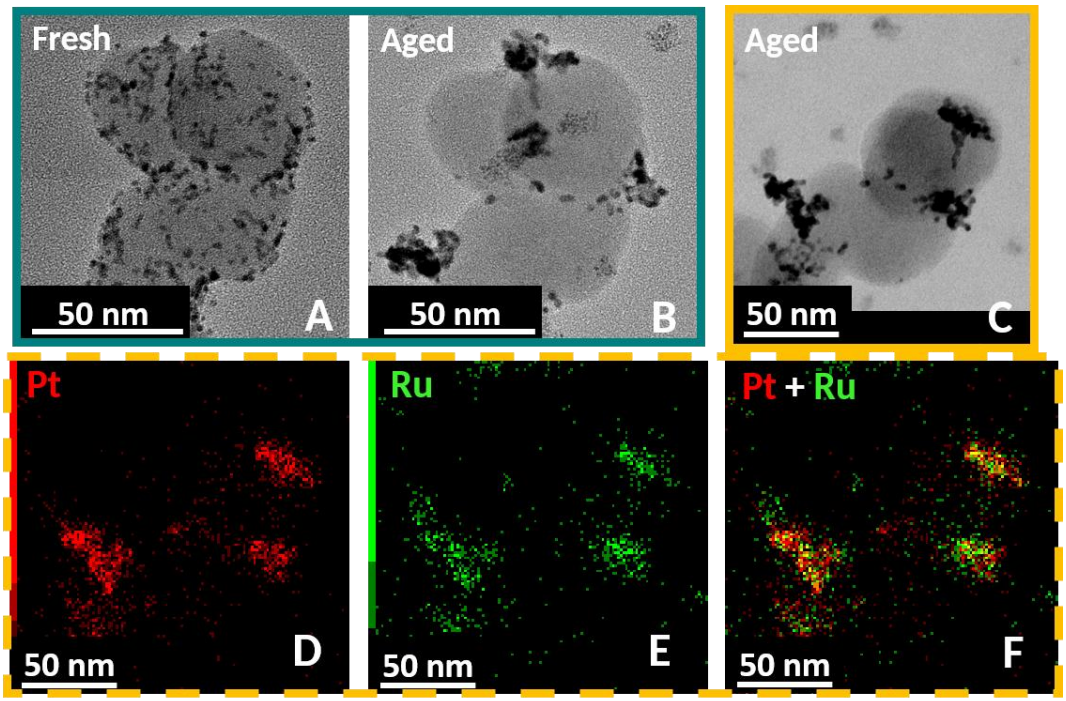

Figure IV.15. IL-TEM micrographs of the 10 wt.% PtRu/C (A) pre and (B) post AST; (C) STEM images and (D, E, F) corresponding X-EDS maps obtained on aged PtRu/C after the AST.

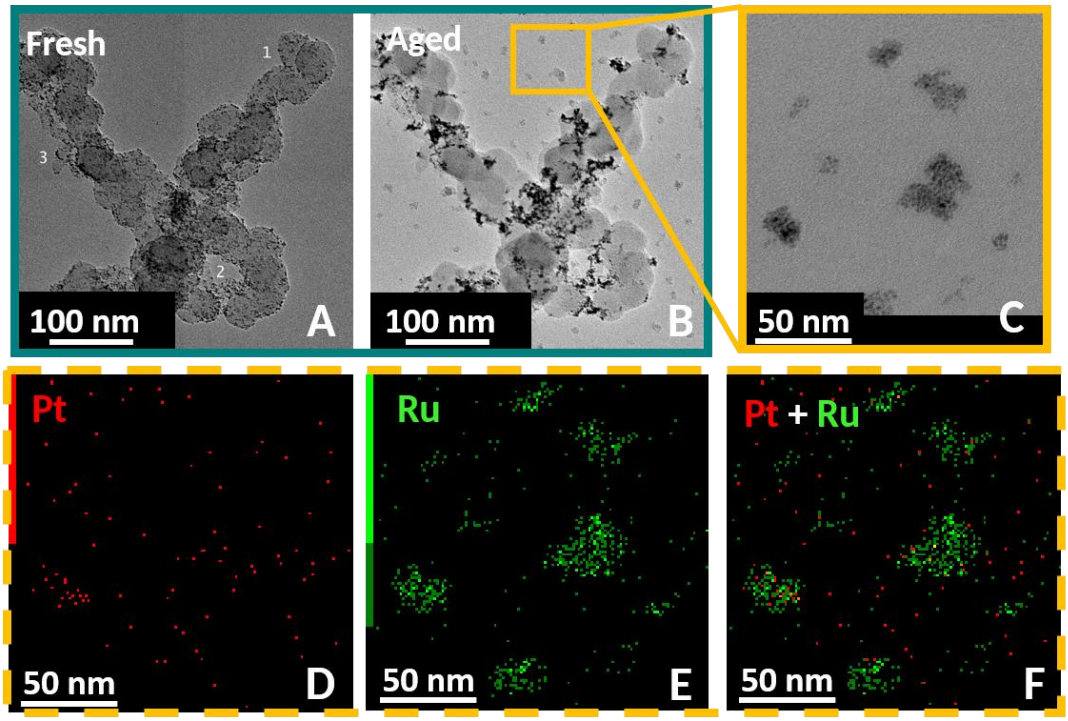

Figure IV.16. IL-TEM micrographs of the 10 wt.% PtRu/C (A) pre and (B) post AST; (C) STEM images and (D, E, F) corresponding X-EDS maps of the deposit on the TEM grid after the AST.

Comparing IL-TEM images and CO_{ads}-stripping voltammograms reveals particularly insightful: indeed the more corroded catalysts are those for which the metal has the larger propensity to electrooxidize CO in 0.1 M NaOH (**Figure IV.14.D.H.L**). To quantitatively illustrate our hypotheses, the average CO_{ads} oxidation potential (μ_{CO}), first introduced by Chattot *et al*. [286], was extracted using the first moment of the potential weight:

$$\mu_{\mathrm{CO}}\ (\mathrm{V}\ vs.\ \mathrm{RHE}) = \int \frac{E \times I}{Q_{\mathrm{T,CO}}} dE$$

where $Q_{\mathrm{T,CO}}$ is the total electric charge of the CO_{ads} stripping voltammogram. The μ_{CO} values are 0.75, 0.79 and 0.92 V *vs.* RHE for PtRu/C, Pt/C and Pd/C, respectively. This calculation indicates that the more active CO_{ads} oxidation electrocatalysts in alkaline media are respectively: PtRu/C > Pt/C >> Pd/C. Strikingly, the same ranking is obtained in terms of "extent of particles detachment". Combining this result with the degradation monitored for the three electrocatalysts, we thus argue that the ability of those electrocatalysts to form CO_2 from CO_{ads} determines its degradation by detachment of the metal NPs upon potential cycling in alkaline electrolyte.

Finally, the areas of the band corresponding to carbonate groups were integrated for PtRu/C and Pd/C (**Figure IV.17.A**). The result show that, similarly to what was observed for 10 wt.% Pt/C in similar conditions, carbonate species are quantitatively produced at potential values above *E* = 0.8 V *vs.* RHE on PtRu/C. This is no surprise in view of the results of X-EDS elemental maps that showed that Ru atoms were dissolved during the AST, and hence did not contribute to the carbon support corrosion. In other words, the 40 wt.% PtRu/C catalyst finally behaves as a 20 wt.% Pt/C in terms of carbon support corrosion, which is confirmed by its intermediate situation in terms of carbonate production (**Figure IV.17.A**). On Pd/C, carbonate species are detected at *E* = 1.1 V *vs.* RHE.

The electrical charge corresponding to each potential step was also calculated. The results, shown in **Figure IV.17.B**, reveal that the charge obtained on PtRu/C is indeed higher to the one obtained on Pt/C and Pd/C because of the concomitance of Ru dissolution and carbonates production. Whatever this slight difference, it is possible to conclude that the degradation mechanism suggested for Pt/C is also essentially valid for PtRu/C and Pd/C, which initiates a possible generalization of the degradation mechanism of carbon-supported PGM in alkaline electrolytes.

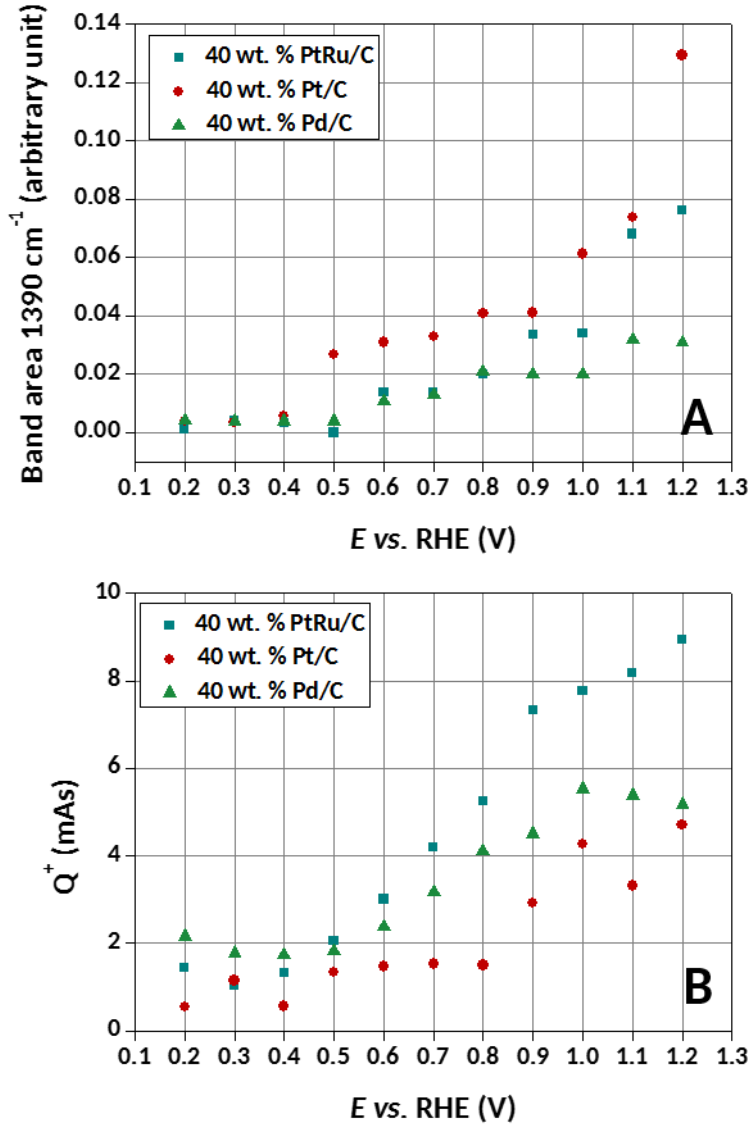

Figure IV.17. (A) Area developed by the 1390 cm^{-1} band at different electrode potential on 40 wt.% PtRu/C, 40 wt.% Pt/C and 40 wt.% Pd/C and (B) corresponding electrical charge associated to each oxidation potential step.

IV.5 Conclusions

In this chapter, we gained fundamental insights into the origin of the detachment of Pt NPs from the carbon support occurring during an AST in alkaline media using *in situ* FTIR spectroscopy, *ex situ* XPS and IL-TEM.

The presence of carbonate features on the FTIR spectra implies that the degradation mechanism of Pt/C electrocatalyst involves the production of carbonates. Thanks to the stepwise oxidation electrochemical protocol, it was shown that carbonates are produced above E = 0.5 V *vs.* RHE for high metal weight fraction and above E = 0.8 V *vs.* RHE for low metal weight fraction. In addition, no carbonate features were detected on the FTIR spectra for the bare Vulcan XC72 (without Pt NPs), demonstrating that the carbonate formation is promoted by the presence of the Pt NPs at the carbon surface. As a result, one can now affirm that Pt NPs assist the corrosion of the carbon support into CO_2, eventually leading to the local production of solid carbonates at the vicinity of the NPs and the carbon support (at least in electrolytes compatible with metal carbonates formation, *i.e.* LiOH, NaOH, KOH, *etc.*). These carbonates in turn destroy the anchoring sites between the NPs and their support, therefore leading to NPs detachment and/or agglomeration.

Combining FTIR spectroscopy and CO_{ads}-stripping measurements, a straightforward relationship emerged between the ability of a material to electrooxidize CO_{ads} into CO_2 (to form carbonates at low potential) and the extent of NPs detachment. As an example, a more pronounced extent of NPs detachment is reported for PtRu/C (with respect to Pt/C and Pd/C), which is able to oxidize CO at lower potential than Pt/C and Pd/C. We thus conclude that the degradation mechanism is, to some extent, similar for PtRu/C, Pt/C and Pd/C, and the extent of degradation simply depends on the ability of the metal NPs to electrooxidize CO-containing surface groups present on the carbon support.

General conclusion and outlook

Facing the energetic and climatic crisis that manifest more and more every day all over the world, the scientific community is working hard to develop new energy production systems that emit a minimum of greenhouse gases. In this field, fuel cells appear as interesting and feasible solutions that could address, in part, the overall energetic crisis and the subsequent climatic crisis. This PhD work was focused on a particular liquid alkaline fuel cell, the direct borohydride fuel cell (DBFC), which offers very interesting thermodynamic and energetic characteristics, in addition to more facile fuel storage and transport than hydrogen. However, the promising features of the DBFC are mitigated by the very complex borohydride oxidation reaction (BOR), which remains misunderstood on most electrocatalysts and in DBFC operating conditions. In addition, and contrary to the common belief, the alkaline environment was recently reported to be very aggressive towards conventional carbon-supported Pt electrocatalysts, but the degradation mechanism was still unknown. In this context this PhD work was motivated by three main questions: (i) How do high fuel concentration and high temperature impact the BOR on carbon-supported Pd-based electrocatalysts? (ii) Is there any merit to create a graded electrocatalyst anode to increase the BOR efficiency and boost the subsequent DBFC performances? (iii) What is the origin of the particles detachment that occurs during a mild accelerated stress test on carbon-supported Pt electrocatalysts in liquid alkaline media?

Firstly, the BOR was investigated on six carbon-supported Pd-based electrocatalysts in rotating-disk electrode configuration, for three $NaBH_4$ concentration (5, 50 and 500 mM) at high temperature (60°C). The influence of several parameters on the BOR kinetics were studied, such as the Pd sites density, the presence of ceria and the catalytic layer thickness. In addition, activity markers were proposed to evaluate the BOR activity, namely the onset potential and the specific and mass-activities obtained at low potential, *i.e.* at E = 0, 0.2 and 0.5 V *vs*. RHE. According to the complex BOR mechanism, the conclusions which result from **CHAPTER II** are very specific to the conditions of the study (nature and structure of the electrocatalysts, electrolyte composition and temperature); however, some points were highlighted.

i. Increasing the $NaBH_4$ concentration up to 50 and 500 mM leads to higher surface poisoning and points towards limiting charge transfer kinetics; however, for the highest $NaBH_4$ concentration, the low OH^- concentration might account for the very slow BOR kinetics;
ii. Increasing the Pd sites density enables to enhance the BOR kinetics when the $NaBH_4$ concentration is 5 and 50 mM, but the influence of the Pd sites density does not show particular trend for 500 mM $NaBH_4$; besides, the onset potential systematically shifts towards negative values when the $NaBH_4$ concentration and the amount of Pd increase;

iii. Contrary to our expectations, the presence of ceria on Pd/C electrocatalyst, which was suspected to boost the BOR kinetics by supplying the Pd surfaces with OH_{ads}, leads to lower BOR activity than the Pd/C electrocatalysts for 5 and 50 mM $NaBH_4$;

iv. At low potential values and low $NaBH_4$ concentrations (5 and 50 mM), the Pd-based electrocatalysts exhibit slower BOR kinetics than Pt/C, likely due to a better HOR activity on Pt/C in comparison to Pd/C; however, for the highest $NaBH_4$ concentration, the BOR kinetics is faster on Pd-based electrocatalysts in comparison to Pt/C, likely owing to more severe poisoning issues at Pt than at Pd in these conditions;

v. Finally, the preliminary study of three different catalytic layer thickness showed that thick electrodes enable to enhance the residence time of electroactive species within the electrode and lead to higher BOR activities, especially for high $NaBH_4$ concentrations.

Overall, the ratio [catalytic sites]/[BH_4^-] as well as the ratio [BH_4^-]/[OH^-] seem to be two crucial properties which are decisive in the apparent BOR kinetics and activity.

Secondly, the impact of the catalytic layer design on the BOR activity was further studied using five different design of catalytic layers made of Pt/C and Pd/C electrocatalysts. Precisely, the electrocatalysts were used as single (Pt/C or Pd/C), mixed (Pt/C + Pd/C) or graded (Pt/C to Pd/C or Pd/C to Pt/C) electrodes in RDE configuration and in H_2O_2-DBFC configuration, for 10 and 100 mM $NaBH_4$ and low temperature (25°C). The conclusions that result from this study depend on the electrolyte (anolyte and catholyte) concentration:

i. For low electrolyte concentration, mixing and grading electrocatalysts enable to enhance the BOR kinetics and activity in comparison to single Pt/C and single Pd/C electrodes; however, the onset potential and open-circuit voltage (OCV) obtained with the mixed and graded electrodes remain similar to the values obtained with single Pt/C, and the H_2 escape is also similar to the single Pt/C electrode; in addition, the results suggest that the mixed and graded electrodes may lead to a similar BOR mechanism than Pt/C electrocatalyst. All this suggest that the behavior of Pt/C dominates in these conditions;

ii. For high electrolyte concentration, the graded electrode lead to similar performances (maximum power density and OCV) than single Pt/C electrode, but the H_2 escape is lower, especially at high cell voltage, with the graded electrodes. The main advantage when using graded-electrocatalysts electrodes is to reduce the H_2 escape;

iii. In both cases, the performances obtained are not an average of the performances obtained with the single Pt/C and single Pd/C electrodes, showing a good synergy of the two electrocatalyst in these configurations.

Finally, the author believe that the cathode was likely limiting in the conditions of the study, and this might explain that the results obtained seem sometimes incoherent, or at least not crystal-clear. Besides, the authors admit that the results obtained are very complex and that the modifications of the BOR mechanism that occur when using the mixed or graded architecture are unclear.

Thirdly, the degradation mechanism of carbon-supported Pt electrocatalyst, occuring during an accelerated stress test (AST) in liquid alkaline electrolyte (0.1 M NaOH) was investigated using *in situ* Fourier transform infrared spectroscopy and identical-location transmission electron microscopy. The AST consisted in 150 CV in the potential range $0.1 < E < 1.23$ V *vs*. RHE at $v = 100$ mV s^{-1} at $T = 25$°C. The AST was also performed with Pd/C and PtRu/C electrocatalysts to generalize our findings. The results showed that:

i. The degradation mechanism of Pt/C in liquid alkaline electrolyte involves the production of carbonates at the vicinity of the Pt|C interface, at rather low or high electrode potential depending on the amount of Pt sites;

ii. The carbonates formation is promoted by the Pt (metal) nanoparticles;

iii. The formation of carbonates results from the formation of CO-containing surface groups that form on the carbon support, which are electrooxidized by the metal NPs; the ability of the latter to electrooxidize those groups is decisive in the extent of the degradation.

The experiments conducted during this PhD enabled to increase the knowledge about the complex BOR and the degradation mechanism of carbon-supported PGM electrocatalysts in liquid alkaline media. Obviously, three years of work were not enough to perform all the experiments that could have enabled to find answers to many questions that arise from the different studies conducted here. Hence, this work opens several outlook:

i. The BOR mechanism occuring on Pd-based electrocatalysts in DBFC operation conditions should be investigated either by DEMS, FTIR or RRDE measurements in order to be able, as it has been done for Pt/C, to deeply understand the BOR mechanism on this material; in addition, the ratio $[BH_4^-]/[OH^-]$ shoud be studied and adapted to the nature of the electrocatalyst;

ii. The addition of ceria on Pd-based electrocatalysts should be tested with better-defined electrocatalyst before concluding that Pd/C-CeO_2 is not a sustainable material for the BOR;

iii. The idea of mixing and grading electrocatalysts to enhance the BOR efficiency is interesting and promising, but the results obtained are very complex and the understanding is tricky. Thus, it seems wise to first check whether the cathode was limiting or not in the overall DBFC performances; then, the cell design and parameters could be optimized. Finally, this architecture could be tested with other electocatalysts, including non-noble metals;

iv. The unstability of carbon-supported PGM electrocatalysts in alkaline media cannot be ignored anymore and should be taken into account in the research of sustainable electrocatalysts for alkaline fuel cells. It would be interesting to detect the transcient CO_2 production involved in this mechanism by DEMS, and to visualize the solid carbonates by advanced TEM-EELS (electron energy loss spectroscopy) techniques. Besides, other AST protocols should be proposed in order to study the durability of the electrodes in other conditions (in presence of the fuel and with another potential range), and potentially become benchmark protocol to be used by the scientic community: this was initited in this thesis (with only two electrocatalysts) but should be pursued.

Last, but not least, to conclude this work with a more general approach, the author is convinced that, in order to fully address the energetic crisis, even if science is offering technological solutions, these latter will for sure be necessary, but not enough to solve rapidly and efficiently the issues at stake. Thus, because not any energy production system can operate with zero impact on the planet, the author would like to invite each and everyone of us to question its own energy consumption, and try to not be influenced by those who makes us believe that we constantly need new and bigger possessions. Then, we could maybe try to operate some changes in our lives, in order to tend towards a better use and share of the planet resources: what are we likely to try?

Annex

Annex 1: Electrocatalysts synthesis

1.A: Pd/C synthesis

The Pd/C electrocatalysts were synthesized by Robert W. Atkinson III from the Naval Research Laboratory (Washington DC, USA) via a vapor deposition method reported previously [287,288]. The carbon support (Vulcan XC-72, Cabot) and powdered precursor (palladium (II) (2,4)-pentanedionate, 99%, Sigma Aldrich) were combined and mixed in a borosilicate vial. Support and precursor masses were chosen to produce 250 mg total of the carbon-supported Pd electrocatalysts in a range of targeted metal weight fractions from 20 to 50 wt.% Pd. Then, the vials were transferred to a vacuum oven. After the oven was sealed, air was evacuated and replaced by dry nitrogen three times. The oven was heated to 170°C at 0.752 atm and allowed to dwell for 15 h. At this temperature and pressure, the precursor sublimed, reacted with the carbon support surface, and Pd nanoparticles were grown on the carbon support. The oven was cooled passively to room temperature before the electrocatalyst powders were removed. The sample masses were recorded to determine final metal weight fraction of Pd deposited on the carbon support and were found to be 22, 33, 44 and 53 wt.% Pd. Samples were heat-treated at 240°C for 2 h in a flowing 10% H_2 (balance Argon) mixture to remove interstitial carbon that was absorbed into the palladium lattice during synthesis from decomposition of the organic ligands in the Pd precursor [289,290]. Those electrocatalysts were used in **CHAPTER II** and **CHAPTER III**.

A similar synthesis was used but with the final heat treatment with a lower temperature (170 instead of 240°C) to reduce the rate of agglomeration: this lead to electrocatalyst with higher ECSA (*ca*. 20 *vs*. 60 $m^2 g_{Pd}^{-1}$). This electrocatalyst was used in the study of **CHAPTER III**.

1.B: Pd/C-CeO_2 synthesis

The Pd/C-CeO_2 electrocatalysts (studied in **CHAPTER II**) were prepared by the group of Hamish A. Miller from the CNR-ICCOM (Florence, Italy) using the following protocol:

(1) Carbon was suspended in water, stirred vigorously for 30 min and sonicated for 20 min. To this mixture, a solution of K_2PdCl_4 in water was slowly added (during *ca*. 1 hour) under vigorous stirring, followed by addition of an aqueous solution of 2.5 M KOH. Next, ethanol was added and the resulting mixture was heated at 80°C for 60 min. The desired product Pd/C was filtered off, washed several times with distilled water to neutrality and finally dried under vacuum at 65°C until constant weigh was reached.

(2) Pd/C was dispersed in ethanol by sonication for 30 min and a THF solution of $Ce(ODe)_4$ was added dropwise in order to obtain a final CeO_2 loading of 40 wt.%. After 30 min of sonication, 20 mL of a 10% solution of H_2O in EtOH was added dropwise to hydrolyze the alkoxide and form amorphous CeO_2, followed by further 30 min of sonication. The solid product was collected by filtration through a 0.45 µm PTFE filter and washed thoroughly with ethanol.

Annex 2: Analytical techniques

2.A: Microscopy techniques

The interaction between an electron beam and a material can produce several signals which enable to get insights into the morphology and structure of the material. In the particular case of transmission electron microscopy, it is required that the thickness of the sample is less than 100 nm, which is the case with the carbon-supported metal nanoparticles studied in this thesis (if supported by a relevant TEM grid baring a carbon or Lacey carbon thin membrane). The electrons are generated by a LaB6 filament, accelerated by a potential field and focused by electrostatic and electromagnetic lenses before reaching the sample. TEM observations were performed by Marian Chatenet using a JEOL 2010 TEM apparatus equipped with an LaB6 filament operating at 200 kV with a point to point resolution of 0.19 nm.

A TEM can be modified into a scanning transmission electron microscope (STEM) and coupled with X-ray energy dispersive spectroscopy (X-EDS) to build elemental maps, giving insights into the sample chemical properties. STEM images and X-EDS elemental maps were acquired by Laetitia Dubau (from LEPMI) using a JEOL 2100F microscope operated at 200 kV equipped with a silicon drift detector (SDD) Centurio retractable detector.

In both cases, the electrocatalyst was deposited (in its powder form or in within a suspension) on a carbon-coated Lacey copper or gold grid (Ted Pella, Inc.).

2.B: X-ray diffraction (XRD)

Based on the diffraction of X-rays on the lattice of a crystalline material, angles and intensities of the obtained signal can be analyzed in order to obtain information on the crystalline structure of a material. X-ray diffraction analyses were performed on a PANalytical X' Pert Pro MPD vertical diffractometer/goniometer equipped with a diffracted beam monochromator using Cu radiation (λ = 0.15418 nm) operating at 45 kV and 40 mA. The diffraction patterns were acquired by Thierry Encinas at the CMTC (Grenoble-INP). The diffraction patterns were obtained for a 2θ

angle between 15 and 139° with a step of 0.033° for 480 s. The spectra were analyzed using the Highscore Plus software package.

2.C: X-ray photoelectron spectroscopy (XPS)

XPS is a photoelectron spectroscopy method that involves the measurement of photoelectron spectra induced by X-ray photons. In a XPS experiment, a sample is bombarded by X-rays with a given wavelength, and produces photoelectrons which are then detected. Photoelectrons have energies specific to each element of the sample surface, which makes it possible to determine the composition of the sample surface.

XPS patterns were acquired by Vincent Martin and obtained using a Thermo Scientific K-alpha spectrometer with a monochromatized Al X-ray source (hν = 1486.6 eV; spot size = 400 µm). Pass energies of 30 and 100 eV were used to record the core level and the survey spectra, respectively. All spectra were acquired using an electron flood gun to compensate possible positive charge accumulation during measurements. The obtained spectra were deconvoluted and fitted using Thermo Scientific™ Advantage Software. The evolution of the oxygen content during the AST was monitored by dividing the peak areas of the O1s and the C1s signal (without the contribution of Nafion®-related envelopes), after proper background subtraction, by their respective atomic sensitivity factors:

$$\left(\frac{\mathrm{O1s}}{\mathrm{C1s}}\right) = \frac{\mathrm{I_{O1s}}}{0.63} \times \frac{0.205}{\mathrm{I_{C1s}}}$$

2.D: Fourier transform infrared spectroscopy (FTIR)

Infrared absorption spectroscopy is a technique used to obtain the absorption spectra of a sample, which is formed as a consequence of the absorption of electromagnetic radiation by molecules which absorb these frequencies of light, because they correspond to frequencies of the molecule bonds vibrations. The energy of a molecule is defined as the sum of the following contributing energy terms: (i) the rotation of the molecule, (ii) the vibration of the atoms which constitute the molecule, (iii) the movements of the electrons within the molecules and (iv) the energy of the translation of the molecule. When the molecule is surrounded by an electromagnetic field, an energy transfer from the electromagnetic field to the molecule is possible, when the Bohr condition is valid:

$$\Delta E = E_1 - E_0 = \mathrm{h}\nu$$

where ΔE is the difference between two energy levels ($E_1 > E_0$), *h* is the Planck constant and v is the frequency of the incident radiation.

The common infrared spectral range covers the wavenumber from 400 to 4000 cm^{-1} and enables to probe the vibrational energy levels of a molecule. A molecule can go into vibrational resonance only if its dipole is not zero, and the chemical bonds can vibrate according to the following movements (illustrated in **Figure A.1**): stretching, bending, rocking, wagging and twisting.

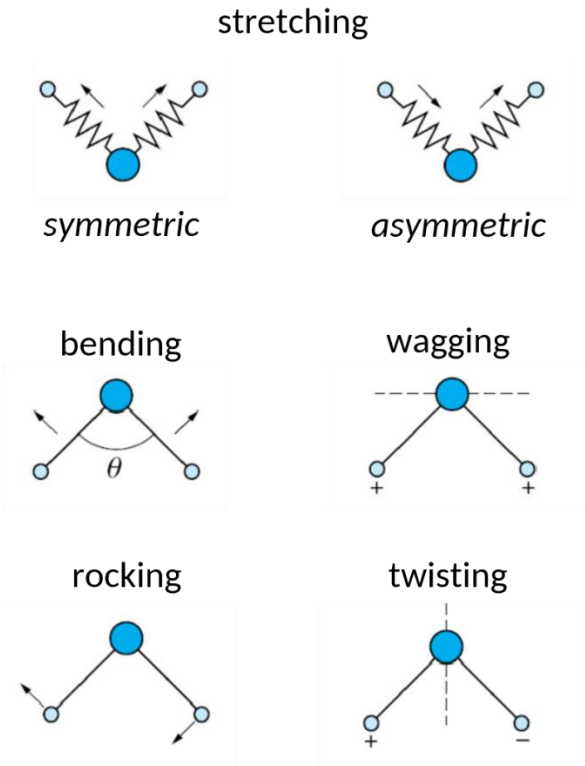

Figure A.1. Illustration of the chemical bonds movements in a molecule.

Annex 3: Electrode preparation for DBFC measurements

The electrodes used for the DBFC measurements were prepared by ultrasonic spray deposition of catalysts suspensions onto bipolar graphite plates via a layer-by-layer method using an automated ultrasonic spray apparatus illustrated in **Figure A.2**; the method is widely described in ref. [291]. Briefly, the base of the apparatus has a computer numerical control (CNC) router table with an adjustable head drive, which serves as the holder for the ultrasonic nozzle. The head is controlled by a software to set fabrication variables such as spray height, spray speed, and automation of repeated steps. The ultrasonic spray system consists of a 10 mL PTFE-tipped plunger and dispenser syringe and a syringe, pump that controls the ink flow rate delivered to the ultrasonic narrow spray atomizer nozzle. A pinpoint spray shaper is connected to the

ultrasonic narrow spray atomizer nozzle, and a gas inlet port at the side of the spray shaper forces the catalyst ink droplet into the pinpoint spray pattern down to 250 µm at the focal point. The catalyst spray pattern consists of four separate and distinct paths to ensure a uniform coating of the catalyst layer, which in our case was made directly on the bipolar graphite plates, as illustrated in **Figure A.3**.

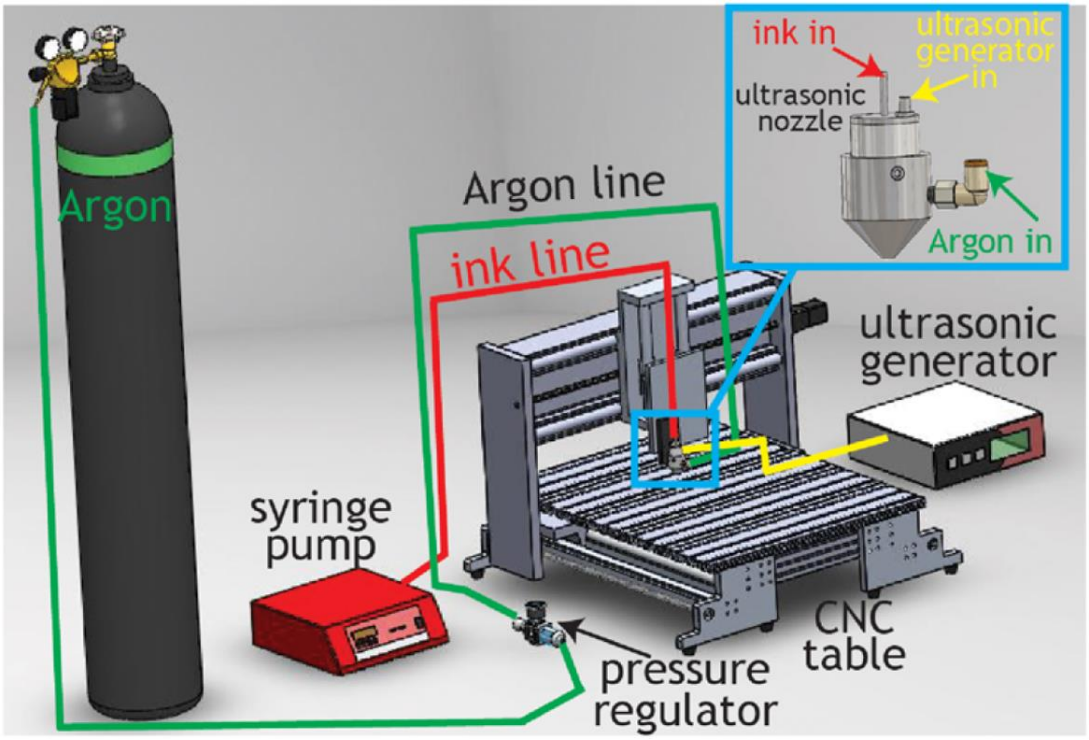

Figure A.2. Schematics of ultrasonic spray deposition apparatus. From ref. [291].

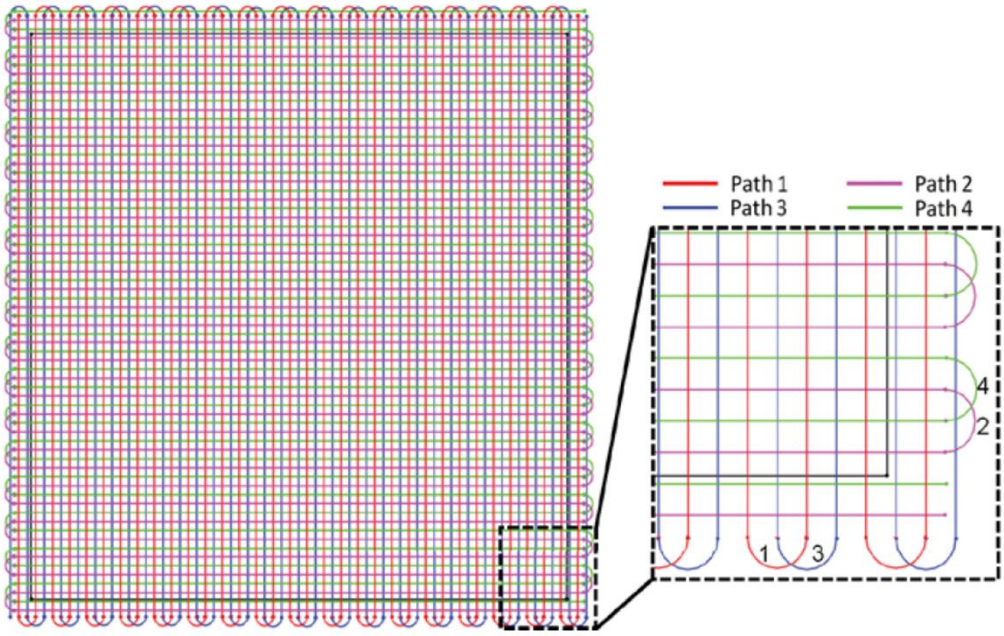

Figure A.3. Ultrasonic spray pattern showing paths #1–4. From ref. [291].

Annex 4: Supplementary figures

Chapter II

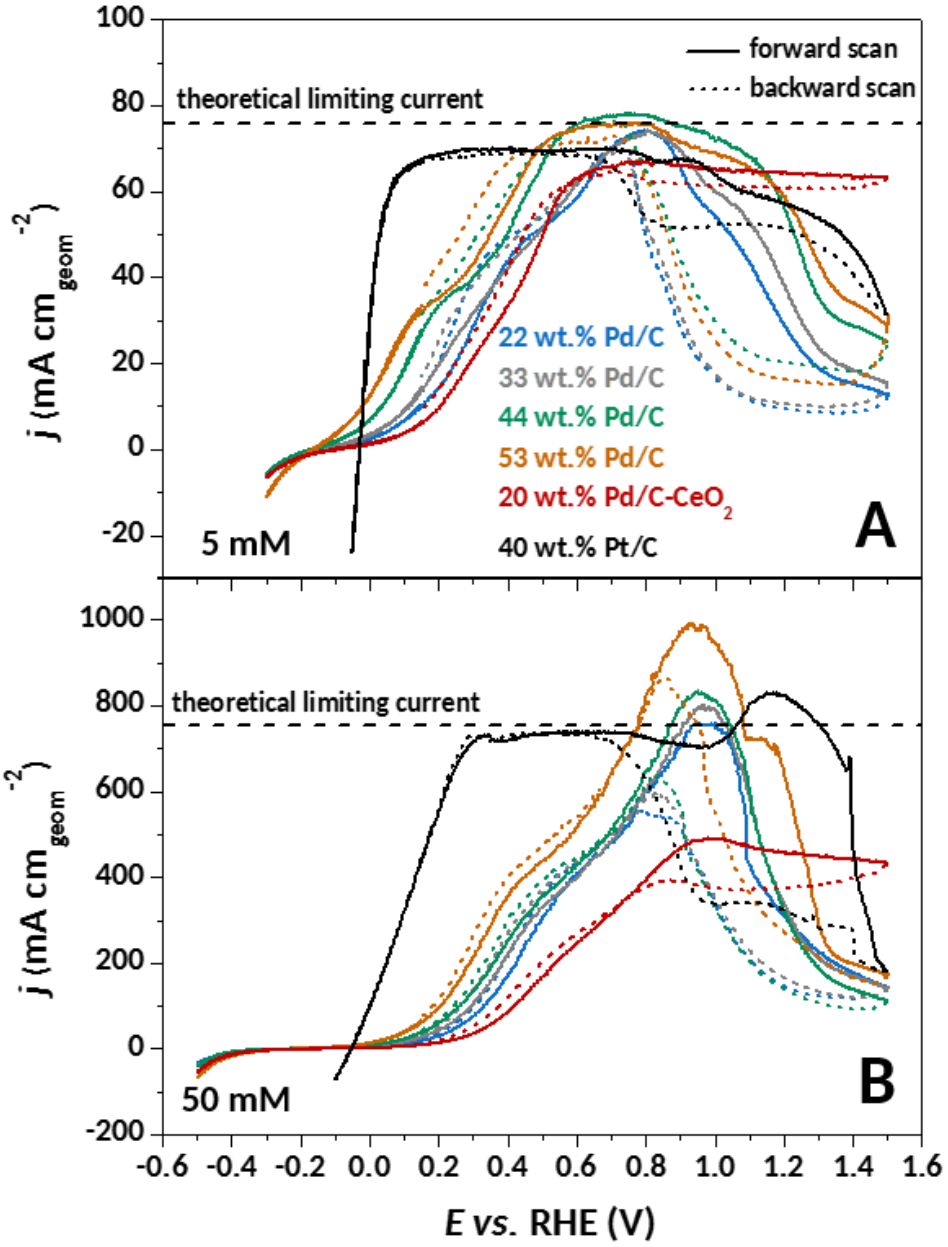

Figure A.4. BOR voltammograms obtained on the electrocatalysts studied in this work for (A) 5 mM $NaBH_4$ and (B) 50 mM $NaBH_4$ in 1 M NaOH. Other conditions: Ar-saturated electrolytes, T = 60°C, v = 20 mV s^{-1}, ω = 1600 rpm.

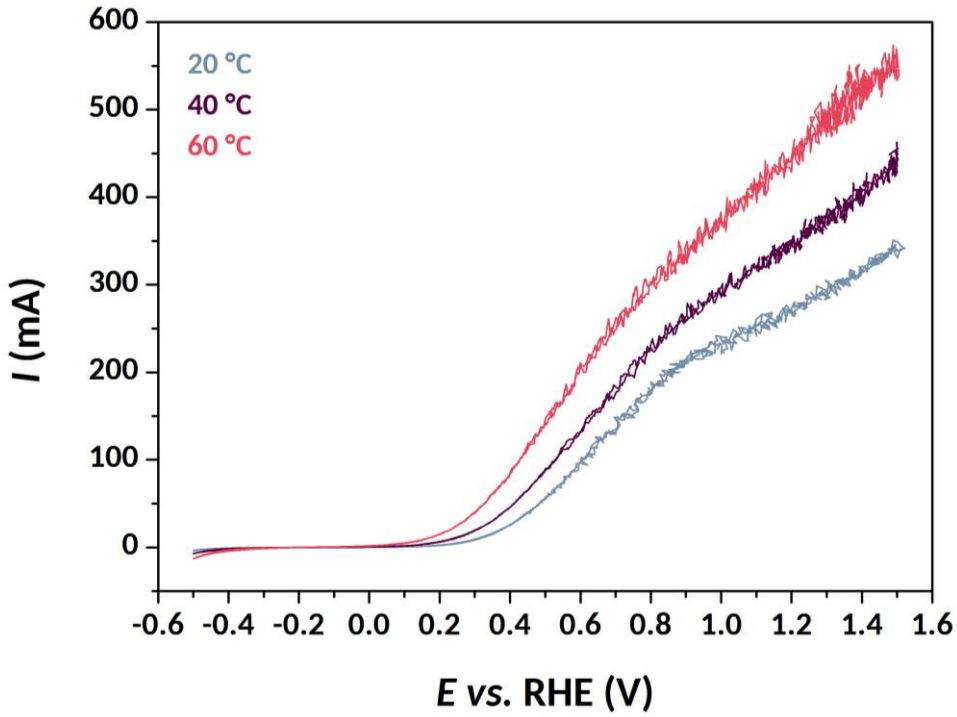

Figure A.5. BOR voltammograms obtained on the 53 wt.% Pd/C electrocatalysts in 500 mM $NaBH_4$ + 1 M NaOH for three temperatures (20, 40 and 60°C). Other conditions: Ar-saturated electrolytes, v = 20 mV s^{-1}, ω = 1600 rpm.

Chapter IV

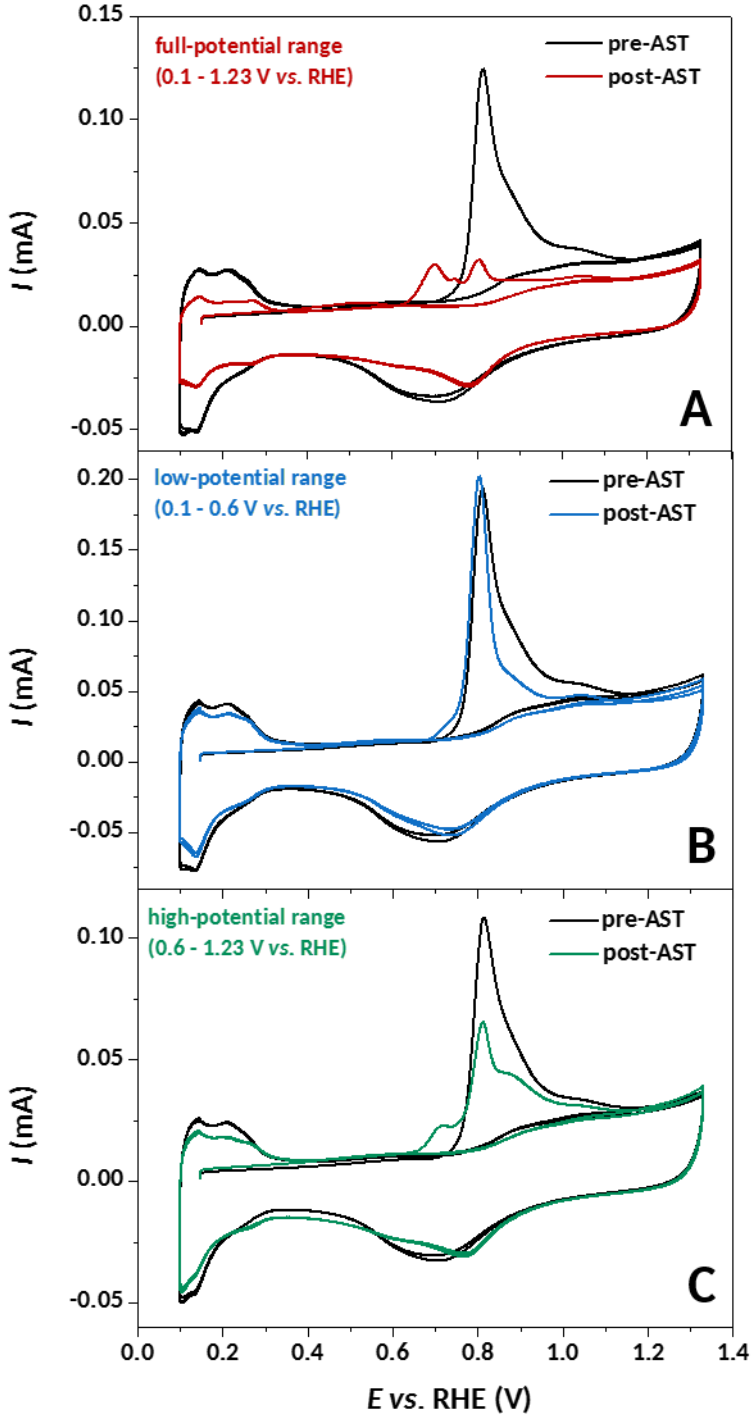

Figure A.6. FTIR spectra obtained under stepwise oxidation conditions from *E* = 0.1 to 1.2 V *vs.* RHE in 0.1 M NaOH on polycrystalline gold. The relative reflectivity is calculated using the spectra obtained at *E* = 0.1 V *vs.* RHE as the reference reflectivity.

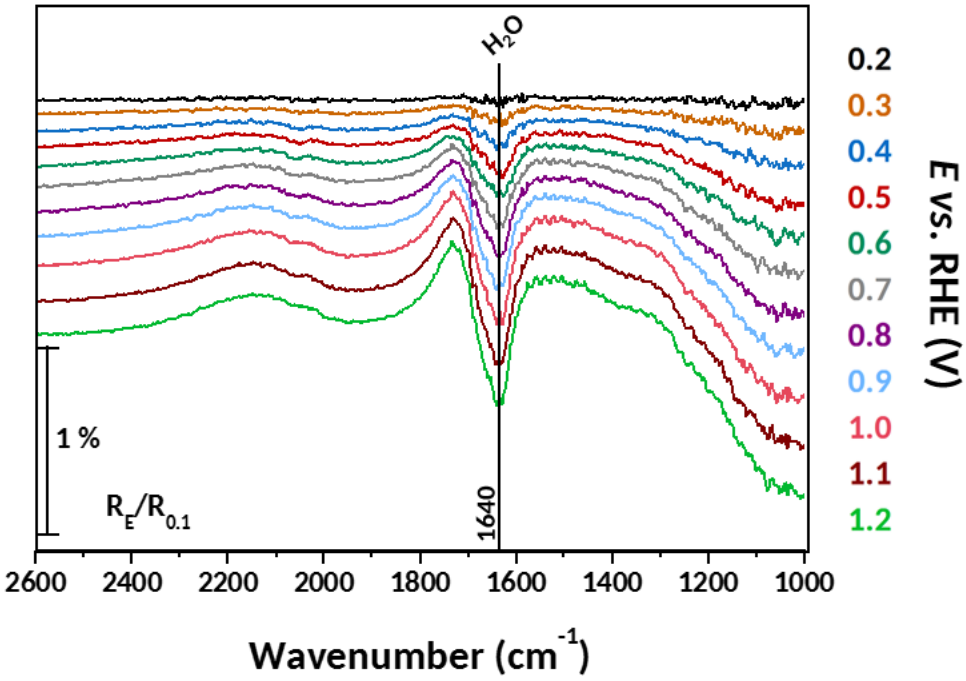

Figure A.7. FTIR spectra obtained under stepwise oxidation conditions from *E* = 0.1 to 1.2 V *vs.* RHE in 0.1 M NaOH on polycrystalline gold. The relative reflectivity is calculated using the spectra obtained at *E* = 0.1 V *vs.* RHE as the reference reflectivity.

References

[1] United Nations Department of Economic and Social Affairs Population Division (2017), World Population Prospects: The 2017 Revision, Key Findings and Advance Tables, n.d.

[2] International Energy Agency, Key world energy statistics, 2017.

[3] T. Blunier, J.A. Chappellaz, J. Schwander, J.-M. Barnola, T. Desperts, B. Stauft, D. Raynaud, Atmospheric methane, record from a greenland ice core over the last 1000 year, Geophys. Res. Lett. 20 (1993) 2219–2222. doi:10.1029/93GL02414.

[4] D.M. Etheridge, L.P. Steele, R.L. Langenfelds, R.J. Francey, J.M. Barnola, V.I. Morgan, Natural and anthropogenic changes in atmospheric CO2 over the last 1000 years from air in Antarctic ice and firn, J. Geophys. Res. Atmos. 101 (1996) 4115–4128. doi:10.1029/95JD03410.

[5] Robert T. Watson, the Core Writing Team, eds., Climate change 2001: Synthesis Report. A contribution of working groups I, II, and III to the Third Assessment Report of the Intergovernmental Panel on Climate Change, Cambridge University Press, 2001.

[6] Intergovernmental Panel on Climate Change, Global Warming of 1.5℃, Summary for Policymakers, 2018.

[7] International Renewable Energy Agency, Global Energy Transformation: A Roadmap to 2050 (2019 Edition), Abu Dhabi, 2019.

[8] C.F. Schoenbein, X. On the voltaic polarization of certain solid and fluid substances, London, Edinburgh, Dublin Philos. Mag. J. Sci. (1839) 43–45. doi:10.1080/14786443908649658.

[9] W.R. Grove, LXXII. On a gaseous voltaic battery, London, Edinburgh, Dublin Philos. Mag. J. Sci. (1842) 417–420. doi:10.1080/14786444208621600.

[10] F.T. Bacon, Fuel cells, past, present and future, Electrochim. Acta. 14 (1969) 569–585. doi:10.1016/0013-4686(69)87042-8.

[11] P. Stevens, F. Novel-Cattin, A. Hammou, C. Lamy, M. Cassir, Piles à combustible, Tech. L'Ingénieur. D3340 (2000) 1–28.

[12] T. Alleau, F. Barbier, Les piles à combustibles : des caractéritiques aux domaines d'applications, Actual. Chim. 252 (2001) 48–57.

[13] K. Mazloomi, C. Gomes, Hydrogen as an energy carrier: Prospects and challenges, Renew. Sustain. Energy Rev. 16 (2012) 3024–3033. doi:10.1016/j.rser.2012.02.028.

[14] G.R. Astbury, A review of the properties and hazards of some alternative fuels, Process Saf. Environ. Prot. 86 (2008) 397–414. doi:10.1016/j.psep.2008.05.001.

[15] M. Balat, Potential importance of hydrogen as a future solution to environmental and transportation problems, Int. J. Hydrogen Energy. 33 (2008) 4013–4029. doi:10.1016/j.ijhydene.2008.05.047.

[16] Association française pour l'hydrogène et les piles à combustible, Production et Consommation d'Hydrogène Aujourd'hui, 2016.

[17] B. Sakintuna, F. Lamaridarkrim, M. Hirscher, Metal hydride materials for solid hydrogen storage: A review, Int. J. Hydrogen Energy. 32 (2007) 1121–1140. doi:10.1016/j.ijhydene.2006.11.022.

[18] Y. Zhu, C. Yang, J. Zhu, L. Li, Structural and electrochemical hydrogen storage properties of Mg2Ni-based alloys, J. Alloys Compd. 509 (2011) 5309–5314. doi:10.1016/j.jallcom.2011.02.017.

[19] W.C. Xu, K. Takahashi, Y. Matsuo, Y. Hattori, M. Kumagai, S. Ishiyama, K. Kaneko, S. Iijima, Investigation of hydrogen storage capacity of various carbon materials, Int. J. Hydrogen Energy. 32 (2007) 2504–2512. doi:10.1016/j.ijhydene.2006.11.012.

[20] R.B. Biniwale, S. Rayalu, S. Devotta, M. Ichikawa, Chemical hydrides: A solution to high capacity hydrogen storage and supply, Int. J. Hydrogen Energy. 33 (2008) 360–365. doi:10.1016/j.ijhydene.2007.07.028.

[21] Afhypac, La distribution de l'hydrogène pour les véhicules automobiles, 2016.

[22] La Région Auvergne Rhône Alpes, Zero Emission Valley (ZEV), le plan régional pour le déploiement de l'hydrogène, remporte l'appel à projet européen Blending call 2017, Lyon, 2017.

[23] B.C. Ong, S.K. Kamarudin, S. Basri, Direct liquid fuel cells: A review, Int. J. Hydrogen Energy. 42 (2017) 10142–10157. doi:10.1016/j.ijhydene.2017.01.117.

[24] M. Chatenet, Tailoring membranes, Nat. Energy. 4 (2019) 261–262. doi:10.1038/s41560-019-0348-8.

[25] M. Kilpatrick, C.D. McKinney, Kinetics of the Reaction of Lithium Borohydride in Aqueous Acid Solution, J. Am. Chem. Soc. 72 (1950) 5474–5476.

[26] H.I. Schlesinger, H.C. Brown, A.E. Finholt, J.R. Gilbreath, H.R. Hoekstra, E.K. Hyde, Sodium

Borohydride, Its Hydrolysis and its Use as a Reducing Agent and in the Generation of Hydrogen, J. Am. Chem. Soc. 75 (1953) 215. doi:10.1021/ja01097a057.

[27] U.B. Demirci, O. Akdim, J. Andrieux, J. Hannauer, R. Chamoun, P. Miele, Sodium borohydride hydrolysis as hydrogen generator: Issues, state of the art and applicability upstream froma fuel cell, Fuel Cells. 10 (2010) 335–350. doi:10.1002/fuce.200800171.

[28] B.H. Liu, Z.P. Li, J.K. Zhu, S. Suda, Influences of hydrogen evolution on the cell and stack performances of the direct borohydride fuel cell, J. Power Sources. 183 (2008) 151–156. doi:10.1016/j.jpowsour.2008.04.079.

[29] C. Kim, K.J. Kim, M.Y. Ha, Investigation of the characteristics of a stacked direct borohydride fuel cell for portable applications, J. Power Sources. 180 (2008) 114–121. doi:10.1016/j.jpowsour.2008.01.082.

[30] C. Kim, K.J. Kim, M.Y. Ha, Performance enhancement of a direct borohydride fuel cell in practical running conditions, J. Power Sources. 180 (2008) 154–161. doi:10.1016/j.jpowsour.2008.01.042.

[31] K. Mochalov, V. Khain, G. Gil'manshin, Kinetic studies on intermediate steps of BH4 hydrolysis, Kinet. i Katal. 9 (1965) 541–544.

[32] R. Retnamma, A.Q. Novais, C.M. Rangel, Kinetics of hydrolysis of sodium borohydride for hydrogen production in fuel cell applications: A review, Int. J. Hydrogen Energy. 36 (2011) 9772–9790. doi:10.1016/j.ijhydene.2011.04.223.

[33] W. Büchner, H. Niederprünt, Sodium borohydride and amine-boranes, commercially important reducting agents., Pure Appl. Chem. 49 (1977) 733–743.

[34] H.I. Schlesinger, H.C. Brown, B. Abraham, A.C. Bond, N. Davidson, A.E. Finholt, J.R. Gilbreath, H. Hoekstra, L. Horvitz, E.K. Hyde, J.J. Katz, J. Knight, R.A. Lad, D.L. Mayfield, L. Rapp, D.M. Ritter, A.M. Schwartz, I. Sheft, L.D. Tuck, A.O. Walker, New Developments in the Chemistry of Diborane and the Borohydrides. I. General Summary1, J. Am. Chem. Soc. 75 (1953) 186–190. doi:10.1021/ja01097a049.

[35] G. Broja, W. Schlabacher, Process for the Production of Alkali Metal Borohydrides, DE Patent 1108670, 1959.

[36] F. Schubert, K. Lang, W. Schlabacher, Process for the Production of Borohydrides, DE Patent 1067005, 1959.

[37] Y. Wu, M.T. Kelly, J. V. Ortega, Review of Chemical Processes for the Synthesis of Sodium Borohydride, 2004.

[38] E.L. Gyenge, C.W. Oloman, Electrosynthesis attempts of tetrahydridoborates, J. Appl. Electrochem. 28 (1998) 1147–1151.

[39] Y. Kojima, T. Haga, Recycling process of sodium metaborate to sodium borohydride, Int. J. Hydrogen Energy. 28 (2003) 989–993. doi:10.1016/S0360-3199(02)00173-8.

[40] Z.P. Li, N. Morigazaki, B.H. Liu, S. Suda, Preparation of sodium borohydride by the reaction of MgH2 with dehydrated borax through ball milling at room temperature, J. Alloys Compd. 349 (2003) 232–236. doi:10.1016/S0925-8388(02)00872-1.

[41] M.E. Indig, R.N. Snyder, Sodium Borohydride, An Interesting Anodic Fuel (1), J. Electrochem. Soc. 109 (1962) 1104–1106. doi:10.1149/1.2425247.

[42] S.C. Amendola, P. Onnerud, M.T. Kelly, P.J. Petillo, S.L. Sharp-Goldman, M. Binder, A novel high power density borohydride-air cell, J. Power Sources. 84 (1999) 130–133. doi:http://dx.doi.org/10.1016/S0378-7753(99)00259-1.

[43] I. Merino-Jiménez, C. Ponce De León, A.A. Shah, F.C. Walsh, Developments in direct borohydride fuel cells and remaining challenges, J. Power Sources. 219 (2012) 339–357. doi:10.1016/j.jpowsour.2012.06.091.

[44] N.A. Choudhury, J. Ma, Y. Sahai, High performance and eco-friendly chitosan hydrogel membrane electrolytes for direct borohydride fuel cells, J. Power Sources. 210 (2012) 358–365. doi:10.1016/j.jpowsour.2012.03.013.

[45] Z. Wang, J. Parrondo, C. He, S. Sankarasubramanian, V. Ramani, Efficient pH-gradient-enabled microscale bipolar interfaces in direct borohydride fuel cells, Nat. Energy. 4 (2019) 281–289. doi:10.1038/s41560-019-0330-5.

[46] D. a Finkelstein, N. Da Mota, J.L. Cohen, H.D. Abruña, Rotating Disk Electrode (RDE) Investigation of BH4− and BH3OH− Electro-oxidation at Pt and Au: Implications for BH4− Fuel Cells, J. Phys. Chem. C. 113 (2009) 19700–19712. doi:10.1021/jp900933c.

[47] D.A. Finkelstein, C.D. Letcher, D.J. Jones, L.M. Sandberg, D.J. Watts, H.D. Abruña, Self-Poisoning during BH4- Oxidation at Pt and Au, and in Situ Poison Removal Procedures for BH4- Fuel Cells, J. Phys. Chem. C. 117 (2013) 1571–1581. doi:10.1021/jp308677f.

[48] B. Molina Concha, M. Chatenet, E.A. Ticianelli, F.H.B. Lima, In situ infrared (FTIR) study of

the mechanism of the borohydride oxidation reaction on smooth Pt electrode, J. Phys. Chem. C. 115 (2011) 12439–12447. doi:10.1021/jp2002589.

[49] F.H.B. Lima, A.M. Pasqualeti, M.B. Molina Concha, M. Chatenet, E.A. Ticianelli, Borohydride electrooxidation on Au and Pt electrodes, Electrochim. Acta. 84 (2012) 202–212. doi:10.1016/j.electacta.2012.05.030.

[50] G. Rostamikia, M.J. Janik, Borohydride Oxidation over Au(111): A First-Principles Mechanistic Study Relevant to Direct Borohydride Fuel Cells, J. Electrochem. Soc. 156 (2009) B86. doi:10.1149/1.3010382.

[51] G. Rostamikia, M.J. Janik, First principles mechanistic study of borohydride oxidation over the Pt(1 1 1) surface, Electrochim. Acta. 55 (2010) 1175–1183. doi:10.1016/j.electacta.2009.10.002.

[52] Z. Jusys, R.J. Behm, Borohydride electrooxidation over Pt/C, AuPt/C and Au/C catalysts: Partial reaction pathways and mixed potential formation, Electrochem. Commun. 60 (2015) 9–12. doi:10.1016/j.elecom.2015.07.021.

[53] K. Wang, J. Lu, L. Zhuang, A mechanistic study of borohydride anodic oxidation, Catal. Today. 170 (2011) 99–109. doi:10.1016/j.cattod.2010.12.023.

[54] P.Y. Olu, A. Bonnefont, M. Rouhet, S. Bozdech, N. Job, M. Chatenet, E. Savinova, Insights into the potential dependence of the borohydride electrooxidation reaction mechanism on platinum nanoparticles supported on ordered carbon nanomaterials, Electrochim. Acta. 179 (2015) 637–646. doi:10.1016/j.electacta.2015.02.158.

[55] P.Y. Olu, A. Bonnefont, G. Braesch, V. Martin, E.R. Savinova, M. Chatenet, Influence of the concentration of borohydride towards hydrogen production and escape for borohydride oxidation reaction on Pt and Au electrodes - experimental and modelling insights, J. Power Sources. 375 (2018) 300–309. doi:10.1016/j.jpowsour.2017.07.061.

[56] K. Jambunathan, B.C. Shah, J.L. Hudson, A.C. Hillier, Scanning electrochemical microscopy of hydrogen electro-oxidation. Rate constant measurements and carbon monoxide poisoning on platinum, J. Electroanal. Chem. 500 (2001) 279–289. doi:10.1016/S0022-0728(00)00344-2.

[57] N.M. Marković, P.N. Ross, Surface science studies of model fuel cell electrocatalysts, Surf. Sci. Rep. 45 (2002) 117–229. doi:10.1016/S0167-5729(01)00022-X.

[58] A. Ohma, K. Shinohara, A. Liyama, T. Yoshidab, A. Daimaruc, Membrane and Catalyst

Performance Targets for Automotive Fuel Cells by FCCJ Membrane, Catalyst, MEA WG, ECS Trans. 41 (2011) 775–784. doi:10.1149/1.3635611.

[59] Departement of Energy, Cell Component Accelerated Stress Test Protocols for PEM Fuel Cells, 2007.

[60] P.Y. Olu, N. Job, M. Chatenet, Evaluation of anode (electro)catalytic materials for the direct borohydride fuel cell: Methods and benchmarks, J. Power Sources. 327 (2016) 235–257. doi:10.1016/j.jpowsour.2016.07.041.

[61] M. V. Mirkin, H. Yang, A.J. Bard, Borohydride Oxidation at a Gold Electrode, J. Electrochem. Soc. 139 (1992) 2212–2217. doi:10.1149/1.2221204.

[62] R.X. Feng, H. Dong, Y.D. Wang, X.P. Ai, Y.L. Cao, H.X. Yang, A simple and high efficient direct borohydride fuel cell with MnO 2-catalyzed cathode, Electrochem. Commun. 7 (2005) 449–452. doi:10.1016/j.elecom.2005.02.023.

[63] H. Çelikkan, M. Şahin, M.L. Aksu, T. Nejat Veziroğlu, The investigation of the electrooxidation of sodium borohydride on various metal electrodes in aqueous basic solutions, Int. J. Hydrogen Energy. 32 (2007) 588–593. doi:10.1016/j.ijhydene.2006.06.065.

[64] X. Geng, H. Zhang, Y. Ma, H. Zhong, Borohydride electrochemical oxidation on carbon-supported Pt-modified Au nanoparticles, J. Power Sources. 195 (2010) 1583–1588. doi:10.1016/j.jpowsour.2009.09.036.

[65] D.A. Finkelstein, C.D. Letcher, D.J. Jones, L.M. Sandberg, D.J. Watts, H.D. Abruña, Self-Poisoning during BH4 – Oxidation at Pt and Au, and in Situ Poison Removal Procedures for BH4 – Fuel Cells, J. Phys. Chem. C. 117 (2013) 1571–1581. doi:10.1021/jp308677f.

[66] M. Chatenet, F. Micoud, I. Roche, E. Chainet, Kinetics of sodium borohydride direct oxidation and oxygen reduction in sodium hydroxide electrolyte. Part I. BH4- electro-oxidation on Au and Ag catalysts, Electrochim. Acta. 51 (2006) 5459–5467. doi:10.1016/j.electacta.2006.02.015.

[67] M. Simoes, S. Baranton, C. Coutanceau, Electrooxidation of sodium borohydride at Pd, Au, and Pd xLAu1-x carbon-supported nanocatalysts, J. Phys. Chem. C. 113 (2009) 13369–13376. doi:10.1021/jp902741z.

[68] A.M. Pasqualeti, P.Y. Olu, M. Chatenet, F.H.B. Lima, Borohydride electrooxidation on carbon-supported noble metal nanoparticles: Insights into hydrogen and hydroxyborane

formation, ACS Catal. 5 (2015) 2778–2787. doi:10.1021/acscatal.5b00107.

[69] P.Y. Olu, C.R. Barros, N. Job, M. Chatenet, Electrooxidation of NaBH4 in Alkaline Medium on Well-defined Pt Nanoparticles Deposited onto Flat Glassy Carbon Substrate: Evaluation of the Effects of Pt Nanoparticle Size, Inter-Particle Distance, and Loading, Electrocatalysis. 5 (2014) 288–300. doi:10.1007/s12678-014-0195-0.

[70] P.Y. Olu, F. Deschamps, G. Caldarella, M. Chatenet, N. Job, Investigation of platinum and palladium as potential anodic catalysts for direct borohydride and ammonia borane fuel cells, J. Power Sources. 297 (2015) 492–503. doi:10.1016/j.jpowsour.2015.08.022.

[71] J.I. Martins, M.C. Nunes, R. Koch, L. Martins, M. Bazzaoui, Electrochemical oxidation of borohydride on platinum electrodes: The influence of thiourea in direct fuel cells, Electrochim. Acta. 52 (2007) 6443–6449. doi:10.1016/j.electacta.2007.04.066.

[72] J.I. Martins, M.C. Nunes, Comparison of the electrochemical oxidation of borohydride and dimethylamine borane on platinum electrodes: Implication for direct fuel cells, J. Power Sources. 175 (2008) 244–249. doi:10.1016/j.jpowsour.2007.09.028.

[73] B. Molina Concha, M. Chatenet, Direct oxidation of sodium borohydride on Pt, Ag and alloyed Pt-Ag electrodes in basic media. Part I Bulk electrodes, Electrochim. Acta. 54 (2009) 6130–6139. doi:10.1016/j.electacta.2009.04.074.

[74] E. Gyenge, Electrooxidation of borohydride on platinum and gold electrodes: Implications for direct borohydride fuel cells, Electrochim. Acta. 49 (2004) 965–978. doi:10.1016/j.electacta.2003.10.008.

[75] E. Gyenge, M. Atwan, D. Northwood, Electrocatalysis of Borohydride Oxidation on Colloidal Pt and Pt-Alloys (Pt-Ir, Pt-Ni, and Pt-Au) and Application for Direct Borohydride Fuel Cell Anodes, J. Electrochem. Soc. 153 (2006) A150. doi:10.1149/1.2131831.

[76] B.H. Liu, Z.P. Li, S. Suda, Electrocatalysts for the anodic oxidation of borohydrides, Electrochim. Acta. 49 (2004) 3097–3105. doi:10.1016/j.electacta.2004.02.023.

[77] Z.P. Li, B.H. Liu, K. Arai, K. Asaba, S. Suda, Evaluation of alkaline borohydride solutions as the fuel for fuel cell, J. Power Sources. 126 (2004) 28–33. doi:10.1016/j.jpowsour.2003.08.017.

[78] P.Y. Olu, B. Gilles, N. Job, M. Chatenet, Influence of the surface morphology of smooth platinum electrodes for the sodium borohydride oxidation reaction, Electrochem. Commun. 43 (2014) 47–50. doi:10.1016/j.elecom.2014.02.018.

[79] D. Duan, X. You, J. Liang, S. Liu, Y. Wang, Carbon supported Cu-Pd nanoparticles as anode catalyst for direct borohydride-hydrogen peroxide fuel cells, Electrochim. Acta. 176 (2015) 1126–1135. doi:10.1016/j.electacta.2015.07.118.

[80] M. Simões, S. Baranton, C. Coutanceau, Influence of bismuth on the structure and activity of Pt and Pd nanocatalysts for the direct electrooxidation of NaBH4, Electrochim. Acta. 56 (2010) 580–591. doi:10.1016/j.electacta.2010.09.006.

[81] J.Q. Yang, B.H. Liu, S. Wu, Carbon-supported Pd catalysts: Influences of nanostructure on their catalytic performances for borohydride electrochemical oxidation, J. Power Sources. 194 (2009) 824–829. doi:10.1016/j.jpowsour.2009.06.034.

[82] B.H. Liu, Z.P. Li, S. Suda, Development of high-performance planar borohydride fuel cell modules for portable applications, J. Power Sources. 175 (2008) 226–231. doi:10.1016/j.jpowsour.2007.09.047.

[83] C. Celik, F.G. Boyaci San, H.I. Sarac, Effects of operation conditions on direct borohydride fuel cell performance, J. Power Sources. 185 (2008) 197–201. doi:10.1016/j.jpowsour.2008.06.066.

[84] J. Ma, Y. Sahai, Effect of electrode fabrication method and substrate material on performance of alkaline fuel cells, Electrochem. Commun. 30 (2013) 63–66. doi:10.1016/j.elecom.2013.02.005.

[85] G. Behmenyar, A.N. Akin, Investigation of carbon supported Pd-Cu nanoparticles as anode catalysts for direct borohydride fuel cell, J. Power Sources. 249 (2014) 239–246. doi:10.1016/j.jpowsour.2013.10.063.

[86] H. Qin, K. Chen, C. Zhu, J. Liu, J. Wang, Y. He, H. Chi, H. Ni, Z. Ji, High electrocatalytic activity for borohydride oxidation on palladium nanocubes enclosed by {200} facets, J. Power Sources. 299 (2015) 241–245. doi:10.1016/j.jpowsour.2015.09.007.

[87] L. Yi, Y. Song, X. Wang, L. Yi, J. Hu, G. Su, W. Yi, H. Yan, Carbon supported palladium hollow nanospheres as anode catalysts for direct borohydride-hydrogen peroxide fuel cells, J. Power Sources. 205 (2012) 63–70. doi:10.1016/j.jpowsour.2012.01.017.

[88] E. Sanli, H. Çelikkan, B. Zühtü Uysal, M.L. Aksu, Anodic behavior of Ag metal electrode in direct borohydride fuel cells, Int. J. Hydrogen Energy. 31 (2006) 1920–1924. doi:10.1016/j.ijhydene.2006.04.003.

[89] E. Sanli, B.Z. Uysal, M.L. Aksu, The oxidation of NaBH4 on electrochemicaly treated silver

electrodes, Int. J. Hydrogen Energy. 33 (2008) 2097–2104. doi:10.1016/j.ijhydene.2008.01.049.

[90] M. Chatenet, M.B. Molina-Concha, N. El-Kissi, G. Parrour, J.P. Diard, Direct rotating ring-disk measurement of the sodium borohydride diffusion coefficient in sodium hydroxide solutions, Electrochim. Acta. 54 (2009) 4426–4435. doi:10.1016/j.electacta.2009.03.019.

[91] B. Molina Concha, M. Chatenet, Direct oxidation of sodium borohydride on Pt, Ag and alloyed Pt–Ag electrodes in basic media. Part II Carbon-supported nanoparticles, Electrochim. Acta. 54 (2009) 6130–6139. doi:10.1016/j.electacta.2009.04.074.

[92] B.H. Liu, Z.P. Li, S. Suda, Anodic Oxidation of Alkali Borohydrides Catalyzed by Nickel, J. Electrochem. Soc. 150 (2003) A398. doi:10.1149/1.1553785.

[93] A. Tegou, S. Armyanov, E. Valova, O. Steenhaut, A. Hubin, G. Kokkinidis, S. Sotiropoulos, Mixed platinum-gold electrocatalysts for borohydride oxidation prepared by the galvanic replacement of nickel deposits, J. Electroanal. Chem. 634 (2009) 104–110. doi:10.1016/j.jelechem.2009.07.016.

[94] J.-H. Kim, H.-S. Kim, Y.-M. Kang, M.-S. Song, S. Rajendran, S.-C. Han, D.-H. Jung, J.-Y. Lee, Carbon-Supported and Unsupported Pt Anodes for Direct Borohydride Liquid Fuel Cells, J. Electrochem. Soc. 151 (2004) A1039. doi:10.1149/1.1756351.

[95] J. Durst, A. Siebel, C. Simon, F. Hasche, J. Herranz, H. a Gasteiger, New insights into the electrochemical hydrogen oxidation and evolution reaction mechanism, Energy Environ. Sci. 7 (2014) 2255–2260. doi:10.1039/c4ee00440j.

[96] W. Sheng, H.A. Gasteiger, Y. Shao-Horn, Hydrogen oxidation and evolution reaction kinetics on platinum: acid vs alkaline electrolytes, J. Electrochem. Soc. 157 (2010) B1529. doi:10.1149/1.3483106.

[97] N.M. Marković, T.J. Schmidt, B.N. Grgur, H.A. Gasteiger, R.J. Behm, P.N. Ross, Effect of Temperature on Surface Processes at the Pt(111)–Liquid Interface: Hydrogen Adsorption, Oxide Formation, and CO Oxidation, J. Phys. Chem. B. 103 (1999) 8568–8577. doi:10.1021/jp991826u.

[98] N.M. Marković, S.T. Sarraf, H.A. Gasteiger, P.N. Ross, Hydrogen electrochemistry on platinum low-index single-crystal surfaces in alkaline solution, J. Chem. Soc., Faraday Trans. 92 (1996) 3719–3725. doi:10.1039/ft9969203719.

[99] J.H. Morris, H.J. Gysling, D. Reed, Electrochemistry of boron compounds, Chem. Rev. 85

(1985) 51–76. doi:10.1021/cr00065a003.

[100] K. Wang, J. Lu, L. Zhuang, Direct determination of diffusion coefficient for borohydride anions in alkaline solutions using chronoamperometry with spherical Au electrodes, J. Electroanal. Chem. 585 (2005) 191–196. doi:10.1016/j.jelechem.2005.08.009.

[101] M.H. Atwan, C.L.B. Macdonald, D.O. Northwood, E.L. Gyenge, Colloidal Au and Au-alloy catalysts for direct borohydride fuel cells: Electrocatalysis and fuel cell performance, J. Power Sources. 158 (2006) 36–44. doi:10.1016/j.jpowsour.2005.09.054.

[102] H. Cheng, K. Scott, Determination of kinetic parameters for borohydride oxidation on a rotating Au disk electrode, Electrochim. Acta. 51 (2006) 3429–3433. doi:10.1016/j.electacta.2005.09.038.

[103] P. Krishnan, T.H. Yang, S.G. Advani, A.K. Prasad, Rotating ring-disc electrode (RRDE) investigation of borohydride electro-oxidation, J. Power Sources. 182 (2008) 106–111. doi:10.1016/j.jpowsour.2008.03.064.

[104] X.B. Zhang, S. Han, J.M. Yan, M. Chandra, H. Shioyama, K. Yasuda, N. Kuriyama, T. Kobayashi, Q. Xu, A new fuel cell using aqueous ammonia-borane as the fuel, J. Power Sources. 168 (2007) 167–171. doi:10.1016/j.jpowsour.2007.03.009.

[105] G. Braesch, A. Bonnefont, V. Martin, E.R. Savinova, M. Chatenet, Borohydride oxidation reaction mechanisms and poisoning effects on Au, Pt and Pd bulk electrodes: From model (low) to direct borohydride fuel cell operating (high) concentrations, Electrochim. Acta. 273 (2018) 483–494. doi:10.1016/j.electacta.2018.04.068.

[106] M. Shao, Palladium-based electrocatalysts for hydrogen oxidation and oxygen reduction reactions, J. Power Sources. 196 (2011) 2433–2444. doi:10.1016/j.jpowsour.2010.10.093.

[107] C. Grimmer, M. Grandi, R. Zacharias, B. Cermenek, H. Weber, C. Morais, T.W. Napporn, S. Weinberger, A. Schenk, V. Hacker, The electrooxidation of borohydride: A mechanistic study on palladium (Pd/C) applying RRDE, ^{11}B-NMR and FTIR, Appl. Catal. B Environ. 180 (2016) 614–621. doi:10.1016/j.apcatb.2015.07.028.

[108] V.L. Oliveira, E. Sibert, Y. Soldo-Olivier, E.A. Ticianelli, M. Chatenet, Investigation of the electrochemical oxidation reaction of the borohydride anion in palladium layers on Pt(111), Electrochim. Acta. 209 (2016) 360–368. doi:10.1016/j.electacta.2016.05.093.

[109] V.L. Oliveira, E. Sibert, Y. Soldo-Olivier, E.A. Ticianelli, M. Chatenet, Borohydride

electrooxidation reaction on Pt(111) and Pt(111) modified by a pseudomorphic Pd monolayer, Electrochim. Acta. 190 (2016) 790–796. doi:10.1016/j.electacta.2016.01.013.

[110] Z.P. Li, B.H. Liu, J.K. Zhu, S. Suda, Depression of hydrogen evolution during operation of a direct borohydride fuel cell, J. Power Sources. 163 (2006) 555–559. doi:10.1016/j.jpowsour.2006.09.037.

[111] B.H. Liu, Z.P. Li, S. Suda, A study on performance stability of the passive direct borohydride fuel cell, J. Power Sources. 185 (2008) 1257–1261. doi:10.1016/j.jpowsour.2008.08.063.

[112] A.G. Oshchepkov, G. Braesch, S. Ould-Amara, G. Rostamikia, G. Maranzana, A. Bonnefont, M.J. Janik, M. Chatenet, E.R. Savinova, Nickel Metal Nanoparticles as Anode Electrocatalyst for Highly-Efficient Direct Borohydride Fuel Cells, ACS Catal. 9 (2019) 8520–8528. doi:10.1021/acscatal.9b01616.

[113] R. Jamard, A. Latour, J. Salomon, P. Capron, A. Martinent-Beaumont, Study of fuel efficiency in a direct borohydride fuel cell, J. Power Sources. 176 (2008) 287–292. doi:10.1016/j.jpowsour.2007.10.036.

[114] X. Geng, H. Zhang, W. Ye, Y. Ma, H. Zhong, Ni-Pt/C as anode electrocatalyst for a direct borohydride fuel cell, J. Power Sources. 185 (2008) 627–632. doi:10.1016/j.jpowsour.2008.09.010.

[115] R.X. Feng, H. Dong, Y.L. Cao, X.P. Ai, H.X. Yang, Agni-catalyzed anode for direct borohydride fuel cells, Int. J. Hydrogen Energy. 32 (2007) 4544–4549. doi:10.1016/j.ijhydene.2007.08.001.

[116] J. Ma, J. Wang, Y. Liu, Iron phthalocyanine as a cathode catalyst for a direct borohydride fuel cell, J. Power Sources. 172 (2007) 220–224. doi:10.1016/j.jpowsour.2007.07.031.

[117] J. Ma, Y. Liu, Y. Liu, Y. Yan, P. Zhang, A membraneless direct borohydride fuel cell using LaNiO3- catalysed cathode, Fuel Cells. 8 (2008) 394–398. doi:10.1002/fuce.200800048.

[118] J. Ma, Y. Liu, P. Zhang, J. Wang, A simple direct borohydride fuel cell with a cobalt phthalocyanine catalyzed cathode, Electrochem. Commun. 10 (2008) 100–102. doi:10.1016/j.elecom.2007.11.006.

[119] Y. gang Wang, Y. yao Xia, A direct borohydride fuel cell using MnO2-catalyzed cathode and hydrogen storage alloy anode, Electrochem. Commun. 8 (2006) 1775–1778. doi:10.1016/j.elecom.2006.08.018.

[120] Z.P. Li, B.H. Liu, K. Arai, S. Suda, A Fuel Cell Development for Using Borohydrides as the Fuel, J. Electrochem. Soc. 150 (2003) A868. doi:10.1149/1.1576767.

[121] N.A. Choudhury, R.K. Raman, S. Sampath, A.K. Shukla, An alkaline direct borohydride fuel cell with hydrogen peroxide as oxidant, J. Power Sources. 143 (2005) 1–8. doi:10.1016/j.jpowsour.2004.08.059.

[122] C. Ponce De León, A. Kulak, S. Williams, I. Merino-Jiménez, F.C. Walsh, Improvements in direct borohydride fuel cells using three-dimensional electrodes, Catal. Today. 170 (2011) 148–154. doi:10.1016/j.cattod.2011.03.010.

[123] K.S. Freitas, B.M. Concha, E.A. Ticianelli, M. Chatenet, Mass transport effects in the borohydride oxidation reaction - Influence of the residence time on the reaction onset and faradaic efficiency, Catal. Today. 170 (2011) 110–119. doi:10.1016/j.cattod.2011.01.051.

[124] N. Duteanu, G. Vlachogiannopoulos, M.R. Shivhare, E.H. Yu, K. Scott, A parametric study of a platinum ruthenium anode in a direct borohydride fuel cell, J. Appl. Electrochem. 37 (2007) 1085–1091. doi:10.1007/s10800-007-9360-y.

[125] H. Cheng, K. Scott, Influence of operation conditions on direct borohydride fuel cell performance, J. Power Sources. 160 (2006) 407–412. doi:10.1016/j.jpowsour.2006.01.097.

[126] K.T. Park, U.H. Jung, S.U. Jeong, S.H. Kim, Influence of anode diffusion layer properties on performance of direct borohydride fuel cell, J. Power Sources. 162 (2006) 192–197. doi:10.1016/j.jpowsour.2006.07.040.

[127] H. Cheng, K. Scott, K. V. Lovell, J.A. Horsfall, S.C. Waring, Evaluation of new ion exchange membranes for direct borohydride fuel cells, J. Memb. Sci. 288 (2007) 168–174. doi:10.1016/j.memsci.2006.11.014.

[128] J. Ma, Y. Sahai, R.G. Buchheit, Evaluation of multivalent phosphate cross-linked chitosan biopolymer membrane for direct borohydride fuel cells, J. Power Sources. 202 (2012) 18–27. doi:10.1016/j.jpowsour.2011.11.003.

[129] F.G. Boyaci San, O. Okur, Ç. Iyigün Karadağ, I. Isik-Gulsac, E. Okumuş, Evaluation of operating conditions on DBFC (direct borohydride fuel cell) performance with PtRu anode catalyst by response surface method, Energy. 71 (2014) 160–169. doi:10.1016/j.energy.2014.04.037.

[130] E. Morallón, J.L. Vázquez, A. Aldaz, Electrochemical behaviour of Pt(111) in alkaline media. Effect of specific adsorption of anions, J. Electroanal. Chem. 334 (1992) 323–338. doi:10.1016/0022-0728(92)80581-N.

[131] J.L. Valdes, H.Y. Cheh, A Systematic Approach to the Determination of Possible Reaction Mechanisms of Oxygen Reduction on Platinum in Alkaline Medium, J. Electrom. Soc. 132 (1985) 2635–2640. doi:10.1149/1.2113638.

[132] X. Ge, A. Sumboja, D. Wuu, T. An, B. Li, F.W.T. Goh, T.S.A. Hor, Y. Zong, Z. Liu, Oxygen reduction in alkaline media: from mechanisms to recent advances of catalysts, ACS Catal. 5 (2015) 4643–4667. doi:10.1021/acscatal.5b00524.

[133] R. Jager, E. Hark, P.E. Kasatkin, E. Lust, Investigation of a carbon-supported Pt electrode for oxygen reduction reaction in 0.1M KOH aqueous solution, J. Electrochem. Soc. 161 (2014) F861–F867. doi:10.1149/2.0491409jes.

[134] E. Härk, R. Jäger, E. Lust, Effect of Platinum Nanoparticle Loading on Oxygen Reduction at a Pt Nanocluster-Activated Microporous-Mesoporous Carbon Support, Electrocatalysis. 6 (2015) 242–254. doi:10.1007/s12678-014-0238-6.

[135] M. Chatenet, F. Micoud, I. Roche, E. Chainet, J. Vondrák, Kinetics of sodium borohydride direct oxidation and oxygen reduction in sodium hydroxide electrolyte. Part II. O2 reduction, Electrochim. Acta. 51 (2006) 5452–5458. doi:10.1016/j.electacta.2006.02.014.

[136] B.H. Liu, Z.P. Li, K. Arai, S. Suda, Performance improvement of a micro borohydride fuel cell operating at ambient conditions, Electrochim. Acta. 50 (2005) 3719–3725. doi:10.1016/j.electacta.2005.01.018.

[137] F.A. Coowar, G. Vitins, G.O. Mepsted, S.C. Waring, J.A. Horsfall, Electrochemical oxidation of borohydride at nano-gold-based electrodes: Application in direct borohydride fuel cells, J. Power Sources. 175 (2008) 317–324. doi:10.1016/j.jpowsour.2007.09.063.

[138] R. Jamard, J. Salomon, A. Martinent-Beaumont, C. Coutanceau, Life time test in direct borohydride fuel cell system, J. Power Sources. 193 (2009) 779–787. doi:10.1016/j.jpowsour.2009.03.057.

[139] J.R. Varcoe, P. Atanassov, D.R. Dekel, A.M. Herring, M.A. Hickner, P.A. Kohl, A.R. Kucernak, W.E. Mustain, K. Nijmeijer, K. Scott, T. Xu, L. Zhuang, Anion-exchange membranes in electrochemical energy systems, Energy Environ. Sci. 7 (2014) 3135–3191.

doi:10.1039/C4EE01303D.

[140] D.R. Dekel, Review of cell performance in anion exchange membrane fuel cells, J. Power Sources. 375 (2018) 158–169. doi:10.1016/j.jpowsour.2017.07.117.

[141] A. Serov, I. V. Zenyuk, C.G. Arges, M. Chatenet, Hot topics in alkaline exchange membrane fuel cells, J. Power Sources. 375 (2018) 149–157. doi:10.1016/j.jpowsour.2017.09.068.

[142] X. Yang, Y. Liu, S. Li, X. Wei, L. Wang, Y. Chen, A direct borohydride fuel cell with a polymer fiber membrane and non-noble metal catalysts, Sci. Rep. 2 (2012) 567. doi:10.1038/srep00567.

[143] X. Yang, X. Wei, C. Liu, Y. Liu, The electrocatalytic application of RuO2 in direct borohydride fuel cells, Mater. Chem. Phys. 145 (2014) 269–273. doi:10.1016/j.matchemphys.2014.01.044.

[144] D. Chen, S. Yu, X. Liu, X. Li, Porous polybenzimidazole membranes with excellent chemical stability and ion conductivity for direct borohydride fuel cells, J. Power Sources. 282 (2015) 323–327. doi:10.1016/j.jpowsour.2015.02.082.

[145] W.C. Schumb, Stability of Concentrated Hydrogen Peroxide Solutions, Ind. Eng. Chem. 41 (1949) 992–1003. doi:10.1021/ie50473a026.

[146] C.G. Arges, V. Prabhakaran, L. Wang, V. Ramani, Bipolar polymer electrolyte interfaces for hydrogen-oxygen and direct borohydride fuel cells, in: Int. J. Hydrogen Energy, Elsevier Ltd, 2014: pp. 14312–14321. doi:10.1016/j.ijhydene.2014.04.099.

[147] M. Ünlü, J. Zhou, P.A. Kohl, Hybrid anion and proton exchange membrane fuel cells, J. Phys. Chem. C. 113 (2009) 11416–11423. doi:10.1021/jp903252u.

[148] P.N. Ross, H. Sokol, The Corrosion of carbon black anodes in alkaline electrolyte I. Acetylene black and the effect of cobalt catalyzation, J. Electrochem. Soc. 131 (1984) 1742–1750. doi:10.1149/1.2115953.

[149] N. Staud, P.N. Ross, The corrosion of carbon black anodes in alkaline electrolyte II. Acetylene black and the effect of oxygen evolution catalysts on corrosion, J. Electrochem. Soc. 133 (1986) 1079–1084. doi:10.1149/1.2108790.

[150] P.N. Ross, M. Sattler, The corrosion of carbon black anodes in alkaline electrolyte III. The effect of graphitization on the corrosion resistance of furnace black, J. Electrochem. Soc. 135 (1988) 1464–1470. doi:10.1149/1.2096029.

[151] N. Staud, S. Harvey, P.N. Ross, The corrosion of carbon black anodes in alkaline electrolyte IV. Current efficiencies for oxygen evoltion from metal oxide-impregnated graphitized furnace blacks, J. Electrochem. Soc. 136 (1989) 3570–3576. doi:10.1149/1.2096511.

[152] H. Cheng, K. Scott, Investigation of Ti mesh-supported anodes for direct borohydride fuel cells, J. Appl. Electrochem. 36 (2006) 1361–1366. doi:10.1007/s10800-006-9199-7.

[153] Z.X. Liu, H.Y. Qin, Z.P. Li, B.H. Liu, K.N. Zhu, Performance degradation of a direct borohydride fuel cell, J. Power Sources. 236 (2013) 17–24. doi:10.1016/j.jpowsour.2013.01.175.

[154] H. Cheng, K. Scott, K. Lovell, Material aspects of the design and operation of direct borohydride fuel cells, Fuel Cells. 6 (2006) 367–375. doi:10.1002/fuce.200500260.

[155] L. Dubau, L. Castanheira, F. Maillard, M. Chatenet, O. Lottin, G. Maranzana, J. Dillet, A. Lamibrac, J.C. Perrin, E. Moukheiber, A. Elkaddouri, G. De Moor, C. Bas, L. Flandin, N. Caqué, A review of PEM fuel cell durability: Materials degradation, local heterogeneities of aging and possible mitigation strategies, Wiley Interdiscip. Rev. Energy Environ. 3 (2014) 540–560. doi:10.1002/wene.113.

[156] R.M. Darling, J.P. Meyers, Kinetic Model of Platinum Dissolution in PEMFCs, J. Electrochem. Soc. 150 (2003) A1523. doi:10.1149/1.1613669.

[157] R. Borup, J. Meyers, B. Pivovar, Y.S. Kim, R. Mukundan, N. Garland, D. Myers, M. Wilson, F. Garzon, D. Wood, P. Zelenay, K. More, K. Stroh, T. Zawodzinski, J. Boncella, J.E. McGrath, M. Inaba, K. Miyatake, M. Hori, K. Ota, Z. Ogumi, S. Miyata, A. Nishikata, Z. Siroma, Y. Uchimoto, K. Yasuda, K.I. Kimijima, N. Iwashita, Scientific aspects of polymer electrolyte fuel cell durability and degradation, Chem. Rev. 107 (2007) 3904–3951. doi:10.1021/cr050182l.

[158] Y. Shao-Horn, W.C. Sheng, S. Chen, P.J. Ferreira, E.F. Holby, D. Morgan, Instability of supported platinum nanoparticles in low-temperature fuel cells, Top. Catal. 46 (2007) 285–305. doi:10.1007/s11244-007-9000-0.

[159] W. Sheng, S. Chen, E. Vescovo, Y. Shao-Horn, Size Influence on the Oxygen Reduction Reaction Activity and Instability of Supported Pt Nanoparticles, J. Electrochem. Soc. 159 (2012) B96–B103. doi:10.1149/2.009202jes.

[160] E. Guilminot, a. Corcella, F. Charlot, F. Maillard, M. Chatenet, Detection of Ptz+ Ions and

Pt Nanoparticles Inside the Membrane of a Used PEMFC, J. Electrochem. Soc. 154 (2007) B96–B105. doi:10.1149/1.2388863.

[161] E. Guilminot, C. Iojoiu, F. Maillard, M. Chatenet, J.-Y. Sanchez, E. Claude, E. Rossinot, Membrane and Active Layer Degradation Following PEMFC Steady-State Operation, J. Electrochem. Soc. 154 (2007) B1106–B1114. doi:10.1149/1.2775282.

[162] K. Yasuda, A. Taniguchi, T. Akita, T. Ioroi, Z. Siroma, Platinum dissolution and deposition in the polymer electrolyte membrane of a PEM fuel cell as studied by potential cycling, Phys. Chem. Chem. Phys. 8 (2006) 746–752. doi:10.1039/b514342j.

[163] J. Xie, D.L. Wood, K.L. More, P. Atanassov, R.L. Borup, Microstructural Changes of Membrane Electrode Assemblies during PEFC Durability Testing at High Humidity Conditions, J. Electrochem. Soc. 152 (2005) A1011–A1020. doi:10.1149/1.1873492.

[164] H.P. Boehm, Surface oxides on carbon and their analysis: a critical assessment, Carbon N. Y. 40 (2002) 145–149. doi:10.1016/S0008-6223(01)00165-8.

[165] B. Avasarala, R. Moore, P. Haldar, Surface oxidation of carbon supports due to potential cycling under PEM fuel cell conditions, Electrochim. Acta. 55 (2010) 4765–4771. doi:10.1016/j.electacta.2010.03.056.

[166] J. Willsau, The influence of Pt-activation on the corrosion of carbon in gas diffusion electrodes - a dems study, J. Electroanal. Chem. 161 (1984) 93–101. doi:10.1016/0368-1874(84)83298-0.

[167] K. Kinoshita, Carbon: Electrochemical and Physicochemical Properties, John Wiley & sons, New York, 1988.

[168] F. Maillard, A. Bonnefont, F. Micoud, An EC-FTIR study on the catalytic role of Pt in carbon corrosion, Electrochem. Commun. 13 (2011) 1109–1111. doi:10.1016/j.elecom.2011.07.011.

[169] P. Yu, M. Pemberton, P. Plasse, PtCo/C cathode catalyst for improved durability in PEMFCs, J. Power Sources. 144 (2005) 11–20. doi:10.1016/j.jpowsour.2004.11.067.

[170] F.R. Nikkuni, L. Dubau, E.A. Ticianelli, M. Chatenet, Accelerated degradation of Pt<inf>3</inf>Co/C and Pt/C electrocatalysts studied by identical-location transmission electron microscopy in polymer electrolyte environment, Appl. Catal. B Environ. 176–177 (2015) 486–499. doi:10.1016/j.apcatb.2015.04.035.

[171] S. Sharma, B.G. Pollet, Support materials for PEMFC and DMFC electrocatalysts - A review, J. Power Sources. 208 (2012) 96–119. doi:10.1016/j.jpowsour.2012.02.011.

[172] P.L. Antonucci, L. Pino, N. Giordano, G. Pinna, A comparative analysis of structural and surface effects in the electrochemical corrosion of carbons, Mater. Chem. Phys. 21 (1989) 495–506. doi:10.1016/0254-0584(89)90148-X.

[173] P. Stonehart, Carbon Substrates for Phosphoric Acid Fuel Cell Cathodes, Carbon N. Y. 22 (1984) 423–431. doi:10.1016/0008-6223(84)90015-0.

[174] O. V. Cherstiouk, A.N. Simonov, N.S. Moseva, S. V. Cherepanova, P.A. Simonov, V.I. Zaikovskii, E.R. Savinova, Microstructure effects on the electrochemical corrosion of carbon materials and carbon-supported Pt catalysts, Electrochim. Acta. 55 (2010) 8453–8460. doi:10.1016/j.electacta.2010.07.047.

[175] K. Artyushkova, S. Pylypenko, M. Dowlapalli, P. Atanassov, Structure-to-property relationships in fuel cell catalyst supports: Correlation of surface chemistry and morphology with oxidation resistance of carbon blacks, J. Power Sources. 214 (2012) 303–313. doi:10.1016/j.jpowsour.2012.04.095.

[176] A. Zadick, L. Dubau, N. Sergent, G. Berthomé, M. Chatenet, Huge Instability of Pt/C Catalysts in Alkaline Medium, ACS Catal. 5 (2015) 4819–4824. doi:10.1021/acscatal.5b01037.

[177] A. Zadick, L. Dubau, U.B. Demirci, M. Chatenet, Effects of Pd Nanoparticle Size and Solution Reducer Strength on Pd/C Electrocatalyst Stability in Alkaline Electrolyte, J. Electrochem. Soc. 163 (2016) F781–F787. doi:10.1149/2.0141608jes.

[178] S. Kabir, A. Zadick, P. Atanassov, L. Dubau, M. Chatenet, Stability of carbon-supported palladium nanoparticles in alkaline media: A case study of graphitized and more amorphous supports, Electrochem. Commun. 78 (2017) 33–37. doi:10.1016/j.elecom.2017.03.017.

[179] A. Zadick, L. Dubau, A. Zalineeva, C. Coutanceau, M. Chatenet, When cubic nanoparticles get spherical: An Identical Location Transmission Electron Microscopy case study with Pd in alkaline media, Electrochem. Commun. 48 (2014) 1–4. doi:10.1016/j.elecom.2014.07.020.

[180] A. Zadick, L. Dubau, K. Artyushkova, A. Serov, P. Atanassov, M. Chatenet, Nickel-based electrocatalysts for ammonia borane oxidation: enabling materials for carbon-free-fuel

direct liquid alkaline fuel cell technology, Nano Energy. 37 (2017) 248–259. doi:10.1016/j.nanoen.2017.05.035.

[181] H.A. Miller, F. Vizza, M. Marelli, A. Zadick, L. Dubau, M. Chatenet, S. Geiger, S. Cherevko, H. Doan, R.K. Pavlicek, S. Mukerjee, D.R. Dekel, Highly active nanostructured palladium-ceria electrocatalysts for the hydrogen oxidation reaction in alkaline medium, Nano Energy. 33 (2017) 293–305. doi:10.1016/j.nanoen.2017.01.051.

[182] M. Martins, B. Šljukić, C.A.C. Sequeira, Ö. Metin, M. Erdem, T. Sener, D.M.F. Santos, Biobased carbon-supported palladium electrocatalysts for borohydride fuel cells, Int. J. Hydrogen Energy. 1 (2016) 0–8. doi:10.1016/j.ijhydene.2016.04.039.

[183] A. Trovarelli, Catalytic properties of ceria and CeO2-containing materials, Catal. Rev. 38 (1996) 439–520. doi:10.1080/01614949608006464.

[184] H.A. Miller, A. Lavacchi, F. Vizza, M. Marelli, F. Di Benedetto, F. D'Acapito, Y. Paska, M. Page, D.R. Dekel, A Pd/C-CeO 2 Anode Catalyst for High-Performance Platinum-Free Anion Exchange Membrane Fuel Cells, Angew. Chemie Int. Ed. 128 (2016) 6108–6111. doi:10.1002/anie.201600647.

[185] Y. Zhao, F. Wang, J. Tian, X. Yang, L. Zhan, Preparation of Pt/CeO2/HCSs anode electrocatalysts for direct methanol fuel cells, Electrochim. Acta. 55 (2010) 8998–9003. doi:10.1016/j.electacta.2010.08.021.

[186] C. Xu, Z. Tian, P. Shen, S.P. Jiang, Oxide (CeO2, NiO, Co3O4 and Mn3O4)-promoted Pd/C electrocatalysts for alcohol electrooxidation in alkaline media, Electrochim. Acta. 53 (2008) 2610–2618. doi:10.1016/j.electacta.2007.10.036.

[187] R.F.B. De Souza, A.E.A. Flausino, D.C. Rascio, R.T.S. Oliveira, E.T. Neto, M.L. Calegaro, M.C. Santos, Ethanol oxidation reaction on PtCeO2/C electrocatalysts prepared by the polymeric precursor method, Appl. Catal. B Environ. 91 (2009) 516–523. doi:10.1016/j.apcatb.2009.06.022.

[188] C. Xu, P. kang Shen, Y. Liu, Ethanol electrooxidation on Pt/C and Pd/C catalysts promoted with oxide, J. Power Sources. 164 (2007) 527–531. doi:10.1016/j.jpowsour.2006.10.071.

[189] Y. Bai, J. Wu, X. Qiu, J. Xi, J. Wang, J. Li, W. Zhu, L. Chen, Electrochemical characterization of Pt-CeO2/C and Pt-CexZr1-xO2/C catalysts for ethanol electro-oxidation, Appl. Catal. B Environ. 73 (2007) 144–149. doi:10.1016/j.apcatb.2006.06.026.

[190] F. Micoud, F. Maillard, A. Bonnefont, N. Job, M. Chatenet, The role of the support in

COads monolayer electrooxidation on Pt nanoparticles: Pt/WOx vs. Pt/C, Phys. Chem. Chem. Phys. 12 (2010) 1182–1193. doi:10.1039/b915244j.

[191] J.A. Rodríguez, J. Hrbek, Inverse oxide/metal catalysts: A versatile approach for activity tests and mechanistic studies, Surf. Sci. 604 (2010) 241–244. doi:10.1016/j.susc.2009.11.038.

[192] J.A. Rodriguez, P. Liu, J. Graciani, S.D. Senanayake, D.C. Grinter, D. Stacchiola, J. Hrbek, J. Fernández-Sanz, Inverse Oxide/Metal Catalysts in Fundamental Studies and Practical Applications: A Perspective of Recent Developments, J. Phys. Chem. Lett. 7 (2016) 2627–2639. doi:10.1021/acs.jpclett.6b00499.

[193] C. Herrmann, G. Perrault, A. Pilla, Dual Reference Electrode for Electrochemical Pulse Studies, Anal. Chem. 40 (1968) 1173–1174. doi:10.1021/ac60263a011.

[194] Y. Garsany, I.L. Singer, K.E. Swider-Lyons, Impact of film drying procedures on RDE characterization of Pt/VC electrocatalysts, J. Electroanal. Chem. 662 (2011) 396–406. doi:10.1016/j.jelechem.2011.09.016.

[195] J.G. Chen, C.W. Jones, S. Linic, V.R. Stamenkovic, Best Practices in Pursuit of Topics in Heterogeneous Electrocatalysis, ACS Catal. 7 (2017) 6392–6393. doi:10.1021/acscatal.7b02839.

[196] A. Czerwiński, The absorption of hydrogen and deuterium in thin palladium electrodes Part I: Acidic solutions, J. Electroanal. Chem. 316 (1991) 211–221. doi:10.1016/0022-0728(91)87047-8.

[197] A. Czerwiński, R. Marassi, The absorption of hydrogen and deuterium in thin palladium electrodes Part II: Basic solutions, J. Electroanal. Chem. 322 (1992) 373–381. doi:10.1016/0022-0728(92)80089-M.

[198] G. Jerkiewicz, Hydrogen sorption at/in electrodes, Prog. Surf. Sci. 57 (1998) 137–186. doi:10.1016/S0079-6816(98)00015-X.

[199] V. Breger, E. Gileadi, Adsorption and Absorption of Hydrogen in Palladium, Electrochim. Acta. 16 (1971) 117–190. doi:10.1016/0013-4686(71)80001-4.

[200] G. Jerkiewicz, Electrochemical Hydrogen Adsorption and Absorption. Part 1: Under-potential Deposition of Hydrogen, Electrocatalysis. 1 (2010) 179–199. doi:10.1007/s12678-010-0022-1.

[201] A. Zalineeva, S. Baranton, C. Coutanceau, G. Jerkiewicz, Electrochemical behavior of unsupported shaped palladium nanoparticles, Langmuir. 31 (2015) 1605–1609. doi:10.1021/la5025229.

[202] M. Grdeń, M. Łukaszewski, G. Jerkiewicz, A. Czerwiński, Electrochemical behaviour of palladium electrode: Oxidation, electrodissolution and ionic adsorption, Electrochim. Acta. 53 (2008) 7583–7598. doi:10.1016/j.electacta.2008.05.046.

[203] D.A.J. Rand, R. Woods, The Nature of Adsorbed Oxygen on Rhodium, Palladium and Gold Electrodes, Electroanal. Chem. Interfacial Electrochem. 31 (1971) 29–38. doi:10.1016/S0022-0728(71)80039-6.

[204] J. Zheng, S. Zhou, S. Gu, B. Xu, Y. Yan, Size-Dependent Hydrogen Oxidation and Evolution Activities on Supported Palladium Nanoparticles in Acid and Base, J. Electrochem. Soc. 163 (2016) 499–506. doi:10.1149/2.0661606jes.

[205] L. Jiang, A. Hsu, D. Chu, R. Chen, Size-Dependent Activity of Palladium Nanoparticles for Oxygen Electroreduction in Alkaline Solutions, J. Electrochem. Soc. 156 (2009) B643. doi:10.1149/1.3098478.

[206] R. Pattabiraman, Electrochemical investigations on carbon supported palladium catalysts, Appl. Catal. A Gen. 153 (1997) 9–20. doi:10.1016/S0926-860X(96)00327-4.

[207] L. Fang, Q. Tao, M. Li, L. Liao, D. Chen, Y. Chen, Determination of the Real Surface Area of Palladium Electrode, Chinese J. Chem. Phys. 23 (2010) 543–548. doi:10.1088/1674-0068/23/05/543-548.

[208] K. Jukk, N. Alexeyeva, C. Johans, K. Kontturi, K. Tammeveski, Oxygen reduction on Pd nanoparticle/multi-walled carbon nanotube composites, J. Electroanal. Chem. 666 (2012) 67–75. doi:10.1016/j.jelechem.2011.12.003.

[209] M. Martins, B. Šljukić, C.A.C. Sequeira, Ö. Metin, M. Erdem, T. Sener, D.M.F. Santos, Biobased carbon-supported palladium electrocatalysts for borohydride fuel cells, Int. J. Hydrogen Energy. 41 (2016) 10914–10922. doi:10.1016/j.ijhydene.2016.04.039.

[210] T. Chierchie, C. Mayer, W.J. Lorenz, Structural changes of surface oxide layers on palladium, J. Electroanal. Chem. Interfacial Electrochem. 135 (1982) 211–220. doi:10.1016/0368-1874(82)85121-6.

[211] K. Gossner, E. Mizera, The Anodic Behaviour of Pd Electrodes in 1 M H2SO4, J, Electroanal. Chem. 125 (1981) 347–358. doi:10.1016/S0022-0728(81)80353-1.

[212] T. Mittermeier, A. Weiss, F. Hasche, H. a. Gasteiger, Activity, Stability and Degradation of Carbon Supported Palladium (Pd/C) Fuel Cell Electrocatalysts for the Oxygen Reduction, ECS Trans. 69 (2015) 303–313. doi:10.1149/06917.0303ecst.

[213] H.A. Gasteiger, S.S. Kocha, B. Sompalli, F.T. Wagner, Activity benchmarks and requirements for Pt, Pt-alloy, and non-Pt oxygen reduction catalysts for PEMFCs, Appl. Catal. B Environ. 56 (2005) 9–35. doi:10.1016/j.apcatb.2004.06.021.

[214] T.J. Schmidt, H.A. Gasteiger, G.D. Stab, P.M. Urban, D.M. Kolb, R.J. Behm, Characterization of High-Surface-Area Electrocatalysts Using a Rotating Disk Electrode Configuration, J. Electrochem. Soc. 145 (1998) 2354–2358. doi:10.1149/1.1838642.

[215] B. Losiewicz, L. Birry, A. Lasia, Effect of adsorbed carbon monoxide on the kinetics of hydrogen electrosorption into palladium, J. Electroanal. Chem. 611 (2007) 26–34. doi:10.1016/j.jelechem.2007.07.025.

[216] S. Pronkin, T. Wandlowski, ATR-SEIRAS - An approach to probe the reactivity of Pd-modified quasi-single crystal gold film electrodes, Surf. Sci. 573 (2004) 109–127. doi:10.1016/j.susc.2004.05.141.

[217] R. Gómez, A. Rodes, J.M. Pérez, J.M. Feliu, A. Aldaz, Electrochemical and in situ FTIRS studies of the CO adsorption at palladium and rhodium multilayers deposited on platinum single crystal surfaces II. Pt(100) substrate, Surf. Sci. 344 (1995) 85–97. doi:10.1016/0039-6028(95)00796-2.

[218] M. Hara, U. Linke, T. Wandlowski, Preparation and electrochemical characterization of palladium single crystal electrodes in 0.1 M H2SO4 and HClO4. Part I. Low-index phases, Electrochim. Acta. 52 (2007) 5733–5748. doi:10.1016/j.electacta.2006.11.048.

[219] S. Henning, J. Herranz, H.A. Gasteiger, Bulk-Palladium and Palladium-on-Gold Electrocatalysts for the Oxidation of Hydrogen in Alkaline Electrolyte, J. Electrochem. Soc. 162 (2015) F178–F189. doi:10.1149/2.1081501jes.

[220] A. Czerwiński, S. Zamponi, R. Marassi, The influence of carbon monoxide on hydrogen absorption by thin films of palladium, J. Electroanal. Chem. 304 (1991) 233–239. doi:10.1016/0022-0728(91)85505-J.

[221] J. Durst, C. Simon, F. Hasche, H.A. Gasteiger, Hydrogen Oxidation and Evolution Reaction Kinetics on Carbon Supported Pt, Ir, Rh, and Pd Electrocatalysts in Acidic Media, J. Electrochem. Soc. 162 (2015) F190–F203. doi:10.1149/2.0981501jes.

[222] M. Shao, J.H. Odell, S. Il Choi, Y. Xia, Electrochemical surface area measurements of platinum- and palladium-based nanoparticles, Electrochem. Commun. 31 (2013) 46–48. doi:10.1016/j.elecom.2013.03.011.

[223] V. Bambagioni, C. Bianchini, Y. Chen, J. Filippi, P. Fornasiero, M. Innocenti, A. Lavacchi, A. Marchionni, W. Oberhauser, F. Vizza, Energy Efficiency Enhancement of Ethanol Electrooxidation on Pd-CeO2/C in Passive and Active Polymer Electrolyte-Membrane Fuel Cells, ChemSusChem. 5 (2012) 1266–1273. doi:10.1002/cssc.201100738.

[224] S. Bernal, J.J. Calvino, G.A. Cifredo, J.M. Gatica, J.A. Pérez Omil, J.M. Pintado, Hydrogen chemisorption on ceria: Influence of the oxide surface area and degree of reduction, J. Chem. Soc. Faraday Trans. 89 (1993) 3499–3505. doi:10.1039/FT9938903499.

[225] J.L.G. Fierro, J. Soria, J. Sanz, J.M. Rojo, Induced changes in ceria by thermal treatments under vacuum or hydrogen, J. Solid State Chem. 66 (1987) 154–162. doi:10.1016/0022-4596(87)90230-1.

[226] B.S. Hobbs, A.C.C. Tseung, The Anodic Oxidation of Hydrogen on Platinized Tungsten Oxides I. Composition of Tungsten Blue in Platinized WO3 Hydrogen Electrocatalyst, Mod. Asp. Electrochem. 119 (1972) 580–583. doi:10.1149/1.2404265.

[227] F. Micoud, F. Maillard, A. Bonnefont, N. Job, M. Chatenet, The role of the support in COads monolayer electrooxidation on Pt nanoparticles: Pt/WOxvs. Pt/C, Phys. Chem. Chem. Phys. 12 (2010) 1182–1193. doi:10.1039/b915244j.

[228] F. Micoud, Influence d'un support MOx (M = W, Ti) sur les propriétés électrocatalytiques de nanoparticules de platine, Institut polytechnique de Grenoble, 2009.

[229] G. Cognard, Electrocatalyseurs à base d'oxydes métalliques poreux pour pile à combustibles à membrane échangeuse de protons, Université Grenobles Alpes, 2017.

[230] B.E. Hayden, D. Pletcher, J.P. Suchsland, L.J. Williams, The influence of Pt particle size on the surface oxidation of titania supported platinum, Phys. Chem. Chem. Phys. 11 (2009) 1564–1570. doi:10.1039/b817553e.

[231] F. Maillard, S. Schreier, M. Hanzlik, E.R. Savinova, S. Weinkauf, U. Stimming, Influence of particle agglomeration on the catalytic activity of carbon-supported Pt nanoparticles in CO monolayer oxidation., Phys. Chem. Chem. Phys. 7 (2005) 385–393. doi:10.1039/b411377b.

[232] B.E. Hayden, Particle size and support effects in electrocatalysis, Acc. Chem. Res. 46

(2013) 1858–1866. doi:10.1021/ar400001n.

[233] B.H. Liu, J.Q. Yang, Z.P. Li, Concentration ratio of [OH-]/[BH4-]: A controlling factor for the fuel efficiency of borohydride electro-oxidation, Int. J. Hydrogen Energy. 34 (2009) 9436–9443. doi:10.1016/j.ijhydene.2009.09.078.

[234] I. Merino-Jimenez, C.P. De Leon, F.C. Walsh, The effect of surfactants on the kinetics of borohydride oxidation and hydrolysis in the DBFC, Electrochim. Acta. 133 (2014) 539–545. doi:10.1016/j.electacta.2014.04.061.

[235] D.M.F. Santos, C. a. C. Sequeira, Determination of Kinetic and Diffusional Parameters for Sodium Borohydride Oxidation on Gold Electrodes, J. Electrochem. Soc. 156 (2009) F67. doi:10.1149/1.3082371.

[236] D.M.F. Santos, C.A.C. Sequeira, Cyclic voltammetry investigation of borohydride oxidation at a gold electrode, Electrochim. Acta. 55 (2010) 6775–6781. doi:10.1016/j.electacta.2010.05.091.

[237] A.J. Bard, L.R. Faulkner, Electrochemical methods - Fundamental and applications, second edition, 2001.

[238] L. Demarconnay, C. Coutanceau, J.M. Léger, Electroreduction of dioxygen (ORR) in alkaline medium on Ag/C and Pt/C nanostructured catalysts - Effect of the presence of methanol, Electrochim. Acta. 49 (2004) 4513–4521. doi:10.1016/j.electacta.2004.05.009.

[239] G.R. Li, Q.Q. Wang, B.H. Liu, Z.P. Li, Porous carbon as anode catalyst support to improve borohydride utilization in a direct borohydride fuel cell, Fuel Cells. 15 (2015) 270–277. doi:10.1002/fuce.201300283.

[240] J. Ma, Y. Sahai, Effect of electrode fabrication method and substrate material on performance of alkaline fuel cells, Electrochem. Commun. 30 (2013) 63–66. doi:10.1016/j.elecom.2013.02.005.

[241] E. Guilminot, A. Corcella, M. Chatenet, F. Maillard, Comparing the thin-film rotating disk electrode and the ultramicroelectrode with cavity techniques to study carbon-supported platinum for proton exchange membrane fuel cell applications, J. Electroanal. Chem. 599 (2007) 111–120. doi:10.1016/j.jelechem.2006.09.022.

[242] R.O. Stroman, G.S. Jackson, Modeling the performance of an ideal NaBH4–H2O2 direct borohydride fuel cell, J. Power Sources. 247 (2014) 756–769.

doi:10.1016/j.jpowsour.2013.08.100.

[243] Y. Zhang, A. Smirnova, A. Verma, R. Pitchumani, Design of a proton exchange membrane (PEM) fuel cell with variable catalyst loading, J. Power Sources. 291 (2015) 46–57. doi:10.1016/j.jpowsour.2015.05.002.

[244] S. Kim, S. Shimpalee, J.W. Van Zee, The effect of stoichiometry on dynamic behavior of a proton exchange membrane fuel cell (PEMFC) during load change, J. Power Sources. 135 (2004) 110–121. doi:10.1016/j.jpowsour.2004.03.060.

[245] M.G. Santarelli, M.F. Torchio, M. Calì, V. Giaretto, Experimental analysis of cathode flow stoichiometry on the electrical performance of a PEMFC stack, Int. J. Hydrogen Energy. 32 (2007) 710–716. doi:10.1016/j.ijhydene.2006.08.008.

[246] C. Ponce de León, F.C. Walsh, A. Rose, J.B. Lakeman, D.J. Browning, R.W. Reeve, A direct borohydride-Acid peroxide fuel cell, J. Power Sources. 164 (2007) 441–448. doi:10.1016/j.jpowsour.2006.10.069.

[247] D. Cao, Y. Gao, G. Wang, R. Miao, Y. Liu, A direct NaBH4-H2O2 fuel cell using Ni foam supported Au nanoparticles as electrodes, Int. J. Hydrogen Energy. 35 (2010) 807–813. doi:10.1016/j.ijhydene.2009.11.026.

[248] W. Haijun, W. Cheng, L. Zhixiang, M. Zongqiang, Influence of operation conditions on direct NaBH4/H2O2 fuel cell performance, Int. J. Hydrogen Energy. 35 (2010) 2648–2651. doi:10.1016/j.ijhydene.2009.04.020.

[249] R.C.P. Oliveira, J. Milikić, E. Daş, A.B. Yurtcan, D.M.F. Santos, B. Šljukić, Platinum/polypyrrole-carbon electrocatalysts for direct borohydride-peroxide fuel cells, Appl. Catal. B Environ. 238 (2018) 454–464. doi:10.1016/j.apcatb.2018.06.057.

[250] L. Yi, B. Yu, W. Yi, Y. Zhou, R. Ding, X. Wang, Carbon-Supported Bimetallic Platinum-Iron Nanocatalysts: Application in Direct Borohydride/Hydrogen Peroxide Fuel Cell, ACS Sustain. Chem. Eng. 6 (2018) 8142–8149. doi:10.1021/acssuschemeng.7b04438.

[251] T.H. Oh, B. Jang, S. Kwon, Performance evaluation of direct borohydride-hydrogen peroxide fuel cells with electrocatalysts supported on multiwalled carbon nanotubes, Energy. 76 (2014) 911–919. doi:10.1016/j.energy.2014.09.002.

[252] J. Liu, L. Yi, X. Wang, Q. Zhao, Y. Zhang, J. Gao, W. Wei, Investigation of nanoporous carbon supported palladium-zinc nanocomposites as anode catalysts for direct borohydride-hydrogen peroxide fuel cell, Int. J. Hydrogen Energy. 40 (2015) 7301–7307.

doi:10.1016/j.ijhydene.2015.04.047.

[253] D. Duan, X. You, J. Liang, S. Liu, Y. Wang, Carbon supported Cu-Pd nanoparticles as anode catalyst for direct borohydride-hydrogen peroxide fuel cells, Electrochim. Acta. 176 (2015) 1126–1135. doi:10.1016/j.electacta.2015.07.118.

[254] M.G. Hosseini, R. Mahmoodi, Ni@M (M = Pt, Pd and Ru) core@shell nanoparticles on a Vulcan XC-72R support with superior catalytic activity toward borohydride oxidation: Electrochemical and fuel cell studies, New J. Chem. 41 (2017) 13408–13417. doi:10.1039/c7nj02585h.

[255] M.G. Hosseini, R. Mahmoodi, Improvement of energy conversion efficiency and power generation in direct borohydride-hydrogen peroxide fuel cell: The effect of Ni-M core-shell nanoparticles (M = Pt, Pd, Ru)/Multiwalled Carbon Nanotubes on the cell performance, J. Power Sources. 370 (2017) 87–97. doi:10.1016/j.jpowsour.2017.10.017.

[256] R.C.P. Oliveira, M. Vasić, D.M.F. Santos, B. Babić, R. Hercigonja, C.A.C. Sequeira, B. Šljukić, Performance assessment of a direct borohydride-peroxide fuel cell with Pd-impregnated faujasite X zeolite as anode electrocatalyst, Electrochim. Acta. 269 (2018) 517–525. doi:10.1016/j.electacta.2018.03.021.

[257] R. Mahmoodi, M.G. Hosseini, H. Rasouli, Enhancement of output power density and performance of direct borohydride-hydrogen peroxide fuel cell using Ni-Pd core-shell nanoparticles on polymeric composite supports (rGO-PANI) as novel electrocatalysts, Appl. Catal. B Environ. 251 (2019) 37–48. doi:10.1016/j.apcatb.2019.03.064.

[258] K.J.J. Mayrhofer, S.J. Ashton, J.C. Meier, G.K.H. Wiberg, M. Hanzlik, M. Arenz, Non-destructive transmission electron microscopy study of catalyst degradation under electrochemical treatment, J. Power Sources. 185 (2008) 734–739. doi:10.1016/j.jpowsour.2008.08.003.

[259] F. Maillard, M. Eikerling, O. V Cherstiouk, S. Schreier, E. Savinova, U. Stimming, Size effects on reactivity of Pt nanoparticles in CO monolayer oxidation: the role of surface mobility., Faraday Discuss. 125 (2004) 357–377; discussion 391-407. doi:10.1039/b303911k.

[260] S. Brimaud, C. Coutanceau, E. Garnier, J.M. Léger, F. Gérard, S. Pronier, M. Leoni, Influence of surfactant removal by chemical or thermal methods on structure and electroactivity of Pt/C catalysts prepared by water-in-oil microemulsion, J. Electroanal.

Chem. 602 (2007) 226–236. doi:10.1016/j.jelechem.2007.01.003.

[261] P. Urchaga, M. Weissmann, S. Baranton, T. Girardeau, C. Coutanceau, Improvement of the platinum nanopartides-carbon substrate interaction by insertion of a thiophenol molecular bridge, Langmuir. 25 (2009) 6543–6550. doi:10.1021/la9000973.

[262] R. Sellin, J.M. Clacens, C. Coutanceau, A thermogravimetric analysis/mass spectroscopy study of the thermal and chemical stability of carbon in the Pt/C catalytic system, Carbon N. Y. 48 (2010) 2244–2254. doi:10.1016/j.carbon.2010.02.034.

[263] C. Lafforgue, M. Chatenet, L. Dubau, D.R. Dekel, Accelerated Stress Test of Pt/C Nanoparticles in an Interface with an Anion-Exchange Membrane - An Identical-Location Transmission Electron Microscopy Study, ACS Catal. 8 (2018) 1278–1286. doi:10.1021/acscatal.7b04055.

[264] Periodic table of element - solubility, (n.d.). https://periodic-table-of-elements.org/SOLUBILITY/potassium_carbonate (accessed May 12, 2017).

[265] P. Pascal, Nouveau traité de chimie minérale, B. Masson, Paris, 1958.

[266] Cesium carbonate, (n.d.). https://www.chemicalbook.com/ChemicalProductProperty_EN_CB3274457.htm (accessed May 12, 2017).

[267] T. Iwasita, F. Nart, In situ infrared spectroscopy at electrochemical interfaces, Prog. Surf. Sci. 55 (1997) 271–340. doi:10.1016/S0079-6816(97)00032-4.

[268] T. Iwasita, A. Rodes, E. Pastor, Vibrational spectroscopy of carbonate adsorbed on Pt(111) and Pt(110) single-crystal electrodes, J. Electroanal. Chem. 383 (1995) 181–189. doi:10.1016/0022-0728(94)03708-B.

[269] B.G. Oliver, A.R. Davis, Vibrational Spectroscopic Studies of Aqueous Alkali Metal Bicarbonate and Carbonate Solutions, Can. J. Chem. 51 (2006) 698–702. doi:10.1139/v73-106.

[270] C. Su, D.L. Suarez, In situ infrared speciation of adsorbed carbonate on aluminium and iron oxides, Clays Clay Miner. 45 (1997) 814–825.

[271] G. García, P. Rodríguez, V. Rosca, M.T.M. Koper, Fourier transform infrared spectroscopy study of CO electro-oxidation on Pt(111) in alkaline media, Langmuir. 25 (2009) 13661–13666. doi:10.1021/la902251z.

[272] S.C. Chang, Y. Ho, M.J. Weaver, Applications of Real-Time FTIR Spectroscopy to the Elucidation of Complex Electroorganic Pathways: Electrooxidation of Ethylene Glycol on Gold, Platinum, and Nickel in Alkaline Solution, J. Am. Chem. Soc. 113 (1991) 9506–9513. doi:10.1021/ja00025a014.

[273] D.R.M. Godoi, H.M. Villullas, F.C. Zhu, Y.X. Jiang, S.G. Sun, J. Guo, L. Sun, R. Chen, A comparative investigation of metal-support interactions on the catalytic activity of Pt nanoparticles for ethanol oxidation in alkaline medium, J. Power Sources. 311 (2016) 81–90. doi:10.1016/j.jpowsour.2016.02.011.

[274] G. Socrates, Infrared and Raman characteristic group frequencies, John Wiley & Sons Ltd, 2001.

[275] P.E. Fanning, M.A. Vannice, A DRIFTS study of the formation of surface groups on carbon by oxidation, Carbon N. Y. 31 (1993) 721–730. doi:10.1016/0008-6223(93)90009-Y.

[276] J. Zawadzki, Infrared Studies Of Aromatic Compounds Adsorbed Oh The Surface Of Carbon Films, Carbon N. Y. 26 (1988) 603–611. doi:10.1016/0008-6223(88)90060-7.

[277] J. Zawadzki, IR spectroscopy studies of oxygen surface compounds on carbon, Carbon N. Y. 16 (1978) 491–497. doi:10.1016/0008-6223(78)90098-2.

[278] B.J. Meldrum, C.H. Rochester, In situ infrared study of the surface oxidation of activated carbon dispersed in potassium bromide, J. Chem. Soc. Faraday Trans. 86 (1990) 2997–3002. doi:10.1039/FT9908602997.

[279] C. Ishizaki, I. Marty, Surface Oxide Structures On A Commercial Activated Carbon, Carbon N. Y. 19 (1981) 409–412. doi:10.1016/0008-6223(81)90023-3.

[280] M. Pourbaix, Atlas of electrochemical equilibria in aqueous solutions, Houston, 1979.

[281] L. Castanheira, L. Dubau, M. Mermoux, G. Berthomé, N. Caqué, E. Rossinot, M. Chatenet, F. Maillard, Carbon corrosion in proton-exchange membrane fuel cells: From model experiments to real-life operation in membrane electrode assemblies, ACS Catal. 4 (2014) 2258–2267. doi:10.1021/cs500449q.

[282] L. Castanheira, W.O. Silva, F.H.B. Lima, A. Crisci, L. Dubau, F. Maillard, Carbon corrosion in proton-exchange membrane fuel cells: Effect of the carbon structure, the degradation protocol, and the gas atmosphere, ACS Catal. 5 (2015) 2184–2194. doi:10.1021/cs501973j.

[283] F. Maillard, E.R. Savinova, P.A. Simonov, V.I. Zaikovskii, U. Stimming, Infrared Spectroscopic Study of CO Adsorption and Electro-oxidation on Carbon-Supported Pt Nanoparticles: Interparticle versus Intraparticle Heterogeneity, J. Phys. Chem. B. 108 (2004) 17893–17904. doi:10.1021/jp0479163.

[284] S. Štrbac, R.R. Adžić, The influence of OH- chemisorption on the catalytic properties of gold single crystal surfaces for oxygen reduction in alkaline solutions, J. Electroanal. Chem. 403 (1996) 169–181. doi:10.1016/0022-0728(95)04389-6.

[285] Y. Yi, G. Weinberg, M. Prenzel, M. Greiner, S. Heumann, S. Becker, R. Schlögl, Electrochemical corrosion of a glassy carbon electrode, Catal. Today. 295 (2017) 32–40. doi:10.1016/j.cattod.2017.07.013.

[286] R. Chattot, T. Asset, P. Bordet, J. Drnec, L. Dubau, F. Maillard, Beyond strain and ligand effects: Microstrain-induced enhancement of the oxygen reduction reaction kinetics on various PtNi/C nanostructures, ACS Catal. 7 (2017) 398–408. doi:10.1021/acscatal.6b02356.

[287] R.W. Atkinson, R.R. Unocic, K.A. Unocic, G.M. Veith, T.A. Zawodzinski, A.B. Papandrew, Vapor synthesis and thermal modification of supportless platinum-ruthenium nanotubes and application as methanol electrooxidation catalysts, ACS Appl. Mater. Interfaces. 7 (2015) 10115–10124. doi:10.1021/am508228b.

[288] S. St. John, R.W. Atkinson, R.R. Unocic, T.A. Zawodzinski, A.B. Papandrew, Ruthenium-alloy electrocatalysts with tunable hydrogen oxidation kinetics in alkaline electrolyte, J. Phys. Chem. C. 119 (2015) 13481–13487. doi:10.1021/acs.jpcc.5b03284.

[289] S.B. Ziemecki, G.A. Jones, D.G. Swartzfager, R.L. Harlow, J. Faber, Formation of Interstitial Pd—C Phase by Interaction of Ethylene, Acetylene, and Carbon Monoxide with Palladium, J. Am. Chem. Soc. 107 (1985) 4547–4548. doi:10.1021/ja00301a031.

[290] A.B. Papandrew, C.R.I. Chisholm, S.K. Zecevic, G.M. Veith, T.A. Zawodzinski, Activity and Evolution of Vapor Deposited Pt-Pd Oxygen Reduction Catalysts for Solid Acid Fuel Cells, J. Electrochem. Soc. 160 (2013) F175–F182. doi:10.1149/2.002303jes.

[291] M.B. Sassin, Y. Garsany, B.D. Gould, K.E. Swider-Lyons, Fabrication Method for Laboratory-Scale High-Performance Membrane Electrode Assemblies for Fuel Cells, Anal. Chem. 89 (2017) 511–518. doi:10.1021/acs.analchem.6b03005.

Résumé

La pile à combustible directe à borohydrures (DBFC en anglais), qui est une sous-catégorie des piles à combustible alcalines, bénéficie des avantages de son combustible, le borohydrure de sodium ($NaBH_4$), qui confère à ce système des caractéristiques thermodynamiques et énergétiques très intéressantes. Cependant, la réaction d'électrooxydation de $NaBH_4$ (BOR en anglais) est très complexe et reste à ce jour encore peu étudiée et mal comprise sur la majorité des électrocatalyseurs (la plupart étant sous forme de nanoparticules métalliques supportées sur des noirs de carbone). De plus, de récentes études ont montré l'agressivité du milieu alcalin sur la durabilité des électrocatalyseurs conventionnels, révélant une grande perte de surface catalytique active, due principalement à un détachement des nanoparticules du support carboné. Dans ce contexte, ces travaux de thèse se sont orientés vers trois axes d'étude : (i) l'étude de la BOR sur des électrocatalyseurs à base de palladium dans des conditions proches des conditions réelles de fonctionnement de la DBFC ; (ii) l'étude de l'impact de la structure de l'anode sur les performances globales de la DBFC, et (iii) l'étude du mécanisme de dégradation d'électrocatalyseurs à base de métaux nobles dans un environnement alcalin. Les expérimentations ont été réalisées en étroite collaboration avec le U.S. Naval Research Laboratory (Washington, USA).

Les résultats obtenus ont montré qu'une grande concentration en $NaBH_4$ entraine un ralentissement de la cinétique de la réaction, due en partie à un fort empoisonnement de la surface catalytique. Par ailleurs, des marqueurs d'activité pour la BOR ont été proposés. Ensuite, l'utilisation d'électrodes à gradient de catalyseurs s'est avérée être une solution prometteuse pour mieux valoriser l'hydrogène produit via des réactions secondaires à la BOR. Enfin, l'utilisation de la spectroscopie infrarouge à transformée de Fourier couplée à de la microscopie électronique en transmission à localisation identique a permis de détecter la formation de carbonates au cours d'un test de vieillissement accéléré d'électrocatalyseurs à base de métaux nobles en milieu alcalin. Ce mécanisme explique, en partie, le détachement des nanoparticules observé au cours du test.

Mots clés : Pile à combustible directe à borohydrures, réaction d'oxydation des borohydrures, palladium, électrocatalyse, mécanismes de dégradation, spectroscopie infrarouge à transformée de Fourier

Abstract

The direct borohydride fuel cell (DBFC), a subclass of alkaline fuel cells, benefits from the advantages of its fuel, sodium borohydride ($NaBH_4$), which exhibits very interesting thermodynamic and energetic characteristics. However, the $NaBH_4$ electrooxidation reaction (BOR) is very complex; to date it remains poorly studied and understood on many electrocatalysts (most of them are in the form of metal nanoparticles supported on carbon black). In addition, recent studies reported the aggressiveness of the alkaline medium on the durability of conventional carbon-supported electrocatalysts, revealing a large loss of the active catalytic surface, mainly due to the detachment of nanoparticles from the carbon support. In this context, this thesis focused on three main areas of study: (i) the study of the BOR on palladium-based electrocatalysts in conditions close to the real operating conditions of the DBFC; (ii) the study of the impact of the anode structure on the overall performance of the DBFC, and (iii) the study of the degradation mechanism of noble metal electrocatalysts in alkaline environment. The experiments were carried out in close collaboration with the U.S. Naval Research Laboratory (Washington, USA).

The results obtained showed that a high concentration of $NaBH_4$ leads to a decrease of the reaction kinetics, due in part to poisoning of the catalytic surface. In addition, activity markers for the BOR have been proposed. Then, the use of catalysts-gradient electrodes proved to be a promising solution to better valorize the hydrogen produced via side reactions of the BOR. Finally, the use of Fourier transform infrared spectroscopy coupled with identical-location transmission electron microscopy enabled to detect the formation of carbonates during the accelerated stress test of carbon-supported noble metal electrocatalysts in alkaline medium, explaining, in part, the detachment of nanoparticles observed during the test.

Keywords: Direct borohydride fuel cell, borohydride oxidation reaction, palladium, electrocatalysis, degradation mechanisms, Fourier-transform infrared spectroscopy